Design and experimental investigation of active distributed temperature sensing probes for thermal anemometry in water

Zur Erlangung des akademischen Grades eines
Doktors der Ingenieurwissenschaften (Dr.-Ing.)
von der KIT-Fakultät für Maschinenbau
des Karlsruher Instituts für Technologie (KIT)

angenommene

Dissertation

von

M.Sc. David Christopher Rautenberg (geb. Lah)

Tag der mündlichen Prüfung:	22.06.2026
Hauptreferentin:	Prof. Dr.-Ing. Bettina Frohnapfel
Korreferent:	Prof. Dr. Dipl.-Geoökol. Christoph Thomas

Abstract

Fiber-optic distributed temperature sensing (DTS) probes for thermal anemometry (TA) are iteratively developed and tested to measure vertically upward water flow velocities in a borehole-mimicking test rig. Quantification of the hydraulic properties of groundwater flows in the Earth's crust is complicated and costly because of the limited accessibility via wells and boreholes and because of the complex composition of the rock and sediment layers in the Earth's crust. Fiber-optic DTS is an established technique for acquisition of distributed temperature profiles in the geoscientific and other technical contexts. The combination of DTS with a TA approach – i.e., utilizing forced-convective heat transfer of a heated glass-fiber cable for velocity determination – promises distributed velocity measurements along the full length of boreholes or wells during pumping tests. This technique would substantially reduce the complexity and time required to acquire flowmeter logs, thereby decreasing the costs for flowmeter log acquisition. However, none of the existing proof-of-concept studies has produced validated velocity measurements; as yet, only a qualitative flowmeter log and a demonstration of sensitivity exist.

The present study, therefore, aims to close the gap from qualitative to quantitative measurements and achieves the measurement of the vertically upward flow velocity in a borehole-mimicking test rig with absolute percentage errors below 35 % within the range of 7.1–47 mm/s. However, this encouraging result is only achieved in deionized water with the most elaborate probe design and calibration of the DTS data with two fiber sections at constant monitored temperatures. Most importantly, when the identical setup is operated with tap water, a pronounced lack of reproducibility in the heat transfer becomes evident: temperature offsets occur that exceed the acceptable uncertainty range for velocity determination by more than an order of magnitude. Furthermore, the heat transfer from the probe's surface to the water depends strongly on the water's properties. In particular, precipitation of dissolved solids and formation of bubbles may occur on the probe's surface, which in turn affects the convective heat transfer. Consequently, the water must be filtered, deionized, and deaerated for accurate TA measurements. Therefore, successful application of TA in boreholes of the Earth's crust is highly unlikely without water treatment. Any sensible future application of fiber-optic TA in water must provide the required water conditions. Nonetheless, multiple innovations in fiber-optic TA probe design are presented. Specifically, the fiber-coiled-in-capillary design is also tested in air: a wind-tunnel test reveals promising results for wind-velocity and wind-direction measurements.

Kurzfassung

Um Geschwindigkeiten von vertikalen aufwärts gerichteten Wasserströmungen zu messen, werden iterativ Sensoren für faseroptische thermische Anemometrie (TA) entwickelt und in einem bohrlochähnlichen Prüfstand getestet. Die faseroptische Temperaturmessung in den Sensoren erfolgt mittels *distributed temperature sensing* (DTS). Die Quantifizierung der hydraulischen Eigenschaften von Grundwasserströmungen in der Erdkruste ist aufgrund der begrenzten Zugänglichkeit über Brunnen und Bohrlöcher sowie der komplexen Zusammensetzung der Gesteins- und Sedimentschichten in der Erdkruste kompliziert und kostspielig. DTS ist als Technologie zur Messung von verteilten Temperaturprofilen mittels Glasfasern im geowissenschaftlichen und anderen technischen Kontexten bereits etabliert. Die Umsetzung von TA mit DTS Temperaturmesstechnik basiert auf der Messung der Temperatur in einem beheizten Glasfaserkabel, welches über geschwindigkeitsabhängige erzwungene Konvektion gekühlt wird. Dieser Ansatz soll ermöglichen während Pumpversuchen Geschwindigkeitsprofile über die gesamte Länge von Bohrlöchern oder Brunnen zu messen. Durch diese verteilte Durchflussmessung soll die Komplexität und der Zeitaufwand für die Aufnahme von *Flowmeter-Logs* deutlich verringert werden, was auch die damit verknüpften Kosten reduzieren würde. Allerdings hat noch keine der bestehenden Machbarkeitsstudien validierte Geschwindigkeitsmessungen gezeigt. Es existieren lediglich eine nicht validierte verteilte *Flowmeter-Log* Messung und ein Sensitivitätsnachweis.

Die vorliegende Studie zielt daher darauf die Lücke von qualitativen zu quantitativen Messungen zu schließen. Die vorliegende Studie zeigt, dass die Messung von vertikal aufwärts gerichteten Wassergeschwindigkeiten in einem bohrlochähnlichen Prüfstand mit absoluten prozentualen Fehlern unter 35 % im Bereich von 7.1–47 mm/s möglich ist. Dieses Ergebnis wird jedoch nur in deionisiertem Wasser mit dem ausgereiftesten Sensorkonzept und mit Kalibrierung der DTS Daten, welche erfordert die Temperatur von zwei Abschnitten der Glasfaser zu überwachen, erreicht. Besonders wichtig ist, dass der identische Aufbau zu einem nicht reproduzierbaren Wärmeübergang führt, wenn der Prüfstand mit Leitungswasser befüllt wird. Denn in diesem Fall treten Temperaturabweichungen im Wärmeübergang auf, die eine Größenordnung über dem maximal zulässigen Fehlerband für TA liegen. Dies geschieht, weil der Wärmeübergang in Wasser stark von den Eigenschaften des Wassers abhängt. Insbesondere können Ausfällungen gelöster Feststoffe und die Bildung von Blasen an der für den konvektiven Wärmeübergang relevanten Oberfläche auftreten und diesen beeinflussen. Folglich muss Wasser für präzise TA Messungen gefiltert, deionisiert und entgast werden. Deshalb ist eine erfolgreiche Anwendung von TA in Bohrlöchern der Erdkruste ohne Wasseraufbereitung höchst unwahrscheinlich. Zukünftige Anwendungen für faseroptische TA in Wasser müssen den erforderlichen Reinheitsanforderungen des Wassers genügen. Nichtsdestotrotz werden in der vorliegenden Studie mehrere Innovationen von Sensorkonzepten für faseroptischen TA vorgestellt. Insbesondere wird ein Sensorkonzept, bei dem eine Glasfaser mehrfach durch dieselbe Kapillare gewickelt wird, auch in Luft getestet: Ein Windkanalversuch zeigt vielversprechende Ergebnisse zur Messung von Windgeschwindigkeit und Windrichtung.

Contents

1 Introduction

1.1 Background

Understanding and monitoring water flows in the Earth's crust is a crucial task in modern societies for a variety of applications. Most importantly, groundwater is a valuable resource for providing drinking water and irrigating crops in agriculture. Effective monitoring helps to ensure sustainable extraction [11, 58], and to predict and mitigate contamination risks [5, 6]. With respect to sustainable energy usage, the exploitation of geothermal energy promises to replace a substantial share of fossil fuel consumption, especially for heating [10, 33]. For example, Germany has significant potential to utilize geothermal energy for heating and power production in three large regions of considerable geothermal potential: the South German Molasse Basin, the Upper Rhine Graben, and the North German Basin [2]. When designing facilities to utilize geothermal energy, the exploration of the ground layers' composition, their permeability to water flows, and the magnitude of existing flow velocities is essential. Further important applications that require reliable subsurface flow monitoring include surveillance of dam erosion [41, 64], dimensioning of artificial ground freezing systems in construction [40], and the exploration of suitable locations for disposal of radioactive waste [14].

Exploring the subsurface composition of the Earth using boreholes as the sole access points is an intricate challenge due to the complex and irregular nature of geological formations. The Earth's layers are typically composed of a variety of materials, including sediments and rocks, which differ widely in their hydraulic properties. Some sedimentary layers may be permeable, allowing water to flow through them, while others may be impermeable, acting as barriers to fluid motion. Additionally, fractured rock formations permit water flow only through fractures, making the hydraulic behavior highly dependent on fracture orientation and connectivity. Adding to the complexity, these layers are generally inhomogeneous in both thickness and spatial distribution, making it difficult to generalize findings from a single borehole to a broader area [7, 54].

A wide range of creative and technologically advanced techniques is employed to investigate subsurface conditions and assess hydrogeological properties. One approach is to test sediment or rock cores obtained during drilling operations: grain-size distribution and composition of sediments, as well as rock analysis techniques, are used to roughly estimate the hydraulic permeability [54]. Furthermore, hydraulic testing plays a central role in characterizing aquifer behavior [25, 54]. In particular, pumping tests are considered highly reliable because they involve prolonged water extraction from a well while monitoring water levels in multiple observation boreholes, thereby providing comprehensive data on aquifer properties over a large area. However, these tests are time consuming and resource intensive [25]. Alternatively, single-borehole hydraulic tests, such as the slug test, apply a rapid pressure change to a sealed borehole and monitor its recovery rate. Accordingly, such tests are faster and more cost-effective solutions for determining hydraulic conductivity and storage properties, yet the measured values depend only on the vicinity of the borehole [25, 74]. A common technique to complement hydraulic tests is the flowmeter measurement, which is carried out with a point sensor such as the impeller flowmeter [49], heat-pulse flowmeter [52], or electromagnetic flowmeter [50]. Typically, a pump connected to the borehole induces a flow rate, and the

flowmeter is traversed through the borehole to measure the depth-dependent vertical flow velocity at multiple, regularly spaced points along the borehole's length. Then, the acquired velocity information is used to identify inflow or outflow zones, such as fractures or permeable sediment layers, along the borehole's depth. Moreover, if the pumping duration is long enough to reach a steady piezometric level in the surrounding sediment layers, their permeability can be realistically estimated with the measured flow velocities [25, 73]. As all state-of-the-art flowmeters are currently limited to point measurements, acquiring a flow profile of a borehole is time consuming and thus expensive.

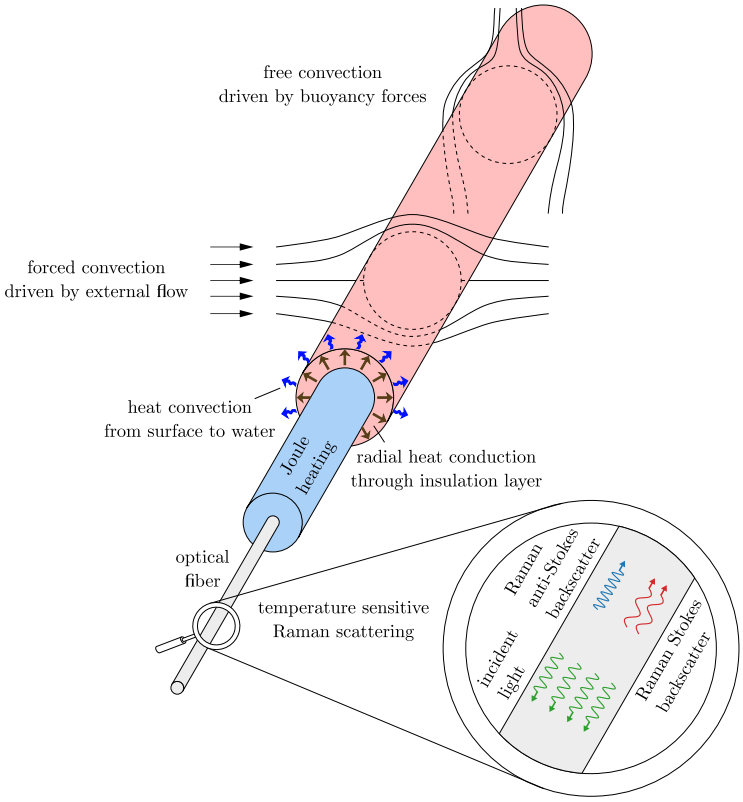

Figure 1.1: This sketch illustrates the underlying physics of fiber-optic thermal anemometry in water with a hybrid cable, which is composed of a glass fiber, a conductive layer, and an insulating sheath. Fiber-optic distributed temperature sensing (DTS) determines the fiber temperature by sensing and processing the temperature-sensitive Raman scattering. Joule heating inside the conductive layer generates a heat flux that is conducted outward. Heat conduction transmits the heat flux to the surface through the insulating layer. Consequently, the submerged heated surface is cooled by velocity-dependent heat convection. As fluid velocity increases, forced convection heat transfer becomes more efficient, while the disturbing influence of buoyancy-driven free convection becomes less significant. The effectiveness of the convective cooling determines the cable's temperature, which is ultimately sensed by the fiber as a velocity-measure.

At first glance, seemingly independent from flowmeter measurements, fiber-optic distributed temperature sensing (DTS) utilizes the temperature-dependent Raman scattering of a laser pulse inside a glass fiber to distributively determine the temperature along the fiber's length [30, 60]. In the environmental context, DTS is well established for temperature profiling [60]. Furthermore, active DTS refers to techniques in which the fiber is actively heated, while the fiber temperature is monitored with DTS. Usually, active DTS is conducted with hybrid cables that contain the glass fiber in the core, surrounded by electrically conductive and electrically insulating sheaths, compare Figure 1.1. The electrically conductive sheath enables resistive heating of the cable. For example, thermal response tests quantify the sediment flow around an actively heated cable buried in sediment [63, 72]. When the actively heated hybrid cable is placed into the free-stream flow

inside a borehole during pumping, its temperature measured by the optical fiber depends on the local flow velocity. Utilizing this convective heat transfer for flow-velocity measurements is known as thermal anemometry (TA). The conventional TA techniques, hot-wire anemometry (HWA) and hot-film anemometry (HFA), are performed by heating short, microscopically thin hot wires or hot films and monitoring their temperature-sensitive electrical resistance [76]. To build a distributed velocity sensor by implementing TA with heated glass fibers, which are capable to distributively measure temperature along their length, has been proposed multiple times [17, 51, 75] and has been validated when applied in air [59, 71]. Applied in water, as sketched in Figure 1.1, this approach has so far been demonstrated to deliver only qualitative information on fluid motion, as summarized in the following.

Read et al. [56] proposed using active DTS as distributed flowmeter in boreholes or wells and directly demonstrated the principle in situ. This new technique introduces a convenient synergy because temperature logging and flowmeter measurements utilize the same sensor, i.e., a fiber-optic cable routed through the borehole. Additionally, this approach simplifies the flowmeter setup as the apparatus to traverse a conventional flowmeter point sensor through the borehole is no longer required. Yet, more importantly, this approach enables spatio-temporal measurements: A flow log of the borehole, acquired in less than a minute, enables monitoring of transient processes, such as fracture interaction between multiple boreholes in the same area.

In their study, Read et al. [56] installed a hybrid cable into a borehole and heated the cable with Joule heating while acquiring the fiber temperature with DTS. Subsequently, they processed the measured distributed temperature profile into a distributed velocity profile using a Nusselt correlation for convective heat transfer. This curve was then compared to existing measurements from a conventional impeller flowmeter. Thereby, they showed that both methods identify the same hydraulically transmissive fractures, yet differences in the obtained velocities remain. In summary, the well-resolved distributed velocity log demonstrates good qualitative behavior in detecting fractures, while the quantitative velocity estimate remains to be validated.

This technique has the potential to substantially advance borehole velocimetry by enabling spatio-temporal measurements. To realize this potential, bridging the current gap toward quantitative water flow velocity measurement is essential.

1.2 Objectives and procedure

To enable the proposed active DTS distributed TA method for velocity measurements in boreholes, the existing gap towards validation of quantitative measurements must be addressed. Therefore, the present study utilizes custom-designed and -built active DTS probes to conduct a fundamental investigation of both DTS measurements and heat-transfer processes in a well-controlled laboratory environment. On the one hand, DTS-measurement uncertainties depend on the processing algorithm of scattered light data into temperature data, device properties (noise, spatial and temporal resolution), and the way the fiber is deployed (light intensity losses due to overall length, splices, connectors, and sharp bends). The heat transfer, on the other hand, consists of conduction and convection: Conductive heat transfer occurs inside the cable, which contains the temperature-sensing optical fiber, electrical conductors as heat source, and protective insulation. Convective heat transfer, which occurs in the water near the cable's surface, consists of water-velocity-dependent forced convection and velocity-independent free convection. The convective heat transfer is sensible to flow topology, like flow direction and buildup of thermal boundary layers, as well as water properties. In particular, the chemical composition of water affects the precipitation of dissolved solids and the formation of gas bubbles on the heated surface, which may impede the heat transfer to

an unknown extent. Thus, the objectives of the present work are in particular to identify specific possibilities, challenges, and limitations in the underlying velocity-dependent heat transfer and its quantification with DTS temperature measurements. Accordingly, the final goal is to quantify the range and uncertainty of this water-flow-velocity measurement technique and to assess its applicability to boreholes in the Earth's crust.

Two procedural conditions are defined at the outset: First, the heated fiber-optic cable shall be oriented either at an angle or perpendicular to the flow direction to minimize boundary-layer buildup, which could otherwise result in cable-length-dependent heat transfer. Second, the experimental setup must fit into an existing borehole-mimicking test rig. In an iterative process, four probe generations, called Probe V1-V4, are developed, built, and investigated. With each iteration, more of the outlined influences on DTS temperature measurements and heat transfer processes are addressed.

The present document first provides an overview of the fundamentals, the heat-transfer modeling, the experimental infrastructure, and methodological approach in Chapters 2 and 3. The initial research stage, which is thoroughly outlined in Chapter 4, is build around the ambitious objective to demonstrate the capability of quantitative measurements not only in the laboratory but also in situ. It clearly demonstrates the velocity dependence of the heat transfer but also reveals a reproducibility issue and multiple challenges in the application of DTS as temperature measurement technique. Thus, the acquired knowledge is considered in a reflection process prior to the second research stage, which is thoroughly outlined in Chapter 5. This second research stage aims to optimize and validate the underlying DTS temperature measurement, investigate the previously observed reproducibility issues, and assess the quantitative measurement capabilities in the laboratory environment only. Eventually, all results are concluded in Chapter 6.

In summary, the present work assesses the capabilities of active DTS as a thermal anemometer for quantitative water-flow velocity measurements. It provides a comprehensive overview and demonstration of *how-to* and *how-not-to* implement TA in water using fiber-optic DTS temperature measurements.

Note that the present work incorporates direct citations from my publications [RRTK24] and [RTK25]. The corresponding sections are put into quotations marks.

2 Fundamentals

The present chapter provides the geoscientific background and the necessary fundamentals of conventional and fiber-optic thermometry and heat transfer. Furthermore, it recalls conventional TA and summarizes existing DTS flow-measurement techniques.

2.1 Geoscientific background

In the context of geologic exploration, the examination of hydraulic properties, like existing flow velocities and permeability of the respective sediment or rock layer, is a complex endeavor. The access to the underground is limited, often to one or a few multiple boreholes, and the Earth's sediment layers are generally irregular and anisotropic. In spite of these limitations, various techniques have been developed to determine the Earth's layers, their properties, and the groundwater transport within the permeable layers.

In the present section, first, a short overview of the fundamentals is provided and the permeability, which is the measurand of interest in geoscientific hydraulic investigations, is introduced with Darcy's law. Then, a brief yet comprehensive overview of established techniques for permeability measurement is given. Finally, the flowmeter logging technique is outlined in more detail, because it is the intended application for the DTS-based thermal anemometer investigated in the present work.

2.1.1 Flow through porous media

To model flow through porous media Darcy's law is widely used. Henry Darcy designed and executed the municipal water supply system in Dijon, which led him to conduct research on flow through sand bed filters. In 1856, he published a study demonstrating that the rate of flow is proportional to the pressure drop through a bed of fine particles [29]. First, a fluid-mechanics-centered approach adapted from Bird et al. [9] and second an application-driven approach adapted from Prinz and Strauß [54] on describing Darcy's law are presented in the following.

Bird et al. [9] assume a homogeneous isotropic porous medium with constant porosity $\epsilon\,[-]$, which is defined as ratio of pore volume to total volume, and a superficial velocity vector $\mathbf{u}_\mathrm{D}\,[\mathrm{m/s}]$ defined as volume flow rate through a unit of cross-sectional area of solid and fluid combined. Then they introduce the smoothed continuity equation

$$\epsilon\frac{\partial\rho}{\partial t} = -(\nabla\cdot\rho\mathbf{u}_\mathrm{D}) \tag{2.1}$$

($\rho\,[\mathrm{kg/m^3}]$ – density) and Darcy's equation

$$\mathbf{u}_\mathrm{D} = -\frac{\kappa}{\mu}(\nabla p - \rho\mathbf{g}) \tag{2.2}$$

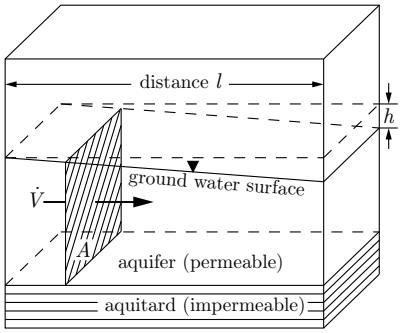

Figure 2.1: Illustration of ground water flow in a permeable subsurface layer for derivation of Darcy's law. Sketch design inspired by [54].

together to describe the motion of fluid in a porous medium. $\kappa\,[\mathrm{m}^2]$ is the permeability of the porous medium, $p\,[\mathrm{kg\,m/s}^2]$ the pressure, $\mu\,[\mathrm{kg/(m\,s)}]$ the dynamic viscosity, and $\mathbf{g}\,[\mathrm{m/s}^2]$ the gravitational acceleration. Both equations are combined to

$$\frac{\epsilon\mu}{\kappa}\frac{\partial\rho}{\partial t} = (\nabla\cdot\rho\,(\nabla p - \rho\mathbf{g})) \tag{2.3}$$

and for an incompressible fluid $\rho = \rho_0$ simplified to

$$\nabla^2 p = 0, \tag{2.4}$$

which is the Laplace equation. This continuum approach for flow through isotropic porous media is valid for a small region of space, which is large with respect to the pore size but small with respect to macroscopic dimensions.

Another approach on Darcy's law outlined by Prinz and Strauß [54] in their geoscientific textbook starts with a sketch similar to Figure 2.1. In the aquifers sediment, to model the ground water flow Darcy's law is introduced as scalar velocity

$$u_\mathrm{D} = \frac{\dot{V}}{A} = K\,i \tag{2.5}$$

with the inclination $i\,[-]$ as ratio of distance l to height difference h. $K\,[\mathrm{m/s}]$ is a coefficient of proportionality and is also called coefficient of permeability. It is linked to the permeability of the porous medium

$$K = \kappa\frac{\rho\,g}{\mu}. \tag{2.6}$$

The permeability of a homogeneous and isotropic aquifer with height H may also be expressed with the transmissivity

$$T = K\,H. \tag{2.7}$$

For various geological technical applications (such as oil and water extraction or deep geothermal power plants), permeability – often in form of the coefficient of permeability K or the transmissivity T – is the measurand that must be quantified by a measurement technique. In practice, the coefficient of permeability ranges from $10^{-2}\,\mathrm{m/s}$ for very permeable coarse sediments to $10^{-10}\,\mathrm{m/s}$ for densely packed nearly impermeable sediment or rock layers. Although all resulting velocities are very small, the logarithmic range which needs to be quantified is large. Therefore, a variety of different methods have been developed, and the most prevalent of these are introduced in Table 2.1. In Subsection 2.1.2 these methods are concisely introduced.

Table 2.1: An overview of methods to measure coefficient of permeability K in situ with their approximate measurement ranges. Adapted from [54], [22], and [25]. Edalat et al. [25] first published such a table, Denzel et al. [22] extended it, and Prinz and Strauß [54] restructured it.

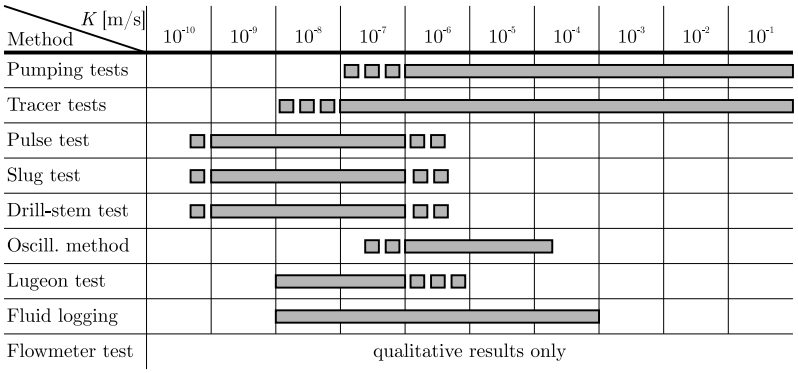

A few concluding remarks on sediment flow and its modeling with Darcy's law remain: Only homogeneous, isotropic sediment with saturated flow (= all void filled with water) is considered here. Of course, the measured Darcy velocity u_D differs from the local velocities experienced by the water. The velocity in the pores may be estimated with the porosity ϵ or an effective porosity ϵ_eff, which considers that a part of the fluid in pore space is immobile

$$u = u_\mathrm{D}/\epsilon \quad ; \quad u_\mathrm{eff} = u_\mathrm{D}/\epsilon_\mathrm{eff}. \tag{2.8}$$

Furthermore, Darcy's law is only valid for slow flows. The Reynolds number

$$Re = \frac{u_\mathrm{D}\, d}{\nu} \tag{2.9}$$

as measure for the ratio of viscous to inertial forces helps to quantify the applicability of Darcy's law. As no sediment is made of uniform spheres, determining the characteristic particle diameter renders difficult. Using the mean grain diameter or d_{10} (the tenth-percentile grain size, i.e., the diameter for which 10 % by mass is finer) are valid options. In general, Darcy's law is valid for Reynolds numbers $Re < 1...10$ [7].

2.1.2 Overview of flow-measurement methods

Table 2.1 shows that a variety of methods exist to determine or estimate the coefficient of permeability with measurements in wells and boreholes. A quick overview of the techniques, focusing only on the principle of the respective method is provided in the following.

During **pumping tests** (see Figure 2.2), water is typically extracted from the aquifer over an extended period of time (ranging from hours to weeks). This leads to a measurable lowering of the groundwater-level at the extraction point and in the surrounding area. The amount of groundwater level decline depends on the volume of water extracted, the permeability of the tested subsurface, and various other hydrogeological parameters. Theis [66] developed a mathematical solution for the transient well flow assuming radial symmetry and a homogeneous, isotropic, and confined aquifer. Based on this solution, a processing method was developed for the time-dependent change of the piezometric surface. Since then, various models have been developed for different combinations of aquifer properties (such as confinement state) and steadiness of the flow. Accordingly, a concept of the aquifers composition must exist to properly evaluate a pumping test. The pumping test is the most accurate test, but it is also the most expensive because of the long duration, the need for

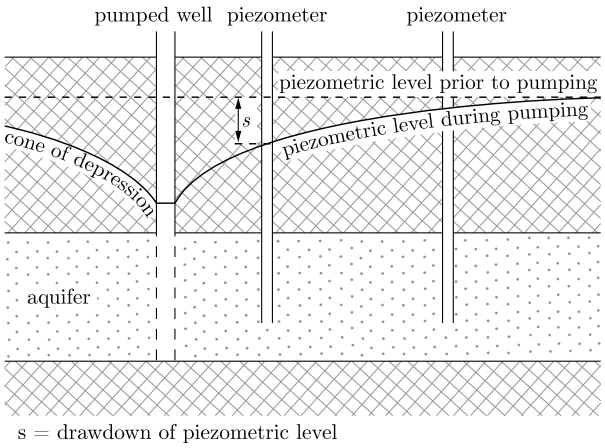

Figure 2.2: During pumping tests, water is extracted from a well and the drawdown of the piezometric level is monitored in additional boreholes nearby. Adapted from [37].

multiple access points, and the effort of disposing of the pumped water, which may be subject to approval by the authorities [25, 37].

The **tracer test** is usually performed in parallel to a pumping test: a tracer substance is inserted into the feed hole and its concentration is analyzed in the extraction hole. Based on such particle-concentration measurements, the relationship between the volume of water extracted during a pumping test, the effective pore volume, and the distance between the feed point and the pumping well can be used to determine the permeability. If the thicknesses and pore volumes of a layered aquifer are known and if the total transmissivity of the rock section is also known, it is possible to determine the transmissivities of individual aquifer layers [25].

Table 2.2: Classification of hydraulic methods to estimate the permeability based on tests in a single borehole. Adapted from [25].

	positive pressure gradient	negative pressure gradient
variable pressure	falling-head test, injection test, infiltration test, pulse test	rising head test, leveling test, slug test, drill stem test
constant pressure	lifting test, refill test, pressure test	drawdown test, short-term pumping test

Compared to the pumping test, the hydraulic methods listed in Table 2.2 can be executed in short time intervals. In the constant pressure tests, water is either supplied or removed with a constant rate leading to a rise or decline of the water surface in the borehole. The water-surface offset and the water supply or removal rate are evaluated to estimate permeability. Variable pressure tests in their simplest form require pumping water into or out of the borehole as preparation, and as soon as the pumping ceases the tests analyze the transient recovery of the water surface level. The more sophisticated variable pressure tests require a sealed test section in which the pressure is monitored. In the **pulse test**, the sealed test section is connected to a water reservoir above the surface with a tube. Initially, a valve separates the high pressure in the tube from the test section. Opening the valve leads to a sudden pressure rise in the test section, which is subject to evaluation. In the **slug test** the sealed test section is connected to an empty tube in which the pressure is equal to the surface pressure. The test section is well below the water surface in the borehole, thus its pressure is much higher. Opening the valve between tube and test section leads to a sudden pressure drop. Consequently, water rises into the tube until the pressure level

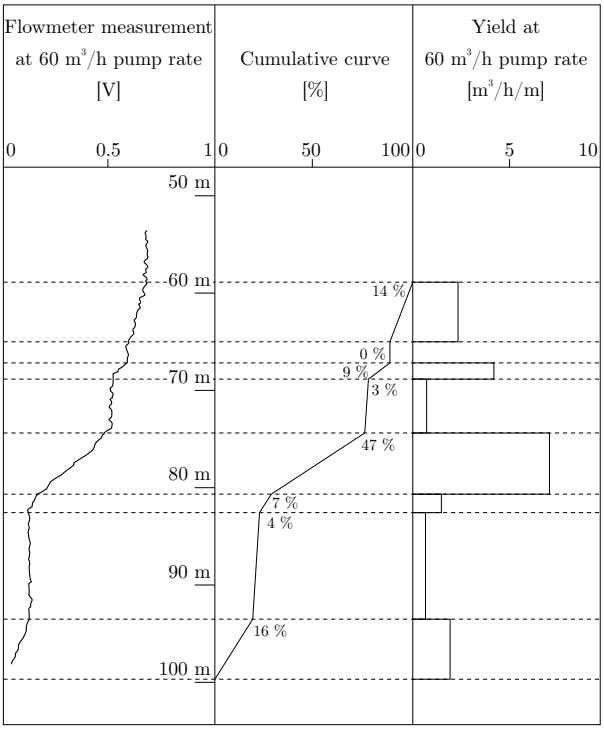

Figure 2.3: Example of a flowmeter log and its processing into a cumulative curve and calculated yield. Adapted from [25].

is recovered. The **drill-stem test** starts identically as the slug test, but the valve is closed again shortly after opening [25].

Several further developments on the ground of the prior hydraulic tests are the oscillatory slug test and the Lugeon test: In the **oscillatory slug test** a pressure sensor is inserted well below the water surface inside a borehole, which is sealed on the top and connected to a pressurized tank and a release valve. First, the borehole is pressurized, which leads to a drop of the water-surface level. Then, the pressure abruptly drops after opening the release valve, and, depending on the aquifers properties, the water surface either slowly returns to its original height or oscillates a few times before reaching its original level. By analyzing of this oscillation, the transmissivity is estimated. The setup for the **Lugeon test** is very similar to the pulse, slug and drill-stem test, but with a test section which is properly sealed using inflatable packers. Subsequently, a high-pressure pump injects water into the packer-sealed section. Both pressure response and volumetric flow rate are monitored and evaluated [25].

The **fluid logging** method is based on measuring the electric conductivity with a logging setup, which moves a sensor through the borehole to produce logs of conductivity over the borehole depth. Before the experiment, the water flooding the boreholes volume is replaced with water of a significantly different electric conductivity. Then under moderate continuous pumping, multiple conductivity logs are created. The water flowing from the aquifer layers into the borehole is identified by the varying conductivity at the corresponding depths [25].

2.1.3 Flowmeter logging

In flowmeter logging a profile of vertical flow rate is measured while water is either pumped from or into a borehole. An exemplary flowmeter profile is visualized in Figure 2.3. The flowmeter log originally consists of a volumetric flow rate measurement that is processed to a cumulative curve

and a yield diagram. These graphs are used to identify more and less permeable layers. However, to quantify the transmissivities from the flowmeter log alone the the test must be run long enough for the piezometric level (compare Figure 2.2) to become steady. Then, the yield of the respective layers can be used for sensible transmissivity (and permeability) estimations [25]. Such estimations always require a reasonable model for the respective layer. For example, an aquifer layer that is confined between two aquitards behaves differently from a phreatic aquifer, which is not confined at its upper surface and whose water level is at atmospheric pressure. Bear [7] derives mathematical models for various cases that enable the determination of permeability based on measured flow rates.

Mostly an impeller is used as flowmeter sensor, which is dragged through the borehole at constant speed. To compensate for the movement velocity of the impeller, a zero-velocity curve is acquired before the experiment when the pump is turned off [49]. Other conventional flowmeter sensors are the heat-pulse flowmeter [52], and the electromagnetic flowmeter [50], which measure the velocity at many points of the borehole instead of being dragged through it.

Read et al. [56] proposed that a flowmeter log may be produced from temperature measurements of an actively heated glass fiber, see Subsection 2.6.2. The fundamental question whether this fiber-optic principal can be reliably utilized as velocity measurement is subject to the present work.

2.2 Temperature metrology

The common techniques in industrial temperature measurement are resistance temperature detectors (RTDs), thermocouples (TCs), liquid-in-glass thermometers, and radiation thermometers:

- Conductive metal-based RTDs utilize that the temperature-dependent electrical resistance of metals is extremely stable and has a well characterizable form with positive relative temperature coefficients. Commonly platinum is used with a base resistance of $100\,\Omega$ (PT100) or $1000\,\Omega$ (PT1000) [26].
- Semiconducting metal based RTDs, called thermistors, have very sensitive negative relative temperature coefficients. Their high sensitivity enables operation with inexpensive direct reading instruments, but their very non-linear characteristic leads to higher uncertainties compared to pure metal RTDs [26].
- TCs exploit electromotive forces between two dissimilar wires – the Seebeck effect. They are simple, reliable and thus widely used in industrial applications. However, when higher measurement accuracies are required, considerable effort for precise cold-junction compensation is needed, and simplicity and cost-effectiveness diminish [26].
- Liquid-in-glass thermometers consist of a bulb filled with liquid and a stem where the liquid rises inside a capillary depending on its temperature sensitive expansion. When properly calibrated and applied, uncertainties as low as $0.005\,^{\circ}\mathrm{C}$ are achievable. Historically, it was the only available measurement technique for scientific research for many decades. Yet, in recent years they have been replaced by the aforementioned methods, whose analog signals can be directly converted into digital signals that are subsequently logged by a computer [26].
- Radiation thermometry, as used with simple infrared sensors and sophisticated infrared cameras, enables non-contact temperature measurement. Its accuracy depends on the knowledge

of the emissivity properties of the measured surface and the temperature background compensation within the instrument [26].

In the present work platinum RTDs are used to monitor temperatures of the water channels (cp. Subsections 3.2.1, 3.2.2) and water baths for DTS calibration (cp. Subsection 3.2.4). TCs are applied inside a layered probe of the setup introduced in Subsection 3.2.2 and on the surfaces of the probes investigated in Section 4.1 and Subsections 4.3.2 and 4.3.3. Therefore, these two techniques are elaborated further in the following.

2.2.1 Thermocouples (TC)

When two dissimilar wires are connected at one end at which a temperature T_1 is present and if the other ends are located in a region with a different temperature T_0, a voltage can be measured at the other end. This behavior is driven by electro-motive forces and is called Seebeck effect. It must be emphasized that this phenomenon is a temperature gradient phenomenon and not a junction phenomenon. Between the free ends, both at temperature T_0 the thermoelectric potential difference is

$$E_{\mathrm{AB}}(T_0 \to T_1) = \int_{T_0}^{T_1} [S_{\mathrm{A}}(T) - S_{\mathrm{B}}(T)]\,\mathrm{d}T. \tag{2.10}$$

$S_{\mathrm{A}}(T)$ and $S_{\mathrm{B}}(T)$ are the Seebeck coefficients of the respective conductors. Only if the respective wire materials are homogeneous throughout the temperature gradient, $E_{\mathrm{AB}}(T_0 \to T_1)$ is a unique function of T_0 and T_1. An inhomogeneity adds a small additional thermopower at its location. To determine T_1 from the measured voltage E_{AB}, T_0 must be measured with a separate sensor, which is called cold-junction compensation [26].

The practical considerations whether to apply TCs in the present work are accuracy and size. TCs are very small consisting of a thin cable with a junction at the cables end, thus they can be inserted into small structures and they can be fixed to a surface with glue or a small piece of thin adhesive tape. In terms of accuracy, TCs perform sufficiently well for technical applications which do not require high accuracy. DIN EN 60584-1:2014-07 states the accuracy for the commonly available TC types (=material combinations) in terms of a limiting deviation that is at best $\pm 0.5\,^{\circ}\mathrm{C}$. Aside the standard applications, high-accuracy TC measurements are possible with high quality TCs and high accuracy cold-junction-compensation, for example inside a triple point cell. However, the complexity of this approach constraints the use of high-accuracy TC measurements to niche applications.

2.2.2 Platinum resistance temperature detectors (RTD)

The electrical resistance of platinum is extremely stable and its function of temperature T in °C is quantified by the simple form

$$R = R_0(1 + A\,T + B\,T^2) \tag{2.11}$$

in the temperature range 0 to 850 °C and

$$R = R_0[1 + A\,T + B\,T^2 + C(T - 100\,^{\circ}\mathrm{C})\,T^3] \tag{2.12}$$

in the range of −200 to 0 °C. R_0 is the resistance at 0 °C and A, B, C are constants (compare DIN EN IEC 60751:2023-06 or Fischer and Fellmuth [26]).

Four uncertainty classes are specified for industrial thermometers in DIN EN IEC 60761. The highest class AA specifies that the measurand must be within a limiting deviation $\pm(0.1\,°\mathrm{C}+0.0017\,|T|)$. This is a convenient definition for mass-produced thermometers because slight imperfections in manufacturing precision lead to offsets in R_0 and impurities in the material lead to variation of the coefficients A, B, and C. If the sensor is calibrated by using multiple fixed points like the triple-point-water, accuracies of up to 10 mK are possible. Also using only one calibration point to correct for the predominant offset error in R_0 leads to accuracies well beyond the specified limiting deviation.

Other sources for uncertainties are self-heating of the resistor by the measurement current, influence of the lead cables resistance, and errors introduced by the electrical device setting the measurement current and evaluating the voltage for the resistivity measurement. The measurement current should be 1 mA or less for the heating to be insignificant [26]. Especially long lead cables introduce an error by adding a resistance to the measured value, which does neither solely depend on the temperature in the measured location nor behaves like the platinum resistor to temperature changes. Usually the lead cable resistance is corrected for by adding one or two cables: In the three-wire configuration the lead resistance is measured and subtracted. In the four-wire configuration two cables are used to supply the current, while the other two wires are used for the voltage measurement. As the current in the measurement wires is negligible, the voltage drop along the wires is insignificant. Every error introduced by the instrumentation used to evaluate the sensor must be considered, especially when widely available, cheap microelectronics are used. With high-end instrumentation, the additional uncertainty is usually very small and specified in the datasheet.

2.3 Distributed temperature sensing (DTS)

DTS refers to the distributed fiber-optic measurement of temperatures. In general, DTS can be achieved with several different methods, of which Raman-DTS is the most widespread and the one sensitive only to temperature, without cross-sensitivity to fiber strain. The present work refers with DTS always to Raman-DTS, which exploits Raman scattering as its measurement principle. Raman scattering is the inelastic scattering of light at matter that either transfers energy to the molecules, called Stokes Raman scattering, or retrieves energy from the molecules, called anti-Stokes Raman scattering. In particular, the anti-Stokes Raman scattering intensity is a sensitive measure of the molecules' temperature.

A DTS device shoots laser pulses into a glass fiber and measures both Raman scattering intensities – Stokes Raman and anti-Stokes Raman – distributively along the fiber distance and processes these into temperature measurements. To process the scattering intensities into temperatures (which is commonly referred to as DTS calibration), the device's algorithm needs a reference fiber section with known temperature and knowledge about differential attenuation. Differential attenuation describes the effect that both scattered signals experience different attenuation when traveling through the optical fiber. Light attenuation in glass fibers is wavelength-dependent and both measured intensities differ significantly in wavelength. Fiber bends with small radii, fiber splices, and fiber connectors are confined locations with high differential attenuation. Furthermore, different glass fibers may have varying differential attenuations, and even throughout an identical fiber this may vary, for example with temperature changes or stress applied to the fiber. In general, the DTS device is not well informed about the differential attenuation of the fiber setup. Therefore, it has been demonstrated that self-calibration by the user [23, 31, 70] outperforms the DTS device's

internal calibration. Such calibration relies on data from monitored constant-temperature sections of the fiber that are implemented with water baths [23, 31, 70] or large metal cylinders [67].

First, the general background of fiber-optic sensing is concisely presented. Then, to introduce the process of DTS calibration by the user, the underlying measurement equation is deduced. Finally, calibration strategies that inform the solution of the measurement equation are described.

2.3.1 Introduction to fiber-optic sensing

Fiber-optic sensors use light to both sense information with an optic sensor and convey the information through an optical fiber. The setup generally consists of an interrogator, a fiber, and a sensor, which may be an optic sensor connected to the fiber, a modified partition of the fiber, or the fiber itself. The interrogator is an opto-electronic system, which emits light into the fiber and senses the returned light by converting it into an electrical signal. The optical fiber conveys the probe light to the optical sensor and returns modulated light to the interrogator. The field of fiber optic sensors is diverse and may be classified by intrinsic and extrinsic sensor design (see Figure 2.4), by topology (see Figure 2.5), by the phenomena influencing the light properties, type of scattering (see Figure 2.6), and by the light property exploited for the fiber-optic measurement [30].

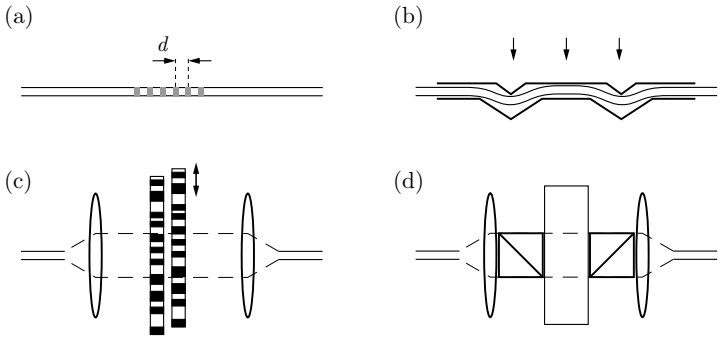

Figure 2.4: Examples of intrinsic (a), (b), and extrinsic (c), (d) fiber-optic sensors. In intrinsic sensors, the light is both modulated and conveyed inside the fiber, while extrinsic sensors use the fiber only to convey the incident and modulated light to and from a sensor. Adapted from [30].

Intrinsic sensors manipulate the light properties within the fiber. For example, in a fiber-Bragg grating (FBG) as displayed in Figure 2.4 (a) the fiber's refractive index is manipulated periodically to reflect a specific wavelength depending on strain and temperature. Tensile strain elongates the grating spacing and temperature changes affect the refractive index offset and influence the grating spacing by thermal expansion. In Figure 2.4 (b) a force or displacement sensor is sketched, where the force-dependent replacement of the upper plate leads to a bend in the fiber that results in increased attenuation at the specific fiber position. In contrast, extrinsic sensors manipulate the light properties outside of fiber and use the fiber only to conduct the optical signal. Figure 2.4 (c) and (d) display an optical encoder sensor, which measures displacement by loss, and a birefringence sensor, which manipulates the light's polarization depending on the stress applied to the birefringent material.

Various topologies exist in fiber-optic sensing because multiplexing enables the connection of multiple sensors to one or two optical fibers as depicted in Figure 2.5 (b) and (c). The multiplexing topologies enable the connection of tens to hundreds of sensors to a single setup. The number of sensors strongly depends on the sensor type. As extreme example, Ma et al. [45] successfully multiplexed 2014 FBGs on a single fiber. Furthermore, Figure 2.5 (d) shows that distributed sensing utilizes the unmodified fiber as distributed sensor. A physical quantity is measured along the

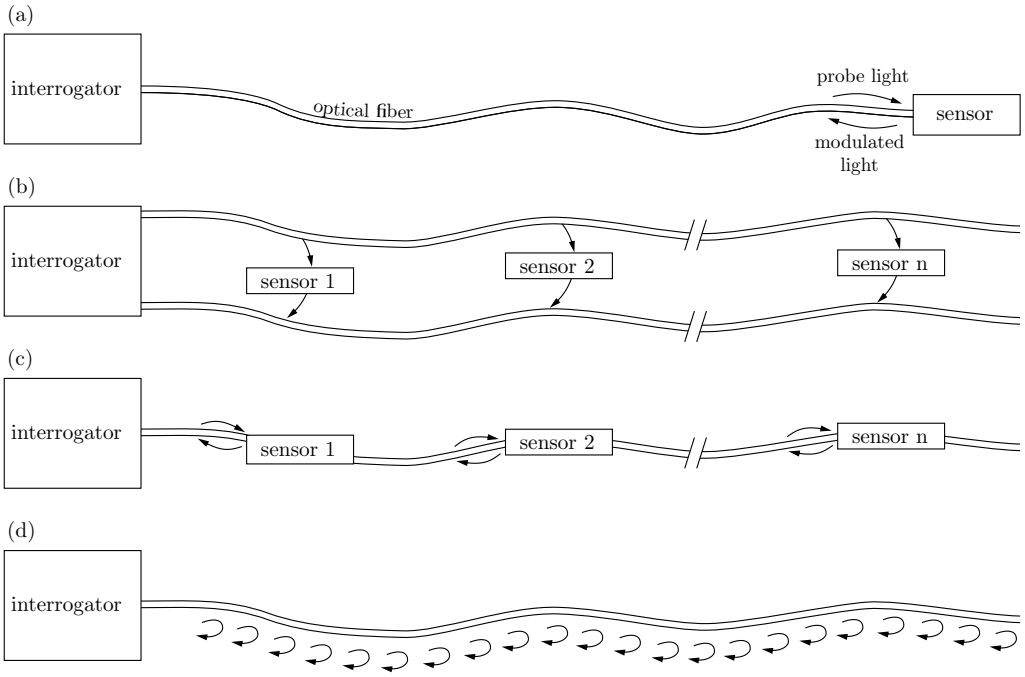

Figure 2.5: Common topologies in fiber-optic sensing are the single sensor configuration (a), multiplexed sensor configurations using two fibers (b) or a single fiber (c), and distributed sensing (d). Adapted from [30].

complete fiber length, which may be several kilometers long and result in thousands of sampling points [60].

The attributes of light, that can be exploited for a sensing task are intensity, propagation time, optical spectrum, polarization, phase, and coherence. Consequently, fiber-optic sensors may be applied to measure a wide variety of measurands such as temperature, elongation, displacement, force, and magnetic field intensity [30].

During elastic scattering, the energy of the incident light remains constant, whereas in inelastic scattering, the energy of the incident light is either increased or reduced. Inelastic scattering with energy decrease is called Stokes scattering. According to

$$E = h_{\mathrm{P}} f \tag{2.13}$$

(h_{P} Planck constant) an energy E decrease results in a lower frequency f and in an increased wavelength λ. During anti-Stokes scattering the opposite happens to the scattered light: increased energy, higher frequency and decreased wavelength. Figure 2.6, sketches the three common scattering types in a qualitative return-signal-over-frequency graph. The inelastic scattering type, called Rayleigh scattering, is the predominant scattering process. It occurs at small-scale fluctuations of the refractive index, which are frozen into the fiber's glass. The other source of small-scale refractive index fluctuations are caused by phonons. Phonons are vibrations in the molecular lattice structure of the fiber's glass, and molecular vibrations caused by stretching, bending or rotation of inner-atomic bonds. Brillouin scattering is the inelastic scattering of light caused by interaction with these lattice structure vibrations. As these are comparably low frequency vibrations in the hypersonic range (10-30 GHz), they cause a small frequency shift. Raman scattering is caused by the incidents light's interaction with the molecular vibrations, which are in the range of ~ 10 THz. Thus, the frequency shift and amount of energy transferred is largest in Raman scattering. The intensity of the anti-Stokes Raman scattering is very sensitive to the materials temperature, while

the Stokes Raman scattering is only slightly temperature sensitive. The ratio of both signals is exploited by Raman DTS for temperature measurements [30].

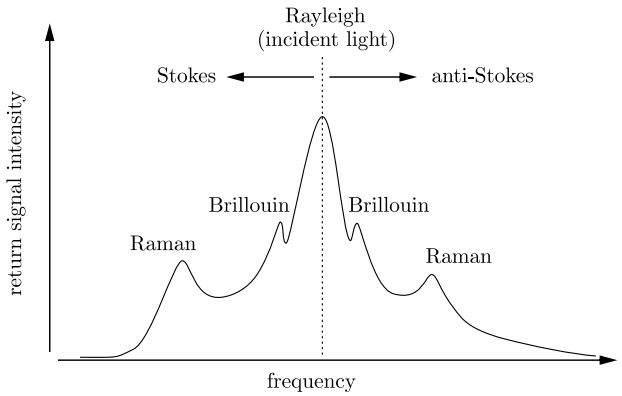

Figure 2.6: Visualization of the three common scattering types with a sketched return signal over frequency graph. Inelastic Rayleigh scattering occurs at the frequency of the incident light and has the highest intensity. Brillouin scattering is inelastic scattering caused by interaction of the incident light with lattice vibrations. Raman scattering is caused by the interaction of the incident light with molecular vibrations, it has the highest frequency shift and lowest intensity. Adapted from [60].

A broad overview of optical fiber technology required to fully understand the design and principles of DTS are given in Chapter 2 of Hartog [30]. These principles are among others the propagation of light in optical fibers, optical fiber design, loss mechanisms (absorption, scattering, and microbending losses), laser properties, and detector technologies.

2.3.2 Derivation of the measurement equation

In the following, the underlying measurement equation of Raman-DTS is deduced and explained, primarily following Des Tombe et al. [23].

DTS is an intrinsic distributed fiber-optic measurement technique, which utilizes inelastic scattering for temperature measurement. The inelastic scattering phenomenon – i.e. Raman scattering – is an interaction between the molecules of the fiber with the incident light emitted by the DTS laser. The light is scattered with a frequency shift either to higher frequency – anti-Stokes scattering – or to a lower frequency – Stokes scattering. The temperature-measurement equation of DTS relates the ratio of Stokes intensity to the anti-Stokes intensity at the location of scattering. Thus, it must consider the wavelength dependent attenuation of both signals between the detector and the location of scattering. Figure 2.7 illustrates this process: The initial laser pulse is first attenuated while traveling through the fiber. Then in the section of interest, the light is scattered and a fraction of the backscattered light is captured by the fiber. Subsequently, the captured light is attenuated again while propagating towards the detector. Below, an energy balance for this process derives the intensity measured at the detector as a function of the initial laser-pulse energy, the light propagation, and the light scattering.

The laser emits a laser pulse into the glass fiber with initial energy E_0, which is attenuated while propagating through the fiber along x with attenuation α_1, i.e.

$$E(x) = E_0 \exp\left(-\int_0^x \alpha_1 \, \mathrm{d}x\right). \tag{2.14}$$

A fraction of the light is scattered, described by the scattering coefficient $S(x)$, and a fraction of this scattered light is captured. The capture fraction R depends on fiber properties like fiber diameter

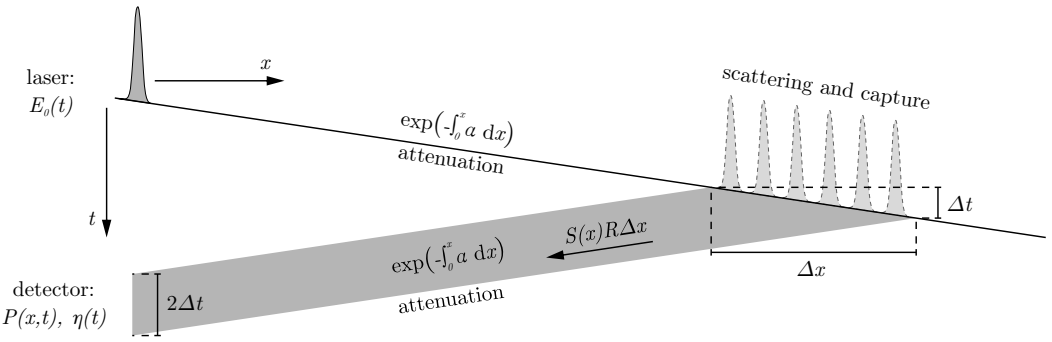

Figure 2.7: Visualization of the light-propagation model utilized in distributed sensing with a x–t diagram sketch. The initial laser pulse $E_0(t)$ is attenuated when propagating through the fiber by various scattering processes. In the region of interest, a fraction of the scattered light is captured $S(x)R\,\Delta x$. The captured light is attenuated again when propagating towards the detector and is finally measured by the detector with efficiency $\eta(t)$. Note that the pulse width widens by a factor of two in the scattering section. Adapted from [23].

and numerical aperture. Consequently, the fraction of the scattered light along a section $\mathrm{d}x$ amounts to $S(x)\,R\,\mathrm{d}x$. When the scattered light propagates back through the fiber it is attenuated again, and the backscattered energy amounts to

$$\Delta E_{\mathrm{BS}} = E_0\,S(x)\,R\,\Delta x\,\exp\left(-2\int_0^x \alpha_1\,\mathrm{d}x\right). \tag{2.15}$$

The width of the backscatter pulse is $2\,\Delta t$ wide because the light refracted at the beginning of Δx travels back in the fiber until the scattering occurs at the end of Δx, compare Figure 2.7. The light propagates with the fiber-specific light speed

$$c = \Delta x/\Delta t \tag{2.16}$$

through the fiber. Thus, the intensity measured by the detector

$$P(x) = \eta\frac{\Delta E_{\mathrm{BS}}}{2\,\Delta t} = \eta\frac{c}{2}\frac{\Delta E_{\mathrm{BS}}}{\Delta x} \tag{2.17}$$

is the backscattered energy per time multiplied with the detector's efficiency η, which accounts for the sensitivity of the detector and the attenuation between the fiber's end and the detector. With equation (2.15) this intensity can be expressed as

$$P(x) = \frac{1}{2}\,E_0\,\eta\,c\,S(x)\,R\,\exp\left(-\int_0^x \alpha_1\,\mathrm{d}x\right). \tag{2.18}$$

This equation is used in optical time-domain reflectometry (OTDR), which evaluates the inelastically scattered light and only measures the attenuation α_1 along the fiber (for example to judge the loss in fiber connections like fusion splices and connectors).

In Raman DTS the light is scattered at two different wavelengths: anti-Stokes Raman and Stokes Raman. Their scattering coefficients differ in magnitude and in temperature sensitivity:

$$S_+(x,T) = \frac{K_+}{\lambda_+^4}\frac{\exp[\gamma/T(x,t)]}{\exp[\gamma/T(x,t)]-1} \tag{2.19}$$

and

$$S_-(x,T) = \frac{K_-}{\lambda_-^4}\frac{1}{\exp[\gamma/T(x,t)]-1} \tag{2.20}$$

are the scattering coefficients for the Stokes wavelength λ_+ and the anti-Stokes wavelength λ_-. K_+ and K_- are coefficients that account for the fraction of molecules in the fiber that contribute to the Raman scattering. γ is the fiber material-dependent sensitivity of Stokes and anti-Stokes scattering to temperature, and T is the temperature along the fiber in Kelvin. As the attenuation in the fiber depends on the wavelength, varying attenuations α_+ and α_- are considered in the powers measured by the detectors

$$P_+(x,t) = \frac{1}{2} E_0 \, \eta_+(t) \, c \, S_+(x,t) \, R \, \exp\left[- \int_0^x (\alpha_1(x') + \alpha_+(x')) \, \mathrm{d}x' \right] \tag{2.21}$$

$$P_-(x,t) = \frac{1}{2} E_0 \, \eta_-(t) \, c \, S_-(x,t) \, R \, \exp\left[- \int_0^x (\alpha_1(x') + \alpha_-(x')) \, \mathrm{d}x' \right]. \tag{2.22}$$

The equation that is used to calculate the temperatures from the measured Stokes and Anti-Stokes intensities is obtained by inserting equations (2.19) and (2.20) into (2.21) and (2.22) and subsequently dividing (2.21) by (2.22):

$$\frac{P_+(x,t)}{P_-(x,t)} = \frac{\eta_+(t) \, K_+ \, \lambda_+^{-4}}{\eta_-(t) \, K_- \, \lambda_-^{-4}} \exp\left(- \int_0^x \Delta\alpha(x') \, \mathrm{d}x' \right) \exp\left(\frac{\gamma}{T(x,t)} \right). \tag{2.23}$$

Here, $\Delta\alpha = \alpha_+ - \alpha_-$ is the differential attenuation. Applying the natural logarithm to the measurement equation yields

$$I(x,t) = -C(t) - \int_0^x \Delta\alpha(x') \, \mathrm{d}x' + \frac{\gamma}{T(x,t)} \tag{2.24}$$

where

$$I(x,t) = \ln\left(\frac{P_+(x,t)}{P_-(x,t)} \right) \tag{2.25}$$

is the logarithmic ratio of the measured intensities and

$$C(t) = \ln\left(\frac{\eta_-(t) \, K_- \, \lambda_-^{-4}}{\eta_+(t) \, K_+ \, \lambda_+^{-4}} \right) \tag{2.26}$$

is a coefficient, which combines the effects of the detectors sensitivities, the additional attenuation between fiber end and detector, and the wavelength dependence of both scattering intensities. Reordering equation (2.24) results in

$$T(x,t) = \frac{\gamma}{I(x,t) + C(t) + \int_0^x \Delta\alpha(x')\mathrm{d}x'}, \tag{2.27}$$

which can be used for temperature measurement, if γ, C, and $\int_0^x \Delta\alpha(x')\mathrm{d}x'$ are known. Consequently, a calibration is necessary to determine these. Therefore, multiple calibration strategies are outlined in the following.

2.3.3 Calibration strategies

To calibrate the constants in the temperature equation (2.27), two monitored constant-temperature sections or a single reference section with sufficient temperature variation are necessary [23]. Furthermore, the fiber configurations, as outlined in Figure 2.8, impact the calibration strategy. The single-ended configuration refers to a fiber that is connected to one port of the DTS device. In single-ended calibration, it must be assumed that the differential attenuation along the fiber is

constant. Short sections with attenuation jumps – so-called step losses – like sharp bends, fusion splices, or connectors can be corrected for by forcing a constant temperature where they are located [31]. In contrast, both the J-fiber configuration and the double-ended configuration enable the measurement of the differential attenuation. In the J-fiber configuration, the additionally needed calibration information is gathered by measuring the temperature at multiple locations with two fiber-coordinates. In the double-ended calibration, both ends of the fiber are connected to the DTS device, and each fiber location is measured twice. First, one channel measures the Stokes and anti-Stokes intensities in forward direction, and consecutively, the other channel measures the intensities backward in the other direction.

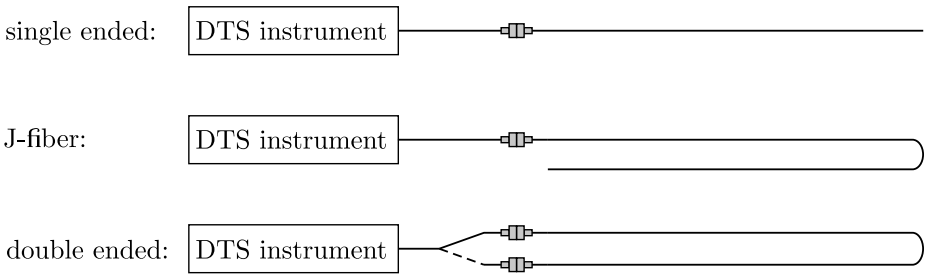

Figure 2.8: Common fiber configurations of DTS setups and visualization of constant temperature sections with $T_1 \neq T_2$. In the J-fiber configuration the fiber is looped at the furthest point, and exactly follows the identical path, as before. Thus, always two fiber coordinates measure the same temperature, which is leveraged in the calibration process. In the double-ended configuration, the fiber is connected to the DTS instrument at both ends and measured by the instrument in both directions. Here, the forward and backward path of the fiber does not need to be identical. Sketch design inspired by [30] and [31].

In the following, the single-ended and double-ended calibration algorithms are explained in more detail (based solely on Des Tombe et al. [23]).

Single-ended calibration

For single-ended calibration, the temperature measurement equation (2.27) is simplified with the assumption of constant differential attenuation along the fiber

$$\int_0^x \Delta\alpha(x')\,\mathrm{d}x' \approx \Delta\alpha\, x. \tag{2.28}$$

To estimate the parameters $C(t)$, γ, and $\Delta\alpha$, a reference section with known temperature is required. When M locations of the fiber are inside this reference section and the temperature of the complete fiber is measured N times, MN observations of equation (2.24)

$$I_{m,n} = \frac{1}{T_{m,n}}\gamma - x_m\Delta\alpha - C_n, \qquad m \in \{1,2,...,M\},\ n \in \{1,2,...,N\} \tag{2.29}$$

exist. The $N+2$ unknown parameters are $C_1, C_2, ..., C_n$, γ, and $\Delta\alpha$. As there are more equations than unknown parameters, linear regression is applied to determine the parameters. In the open-source Python package *dtscalibration* by Des Tombe et al. [23], the equations are solved by adding a residual term to each observation equation and minimizing the sum of the squared weighted residuals.

Double-ended calibration

In the double-ended setup, the temperature along the fiber is measured from two directions. $T_\mathrm{F}(x,t)$ is the temperature measured in the first (forward) channel of the DTS device, and $T_\mathrm{B}(x,t)$ is the temperature measured in the second (backward) channel. The coordinate x is defined in forward

direction, starting with $x = 0$, where the fiber is connected to the first channel. The signals from both channels must match in x coordinates. Therefore, the backward signal must be flipped and aligned with the forward signal in a preprocessing step. For the calibration, it is assumed that both signals are acquired at the same time, but, in reality, the DTS device measures both signals consecutively. The acquisition time is in the range of seconds to a few minutes, depending on the DTS device and its settings.

To slightly modify equation (2.27) for the double-ended calibration, the limits of the attenuation integral are reformulated for the forward signal

$$\int_0^x \Delta\alpha(x')\,\mathrm{d}x' = \int_0^{x_1} \Delta\alpha(x')\,\mathrm{d}x' + \int_{x_1}^x \Delta\alpha(x')\,\mathrm{d}x' = \int_0^{x_1} \Delta\alpha(x')\,\mathrm{d}x' + A(x) \tag{2.30}$$

and the backward signal

$$\int_x^L \Delta\alpha(x')\,\mathrm{d}x' = \int_{x_1}^L \Delta\alpha(x')\,\mathrm{d}x' - \int_{x_1}^x \Delta\alpha(x')\,\mathrm{d}x' = \int_{x_1}^L \Delta\alpha(x')\,\mathrm{d}x' - A(x) \tag{2.31}$$

with an arbitrary coordinate x_1 of the fiber. With this definition, both equations contain the identical attenuation integral from x_1 to x, which is abbreviated as $A(x)$. The integrals independent of x must result in a constant value. These constant-value integrals are added to the coefficient $C(t)$ from equation (2.27), i.e., for the forward channel

$$D_\mathrm{F}(t) = C_\mathrm{F}(t) + \int_0^{x_1} \Delta\alpha(x')\ \mathrm{d}x' \tag{2.32}$$

and the backward channel

$$D_\mathrm{B}(t) = C_\mathrm{B}(t) + \int_{x_1}^L \Delta\alpha(x')\ \mathrm{d}x'. \tag{2.33}$$

With $A(x)$, $D_\mathrm{F}(t)$, and $D_\mathrm{B}(t)$, equation (2.27) becomes

$$T_\mathrm{F}(x,t) = \frac{\gamma}{I_\mathrm{F}(x,t) + D_\mathrm{F}(t) + A(x)} \tag{2.34}$$

for the forward channel, and

$$T_\mathrm{B}(x,t) = \frac{\gamma}{I_\mathrm{B}(x,t) + D_\mathrm{B}(t) - A(x)} \tag{2.35}$$

for the backward channel. At M locations along the calibration section and N measurements with both signals, $2\,NM$ equations exist for the parameter calibration:

$$I_{\mathrm{F},m,n} = \frac{1}{T_{m,n}}\gamma - D_{\mathrm{F},n} - A_m, \qquad m \in \{1,2,...,M\},\ n \in \{1,2,...,N\} \tag{2.36}$$

$$I_{\mathrm{B},m,n} = \frac{1}{T_{m,n}}\gamma - D_{\mathrm{B},n} + A_m, \qquad m \in \{1,2,...,M\},\ n \in \{1,2,...,N\} \tag{2.37}$$

As x_1 is set to be the first point in the calibration section, A_1 is by definition zero. Consequently, γ, $M-1$ parameters of A_m, $2N$ parameters of $D_{\mathrm{F},n}$, and $D_{\mathrm{B},n}$ result in $2N+M$ unknowns. Similar to the single-ended calibration, a regression algorithm that minimizes the sum of squared residuals is applied to estimate these parameters in the Python package *dtscalibration*. At all locations p outside the reference section, the differential attenuation parameter A_p is calculated by setting $T_\mathrm{F} = T_\mathrm{B}$.

With all parameters estimated, two temperature signals T_F and T_B exist for all locations and time instances. Furthermore, a variance estimation of the calculated temperature signals is implemented in the calibration code. The variance of a temperature signal increases with distance, i.e., the forward signal has the smallest variance at the Channel 1 connector and the highest variance at the Channel 2 connector (vice versa for the backward signal). Therefore, a weighted temperature $T_\mathrm{W}(T_\mathrm{F}, T_\mathrm{B})$ is calculated by inverse-variance-weighted time averaging. For a more detailed description of the calibration algorithm and its implementation, see Des Tombe et al. [23].

Note on number of reference sections

Either two reference sections at two distinct constant-temperature reference section or one reference section at sufficiently varying temperature are required. This ensures that the calibration algorithm successfully differentiates between $\gamma/T_{m,n}$ and $x_m\Delta\alpha + C_n$ in single-ended calibration and between $\gamma/T_{m,n}$ and $D_{\mathrm{F},n}$ ($D_{\mathrm{B},n}$) in double-ended calibration [23]. In the present work two constant-temperature sections are applied.

See Appendix C for a demonstration of the impact of both calibration methods on the measured DTS data.

2.3.4 Performance criteria

Six performance criteria of DTS devices are introduced in the following: distance range, sampling interval, spatial resolution, measurement time, temperature resolution, and temperature accuracy. Furthermore, the procedures of quantifying spatial resolution and temperature accuracy are described. See Hartog [30] for a more comprehensive elaboration on all of those criteria.

The distance range is the maximum fiber length that can be measured with a DTS device. The sampling interval is the minimum distance between two sampling points. Each sampling point returns a measured value that is influenced by a distance larger than the sampling interval. This sampling-point-influencing distance is quantified by the spatial resolution. The measurement time is the duration that it takes the DTS device to return a measurement set for the full fiber length. A longer measurement time usually increases the signal-to-noise ratio, but it smears transient changes. Usually, DTS devices offer multiple measurement time settings. The temperature resolution is the minimum temperature step that can be resolved; it is influenced by the signal-to-noise ratio and is a measure of repeatability. The temperature accuracy is not only a measure of the DTS device, as it is influenced by the calibration algorithm and the fiber setup, which introduces signal attenuation by splices, connectors, sharp fiber bends, and overall fiber length.

Typical ranges of the criteria are $2 - 50\,\mathrm{km}$ of distance range, $0.25 - 2\,\mathrm{m}$ of sampling interval, $0.25 - 2\,\mathrm{m}$ of spatial resolution, $2\,\mathrm{s} - 2\,\mathrm{min}$ of measurement time, and $0.01 - 0.5\,^\circ\mathrm{C}$ of temperature resolution. These ranges are very wide and highlight that each DTS device is a compromise optimized towards a certain performance criterion. A device optimized for maximum distance range will also have large sampling intervals, a wider spatial resolution, and require a longer measurement time. In contrast, a device optimized for short spatial resolution and short measurement time must compromise on the distance range.

Spatial resolution and accuracy are the most difficult properties to precisely quantify in a DTS system. Both are discussed separately below.

Simon et al. [62] reviews various methods to evaluate the spatial resolution. The methods are centered on the observation of the response to a step change in temperature. The more elaborate methods are to fit a Gaussian function to the step change, or to analyze the derivative of the step

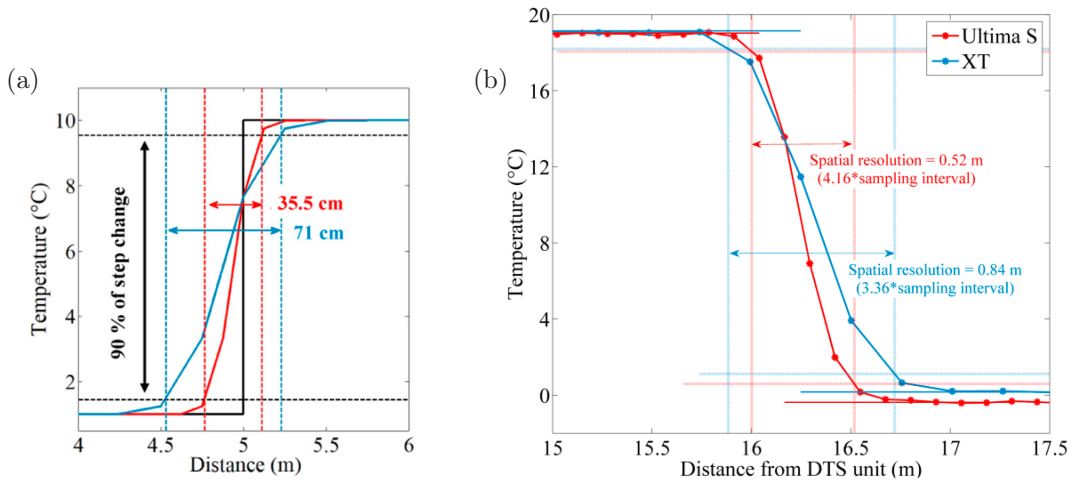

Figure 2.9: (a) Illustration of the 90 % step change method with simulated data, and (b) application of the 90 % step change method to determine the spatial resolution of two DTS devices. (Both subfigures reprinted from [62], which is published under CC BY license).

change, yet the simplest and more widespread approach is to measure the 90 % distance of the step change, as demonstrated in Figure 2.9 (a). Therefore, the fiber distance between 5 % and 95 % of the temperature step is measured. The measured values in Figure 2.9 (b) are slightly higher than the values given in the respective devices' datasheets. The manufacturer transparently provides information on how they define spatial resolution in a user guide [61]. They also use *the* 90 % *step change method*, but they measure the distance between 10 % and 90 % of the temperature step, which only spans 80 % of the step. Thus, datasheet information on this value must be considered with care if the definition used by the manufacturer is not transparently provided.

A demonstration of high-accuracy temperature measurement performance is shown by Des Tombe et al. [23] in the same publication as the calibration algorithm described in Subsection 2.3.3. They demonstrate a high-accuracy temperature measurement in a monitored validation section. They report an error, defined as the difference between reference sensor and fiber temperature, of 0.06 °C. This example shows that a well calibrated DTS setup is capable to measure temperatures with quantifiable, high accuracy. Yet, this example is not representative for any other DTS measurement that is differently calibrated or has a different fiber-setup. A clear indicator of that is, that DTS manufacturers never provide information on measurement accuracy. For each measurement setup interested in accuracy, the accuracy must be investigated within the setup.

2.4 Heat transfer

The investigated method in the present work intends to measure fluid flow velocities by quantifying the velocity dependence of convective heat transfer. The applied probes are modeled as long cylinders with multiple sheaths. Radial heat conduction governs the heat transfer inside the cylinder, and heat convection governs the heat transfer outside the cylinder. Therefore, this section outlines the basic principles of heat transfer, deduces the heat diffusion equation, and outlines the relevant nondimensional numbers for the subsequently investigated conjugate heat transfer.

2.4.1 Conduction, convection and radiation

"Heat transfer (or heat) is thermal energy in transit due to a temperature difference." Incropera [32, page 2] Heat transfer is classified into three categories: heat conduction, heat convection, and heat radiation.

Heat **conduction**, considered at the molecular level, is the transfer of energy from more energetic particles to less energetic ones. In a fluid or gas without bulk motion, the molecules exhibit random translational motion, internal rotation, and vibrational motion. In a solid, molecules are fixed in a lattice except for moving free electrons in electrically conducting solids. Thus, lattice vibrations and lattice waves occur. Higher temperature is the result of molecules having higher molecular energy, which equals higher intensity of motions, and during collisions energy is transferred to molecules with less energy. Consequently, conductive heat transfer is always directed from matter at higher temperature toward matter at lower temperature.

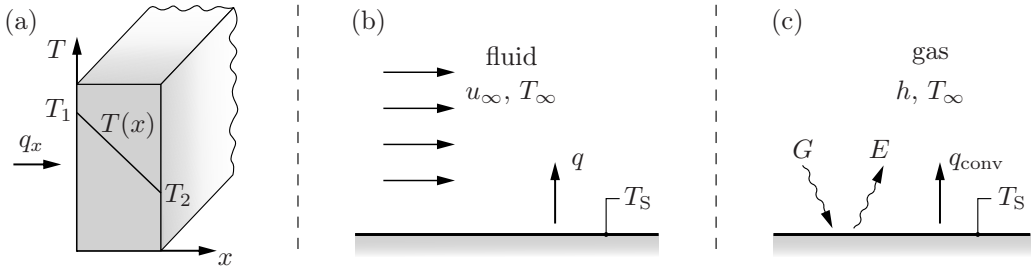

Figure 2.10: Sketch visualizing the heat transfer phenomena: (a) demonstrates one-dimensional heat conduction through a solid plate, (b) sketches heat convection from a surface at T_S to a fluid at T_∞, and (c) highlights thermal radiation from a surface E and irradiation G. Adapted from [32].

Conductive heat transfer is described by *Fourier's law*

$$q_x = -k\frac{\mathrm{d}T}{\mathrm{d}x}. \tag{2.38}$$

Here, q_x [W/m^2] is the heat flux in x-direction, k [W/(mK)] represents the thermal conductivity, and T [K] is the temperature. The resulting temperature profile of one-dimensional heat conduction inside a solid is sketched in Figure 2.10 (a).

Figure 2.10 (b) sketches the case where heat is transferred from a hot solid to a moving fluid. In fluids, bulk motions (advection) exist that are either driven by external means or driven by the thermal inhomogeneity. Because fluid density is temperature-dependent, temperature inhomogeneities induce density inhomogeneities, which in turn lead to either buoyancy-driven flow or thermal stratification. Advective transport of heat in moving fluids is either quantified by the simplified concept of convection or it must be computed, which requires the solution of the Navier–Stokes equation and energy equation for the moving fluid. However, to solve the Navier–Stokes equation is too resource-intense or not possible for most applications. Consequently, the concept of **convection** is a simplified approach to heat transfer that comprises both conduction by random molecular motion (diffusion) and macroscopic fluid motion (advection). More specifically, it is called *forced* convection if the flow is driven by external means and *free* or *natural* convection when the flow is buoyancy-driven. The convective heat transfer is modeled by *Newton's law of cooling*

$$q = h(T_S - T_\infty). \tag{2.39}$$

h [W/(m^{2}K)] is the heat transfer coefficient, T_S [K] is the surface temperature, and T_∞ [K] is the fluid's bulk temperature. The value of the heat transfer coefficient must either be measured or determined from empirical correlations that in turn are based on measurements. It may also be computed by solving the Navier–Stokes and energy equations using various simulation algorithms to compare numerical to experimental or empirical results.

In addition to conduction and convection, all matter at non-zero temperature emits thermal **radiation**. The technical context mostly focuses on radiation from solids (as sketched in Figure 2.10 (c)), because many liquids are opaque to radiation (for example water) and gases contribute often very little to technical radiation problems, such as heating in a furnace. The radiation energy is transported by electromagnetic waves / photons and is modeled by the *Stefan–Boltzmann* law

$$E_\mathrm{b} = \sigma T_\mathrm{S}^4. \tag{2.40}$$

$\sigma = 5,67 * 10^{-8}\,\mathrm{W/(m^2K^4)}$ is the *Boltzmann* constant, and E_b [W/m^2] is the emissive power per unit area emitted by an ideal radiator, a so-called black body. A realistic surface has an emissivity ϵ, which is defined in the range $0 \leq \epsilon \leq 1$, and thus an emissivity

$$E = \epsilon \sigma T_\mathrm{S}^4. \tag{2.41}$$

The radiation impacting onto a surface G is called irradiation. A fraction of the irradiation is absorbed by the surface. The absorbed fraction is quantified by the absorptivity α, which is also defined in the range from 0 to 1. The net radiative heat flux from a surface amounts to

$$q_\mathrm{rad} = \epsilon \sigma T_\mathrm{S} - \alpha G. \tag{2.42}$$

2.4.2 Heat diffusion equation

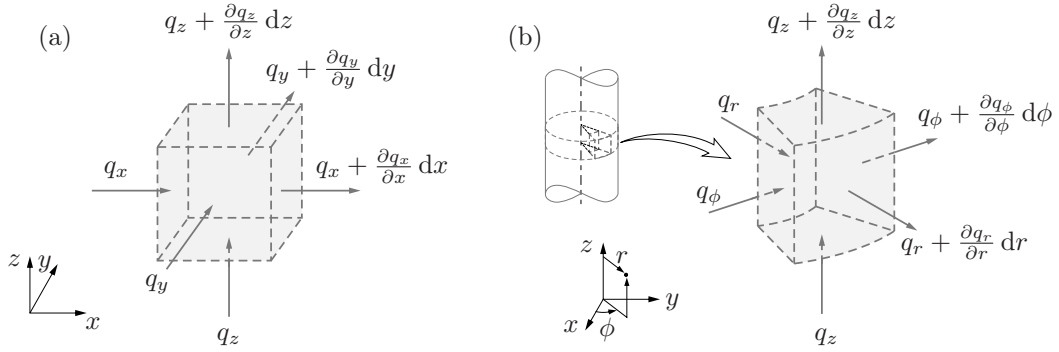

Figure 2.11: Finite volume (a) in cartesian coordinates and (b) in cylindrical coordinates. Adapted from [32].

The heat diffusion equation describes three-dimensional heat conduction inside a homogeneous medium without advective motion, such as a solid or a motionless fluid. In the following, the heat diffusion equation is derived from the conservation of energy for Cartesian coordinates, stated for cylindrical coordinates, and solved for steady, one-dimensional heat conduction in radial direction.

Figure 2.11 (a) displays a differential volume in Cartesian coordinates. The conservation of energy

$$\dot{E}_\mathrm{in} - \dot{E}_\mathrm{out} + \dot{E}_\mathrm{g} = \dot{E}_\mathrm{st}. \tag{2.43}$$

is the net rate of the volume's heat conduction $\dot{E}_{\text{in}} - \dot{E}_{\text{out}}$ plus the rate of energy converted into heat $\dot{E}_{\text{g}}$ equal to the rate of energy stored in the volume $\dot{E}_{\text{st}}$. The rate of energy converted into heat

$$\dot{E}_{\text{g}} = \dot{q}_{\text{g}} \, \mathrm{d}x \, \mathrm{d}y \, \mathrm{d}z \tag{2.44}$$

is defined by the volume specific heat generation rate $\dot{q}_{\text{g}}$ [W/m^3] integrated over the volume. It may be positive when a heat source, such as an exothermic reaction or Joule heating, is present, or it may be negative for a heat sink, such as an endothermic reaction. When no phase change occurs in the medium, i.e., latent energy effects are not considered, the rate of energy stored in it becomes

$$\dot{E}_{\text{st}} = \rho c_p \frac{\partial T}{\partial t} \, \mathrm{d}x \, \mathrm{d}y \, \mathrm{d}z. \tag{2.45}$$

The product of the matter's density ρ [kg/m^3] and specific heat c_p [J/(m^{3}K)] is the volumetric heat capacity at constant pressure, which measures the ability of a material to store thermal energy. The energy rate balance

$$-\frac{\partial q_x}{\partial x}\mathrm{d}x - \frac{\partial q_y}{\partial y}\mathrm{d}y - \frac{\partial q_z}{\partial z}\mathrm{d}z + \dot{q}_{\text{g}} \, \mathrm{d}x \, \mathrm{d}y \, \mathrm{d}z = \rho c_p \frac{\partial T}{\partial t} \, \mathrm{d}x \, \mathrm{d}y \, \mathrm{d}z \tag{2.46}$$

together with Fourier's law, see equation (2.38), is divided by the volume $\mathrm{d}x \, \mathrm{d}y \, \mathrm{d}z$. This results in the general form of the heat diffusion equation

$$\frac{\partial}{\partial x}\left(k\frac{\partial T}{\partial x}\right) + \frac{\partial}{\partial y}\left(k\frac{\partial T}{\partial y}\right) + \frac{\partial}{\partial z}\left(k\frac{\partial T}{\partial z}\right) + \dot{q}_{\text{g}} = \rho c_p \frac{\partial T}{\partial t}. \tag{2.47}$$

In cylindrical coordinates (compare Figure 2.11 (b)), the general form of the heat diffusion equation becomes

$$\frac{1}{r}\frac{\partial}{\partial r}\left(kr\frac{\partial T}{\partial r}\right) + \frac{1}{r^2}\frac{\partial}{\partial \phi}\left(k\frac{\partial T}{\partial \phi}\right) + \frac{\partial}{\partial z}\left(k\frac{\partial T}{\partial z}\right) + \dot{q}_{\text{g}} = \rho c_p \frac{\partial T}{\partial t}. \tag{2.48}$$

For the heat transfer modeling in Subsection 3.1.1, equation (2.48) is simplified with the assumption of steady state heat transfer in radial direction: In steady state, the temperature is constant over time, thus, the rate of energy stored in the volume must be zero. One-dimensional radial heat conduction means that the temperature T is independent of the ϕ and z coordinates. Additionally, the thermal conductivity k is assumed to be constant in the cylinder. Consequently, the simplified heat diffusion equation becomes

$$k\frac{1}{r}\frac{\mathrm{d}}{\mathrm{d}r}\left(r\frac{\mathrm{d}T}{\mathrm{d}r}\right) + \dot{q}_{\text{g}} = 0. \tag{2.49}$$

As $T(r)$ is only a function of r, the partial derivate is equal to the total derivate. To solve this equation, it is integrated twice:

$$r\frac{\mathrm{d}T}{\mathrm{d}r} = \frac{\dot{q}_{\text{g}}}{k}\frac{r^2}{2} + C_1 \tag{2.50}$$

$$T(r) = \frac{\dot{q}_{\text{g}}}{k}\frac{r^2}{4} + C_1 \ln r + C_2. \tag{2.51}$$

The constants C_1 and C_2 are to be determined by inserting appropriate boundary conditions into equations (2.50) and (2.51).

2.4.3 Relevant dimensionless numbers

The considered heat transfer problem in the present work contains both heat conduction inside a solid and heat convection from this solid to a fluid. This setting is also referred to as conjugate

heat transfer. Radiation is not relevant in the present case because water as the considered fluid is opaque to heat radiation.

When working with heat transfer problems, it is helpful to consider the relevant dimensionless numbers for two reasons. First, describing the problem nondimensionally allows scaling. Thus, experimental data from similar experiments with similar geometries but differences in size or fluid properties can be transferred to the problem under investigation. In the field of heat and mass transfer, large experimental datasets are fitted to find functions – so called empirical correlations – that quite accurately represent the underlying physics in their validity range. The certainty of these empirical correlations depends strongly on the discrepancies, i.e., where similarity cannot be achieved, between the intended application and the reference experiment used to generate the empirical correlation. Furthermore, in the engineering context, similarity is often exploited to perform experiments on a different scale (usually smaller and thus cheaper) before building and testing the final product. The second advantage of approaching a heat transfer problem nondimensionally occurs in problems in which multiple heat transfer mechanisms coexist. Ratios of dimensionless numbers describing specific mechanisms reveal, whether both effects occur in a similar order of magnitude or whether one effect prevails, rendering the other less important or even negligible.

In convective heat transfer, the **Nusselt** number

$$Nu = \frac{hL_{\mathrm{char}}}{k_{\mathrm{f}}} \tag{2.52}$$

is defined as the ratio of the convective heat transfer coefficient h to the thermal conductivity of the fluid k_{f}, multiplied by the characteristic length scale L_{char}, and provides a measure of the heat transfer efficiency. Substituting h from equation (2.39) leads to

$$Nu = \frac{q}{T_{\mathrm{S}} - T_{\infty}} \frac{L_{\mathrm{char}}}{k_{\mathrm{f}}}, \tag{2.53}$$

which enables direct computation of Nu when heat flux, surface temperature, and ambient temperature are measured. The **Prandtl** number

$$Pr = \frac{\nu}{a} \tag{2.54}$$

is defined by the ratio of the fluid's kinematic viscosity, also called momentum diffusivity, ν, to its thermal diffusivity

$$a = \frac{k}{\rho c_p} \tag{2.55}$$

(recall: k thermal conductivity, ρ density, and c_p specific heat). Pr depends only on the fluid type and the fluid state. The **Reynolds** number

$$Re = \frac{uL_{\mathrm{char}}}{\nu} \tag{2.56}$$

is defined with the fluid's velocity u and represents the velocity dependent influence of forced convection in Nusselt correlations of the heat transfer. In general, Re is the ratio of the inertial forces to the viscous forces within the fluid. During natural convection, the heating or cooling of the fluid affects its density, which then generates a buoyancy-driven flow. Buoyancy arises from density variations within a gravitational field characterized by the gravitational acceleration g. With the expansion coefficient

$$\beta = -\frac{1}{\rho}\left(\frac{\partial \rho}{\partial T}\right)_p \tag{2.57}$$

and the characteristic length L_{char}, a velocity

$$u = \sqrt{g\beta(T_{\mathrm{S}} - T_{\infty})L_{\mathrm{char}}} \tag{2.58}$$

that is driven by buoyancy can be estimated. The **Grashof** number

$$Gr = \frac{g\beta(T_{\mathrm{S}} - T_{\infty})L_{\mathrm{char}}^3}{\nu^2} \tag{2.59}$$

may be interpreted as a squared Reynolds number, built with the buoyancy-driven velocity, and represents the ratio of buoyant forces to viscous forces. In the data processing of the present work, the expansion coefficient is estimated as

$$\beta \approx -\frac{1}{\rho(T_{\mathrm{m}})}\left(\frac{\rho(T_{\mathrm{S}}) - \rho(T_{\infty})}{T_{\mathrm{S}} - T_{\infty}}\right) \tag{2.60}$$

for water with its densities at T_{S}, T_{∞}, and $T_{\mathrm{m}} = (T_{\mathrm{S}} + T_{\infty})/2$. The water densities are retrieved from a lookup table [42].

In most flow scenarios, the convective heat transfer between a surface and a single-phase fluid may be fully described by an equation of the form

$$Nu(Re, Gr, Pr, \kappa_i) \tag{2.61}$$

for a specific geometry. In specific cases, Nu may depend on more dimensionless numbers. For example, in compressible gaseous flow the Mach number may be relevant, and when considering small heated objects such as hot-wires in thin atmospheres, the additional consideration of the Knudsen number may be necessary. κ_i are ratios of lengths specifying the geometry, which are usually constant values if the geometries do not differ. Yet, especially when the same geometry is built twice at two largely different length scales it is difficult or impossible to achieve similarity between the smallest and largest lengths of a system. Examples are the ratio of surface roughness height to characteristic length, or in turbomachinery the ratio of gap height between rotor blade and housing to diameter of the rotor. In the following, geometric similarity is assumed and κ_i omitted from the formulas.

Natural convection occurs at every heated surface. Depending on the surface temperature and on the fluid velocity, which is forced by external means, natural convection may be dominant or negligible compared to forced convection. The **Richardson** number

$$Ri = \frac{Gr}{Re^2}, \tag{2.62}$$

which is the ratio of buoyant forces to inertial forces, is used to estimate which of these effects predominates the convective heat transfer. For $Ri \gg 1$, natural convection is dominant and Nu is solely a function of Gr and Pr: $Nu(Gr, Pr)$. In contrast, for $Ri \ll 1$, forced convection is dominant and $Nu(Re, Pr)$ is valid. For the Ri range in between both effects must be considered, i.e., $Nu(Re, Gr, Pr)$.

In conjugate heat transfer, both heat conduction through a solid and heat convection from the solid's surface to a fluid exist. For one-dimensional steady-state heat transfer in Cartesian coordinates, as sketched in Figure 2.12, the **Biot** number is defined as

$$Bi = \frac{h}{k_{\mathrm{s}}}l \tag{2.63}$$

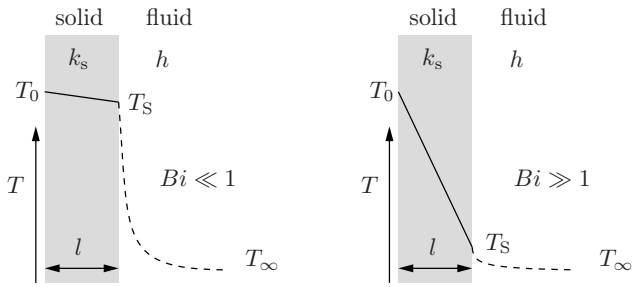

Figure 2.12: Sketch to visualize that $Bi \ll 1$ describes dominant heat convection and $Bi \gg 1$ describes dominant heat conduction in conjugate heat transfer.

and relates the heat conduction resistance in the solid l/k_s to the heat transfer resistance by convection $1/h$. The Biot number may also be more generally expressed as

$$Bi = \frac{R_{\text{cond}}}{R_{\text{conv}}} \tag{2.64}$$

with R_{cond} and R_{conv} as resistances to conduction and convection, respectively. As the heat flow rate

$$\dot{Q} = \frac{1}{R_{\text{cond}}}(T_0 - T_S) = \frac{1}{R_{\text{conv}}}(T_S - T_\infty) \tag{2.65}$$

must be constant for both convection and conduction, the Biot number becomes

$$Bi = \frac{T_0 - T_S}{T_S - T_\infty}. \tag{2.66}$$

The hot-side temperature T_0, the surface temperature T_S, and the ambient temperature T_∞ are defined in Figure 2.12. For $Bi \ll 1$, the resulting temperature drop occurs predominantly in the fluid, and for $Bi \gg 1$, in the solid.

The **Peclet** Number

$$Pe = Re\, Pr \tag{2.67}$$

may be interpreted as the ratio between diffusion time and advection time. The term convection includes both heat diffusion between the fluid's molecules and heat advection caused by the fluid's bulk motion. In most technical cases, heat diffusion is only relevant very close to the surface, as advection leads to mixing and thus predominates the heat transfer, i.e., $Pe \gg 1$. However, $Pe \ll 1$ occurs in specific, more unusual contexts, and consequently, heat conduction is then the prevalent heat transfer phenomenon inside the fluid. For example, in liquid metal flows, $Pe \ll 1$ may hold depending on the metal and the velocity. Another example in the geoscientific context is heated flow through porous media, compare method (i) in Subsection 2.6.1. Here, the advection is restricted by the porous medium and Re becomes very small.

The **Rayleigh** number

$$Ra = Gr\, Pr \tag{2.68}$$

may be similarly interpreted as the Peclet number in natural convection problems. Recall that $Ri \gg 1$ is required for predominant natural convection. For small Ra, conductive heat transfer is relevant inside the fluid domain, and for large Ra, conductive heat transfer is negligible because of the prevalent natural convection.

2.4.4 Empirical correlations

The heat transfer coefficient h from Newton's law in equation (2.39) aggregates all physical phenomena of convective heat transfer. Analytical solutions exist only for cases that are limited to simple geometries and laminar flow. For more complex cases, h must either be estimated numerically or with empirical correlations.

The geometry relevant in the present work is a cylinder in cross flow, i.e., the cylinder's axis is positioned perpendicular to the flow direction. Multiple empirical correlations exist to describe the convective heat transfer for this particular case. Throughout the present work, the correlation by Gnielinski [28] is used as the forced-convection comparison case for the acquired experimental data. Churchill and Chu [20] present a correlation to describe natural convection at a horizontal cylinder, and Chen et al. [18] propose to merge natural-convection and forced-convection correlations to describe mixed convection. In the following, the just-named correlations are introduced. Furthermore, they are visualized in graphs together with other similar correlations.

Gnielinski [28] gathered much experimental data from the literature, which covers broad ranges of Re and Pr, and found that the equation

$$Nu_l = Nu_{l,\min} + \sqrt{Nu_{l,\mathrm{lam}}^2 + Nu_{l,\mathrm{turb}}^2} \tag{2.69}$$

matched well with the experimental data. Therefore, he used the laminar solution of the flat-plate boundary-layer equations by Pohlhausen

$$Nu_{l,\mathrm{lam}} = 0.664\, Re_l^{1/2}\, Pr^{1/3}, \tag{2.70}$$

the turbulent-regime correlation by Petukhov and Popov [53]

$$Nu_{l,\mathrm{turb}} = \frac{0.037\, Re_l^{0.8}\, Pr}{1 + 2.443\, Re_l^{-0.1}\, (Pr^{2/3} - 1)}, \tag{2.71}$$

and $Nu_{l,\min} = 0.3$. With different $Nu_{l,\min}$ values and respective characteristic length definitions, equation (2.69) is valid for the flow along a flat plate, the flow around a cylinder, and the flow around a sphere. Gnielinski [28] defined the cylinder's overflow length

$$L_{\mathrm{char}} = \frac{\pi\, d}{2} \tag{2.72}$$

as the characteristic length. When dimensionless numbers contain the subscript l, the cylinder's overflow length, equation (2.72), is used as characteristic length. The more common case in the literature is to use the cylinder's diameter as characteristic length

$$L_{\mathrm{char}} = d. \tag{2.73}$$

Dimensionless numbers calculated with the diameter as characteristic length are not subscripted. The differing characteristic length definitions result in

$$Re = \frac{2}{\pi}\, Re_l \tag{2.74}$$

and

$$Nu = \frac{2}{\pi}\, Nu_l, \tag{2.75}$$

which must be considered when comparing $Nu - Re$ correlations from varying sources.

Figure 2.13 provides such a comparison of forced-convection correlations from multiple sources. Similar to Gnielinski [28], Churchill and Bernstein [19] gathered a large amount of literature data and formulated an improved correlation based on an existing correlation by Tsubouchi and Masuda [69]. Kramers [36], Collis and Williams [21], and McAdams [47] are older correlations from the 1940s and 1950s. The correlations from Collis and Williams and McAdams are for air only. Thus, they are plotted only in the lower diagrams of Figure 2.13. The correlation by King [35] is the two-dimensional analytical solution for the flow around a heated cylinder that assumes potential flow. Its approximation by Collis and Williams (eq. 9 in [21]) is plotted in Figure 2.13.

When comparing the various correlations in Figure 2.13, one recognizes in the linear diagrams (left column) for the low-Re range that King overestimates Nu_l, while $Nu_{l,\mathrm{turb}}$ by Petukhov and Popov, which is not valid in the low-Re range, underestimates Nu_l. The other correlations correspond fairly well in this low-Re range. In the logarithmic diagrams, the slopes of the Gnielinski, and Churchill and Bernstein equations increase at $Re \approx 10^5$ to match data acquired at high Re.

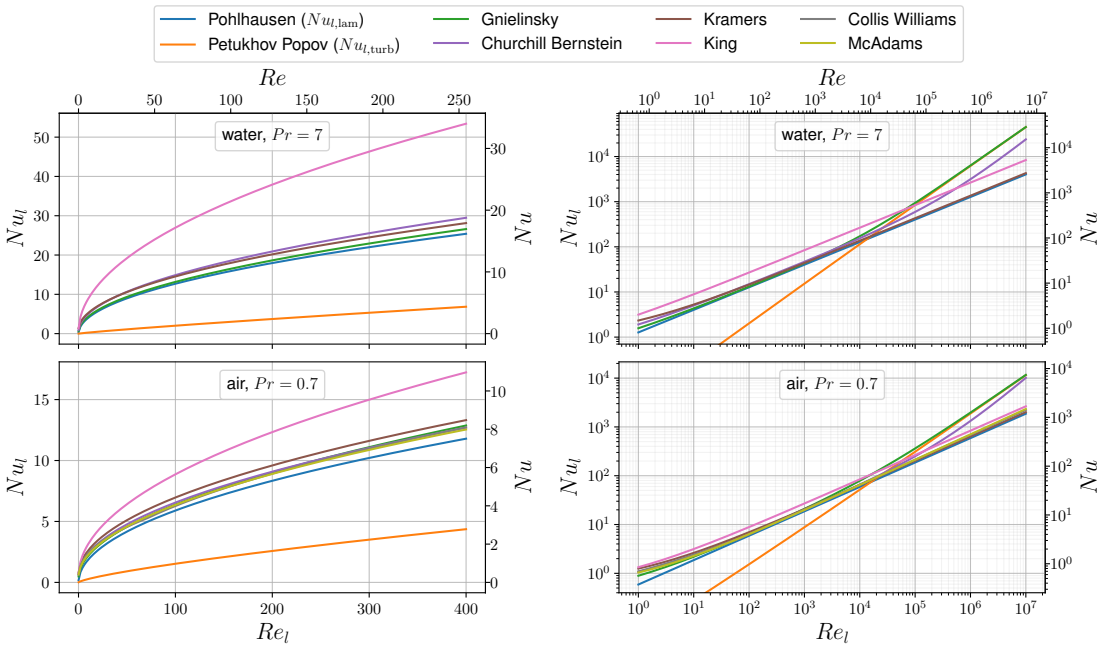

Figure 2.13: Visualization of multiple forced-convection $Nu(Re, Pr)$ correlations for $Pr = 7$ (upper plots) and $Pr = 0.7$ (lower plots). The correlations are displayed with linear axes scaling in the Re range relevant to the present work on the left side and with logarithmic axes scaling covering a wider range on the right side.

If the cross-flow velocity of the cylinder is either small or nonexistent, natural convection heat transfer, i.e., $Nu(Gr, Pr)$ must be considered. For that case, empirical correlations for natural convection exist, such as that from Churchill and Chu [20]

$$Nu = \left[0.6 + 0.387 \left(\frac{Gr\,Pr}{[1 + (0.559/Pr)^{9/16}]^{16/9}} \right)^{1/6} \right]^{1/2} . \tag{2.76}$$

To estimate the heat transfer of the mixed-convection regime, i.e., $Ri \sim 1$, Chen et al. [18] suggest to use

$$Nu^3 = Nu_\mathrm{f}^3 + Nu_\mathrm{n}^3 \tag{2.77}$$

when the flow directions of natural and forced convection are parallel, and

$$Nu^3 = Nu_\mathrm{f}^3 - Nu_\mathrm{n}^3 \tag{2.78}$$

when the directions counteract. Figure 2.14 displays the enhancing mixed-convection approach from equation (2.77) with the Gnielinski correlation, equation (2.69), as Nu_f, and the Churchill and Chu correlation, equation (2.76), as Nu_n. $Pr = 7$ is used, and the plotted Grashof numbers (cp. equation (2.59)) are calculated with cylinder diameter $d = 4.2\,\mathrm{mm}$, surface temperatures $20.5\,^\circ\mathrm{C}$, $25\,^\circ\mathrm{C}$, and $30\,^\circ\mathrm{C}$, and ambient temperature $T_\infty = 20\,^\circ\mathrm{C}$.

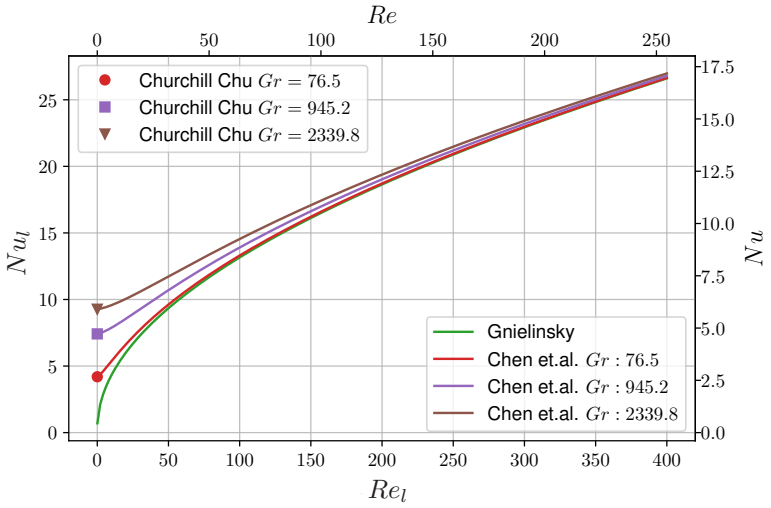

Figure 2.14: Visualization of correlations representing combined free and forced convection at $Pr = 7$ with the approach by Chen et al. equation (2.77). Gnielinski, equation (2.69), represents forced convection, and Churchill and Chu, equation (2.76), represent free convection at various Grashof values. The displayed Gr values are calculated for a cylinder with $d = 4.2\,\mathrm{mm}$, $T_\mathrm{S} = [20.5, 25, 30]\,^\circ\mathrm{C}$ and $T_\infty = 20\,^\circ\mathrm{C}$ according to equation (2.59).

The curves in Figure 2.14 visualize the interplay of free and forced convection for realistic Grashof numbers in the Reynolds number range relevant to the present work: They demonstrate that free convection is clearly dominant for all plotted cases in the range $Re < 10$. Furthermore, they show that the Reynolds number range of the mixed-convection regime strongly depends on the Grashof number and thus on the heating power, which controls the surface temperature T_S.

2.5 Conventional thermal anemometry (TA)

Hot-wire anemometry (HWA) and hot-film anemometry (HFA) are well-established thermal flow measurement techniques. Both consist of a temperature-dependent electrical resistor that is heated via Joule heating and placed into a flow. Figure 2.15 visualizes a hot-wire probe and its energy balance

$$P_\mathrm{el} = \dot{Q}_\mathrm{conv} + \dot{Q}_\mathrm{cond} + \dot{Q}_\mathrm{rad} \tag{2.79}$$

that is utilized for the flow measurement. The electrical power P_el is dissipated by Joule heating in the wire: $\dot{Q}_\mathrm{conv}$ is the heat rate transferred to the fluid via natural and forced convection, $\dot{Q}_\mathrm{cond}$ is the conductive heat rate transferred to the prongs, and $\dot{Q}_\mathrm{rad}$ is the net radiative heat rate transferred to the environment. Natural convection, radiation, and conduction effects are

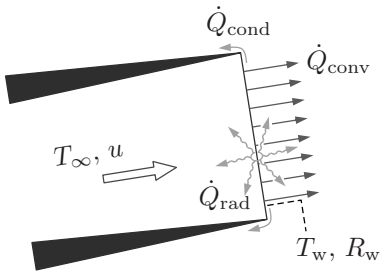

Figure 2.15: Illustration of the heat transfer occurring at a heated hot wire: The hot-wire probe consists of a wire which is soldered to the tips of two prongs. Common hot-wire dimensions are a diameter of 5 µm and a length of 1.5 mm [76]. The wire is heated by Joule heating and primarily transfers heat to the fluid via convection, but conduction to the prongs and radiation also occur. Adapted from [76].

considered to be minor compared to the forced-convection heat transfer, which simplifies the energy balance to

$$P_\mathrm{el} \stackrel{!}{=} \dot{Q}_\mathrm{conv} = hA(T_\mathrm{w} - T_\infty). \tag{2.80}$$

T_w is the wire's temperature, T_∞ is the ambient temperature, A is the wire's surface area, and h is the velocity-dependent convective heat transfer coefficient. The wire's electric resistivity

$$R_\mathrm{w} = R_0 \left[1 + \alpha \left(T_\mathrm{w} - T_0\right)\right] \tag{2.81}$$

(R_0 cold resistance at T_0, α temperature coefficient) is in good approximation a linear function of the wire's temperature T_w [76] and measured by the electric circuit with $R_\mathrm{w} = E/I$ (E [V] – voltage, and I [A] – current). By inserting a Nusselt correlation, such as equation (2.69), into equation (2.80), a function for the flows velocity can be derived. However, because of the simplifications in the modeling, the uncertainty of geometry and material parameters, and the uncertainty of Nusselt correlations, each hot-wire is calibrated. Commonly, a calibration function in the form

$$E^2 = (A + B\,u^n)(T_\mathrm{w} - T_\infty) \tag{2.82}$$

is used [76]. A, B, and n are constants to be determined by the calibration procedure. Best practice is to calibrate each sensor twice, before and after the experiment.

Two operating modes, constant current anemometry (CCA) and constant temperature anemometry (CTA), exist in TA. CCA supplies a constant current, which results in fluctuations of the wire temperature in response to flow velocity changes. In contrast, CTA keeps the wire temperature constant with a fast electronic control circuit. Keeping a constant wire temperature has the advantage of decreasing stress on the wire due to thermal expansion, and, more-importantly, with CTA higher velocity fluctuation frequencies can be resolved. Because of their fast frequency response, hot-wires are the technique of choice for measuring wall turbulence [76]. The main limitation of HWA is the fragility of the thin (diameter $d \leq 5\,\mu\mathrm{m}$) wire, which limits its application to clean gaseous flows [76].

HFA utilizes thin metal films applied onto a solid surface, as displayed in Figure 2.16, instead of thin wires. These hot films are more robust and applicable to liquid flows. On the downside, hot films have increased thermal inertia and decreased frequency response compared to hot wires.

Bruun [12] reviews the application of HFA in water and clearly outlines specific challenges related to TA in water: **Electrolysis** leads to a slight but continuous reduction of film thickness, which leads to a drift in cold resistance. This must be solved by coating the hot film with an insulating layer. Coating the film with a 1–2 µm thick quartz coating proved reliable to prevent electrolysis. **Bubble formation on the probe** occurs in air-saturated water on heated surfaces, as the solubility of

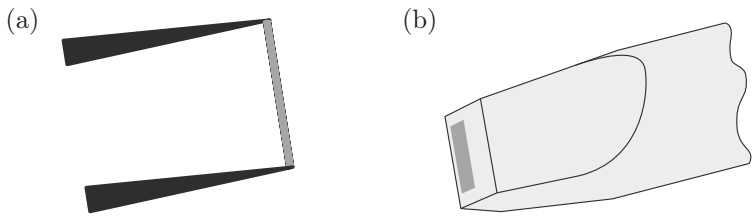

Figure 2.16: Sketch outlining two hot-film probe designs. (a) depicts two prongs holding a glass rod that is covered by a quartz-coated platinum film. Typical glass rod diameters are 25–150 µm [12]. (b) depicts a wedge-shaped quartz rod with a quartz-coated platinum film. Such a hot film covers typically an area of 100 µm × 1 mm [12]. See Bruun [12] for precise drawings of hot-film probes. Sketch design (b) inspired by [12].

gases decreases with increasing water temperature. These bubbles influence the heat transfer. Thus, bubble formation must be prevented by deaerating the water. **Probe contamination** by deposition of solid particles or algae growth on the hot film also influences the heat transfer. It is advised to use deionized water only. During long-term studies, the water should be filtered through a 2 µm filter to prevent particle contamination and cooled to $\leq 16\,^{\circ}\mathrm{C}$ to prevent algae growth. Jimenez et al. [34] reported that limited probe contamination may be corrected for, yet bubble formation leads to unrecoverable results. Tselentis [68] discusses the impact of probe contamination when applied in water wells and concludes that this approach is unfeasible.[1]

2.6 DTS-based flow measurement methods

In the previous two decades, multiple approaches emerged that utilize DTS temperature measurements for flow velocity measurements in the environmental context. In the following, these approaches are categorized into four methods, and method (iii), which is pursued in the present work, is outlined in more depth in Subsection 2.6.2 by summarizing the publication of Read et al. [56].

2.6.1 Overview of methods

In the environmental context, four methods exist to determine flow velocities with DTS temperature measurements:

(i) The measurement of sediment flow with the analysis of the temperature response curve of an actively heated DTS fiber, which is buried in the sediment, allows velocity measurements in the range of 1×10^{-5} to 5×10^{-2} m/s [63].

(ii) Thermal advection tests quantify the vertical movement of a heated water section inside a borehole, by monitoring the borehole's temperature distributedly with DTS. When a vertical flow exists in the borehole, the movement of the heated water section is revealed in the distributed temperature log [8].

(iii) TA of the vertical water flow of a borehole with an actively heated DTS fiber [56]. (Focus of the present work.)

(iv) TA of atmospheric wind speeds with an actively heated DTS fiber [38].

[1] The recommendation of the HFA literature to use deaerated, deionized, and filtered water was not followed throughout the present work. Only after the acquisition of the data presented in Chapter 5 was the HFA literature reviewed a second time with a focus on phenomena that influence the heat transfer.

Method (i) is widely used in both scientific research [4, 24, 63, 72] and commercial projects[2], method (iv) is established as scientific measurement technique [38, 39, 71], and methods (ii) and (iii) are proposed and demonstrated to some extent [8, 56], but do not seem to be established. In the following, methods (i) and (ii) are differentiated from the TA methods (iii) and (iv), and the preexisting works for the TA methods, especially in water, are outlined.

Method (i) considers conductive heat transfer from the probe to the environment and advective transport of the heated fluid. It presumes that the movement of the fluid is sufficiently confined by the sediment that natural convection is negligible. Traditionally, it is modeled with a moving instantaneous line source (MILS) by Carslaw and Jaeger [13]. The MILS is the two-dimensional version of the heat diffusion equation (2.47) for a heated point source that moves in positive x-direction to mimic a flow velocity. Depending on the research group, this method is called *thermal response test* [3, 72], *heat pulse response* [24], or *active-DTS* [63]. Simon et al. [63] provides a comprehensive overview of the methodology, including the MILS model, a numerical simulation that additionally considers the impact of the heated cable, a laboratory experiment, and detailed instructions on how to apply the method. This method is clearly distinct from TA, as it can only be applied in sediment flows at very small flow rates, where heat conduction is the dominant heat transfer mechanism at the cable's surface.

Method (ii) utilizes a heating element located somewhere in the borehole to heat the fluid locally. After heating the fluid section, a pump connected to the borehole is turned on, and the heated fluid section begins to travel through the borehole. At inflow or outflow zones, the heated fluid's temperature and velocity change. Compared to the other methods, which use actively heated fibers and evaluate the heat transfer during heating, this method passively monitors the temperature and does not apply heat transfer modeling.

TA with optical fibers applied in air flows, method (iv), has been proposed multiple times with various fiber-optic measurement techniques and fiber-heating principles [16, 27, 43, 44, 51]. The technique gained attention for the measurement of atmospheric flows, which previously relied on point measurement techniques. The fiber-optic, distributed velocity measurement enables the quantification of large flow structures in atmospheric flows. First demonstrated by Sayde et al. [59], an actively heated DTS fiber can serve as a more than 100 m-long distributed hot wire to provide distributed velocity measurements for the quantification of atmospheric flows. Since then, this approach was revisited with wind-tunnel studies for validation [71] and to investigate directional sensitivity [38], and applied in multiple field studies [1, 39, 46].

2.6.2 TA in water

Among the four DTS velocimetry methods presented in Subsection 2.6.1, method (iii) refers to TA in water, which is much less investigated compared to method (iv), TA in air. Read et al. [56] introduced and demonstrated this concept. Their work is summarized and discussed below. The second preceding work on method (iii) from Renner [57] is described and its data are reevaluated in Section 4.2.

As displayed in Figure 2.17, Read et al. [56] fixed two fiber-optic cables in the borehole, one unheated to measure the ambient temperature and one heated to measure the cable's core temperature. To process the temperature measurements from both cables into velocity information, they

[2] For example, *Solexperts AG* commercially performs tests according to method (i), referring to it as the enhanced geothermal response test (`https://www.solexperts.com/de/dienstleistungen/egrt`, link retrieved 19.01.2026).

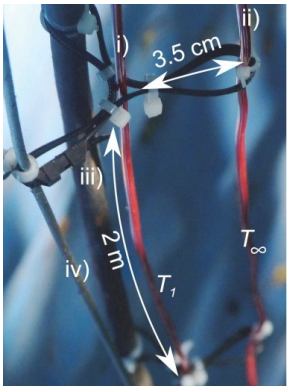

Figure 2.17: Experimental setup of Read et al. [56] that is inserted into a borehole for in situ flow-velocity measurements. The setup consists of four cables: i) a centrally held heated fiber-optic cable, ii) a reference fiber-optic cable, iii) a cable for power supply, and iv) a steel rope. The cables are fixed every two meters with cable ties for proper positioning. Figure reprinted from [56] with permission from AGU.

first deduce a temperature drop caused by radial heat conduction through the cables insulation to attain the temperature difference between the heated cables surface and the ambient temperature. Subsequently, this distributed ΔT is related to flow velocities using a Nusselt number correlation. Equation (2.77) is applied together with Nu_f as Pohlhausen's solution, equation (2.70), and Nu_n fitted to the value 86. The borehole diameter, $L_\mathrm{char} = 0.11\,\mathrm{m}$, is chosen as characteristic length.[3]

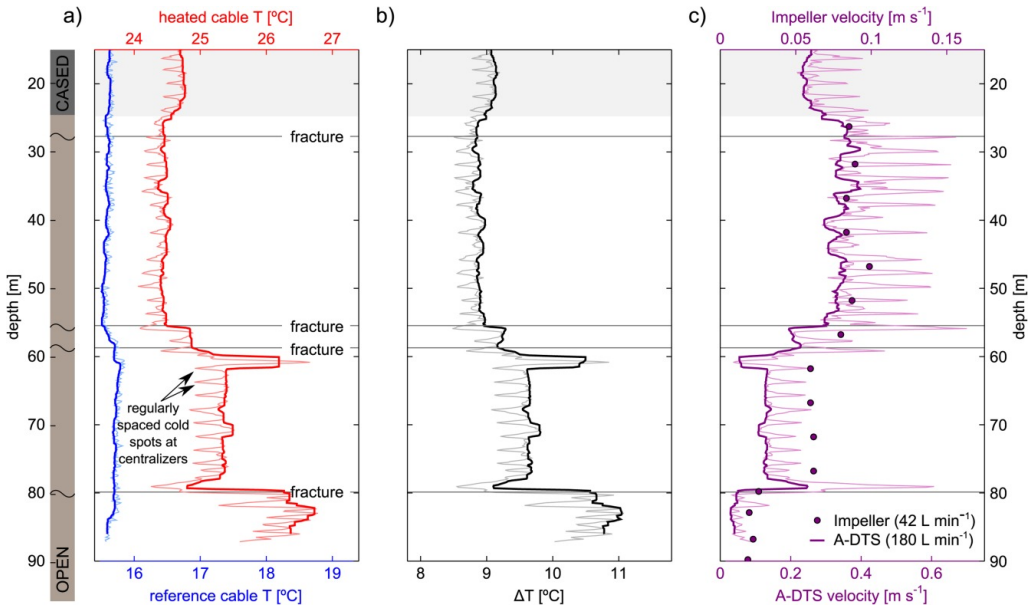

Figure 2.18: Results of the in situ study by Read et al. [56]. The measured temperatures T, temperature differences ΔT, and the estimated velocity are plotted along the borehole's depth in a), b), and c), respectively. Unfiltered data are displayed with a thin line, and filtered data with a thick line. In c), the flow rate is additionally compared to previous impeller flowmeter measurements. Figure reprinted from [56] with permission from AGU.

Figure 2.18 (a) shows the 5-minute averaged temperature during a test conducted at a heating power of 21.8 W/m and a pump flow rate of 180 L/min, with water extracted from the borehole. The trace of the heated cable reveals mixing artifacts every two meters, which are clearly linked to the cable ties that fix the cables in position every two meters. After filtering, two other artifacts at

[3] This unconventional characteristic-length choice leads to the comparatively high Nu_n value. For comparison, the Nu_n displayed in Figure 2.14 for a similar case are an order of magnitude smaller.

60 and 79 m remain. Read et al. assume that the heated cable may be in contact with the borehole wall at the 60 m artifact and that the inflow from the 80 m fracture leads to a more complex flow topology with more efficient heat transfer. Figure 2.18 (b) reveals the distributed ΔT trace and (c) shows the estimated velocity data, together with reference data from an impeller flowmeter at a different flow rate.

Read et al. state that the observed discrepancies between the distributed velocity measurements and the impeller flowmeter measurements cannot be clearly interpreted because a borehole may behave differently when stressed with different flow rates. They conclude that the technique is a feasible approach to spatially and temporally monitor vertical flow rate in boreholes, and they stress the facts that the technique is capable of monitoring multiple boreholes at a site and that the capability to monitor temporal changes may be advantageous. Furthermore, they state that future work is needed to address the issues of field deployment, i.e., the mixing at the centralizing mechanism, to investigate the sensitivity to flow direction, and to optimize the sensitivity range for the desired application.

As a critical remark, Read et al. report that they investigated flow rates ranging from 5.2 to 181 l/min, and in their results graphic Figure 2.18, they show only the largest flow rate for comparison with the reference measurement at 42 l/min. No comment on their investigations at other flow rates exists. Thus, the reader may assume that data acquired at flow rates more similar to the reference measurement also do not correspond well with it. In conclusion, from the perspective of the present work, the study by Read et al. shows a promising qualitative distributed flowmeter log measurement and demonstrates that a fundamental gap exists toward quantitative velocity measurement with fiber-optic TA.

3 Methodology

The present study consists of two stages that investigate in total four fiber-optic probe iterations for TA in water. The first stage, described in Chapter 4, presents and investigates the first two probe iterations. These investigations demonstrate sensitivity but also reveal a variety of issues. Chapter 5 presents the second stage that aims to systematically uncover the origins of previously unknown influences, acquire reproducible measurements, and quantify the uncertainty of the measurement technique.

In both stages, the identical heat-transfer model for one-dimensional radial conjugate heat transfer is applied, and similar experimental equipment is used. Below, the heat-transfer modeling is outlined in Section 3.1, and the experimental equipment is introduced in Section 3.2. Subsequently, Section 3.3 presents a roadmap of the iterative research steps and outlines the assumptions, hypotheses, and objectives for each iteration.

3.1 Heat-transfer analysis

The measurement principle investigated in the present study aims to exploit the heat transfer of a heated hybrid cable to measure the velocity of the water surrounding the cable (see Figure 1.1). Both the cable's core temperature and the heat flux are known: the core temperature is measured with fiber-optic DTS, and the heat flux is controlled by the electrical power supply. The velocity dependence of the heat transfer is analyzed here using a simplified analytical approach for heat conduction inside the cable and an empirical approach to quantify heat convection outside the cable.

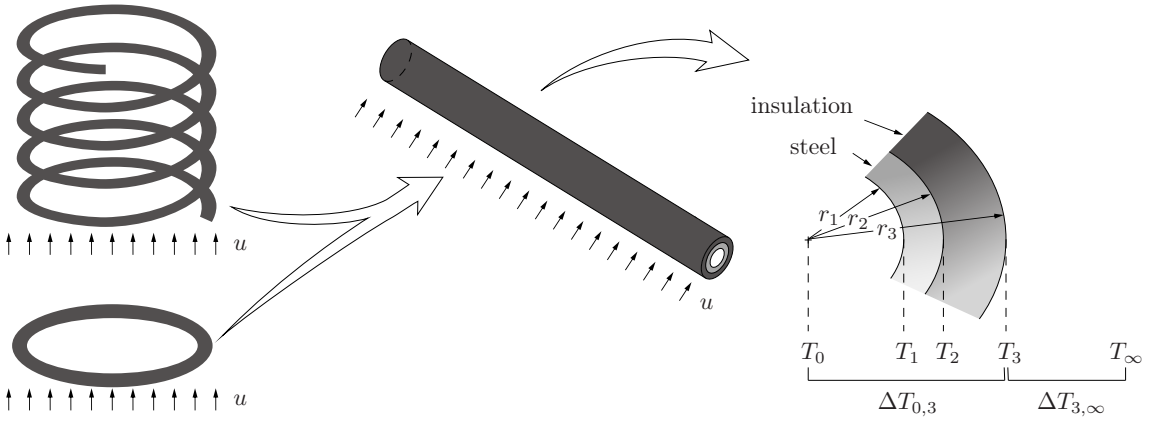

Figure 3.1: Sketch to visualize the two abstraction steps of the heat-transfer modeling. First, the probe geometries (compare Section 3.2.5) are assumed to behave similarly to a long cylinder in crossflow. Second, the heat transfer is assumed to be uniform along the cylinder's length and circumference, occurring only in radial direction.

Figure 3.1 sketches the abstraction steps in the heat-transfer modeling. In the first abstraction level, the rather complex probe geometries are simplified: if only a small section of the real probe's

cable is considered, if the cable's diameter is much smaller than the helix (or ring) diameter, and if the inclination of the helix is small, then the considered cable section is similar to a cylinder placed in crossflow. In the second abstraction level, it is assumed that the convective cooling at the cylinder's surface is uniform and that no temperature fluctuations occur along the cylinder's circumference and length. Therefore, the heat conduction inside the cable occurs only in radial direction.

Subsection 3.1.1 describes the radial heat conduction modeling using the heat diffusion equation, and the heat convection modeling at the cable's surface. Subsequently, Subsections 3.1.2 and 3.1.3 evaluate the modeling of the heat transfer for realistic cylinder diameters, heating rates, and thermal conductivities. In Subsection 3.1.2 the temperature-velocity dependence is evaluated for various heating rates and velocities, and the implications of a temperature-measurement uncertainty of 0.1 °C on the measurement range are discussed. Subsection 3.1.3 demonstrates that heat conduction dominantly contributes to the measured temperature difference between the cable's core and the water's ambient temperature.

3.1.1 Conjugate heat-transfer modeling

"The conjugate heat transfer is modeled by simplifying the geometry to a very long cylinder in crossflow. The cylinder consists of multiple rotationally symmetric layers (see Figure 3.2). The innermost layer, from $r = 0$ to r_1, contains glass fibers used for the DTS temperature measurement. The next layer, from r_1 to r_2, is made of stainless steel and serves as a uniform heat source through Joule heating. The outermost layer, from r_2 to r_3, electrically insulates the stainless steel layer from the surrounding fluid and also – unavoidably – provides effective thermal insulation.

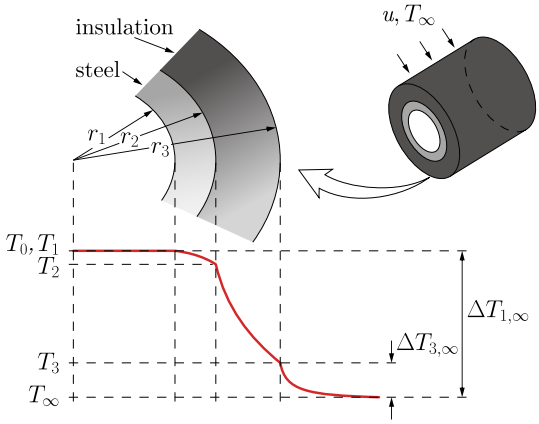

Figure 3.2: "Sketch of the probe's cross-section with a qualitative graph of the temperature along the probe's radial coordinate. The cross-section consists of a capillary core filled with glass fibers, a stainless steel layer, and an insulation layer. In the cylinder's core, the temperature is constant at $T_0 = T_1$, whereas in the stainless steel layer, heat is dissipated via Joule heating and efficiently conducted outward. In the insulation layer, radial heat conduction is less efficient; therefore, the temperature drops significantly to T_3. The cylinder is surrounded by a fluid at T_∞ with velocity u. For convective heat transfer, only $\Delta T_{3,\infty}$ is relevant, yet $\Delta T_{1,\infty}$ is measured." [RTK25] (Figure reprinted from [RTK25].)

To calculate the temperature profile within the cylindrical sections, steady-state heat conduction in the radial direction only is considered and the general heat equation

$$\frac{1}{r}\frac{\partial}{\partial r}\left(kr\frac{\partial T}{\partial r}\right) + \dot{q}_\mathrm{g} = 0 \tag{3.1}$$

is integrated twice (see, for example, Chapter 3.5 in Incropera et al. [32]). In the innermost region, the temperature $T_0 = T_1$ must be constant in steady state, while the temperature differences between the cylindrical layers are given by

$$\Delta T_{1,2} = T_1 - T_2 = \frac{\dot{q}_\mathrm{g}}{4\,k_\mathrm{st}} \left[r_2^2 - r_1^2 \left(1 + \ln \frac{r_2}{r_1} \right) \right] \tag{3.2}$$

and

$$\Delta T_{2,3} = T_2 - T_3 = \frac{\dot{q}_\mathrm{g}\,(r_2^2 - r_1^2)}{2\,k_\mathrm{i}}\, \ln \frac{r_3}{r_2}, \tag{3.3}$$

where k_st and k_i are the thermal conductivities of the steel and insulation layers, respectively." [RTK25] The source term

$$\dot{q}_\mathrm{g} = \frac{\dot{Q}}{\pi (r_2^2 - r_1^2)\, l} \tag{3.4}$$

is defined by uniform Joule heating in the volume of the steel layer. Note that the heat flow rate

$$\dot{Q} \stackrel{!}{=} P_\mathrm{el} \tag{3.5}$$

equals the dissipated electrical power, and l describes the cylinder's length.

"In general, heat transfer from a shell to the surrounding fluid occurs through convection and radiation. Liquids, however, are considered opaque to radiation [32]; thus, only convection is considered here. The convective heat transfer between the cylinder's surface and the surrounding fluid depends on various factors such as fluid velocity, buoyancy effects, thermal properties of the fluid, and geometry. It is classified into free convection, caused by buoyancy induced flows, and forced convection, which exists when a flow is induced by an external bulk flow. Both effects are encapsulated in the heat transfer coefficient h when applying Newton's law to calculate the temperature difference[1]

$$\Delta T_{3,\infty} = T_3 - T_\infty = \frac{1}{h} \frac{\dot{q}_\mathrm{g}\,(r_2^2 - r_1^2)}{2\,r_3}. \tag{3.6}$$

To determine the heat transfer coefficient h, empirical correlations for the Nusselt number

$$Nu = \frac{h\,L_\mathrm{char}}{k_\mathrm{w}} = f(Re, Gr, Pr) \tag{3.7}$$

may be used (k_w: thermal conductivity water, L_char: characteristic length)." [RTK25] Recall that the Nusselt number Nu, Reynolds number Re, Prandtl number Pr, Grashof number Gr, and empirical correlations are introduced in detail in Subsections 2.4.3 and 2.4.4. Using an appropriate empirical correlation, such as the one by Gnielinski [28] given in equation (2.69), the dependence of the heat-transfer coefficient h on the velocity u can be quantified. Next, this dependency is utilized to estimate the measurement range.

3.1.2 Estimation of the measurement range

Empirical correlations enable to compute the dependence of the temperature difference $\Delta T_{3,\infty}$ on the water velocity u. Figure 3.3 displays $\Delta T_{3,\infty}$–u curves for various cylinder diameters and heating powers, which are computed using equation (2.77) by Chen et al. [18]. Note that equation (2.77) combines both the forced-convection correlation by Gnielinski (equation (2.69)) and

[1] recall equation (2.39) and that the heat flow rate at the cylinder's surface is equal to the heat generation rate $\dot{Q} = q\,2\pi\,r_3\,l = \dot{q}_\mathrm{g}\,\pi\,(r_2^2 - r_1^2)\,l$

the free-convection correlation by Churchill and Chu [20] (equation (2.76)), and recall that equation (2.77) is plotted nondimensionally in Figure 2.14. For the following investigation, equation (2.77) is reformulated as $\Delta T_{3,\infty} = f(d, \dot{Q}/l, u, T_3)$ and solved numerically because of the non-linear dependence on T_3 that is introduced by the Gr–dependence.

Figure 3.3 demonstrates the hyperbolic relationship between $\Delta T_{3,\infty}$ and u. Furthermore, it shows that the hyperbolic functions shift towards higher $\Delta T_{3,\infty}$ and that the velocity range with a moderate slope increases with increasing heat flux

$$q = \frac{\dot{Q}}{\pi d\, l} \tag{3.8}$$

(d – cylinder's diameter, l – cylinder's length). At the $d = 4\,\mathrm{mm}$ and $\dot{Q}/l = 20\,\mathrm{W/m}$ curve, gray lines indicate how uncertainties in the temperature measurement propagate to the velocity determination. A measurement uncertainty range of $\pm 0.1\,^\circ\mathrm{C}$ at $1.5\,^\circ\mathrm{C}$ propagates to a measured velocity of $11.3\,[-1.4; +1.7]\,\mathrm{mm/s}$, and an uncertainty range of $\pm 0.1\,^\circ\mathrm{C}$ at $0.6\,^\circ\mathrm{C}$ propagates to a measured velocity of $69.5\,[-17.9; +28.8]\,\mathrm{mm/s}$.

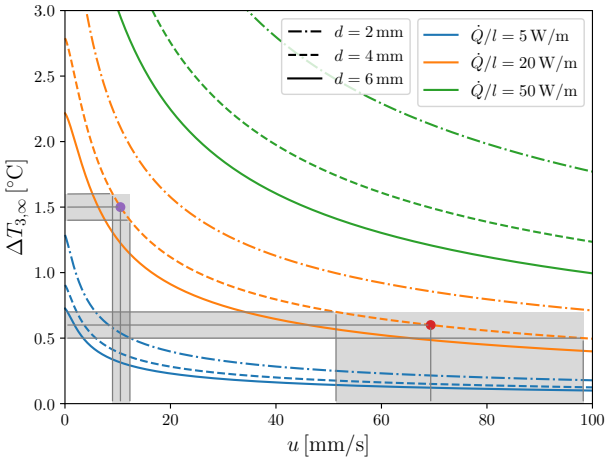

Figure 3.3: Evaluation of equation (2.77) with equations (2.69) and (2.76) for selected cylinder diameters and heating powers to demonstrate the $\Delta T_{3,\infty}$–u relation. Gray regions indicate propagation of $\Delta T_{3,\infty}$ uncertainties to u uncertainties.

The analysis of the uncertainty propagation leads to two take-home messages: First, the measurement range towards higher velocities is limited by the uncertainty of $\Delta T_3, \infty$. Second, the measurement uncertainty decreases with increasing heat flux because of the increasing slope of the $u - \Delta T_{3,\infty}$ curve.

The second take-home poses the question how increasing heat flux impacts the measurement technique: Most importantly, higher heat flux leads to stronger buoyancy forces, which drive free convection. Compared to forced convection, free convection is not velocity dependent, and if it becomes dominant at $Ri \ll 1$ (compare equation (2.62)), $\Delta T_{3,\infty}$ is only barely or not at all a function of u. This argument becomes relevant for very small flow velocities. Thus, they should be measured with smaller heat fluxes. Another critique of the second take-home message is the intrusiveness: In the here modeled scope of a cylinder in crossflow, which never sees the fluid of its wake again, it is irrelevant that the cylinder heats up the fluid. However, in the borehole context it becomes problematic if multiple sensors operate at the same time at different borehole heights because the wake of one sensor influences the next sensor.

Based on the discussed pros and cons of increased heat fluxes, it is expected that different heat flux levels are necessary to cover a wide velocity range. Consequently, a wide range of heating powers is covered in the experiments of Chapters 4 and 5.

3.1.3 Assessment of the heat-conduction impact

As discussed alongside Figure 3.2 and equations (3.2) and (3.3), heat conduction inside the cylinder contributes with $\Delta T_{1,3}$ to the measured temperature difference between the cylinder core T_0 and the fluid bulk temperature T_∞. Here, the influence is demonstrated for an exemplary cylinder with properties specified in Table 3.1. These values are oriented on the actual probes, (compare Subsection 3.2.5).

Table 3.1: Geometrical dimensions and thermal conductivities of the cylinder's layers that are used for the exemplatory calculation of the heat-conduction impact. The thermal conductivities refer to steel and the insulation layer. Compare Figure 3.2 for an illustration of such a cylinder.

Variable	Quantity
r_1	0.5 mm
r_2	1 mm
r_3	2 mm
k_{st}	$15\,\mathrm{W\,m^{-1}\,K^{-1}}$
k_{i}	$0.28\,\mathrm{W\,m^{-1}\,K^{-1}}$

Figure 3.4 shows the evaluation of equations (3.2) and (3.3) for a length-specific heating power of $\dot{Q}/l = 20\,\mathrm{W/m}$ for the highlighted points in Figure 3.3 with $\Delta T_{3,\infty}$ values of 0.6 and 1.5 °C. This graph clearly demonstrates that most of the measured temperature drop between optical fiber at $r = 0$ and fluid-bulk temperature occurs within the insulative sheath of the cylinder. Fortunately, this temperature offset in the cylinder remains constant for each heating power. Thus, it can be computed and subtracted from the measured temperature difference $\Delta T_{1,\infty}$ to obtain the velocity-dependent fraction $\Delta T_{3,\infty}$.

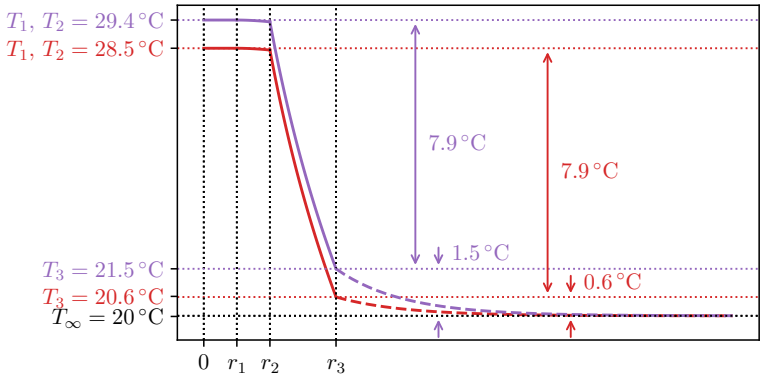

Figure 3.4: Radial heat conduction inside a layered cylinder as sketched in Figure 3.2 with the material properties provided in Table 3.1. Two graphs are calculated with a length-specific heating power of $Q/l = 20\,\mathrm{W/m}$ and $\Delta T_{3,\infty}$ values of 0.6 and 1.5 °C, which correspond to the same conditions as the highlighted points in Figure 3.3.

More theoretically interpreted, the larger temperature offset inside the insulative sheath means that $Bi > 1$. The Biot number is evaluated according to equation (2.66) for the Table 3.1 parameters

and the dashed $Q/l = 20\,\mathrm{W/m}$ curve from Figure 3.3, and is displayed in Figure 3.5. This plot demonstrates that $Bi > 1$ holds true for all flow velocities. Accordingly, in the present TA method, heat conduction is non-negligible, which is a significant contrast to the conventional TA methods HWA and HFA.

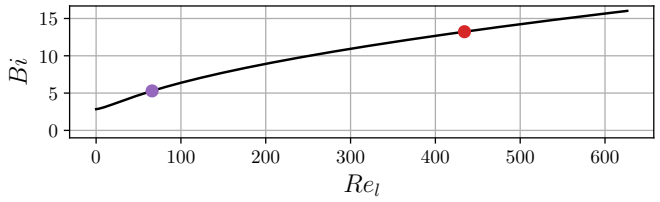

Figure 3.5: *Bi–Re* graph for the modeled cylinder in cross flow. The values in Table 3.1 are used to compute the radial heat conduction, and for the heat-convection modeling, the dashed $Q/l = 20\,\mathrm{W/m}$ line of Figure 3.3 is applied. The highlighted points correspond to the conditions depicted in detail in Figure 3.4.

3.2 Experimental infrastructure

Since the experiments described in the following two chapters mostly share the same experimental infrastructure, it is introduced below prior to the specific discussions in Sections 4 and 5.

3.2.1 Borehole test rig

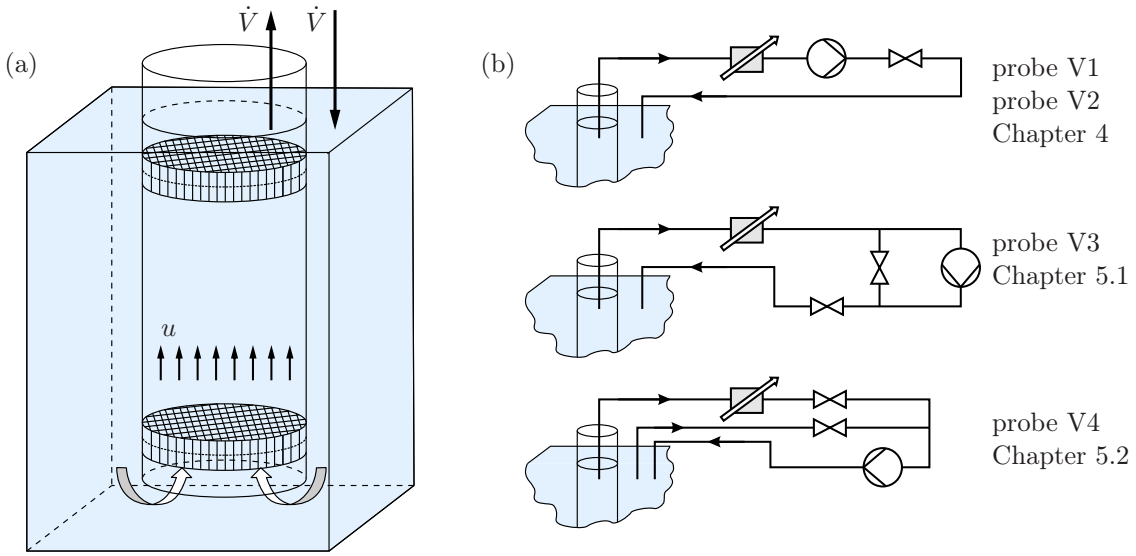

Figure 3.6: Introduction of the borehole test rig. (a) Sketch of the test rig consisting of a 2.1 m-long pipe with an inner diameter of 151 mm placed inside a large water tank. The indicated sieves and flow straighteners are inserted only for the investigation with Probe V4. (b) Piping diagram sketches outlining the positions of the flow-rate sensor, the pump, and the valves. First, the flow rate is controlled by throttling it with one valve. Later, bypasses are introduced for more consistent throttling at low flow rates.

The borehole test rig, which consists of a water tank with a pipe placed inside, is depicted in Figure 3.6 (a). The pipe is 2.1 m long and has a diameter of 151 mm. It is fixed into position with a pipe fitting that is glued to the tank's ground plate. Furthermore, this fitting is perforated with

large holes to enable water exchange between the tank and the pipe. The tank itself is a 2.25 m long pipe with a diameter of 0.5 m. The test rig was built and first operated by Renner [57].

The fiber-optic probes are placed in the inner pipe at half height. They experience a steady vertical velocity that is always directed upwards. Assuming bulk flow, the velocity is constant throughout the cross section. The bulk velocity in the inner pipe

$$u = \frac{\dot{V}}{A_{\mathrm{eff}}} = \frac{\dot{V}}{\pi\, d_{\mathrm{p}}^2/4 - A_{\mathrm{b}}} \tag{3.9}$$

is calculated with the monitored volume flow rate $\dot{V}$ divided by the effective cross-sectional area A_{eff}. d_{p} is the pipe's diameter, and A_{b} is the area blocked by the probe. To ensure validity of the bulk-flow assumption, flow straighteners and sieves are installed at both ends of the pipe for the Probe V4 experiments in Section 5.2. The flow straighteners are slightly oversized so they remain in position after insertion. At both ends, a pair of flow straighteners is inserted with a sieve in between them.

Figure 3.6 (b) illustrates three piping schematics that contain the volume flow rate sensor (*Kobold MIM-1220H*), the pump (*LINN MXH 202E*), and valves that throttle the pump to control the flow rate. During the experiments with Probe V1 and Probe V2, which are presented in Sections 4.2 and 4.3, one valve throttles the flow rate. Throttling with only one valve may lead to oscillations in flow rate, especially at the smallest flow rates. Therefore, constant attention is necessary during the acquisition of low-velocity measurement points in the single-valve configuration. If flow rate oscillations occur, the valves are opened before re-setting the intended velocity and repeating the measurement. For the experiments with Probe V3, which are presented in Section 5.1, a bypass valve is added, which significantly reduces the flow-rate oscillations at small flow rates, but does not eliminate them. Thus, constant attention remains necessary during data acquisition. However, for the experiments with Probe V4, which are presented in Section 5.2, the bypass loop is extended with the tank volume. This improvement eliminates the prior observed velocity fluctuations. Furthermore, the manual valves are replaced by electrical valves (*B-HEAD-S90A-24AFA*). With a control program that has the flow-rate measurement data as input, the valve control is automated, which enables autonomous test-rig operation.

This setup is capable of covering the flow-rate range of 0–55 l/min. Increments of approximately 2.5 l/min are realizable with the first two valve configurations, and increments of 1.25 l/min can be adjusted with the third valve configuration.

3.2.2 Transparent water channel

A transparent water channel is used for two experiments in Chapter 4. First, in Section 4.1, the underlying heat transfer is investigated with conventional temperature measurement sensors, and second, in Section 4.3, it is used to test a borehole probe in horizontal flow.

The channel design follows the layout of Prandtl's water channel, i.e., as a rectangular channel with a return loop below the channel. Furthermore, its walls consist of transparent plates to enable the application of optical flow measurement techniques. Figure 3.7 (a) displays a side view of the measurement section and highlights the locations of the particle image velocimetry (PIV) evaluation area and the heated cylinder that is investigated in Section 4.1. PIV is an optical measurement technique, in which particles are added to the fluid and a camera records a cross sectional plane that is illuminated by a light sheet with an intense light source. In two consecutive images, the particle displacement is a measure of the velocity, assuming that the particles follow the

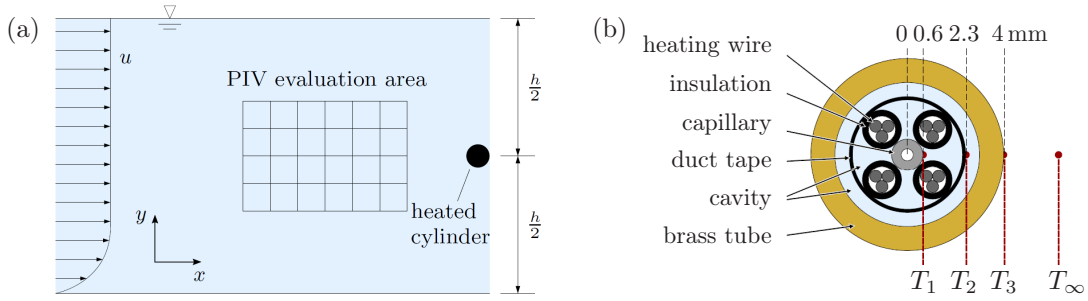

Figure 3.7: (a) Measurement section of the transparent water channel and (b) detail of the heated cylinder's cross section. (Both subfigures reprinted from [RRTK24])

flow. A cross-correlation algorithm determines the particle movement using image snippets, called interrogation areas, which are indicated by the grid in the sketch. Please refer to [15, 55] for more detailed explanation of PIV. A *Quantel Evergreen* laser is used for illumination and a *pco.edge 5.5 sCMOS* Camera to record the images. Figure 3.7 (b) shows a sketch of the heated cylinder's cross-section. It consists of a brass tube filled with heating wires arranged around a steel-capillary. The cavities are filled with heat conduction paste, and TCs are fixed at three locations to measure T_1, T_2, and T_3. Two TCs are fixed at each cross-section location along the cylinder's length. Note that the TCs for the T_3 measurement are fixed to the top of the cylinder instead of the right side (as suggested by the sketch in Figure 3.7 (b)) because flow separation occurs on the right side of the cylinder. T_∞ is measured with a PT1000 sensor upstream of the heated cylinder. Although this early-stage, design introduces considerable positioning errors, it proves sufficient for the purpose of the intended proof-of-concept experiment described in Section 4.1.

3.2.3 Measurement equipment

The measurement devices used for data acquisition are introduced here, along with their relevant specifications.

Throughout the present work, two DTS devices, *AP Sensing N43856B* and *Silixa Ultima XT M*, are applied. In Chapter 4 only the *AP Sensing* device is used, while both devices are applied in Chapter 5. According to their datasheets, the devices have the following properties: The *AP Sensing N43856B* has a spatial resolution of 0.5 m, a minimum sampling interval of 0.25 m, and a maximum distance range of 12 km. The *Silixa Ultima XT M* has a spatial resolution of 0.65 m, a temperature resolution of 0.01 °C, a minimum sampling interval of 0.25 m, and a maximum distance range of 10 km. None of the datasheets specify temperature-measurement accuracy, most likely because it highly depends on the calibration and the signal-loss sources in the fiber-optic setup (sharp bends, connectors, splices, and fiber length).

For conventional temperature measurements with RTDs and TCs, a *NI cDAQ-9188* chassis with a *NI 9219* module for RTDs measurements and a *NI 9213* module for TC measurements is used. The highest sampling rate of both modules is 2 Hz, and for both modules the uncertainties introduced by the electronics are far below the physical sensor uncertainties. The sensor uncertainties of the PT1000 probes used are $0.1\,°\mathrm{C} + 0.0017\,|T|$ (Class AA according to DIN EN 60751:2009-05), and the uncertainty of the type T TCs is $\pm 0.5\,°\mathrm{C}$ (according to DIN EN 60584-1:2014-07).

In the test rig, the *Kobold MIM-1220H* is used to measure the volume flow rate. It has an accuracy of $\pm 0.8\,\mathrm{l/min} + 0.005\,\dot{V}$ and a repeatability of $\pm 0.002\,\dot{V}$. Furthermore, the *Kobold MIM-1220H* contains a PT1000 temperature sensor with an accuracy of $\pm 2\,°\mathrm{C}$.

3.2.4 DTS calibration setup

To quantify and improve the accuracy of the DTS measurements using the double-ended calibration algorithm from Subsection 2.3.3, reference temperatures from two monitored fiber sections are required. Figure 3.8 "illustrates the fiber setup together with a temperature profile plotted over the fiber length. At one end, both fibers of the 80 m long duplex cable are connected to a DTS device." [RTK25] A duplex cable consists of two glass fibers, each covered with protective sheaths that are fused together. "The duplex cable then passes through three water baths before one fiber is routed through the probe's two rings[2], after which both fibers are joined with a fusion splice. Two of the baths, respectively, maintained at 50 °C and 0 °C, are used for calibration of the DTS data, while a third bath at 35 °C serves for validation purposes. Each water bath consists of a large insulated container, an insulated lid, and a hollow torus fixed to the lid using a pipe clamp. Approximately 10 m of duplex cable and a PT1000 temperature sensor are inserted into each torus. This design ensures that the duplex cable coils are always positioned approximately at half the height of the container and prevents direct contact with ice cubes or the heater. The ice cubes are used to maintain the temperature in the cold baths, while *Steba SV 50* heaters with an integrated circulation pump are inserted into openings of the hot baths lids." [RTK25]

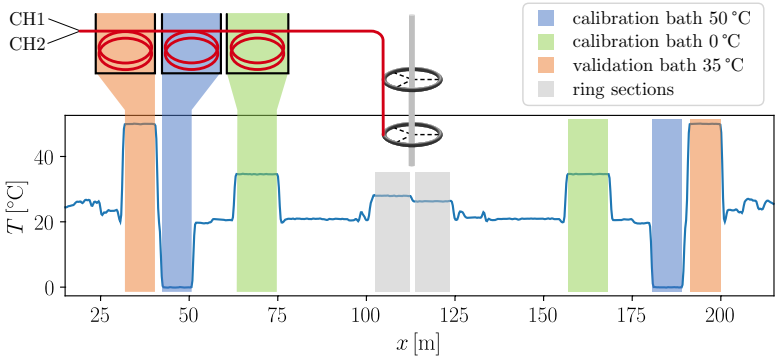

Figure 3.8: "DTS setup visualization: The measured temperature is plotted against the fiber distance, accompanied by a sketch illustrating the locations of the water baths and the probe. The duplex cable containing both fibers passes through the water baths, but only one fiber of the duplex cable passes through the ring sections. After the second ring, it is spliced to the other fiber of the duplex cable. Consequently, the bath sections appear twice in the temperature trace." [RTK25] (Figure reprinted from [RTK25])

With the PT1000 sensors, the bath temperatures are independently monitored, which is demonstrated in Figure 3.9 with a representative dataset. The heated baths experience temperature fluctuations of less than ±0.02 °C and the temperature of the ice bath remains constant in the displayed scale. The reference temperature measurements from the hot and cold baths are used to calibrate the DTS measurement with the double-ended calibration algorithm by Des Tombe et al. [23], as introduced in Subsections 2.3.2 and 2.3.3. The validation bath data can be used to estimate the DTS measurement uncertainty, as done in Appendix C.3. Furthermore, in Subsection 5.2.2 the validation bath is used to directly estimate the uncertainty of Ring 1 from Probe V4.

[2] referring to Prove V4; the identical calibration setup is also used for Probe V3 as shown in Appendix C. Both probes are introduced in Subsection 3.2.5.

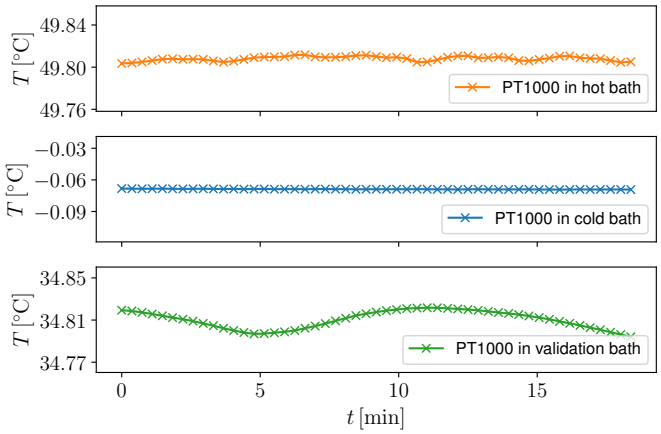

Figure 3.9: Representative temperature measurements in the calibration baths and validation bath with immersed PT1000 sensors. In the heated baths, the temperature exhibits slight fluctuations (within ±0.02 °C), whereas in the cold bath it remains stable.

3.2.5 Evolution of probe designs

Throughout Chapters 4 and 5, four probe generations are investigated consecutively. Probe V1 is a helically wound hybrid cable, Probe V2 is a borehole-ready prototype with a helically shaped sensor section, Probe V3 is a helically wound steel capillary, and Probe V4 is the composition of two capillary rings filled with fiber coils. Each probe is described here, and the iterative development process leading to these probe generations is outlined in the following Subsection 3.3.

Probe V1 – hybrid cable helix

Probe V1, built by Renner [57], consists of a helically wound hybrid cable, as depicted in Figure 3.10 (a). It is wound around a holding structure that consists of 15×15 mm wooden strips, which are fixed to a *DN75* pipe. The helix consists of 21 windings with a diameter of 105 mm and a pitch of 15 mm. Consequently, it contains a total cable length of $21\sqrt{(\pi\,0.105\,\mathrm{m})^2 + (0.015\,\mathrm{m})^2} = 6.9\,\mathrm{m}$.

These wooden strips are engraved with regularly spaced grooves angled at 5.2 ° to fix the cable into position. Figure 3.10 (b) highlights, that the hybrid cable consists of five layers surrounding the glass fiber in its core. First a steel capillary, then two conductive layers separated by an insulation layer, and an outer protective sheath. For the heat-conduction calculation the cross section is abstracted, merging both conductive layers and the insulation in between to a single homogeneous layer. As discussed in Subsection 3.1.3, the insulation layer contributes dominantly to the measured $\Delta T_{3,\infty}$. The cable's cross-section dimensions and the estimated effective thermal conductivity of the insulation layer are provided in Table 3.2. Note, that no precise information on the thermal conductivity k_i is available. Thus, the given value is an estimation from Section 4.2.

Table 3.2: Dimensions of the hybrid cable's cross section and estimated thermal conductivity of the outer sheath for the cable used in Probe V1.

Variable	Quantity
d_1	$1.3 \pm 0.1\,\mathrm{mm}$
d_2	$4.0 \pm 0.1\,\mathrm{mm}$
d_3	$6.0 \pm 0.1\,\mathrm{mm}$
k_i	$0.19\,\mathrm{W\,m^{-1}\,K^{-1}}$

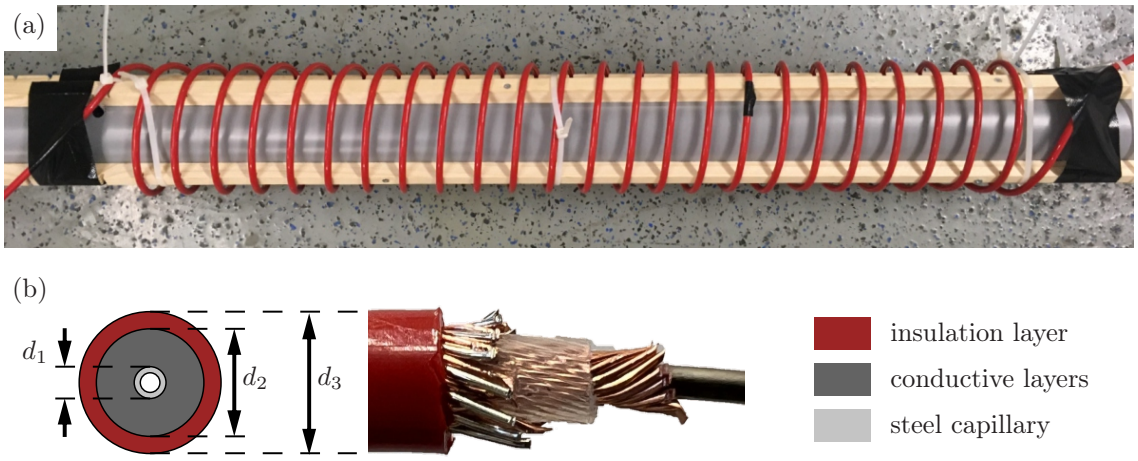

Figure 3.10: Introduction of the first probe generation, Probe V1, built by Renner [57]. The probe consists of a hybrid cable wound into a helical form, which is fixed to a holding structure. (a) depicts a photograph of the probe (printed with permission from Tom Renner), and (b) depicts the partially stripped hybrid cable alongside a simplified cross-section sketch.

Probe V2 – borehole-ready prototype

Probe V2 is a borehole-ready prototype depicted in Figure 3.11 (a), which was designed and built by *Solexperts GmbH* in a collaborative project. It primarily consists of a helix with two windings that is connected to a cylindrical housing. The helix is made of a copper pipe filled with a heating cable that is wound around a steel capillary, which contains the glass fiber, and all gaps are filled with heat-conduction paste. Figure 3.11 (b) depicts the cross section of this composite helix pipe and depicts how the heating cable is wound around the steel capillary. The copper pipes diameter d_3 is 6.4 mm. The copper-pipe length in the two helix revolutions is 0.51 m (diameter of 8 cm and pitch of 2.5 cm) and the overall exposed length of the copper pipe is 0.73 m. Between housing and helix two smaller cylinders contain the electrical connection from the copper supply cable to the heating wire and heat conduction paste that fills remaining cavities. If the connection was inside the larger cylinder housing, the heating wire would overheat. The cylindrical housing is a sealed

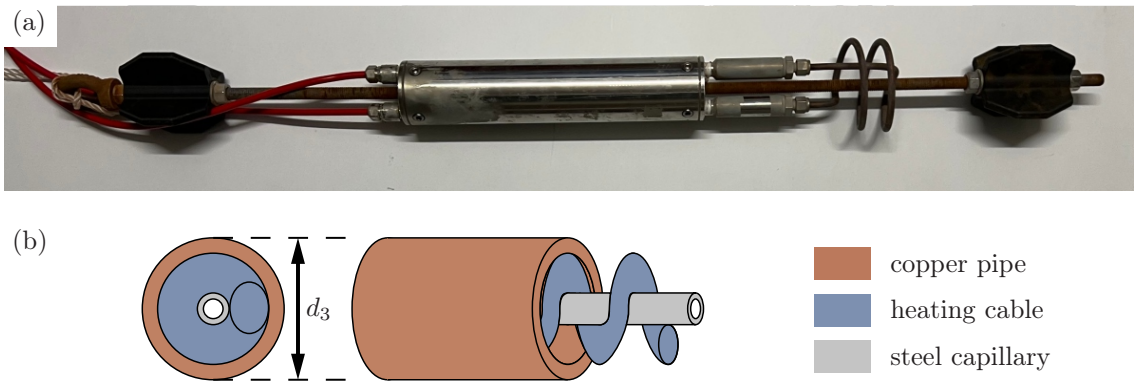

Figure 3.11: Introduction of the second probe generation, Probe V2, built by *Solexperts GmbH* during a collaborative project. The probe comprises a helically bent copper pipe connected to a sealed body within which the fibers and electrical conductors are connected to the supply cables. The helically bent copper pipe is filled with a heating cable, a steel capillary that contains a glass fiber, and heat-conduction paste to fill remaining voids. Two cylinders that encapsulate the connection of the heating cable to a copper cable are located between the body and the helix. Without these cooling bodies, the heating cable would overheat inside the large cylinder. (a) presents a photograph of the probe, and (b) depicts two sketches. One sketch shows the cross section, and the other visualizes how the heating cable is wound around the capillary.

hollow steel cylinder that contains electrical and fiber-optic wiring that connects the hybrid cables to the fiber and heating wire inside the helix.

Probe V3 – helix-shaped capillary probe

Probe V3 is an optimization of the previous design towards less thermal and hydraulic intrusiveness, while at the same time increasing the fiber length for a better DTS signal. In contrast to the prior Probe V2, this probe is only meant to be a laboratory prototype. Figure 3.12 displays Probe V3 and a cross-section sketch of the probe's insulated capillary. Aside from the helix, the probe consists of two bodies that enclose the electrical connections to the capillaries' ends and contain fiber-optic wiring. One of the bodies connects to the fiber-optic duplex cable, while the other contains a fusion splice, which connects both glass fibers. The manufacturing process of this probe is described in Appendix A.1.

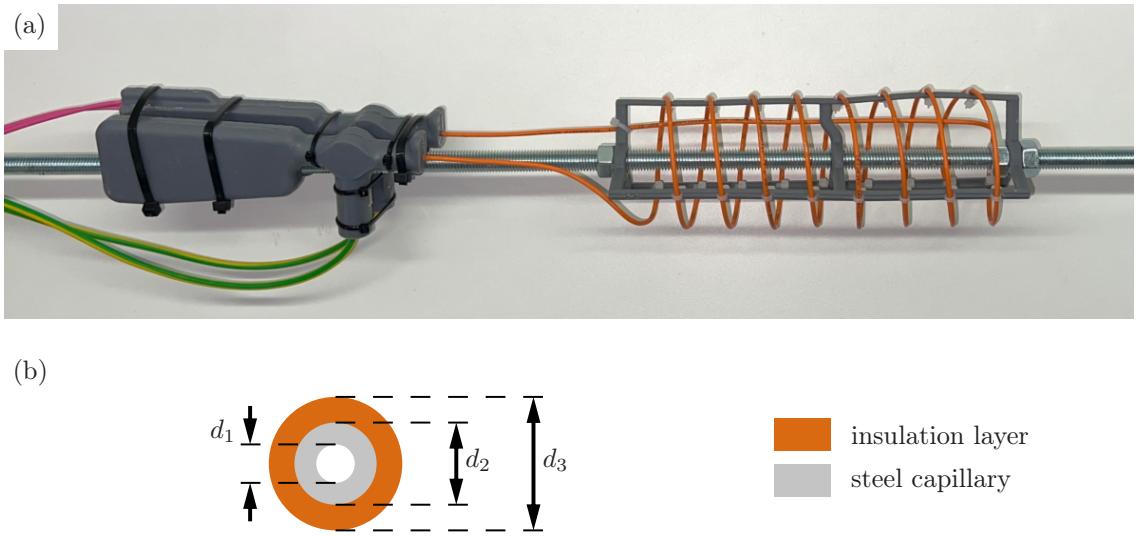

Figure 3.12: Introduction of the third probe generation, Probe V3. This probe uses an approximately 2.5 m-long, thin capillary as heat source (via Joule heating), which results in a small diameter of the capillary's cross section. A slender 3D-printed support structure maintains the helical shape, and 3D-printed housings enclose the fiber loops, a fiber splice, and the electrical connections. (a) shows a photo of the probe, and (b) presents a cross-section sketch of the insulated capillary used to build the helix.

In contrast to the prior probes, Probe V3 utilizes the steel capillary as resistive heater instead of additional conductors. This approach significantly reduces the outer diameter and the surface area of the helix. As a smaller surface area leads to a higher heat flux at identical heating power per cable length, less absolute heating power is necessary, which reduces the thermal intrusiveness. The hydraulic intrusiveness is also reduced by the smaller diameter d_3 and by the smaller volume of the 3D-printed connector housings. The heated capillary-length is 2.54 m, and Table 3.3 quantifies

Table 3.3: Cross-section dimensions, electrical resistance, and the insulative sheath's thermal conductivity range for the helix-shaped capillary probe, Probe V3.

Variable	Quantity
d_1	0.75 mm
d_2	1.59 mm
d_3	2.6 ± 0.2 mm
R	$1.247 \pm 0.27\,\Omega$
k_i	$0.22 \ldots 0.43\,\mathrm{W\,m^{-1}\,K^{-1}}$

the dimensions of the insulated capillaries' cross-section, the independently measured electrical resistance (see Appendix A.1), and provides a value range for the thermal conductivity of the protective sheath. The sheath is a re-used outer sheath from a fiber-optic patch cable, which is made of polyolefin. In contrast to probes V1 and V4, a more exact value for the sheath's thermal conductivity is not retrospectively estimated.

Probe V4 – double-ring capillary probe

Probe V4 as presented in Figure 3.13 (a) is an optimization of the prior Probe V3 driven by the objective to further increase the contained fiber length. This design retains the approach of using the steel capillary that surrounds the fiber as heat source but the geometry changes from a helix to two open rings. The increase in fiber length is attained by threading the glass fiber multiple times through each ring. Consequently, each ring contains a fiber coil of approximately nine meters fiber length. The manufacturing process is outlined in Appendix A.2. The double-ring design enables the parallel measurement of the water's ambient temperature with one unheated ring, while the other ring is heated.

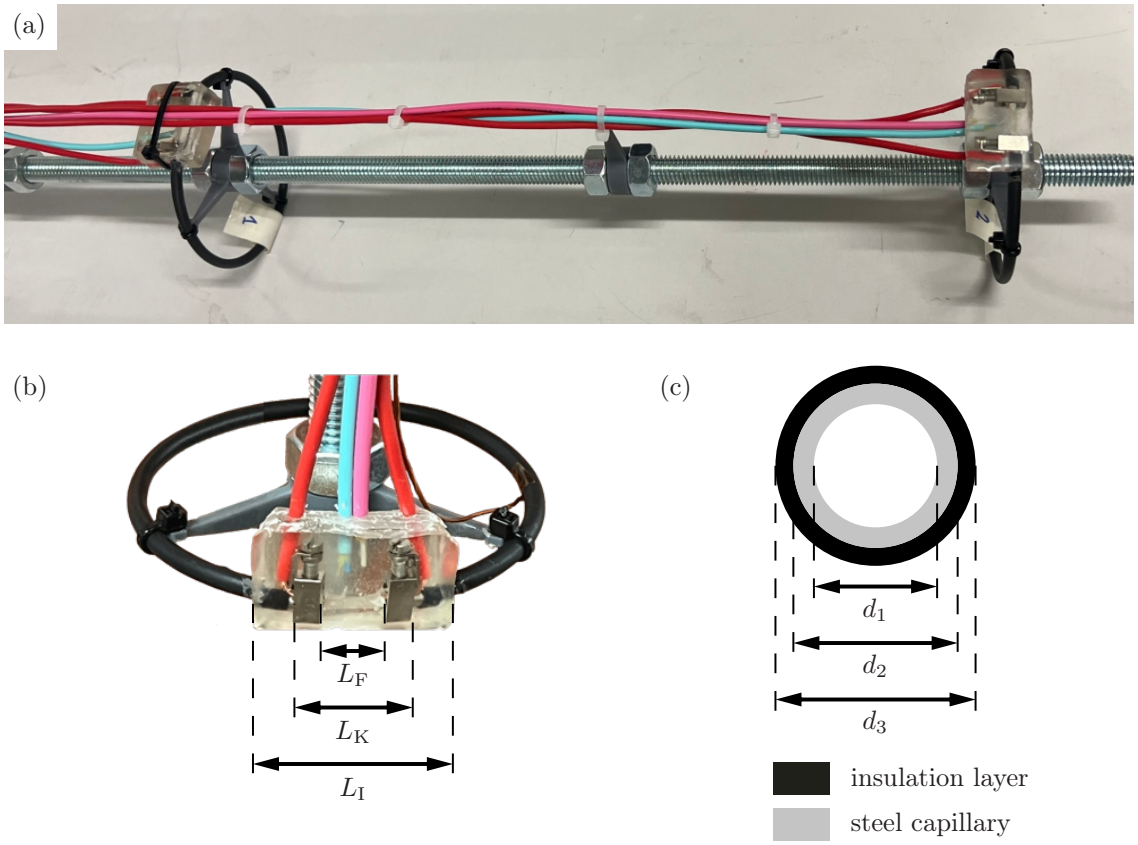

Figure 3.13: Introduction of the fourth probe generation, Probe V4. It comprises two heatable, insulated capillaries bent into open rings. Glass fibers are threaded multiple times through each ring, resulting in a coiled fiber length of 9 m per ring. The entering and exiting glass fibers, together with the electrical wire connection, are cast with epoxy for protection. (a) shows a photo of the double-ring probe, (b) shows a close-up of the lower ring, Ring 2, and (c) presents a cross-section sketch of the ring's capillary.

Figure 3.13 (b) displays a photo of one of the rings, and (c) depicts a cross-section sketch. Each ring is electrically insulated with heat shrinking tubing, connected to two patch cables, which encapsulate the entering and exiting glass fiber, and clamped to two electrical wires. The open ring region is cast together with all connections into epoxy for protection. Three lengths are

identified in this epoxy-cast region: the free length L_F, the clamped length L_K, and the epoxy-insulated length L_I. Table 3.4 "provides the rings dimensions, electrical resistance R and the heat conductivities of the probes sheath layers. Due to the early stage of the proof-of-concept sensor, the parameters of the insulation layer are particularly uncertain. The shrinking is not perfect, which leads to an uncertainty in d_3 and, moreover, the thermal conductivity of the applied material is unknown."[RTK25] However, as the material is polyolefin, its thermal conductivity range is 0.22–0.41 $\mathrm{W\,m^{-1}\,K^{-1}}$. The value given in Table 3.4 is retroactively estimated by comparing the dimensionless results with an empirical correlation in Subsection 5.2.4.

Table 3.4: "Dimensions of the double-ring probe and physical quantities of its materials." [RTK25] d_1, d_2, and d_3 are cross-section dimensions; D is the ring diameter; L_F, L_K, and L_I are ring gap dimensions; L_R is the distance between ring 1 and ring 2; R is the electrical resistance; and k_st and k_i are thermal conductivities of capillary and insulation. (Table reprinted from [RTK25])

Variable	Quantity
d_1	$2.4 \pm 0.1\,\mathrm{mm}$
d_2	$3.1 \pm 0.1\,\mathrm{mm}$
d_3	$4.2 \pm 0.3\,\mathrm{mm}$
D	$81 \pm 0.5\,\mathrm{mm}$
L_F	$15 \pm 0.5\,\mathrm{mm}$; $11.5 \pm 0.5\,\mathrm{mm}$ *
L_K	$24 \pm 0.5\,\mathrm{mm}$; $22 \pm 0.5\,\mathrm{mm}$ *
L_I	$31.9 \pm 0.1\,\mathrm{mm}$; $32.1 \pm 0.1\,\mathrm{mm}$ *
L_R	$315 \pm 1\,\mathrm{mm}$
R	$48 \pm 3\,\mathrm{m\Omega}$
k_st	$15\,\mathrm{W\,m^{-1}\,K^{-1}}$
k_i	$0.28\,\mathrm{W\,m^{-1}\,K^{-1}}$

* For Ring 1 (upper) and Ring 2 (lower), respectively.

3.3 Outline of iterative research procedure

Throughout the present work, four probe generations are investigated. After investigating the second probe generation, a reflective stage prompts major revisions to an underlying assumption and the general research objective. A second reflective stage, after investigating the third probe generation, leads to the design of the fourth probe generation and minor revisions to the procedure. The development history of this iterative process is outlined below to sketch the structure of Chapters 4 and 5, which comprehensively present the experimental procedure and the results of this study.

In advance of the present study, Renner [57] designed and built both the borehole-mimicking laboratory setup and Probe V1, and subsequently acquired data that demonstrate the sensitivity of the measured temperature difference $\Delta T_{1,\infty}$ between the optical fiber and the bulk water temperature to the flow rate $\dot{V}$. The course of action for Chapter 4 is outlined in Table 3.5 based on the results by Renner and a review of the literature. This first literature review focused on the underlying conjugate heat transfer and led to the analysis presented in Section 3.1. Table 3.5 is structured by first stating the assumptions and hypotheses and, consequently, outlining the strategies to meet the respective objectives.

As will be concluded in Section 4.4, the results of this initial stage are ambiguous. On the one hand, validation of the radial conduction model and of the Gnielinski correlation as reference are

successful, and the re-evaluation of the Probe V1 data further underlines that this processing approach is sensible. On the other hand, the inability to clearly measure the heated-fiber temperature of Probe V2 with the DTS, and the observed large offsets between measurement sets ultimately prevent the execution of SO4, and SO5 (see Table 3.5). The cause of the observed uncertainties is suspected in both the DTS measurement and a modeling gap: influences of changing water properties and the precipitation of dissolved solids, which deposit on the probe's surface are not considered.

Table 3.5: Assumptions and hypotheses followed by strategies and objectives of the initial research stage with Probe V1 and Probe V2.

Assumptions	
A1:	Radial heat conduction inside the cable is a function of constant material properties and heat flux, only. The resulting $\Delta T_{1,3}$ can be corrected for using equations (3.2) and (3.3).
A2:	The convective heat transfer at the cable's surface is predominantly governed by forced convection, which depends on flow velocity and constant conditions such as the setup geometry and water properties (i.e., thermal resistivity k and viscosity ν).
A3:	The cylinder-in-cross-flow analogy can be applied to the probe geometry. Therefore, Nusselt correlations for a cylinder in cross-flow are a sensible reference.
A4:	DTS measurements are able to reliably measure the fiber-temperature when applied according to the device's user manual.
A5:	The probe is intrusive, as it disturbs the flow in the test rig. However, since this disturbance is consistent, calibration will account for this systematic effect.
Hypotheses	
H1:	The assumed dependency of the convective heat transfer on flow velocity can be exploited for flow-velocity measurements in water.
H2:	When the probes are calibrated in the borehole-mimicking test rig, the calibration function remains valid for application in boreholes, provided that water temperature, water properties, and borehole diameter remain sufficiently similar.
Strategies & Objectives	
SO1:	Assess, through a heat-transfer validation experiment with conventional sensors, whether the radial conduction model from Section 3.1 is correct and whether the Nusselt correlation by Gnielinski [28] is a sensible reference.
SO2:	Re-examine and analyze the existing Probe V1 data [57] with a correction for the conductive temperature drop across the cable's insulation layer $\Delta T_{1,3}$ and compare the resulting dimensionless Nu–Re data to existing literature references.
SO3:	Conduct laboratory experiments to investigate and determine the calibration function of Probe V2; considering the reproducibility issue identified in the Probe V1 data, focus on reproducibility.
SO4:	Evaluate the velocity-measurement uncertainties and the measurement range of Probe V2.
SO5:	Apply Probe V2 in a real borehole for velocity measurements to demonstrate its measurement capabilities in a realistic application.

In consequence, the focus shifts toward the DTS temperature measurement, because only with an accurate temperature measurement this technique will be feasible. As long as additional unmodeled influences on the heat transfer cannot be distinguished from temperature measurement errors, no clear conclusions can be drawn. Consequently, the overarching goal changes from '*calibrating the sensor and applying it in a real borehole*' toward fundamental investigations:

1. Demonstrate that DTS is capable to accurately measure the fiber temperature using probe designs optimized for DTS performance.
2. Investigate the heat transfer exclusively in the laboratory, questioning whether the modeling covers all relevant phenomena.

A deeper review of the DTS literature [23, 30, 31, 60, 62, 70] indicates that the heated fiber section should be at least two to three times the spatial resolution specified in the device's datasheet (compare definition of DTS resolution in Subsection 2.3.4). Moreover, to achieve optimal accuracy, the scattering intensities acquired by the DTS should be converted to temperatures using an algorithm that employs reference measurements from two calibration baths (compare Subsections 2.3.3 and 3.2.4), instead of relying on the device's internal temperature processing.

Accordingly, the second stage of the present study starts by optimizing the setup for better DTS performance, designing the next probe generation, and introducing calibration of DTS data. Probe V3, as introduced in Subsection 3.2.5, remains in the helical shape of the previous probes but includes a fiber length more than four times the spatial resolution specified in the datasheet of the *AP Sensing N43856B* DTS. Based on the prior findings, the DTS-related assumption A4 is adjusted, assumption A6 is added, and the strategies and objectives are reformulated in Table 3.6. The examination of Probe V3 in Subsection 5.1.1 reveals that the DTS device used exhibits an uncommon overshoot phenomenon[3], which makes it difficult to clearly identify the sensor temperature. Tests outlined in Appendix C.3 indicate that the temperature measurement uncertainty along the fiber of the Probe V3 setup is less than 0.5 °C. Furthermore, the results of Probe V3 in the test rig reveal in Subsection 5.1.3 that under identical heating and flow conditions offsets larger than the estimated DTS measurement uncertainty occur, which indicates a lack of reproducibility of the heat transfer itself. However, since the trust in the measured DTS temperature remains limited, still, no definitive conclusions are drawn.

After reflecting on the Probe V3 results, the next sensor generation, Probe V4, is built by coiling 9 m of fiber into each of two ring-shaped capillaries. This design enables a more precise probe-temperature measurement, which is less influenced by the aforementioned DTS device's overshoot phenomenon. In Section 5.2, Probe V4 is investigated under the same assumptions and hypotheses as the prior probe generation. The strategies and objectives outlined in Table 3.6, are followed and accomplished with a focus on DTS measurement uncertainties: The temperature measurement uncertainty of Ring 1 of Probe V4 is determined for both DTS devices in Subsection 5.2.2, which satisfies SO1. The reproducibility, SO2, is investigated in Subsection 5.2.4 through an extensive parameter study for broad heating-power and flow-rate ranges and also for two DTS devices and two water types: tap water and deionized water. In addition to clearly showing the negative impact of limescale deposition in tap water, gas-bubble formation is identified as another unmodeled factor and is examined in Subsection 5.3.2. For the best-case combination of the *Silixa* DTS and deionized water in Subsection 5.2.4, a measurement range with confined error margins is attained for Probe V4 (SO3).

Although outside the primary scope of the present work, the fiber-coiled-in-capillary design developed for Probe V4 can be adapted to enable direction-sensitive velocity measurements in air.

[3] The overshoot phenomenon does not occur in published data from other DTS devices. In the open source Python package *dtscalibration* by Des Tombe et al. [23] (`https://github.com/dtscalibration/python-dts-calibration/tree/main/tests/data`) data from seven DTS devices of three brands are published. Only the *AP Sensing N43856B* exhibits this overshoot behavior. Correspondence with the manufacturer led to the hypothesis that the overshoot may be connected to the pulse compression coding used (see Section "3.3.3.4 Pulse compression coding" in Hartog [30]).

Table 3.6: Modifications in the assumptions, strategies, and objectives for the second research stage involving Probe V3 and Probe V4 with respect to the initial stage, which is outlined in Table 3.5. The hypotheses remain identical to the initial stage.

Assumptions	
A1, A2, A3, and A5 are identical to Table 3.5	
A4:	If DTS measurements are calibrated using reference sections and the heated fiber section is of adequate length, the probe's fiber temperature can be determined with sufficiently small uncertainty.
A6:	The influence of unmodeled phenomena, like precipitation of solids from the water on the probe's surface remains small.
Strategies & Objectives	
SO1:	Design and build a new probe with increased fiber length, implement the DTS calibration procedure, and demonstrate the temperature-measurement capability of the probe.
SO2:	Conduct laboratory experiments to investigate the reproducibility of the probe and to determine its calibration function.
SO3:	Evaluate the velocity-measurement uncertainties and the measurement range of the probe to quantify its measurement capabilities.

Appendix D concisely motivates this concept and demonstrates it through a wind-channel experiment.

4 Proof-of-concept investigation

The present chapter comprises three parts, which intend to pursue the objectives outlined in Table 3.5. Section 4.1 aims to validate the modeling outlined in Section 3.1 with a simplified water-channel experiment (SO1 in Table 3.5). Section 4.2 revisits the existing measurement set by Renner [57] with Probe V1 in the laboratory test rig. The existing $\Delta T_{1,\infty}$ results are processed into $\Delta T_{3,\infty}$ and, subsequently, converted into Nu results (SO2 in Table 3.5). Then, the next probe generation, Probe V2, is investigated stepwise in Section 4.3. First, only the helix's temperature-measurement capability is tested. Next, the heated probe is investigated in the horizontal flow of the transparent water-channel. Finally, it is investigated in the upward vertical flow of the borehole-mimicking test rig (SO3 in Table 3.5).

4.1 Model validation with optical velocimetry

To validate the heat transfer analysis presented in Section 3.1, a simplified experiment in a water channel is conducted with conventional temperature sensors and precise optical velocity measurements. In detail, the first objective is to examine whether the empirical correlations (compare Subsection 3.1.2) are a sensible reference for the forced convection heat transfer at the probe's surface. The second objective is to prove – with independent measurements – that heat conduction dominantly contributes to the measured temperature difference $\Delta T_{1,\infty}$ between the cable's core and the water's ambient temperature, as described in Subsection 3.1.3.

Originally, a third objective was to test an FBG-imprinted glass fiber for temperature measurements inside the probe's capillary (see Figure 3.7 (b)). FBGs are engraved into the fiber at specific locations, and their measured signals can be exactly traced back to each grating position. Therefore, they have an extraordinary spatial resolution compared to DTS. However, temperature measurement with FBGs is always cross-sensitive to strain at the fiber. Even though the fiber was protected from external strain by inserting it into a thin stainless steel capillary, the temperature measurement exhibited large uncertainties on the order of $\pm 5\,^{\circ}\mathrm{C}$. Accordingly, the FBG approach was discarded and is not detailed further in the present work.

The experimental setup consists of a rectangular water channel and a self-built layered cylindrical probe, as introduced in Subsection 3.2.2 with Figure 3.7. To measure T_1, T_2, and T_3, three times two type T TCs are installed at three sheath positions: $r_1 = 0.6\,\mathrm{mm}$, $r_2 = 2.3\,\mathrm{mm}$ inside the brass tube, and $r_3 = 4\,\mathrm{mm}$. The water's ambient temperature T_∞ is measured downstream of the cylinder with two PT1000 sensors. To reduce the systematic error between the TCs, they are offset-calibrated before starting the experiment, using the PT1000 measurements as ground truth. The water channel rests for multiple hours before the offset calibration so that all temperatures are expected to be equal. Note that the PT1000 sensors are mounted at the same height as the probe's cylinder so that no offsets occur due to thermal stratification.

Further systematic temperature-measurement uncertainties of the TCs are introduced by the probe design. First, the positioning of the layers and TCs inside the brass tube (compare Figure 3.7 (b)) is uncertain. Second, thin glue strips are used to fix the TCs to the tube's surface. These glue

Table 4.1: Parameter space investigated during the model-validation test in the water channel: heating current and flow velocity, together with their corresponding conversions into heating power per unit length and to Reynolds numbers (compare Equation 2.74).

Set current and corresponding heating power per length								
I	[A]	3	5.3	6.5				
P_{el}/l	[W/m]	4.8	15.0	22.5				
Set volume flow rate with corresponding Re and Re_l								
u	[l/min]	0	10	15	20	30	50	80
Re	[–]	0	80	120	160	240	400	640
Re_l	[–]	0	125.7	188.5	251.3	377.0	628.3	1005.3

strips may be thin, yet heat conduction through them leads to a minor systematic overestimation of T_3.

Table 4.1 outlines parameter space defined by heating power and flow velocity. The probe has an electrical resistance of 138.5 mΩ and is heated by a constant electrical current. For precise velocity reference, the velocity is determined locally in front of the cylinder using PIV. "The desired velocity information are estimated from 24 interrogation areas of 128 × 128 px (11.6 × 11.6 mm) upstream of the cylinder, which are evaluated with *PIVview* software and averaged across 10 image pairs per measurement to ensure velocity standard deviations $\sigma_u < 5\,\%$ of the respective flow speeds u. The interrogation areas overlap by 4 % and the time delay between consecutive frames is varied from $0.02 - 0.1$ s to ensure a pixel displacement in the range of 8 to 20 px." [RRTK24]

Each combination of the parameters in Table 4.1 is set once and held for 8 min. The transient temperature change occurs within the first 1 to 2 min, and the data from the last 2.5 min are considered to be in steady state and are averaged. Figure 4.1 displays the unprocessed measured temperature data for one of the 2.5 min averaging intervals. Two TC signals are plotted for the T_1, T_2, and T_3 locations, and two PT1000 signals are plotted for T_∞. The plot demonstrates that the temperature drop in the conductive region inside the probe, $\Delta T_{1,3}$, is much larger than that in the convective region outside the probe, $\Delta T_{3,\infty}$.

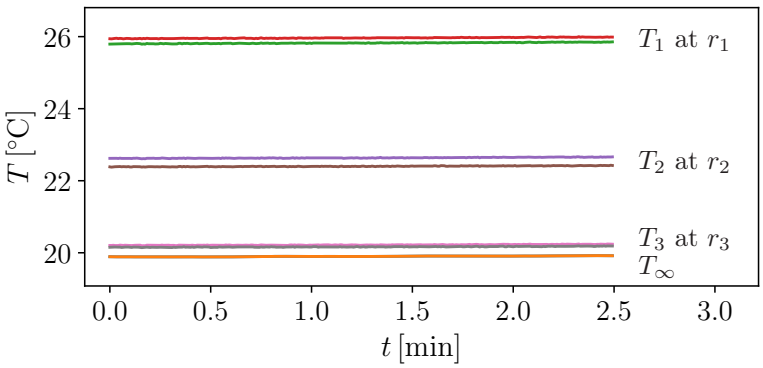

Figure 4.1: Graph depicting unprocessed temperature measurement data from an exemplary measurement with the parameters set to $I = 3\,\mathrm{A}$ and $u = 8.4\,\mathrm{mm/s}$. T_1, T_2, and T_3 are each measured with two thermocouples, which are positioned as detailed in Figure 3.7 (b). T_∞ is measured with two PT1000 sensors located far downstream in the water channel.

The Biot number is computed using equation (2.66), with $T_0 = T_1$ and $T_\mathrm{S} = T_3$. Thus, the ratio of conductive to convective temperature drop is evaluated for all measurements and is visualized in Figure 4.2 (a). "While the heat convection resistance decreases with increasing flow velocity, the heat conduction resistance is independent of flow velocity changes. Thus, a monotonic increase

of Bi over Re is expected and revealed by the results (see Figure 4.2 (a)). The practical consequences are exemplarily emphasized for the temperature measurements of the $P_{el}/l = 22.5\,\mathrm{W/m}$ experiments in Figure 4.2 (b). The total measured temperature difference between the glass fiber in the probe center[1] and the environment, $T_1 - T_\infty$, consists of a dominant nearly constant offset of $T_1 - T_3 \approx 25\,\mathrm{K}$ inside the probe and an accordingly diminished relevant temperature difference for the velocity measurement in the range of $0.4 < T_3 - T_\infty < 2.0\,\mathrm{K}$." [RRTK24]

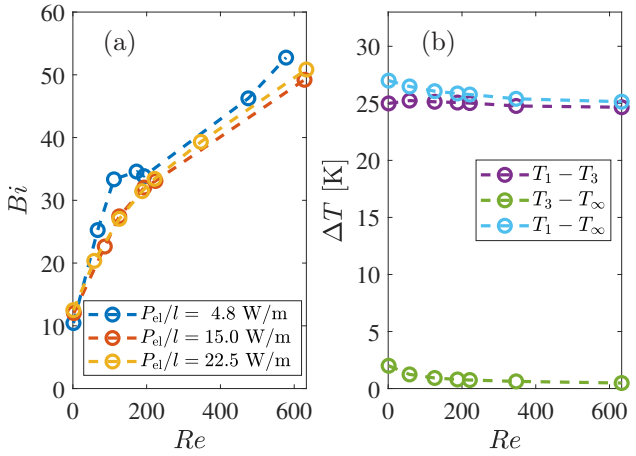

Figure 4.2: "Results of the water-channel experiments; (a) $Bi - Re$ diagram for varying power per cable length P_{el}/l, which emphasizes the dominant heat-conduction resistance of the probe ($Bi > 1$); (b) $\Delta T - Re$ plot for the $P_{el}/l = 22.5\,\mathrm{W/m}$ measurement series reveals that the relevant temperature difference for the velocity measurement is only a small fraction of the total temperature difference." [RRTK24] (Figure reprinted from [RRTK24] with typo correction: $P_{el}/l = 4.1\,\mathrm{W/m}$ corrected to $4.8\,\mathrm{W/m}$)

To evaluate the first objective – whether the empirical correlations fit as reference for the convective heat transfer – the measured $\Delta T_{3,\infty}$ values are converted into Nu values using equation (2.53). Then, they are plotted in Figure 4.3 together with two correlations, one by Gnielinski [28] and one by King [35]. In general, the measured data correspond well with the correlation from Gnielinski. Around $Re = 100$ the $4.8\,\mathrm{W/m}$ measurements seem to be outliers towards higher values. No clear explanation exists for this behavior. The measured data tend toward higher Nu values in the lower Re range, and in the higher Re range they tend towards lower Nu values. Both deviations are explainable: First, the Gnielinski correlation is a correlation for forced convection only. Thus, when natural convection becomes relevant at small velocities, the correlation is expected to underestimate Nu (compare also Figure 2.14). With regard to the underestimation of Nu in the higher Re range, recall that the TCs at the probe's surface are glued to the surface with thin adhesive strips, which leads to a systematic overestimation of T_3. This overestimation is very small, but the $\Delta T_{3,\infty}$ values are also small (compare Figure 4.2 (b)) in the higher Re range. As the calculated Nu values are inversely proportional to the measured $\Delta T_{3,\infty}$, an overestimation of T_3 leads to an underestimation of Nu.

In conclusion, both objectives of this experiment are met. Regarding the first objective, it is shown that the empirical correlations provide a good reference for the convective heat transfer, which shall be utilized for velocity measurements. Thus, preliminary design calculations based on correlations such as the measurement range estimation in Figure 3.3 result in sensible values. Furthermore, the correlations remain a sensible reference for measurement data, in particular when the cable's thermal conductivity is uncertain and must be fitted. However, the measured data do not perfectly match the correlation, and thus calibration is required for accurate velocity

[1] Note that no glass fiber is used in this particular experiment. However, in all subsequent experiments, T_1 is measured using a glass fiber.

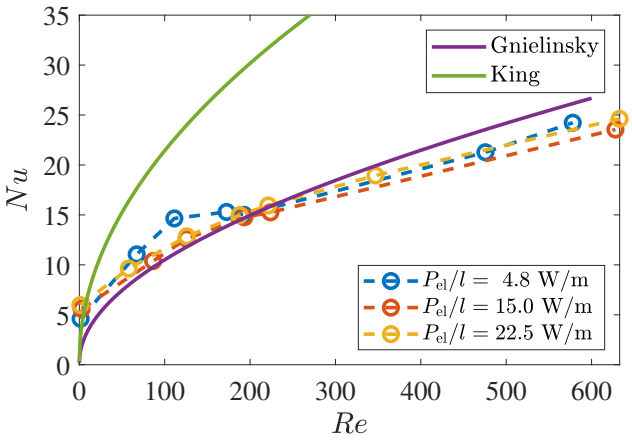

Figure 4.3: Results of the water channel measurements displayed non-dimensionally in a $Nu - Re$ diagram in comparison to the correlations of King [35] and Gnielinski [28]. (similar to Figure 8 in [RRTK24])

measurements. Concerning the second objective, it is clearly shown that only $\Delta T_{3,\infty}$ depends on the velocity. Consequently, the measured temperature drop $\Delta T_{1,\infty}$ must be separated into a conductive part $\Delta T_{1,3}$ and a convective part $\Delta T_{3,\infty}$, as depicted in Figure 3.4.

4.2 Analysis and reevaluation of the Probe V1 data

The first probe, Probe V1, is a helically wound hybrid cable, which is introduced in Subsection 3.2.5 and depicted in Figure 3.10. Renner [57] built both Probe V1 and the borehole-mimicking test rig (see Figure 3.6) and investigated the probe in the test rig during the course of his master's thesis. The key results from Renner's investigation are shown in Figure 4.4 and discussed in the following. Subsequently, the data from Renner are reevaluated using the heat-transfer modeling proposed in Section 3.1 and compared to empirical correlations from the literature.

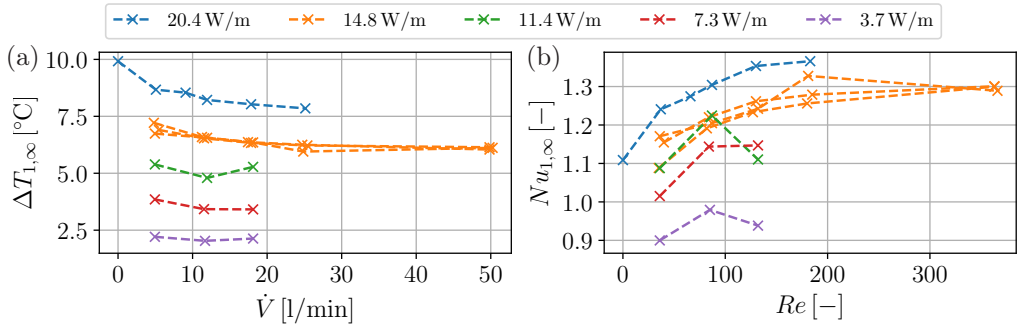

Figure 4.4: Data from the investigation of Probe V1, plotted as processed by Renner [57]. The data consist of seven datasets at various cable-length specific heating powers P_{el}/l. (a) Measured temperature difference $\Delta T_{1,\infty}$ over set volume flow rate $\dot{V}$. (b) $Nu_{1,\infty} - Re$ plot, where $Nu_{1,\infty}$ is computed using $\Delta T_{1,\infty}$.

Renner [57] installed Probe V1 in the test rig and examined it with five heating power levels ranging from 3.7 to 20.4 W/m at flow rates from 0 to 50 l/min. T_1 is determined by averaging the DTS measurement along the helix fiber length, while both T_∞ and $\dot{V}$ are acquired with the *Kobold MIM-1220H* volume flow sensor. The nondimensional numbers relevant for the investigated forced convection heat transfer are the Nusselt and Reynolds numbers. To calculate Re, first the bulk velocity u is computed using equation (3.9) with the borehole's inner pipe diameter $d_p = 152\,\text{mm}$ and the area A_b blocked by the packer's pipe, which amounts to $A_b = \pi(75\,\text{mm}/2)^2$. Then, according to equation (2.56), Re is computed assuming a constant kinematic viscosity of water of

$10^{-6}\,\mathrm{m}^2/\mathrm{s}$ and using $L_{\mathrm{char}} = 6\,\mathrm{mm}$, which is the hybrid cable's diameter. Nu is computed with equation (2.53), yet it is assumed that the measured fiber temperature T_1 is representative of the cable's surface temperature T_{S}. Nusselt numbers calculated with this assumption are indexed as $Nu_{1,\infty}$.

Figure 4.4 displays the measured data in two plots: a dimensional $\Delta T_{1,\infty} - \dot{V}$ plot and a nondimensional $Nu_{1,\infty} - Re$ plot. The measured data in Figure 4.4 (a) at higher heating powers of 14.8 and 20.4 W/m clearly reveal the expected sensitivity of temperature difference to flow rate. However, the data at lower heating powers do not consistently show this trend. As some measurement points seem to be outliers, interrupting the trends of constant-heating-power data sets, the displayed data still suggest that a measurable dependence between velocity and measured fiber temperature exists and that the uncertainties in the current system are high. In the $Nu_{1,\infty} - Re$ plot, Figure 4.4 (b), the computed Nusselt numbers are an order of magnitude smaller than expected (for example, compare with Figure 4.3). These small $Nu1,\infty$ values result from neglecting the temperature drop inside the cable, $\Delta T_{1,3}$.

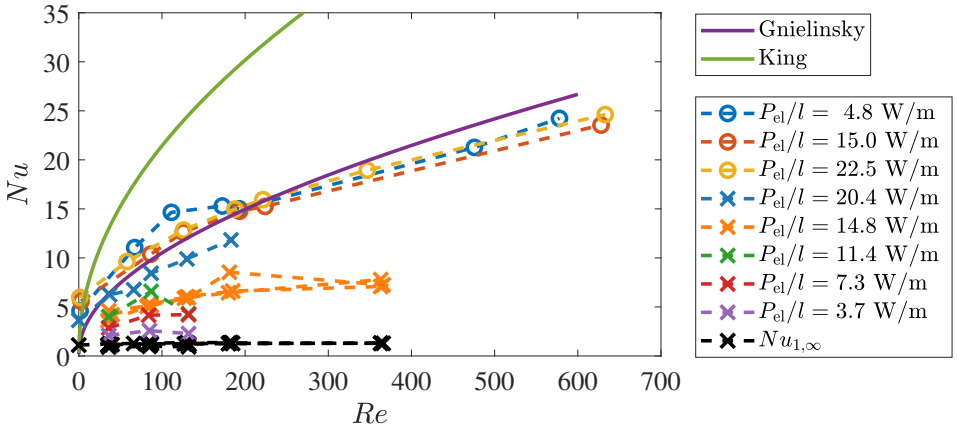

Figure 4.5: Comparison of Probe V1 data measured in the borehole test rig (x marker) to the water channel measurements (∘ marker) and correlations by King [35] and Gnielinski [28]. All $Nu_{1,\infty}$ data from Figure 4.4 (b) are displayed using black x markers. (similar to Figure 8 in [RRTK24])

To compare the results with literature data in the form of empirical correlations and with the water-channel data of the previous section, the heat conduction inside the hybrid cable must be estimated. The geometrical data of the cable are known, see Table 3.2, but the thermal conductivity k_{i} of the cable's insulative sheath is not. Therefore, low values common for cable sheath materials around $0.2\,\mathrm{W/(mK)}$ are tested to first evaluate $\Delta T_{2,3}$ with equation (3.3) and then Nu with equation (2.53). $T_1 \approx T_2$ is assumed for simplicity because $\Delta T_{1,2} \ll \Delta T_{2,3}$. Figure 4.5 shows the Nu results when $\Delta T_{2,3}$ is calculated with $k_{\mathrm{i}} = 0.19\,\mathrm{W/(m\,K)}$ in comparison to empirical correlations, to the water-channel measurements, and to the $Nu_{1,\infty}$ data. The *corrected* data from Probe V1 (x marker) stand out because they still remain at smaller Nu than the Gnielinski correlation and the water-channel results (o marker). Furthermore, these data stand out because the different measurement sets at various heating powers spread over a wide Nu range. This spreading contrasts with the expectation that one line in the dimensionless $Nu-Re$ diagram should describe the relevant physics and be valid for all investigated heating powers. Selecting different k_{i} values results in a vertical shift of the Probe V1 data in the $Nu - Re$ diagram, but this does not reduce the spreading.

In conclusion, this first investigation with Probe V1 successfully demonstrates the sensitivity of measured temperatures to velocity changes with the data acquired at high heating powers. Furthermore, when the insulation in the cable's sheath is considered, the resulting Nu are in the same order of magnitude as the Nu measured in the water channel and as the Nu by the Gnielinski

correlation. However, three issues are identified: First, the measurement uncertainty appears to be high because several outliers appear to be contained in the measurement sets. The outliers disturb the expected trend that increasing velocities correspond to more effective heat transfer and, thus, lower $\Delta T_{1,\infty}$. Second, the insulative impact cannot be precisely quantified due to limited knowledge of the material properties. Third, in the $Nu - Re$ diagram, the Probe V1 data spread over a wide Nu range instead of collapsing onto a single line, which also suggests uncertainties in the acquisition and processing of the data.

4.3 Investigation with borehole-ready prototype Probe V2

The second probe iteration, Probe V2, is a borehole-ready prototype built by *Solexperts GmbH*, which is introduced in Subsection 3.2.5 with Figure 3.11. Driven by the goal of demonstrating its measurement capabilities in a real borehole, it is designed with the focus to withstand the challenging conditions encountered in boreholes: high pressure, elevated temperature, and the potential impact of stones and sediment. As outlined in Table 3.5 with SO3, SO4, and SO5, the objectives are to first test Probe V2 in the laboratory by investigating its uncertainties and measurement range, and subsequently to apply it in a real borehole. Only the first step of laboratory testing with its challenges and lessons learned is presented in this section, because after conducting this step the research process was paused for a review, which led to the approach outlined in the next chapter.

This examination of Probe V2 in the laboratory is presented in three subsections below. First, the probe's temperature-measurement capabilities are investigated by inserting the helix stepwise into a controlled hot water bath. Second, as the helix fits well into the transparent water channel (compare Subsection 3.2.2), it is tested there for its capability to measure flow directed perpendicular to the probe's axis. Third, in the borehole-mimicking test rig (see Subsection 3.2.1), its capability to measure vertical flow along the probe's axis is tested.

4.3.1 Preexamination

The capability of Probe V2 to measure a specific temperature is investigated by immersing the probe's helix stepwise into heated water. This is a spatial-resolution test, which aims to quantify how well the DTS is capable to measure the helix temperature with the fiber contained in it. Recall that the spatial resolution is defined as the distance required to cover 90 % of a step change (see Figure 2.9). The fiber length in the helix is 0.73 m, and the spatial resolution of the *AP Sensing N43856B* DTS is specified as 0.5 m in its datasheet.

The test conditions are:

- The DTS device is set to double-ended mode with a measurement time of 60 s, and the internal temperature processing of the device is used. No external calibration is applied.
- The water temperature is heated to 70 °C and controlled with a *Steba SV 50* heater.
- The probe's helix is immersed stepwise into the water: (1) not immersed, (2) approximately half immersed, (3) helix completely immersed, and (4) helix together with a part of the probe body immersed.

The test results are shown in Figure 4.6. At the bottom of the figure, the immersion steps are shown with photographs and above these, the DTS temperature measurement results are plotted: on the

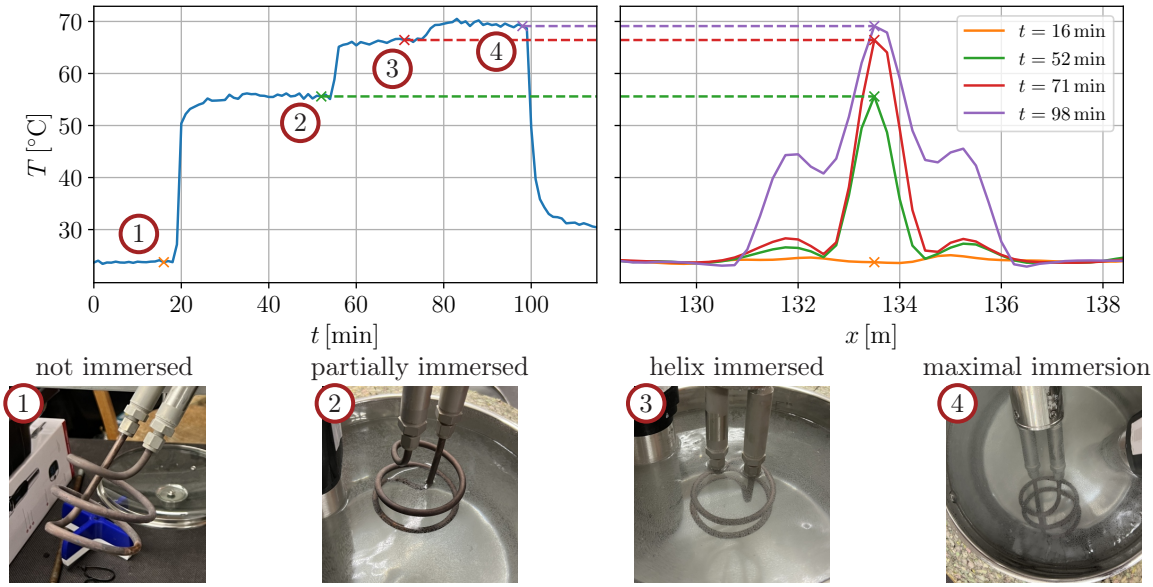

Figure 4.6: Investigating the spatial resolution of the fiber-optic DTS measurement with Probe V2. The probe's helix is immersed stepwise into warm water at 70 °C and held at the depicted immersion positions. The left graph shows the time series of maximum peak temperatures measured by the DTS. The right graph shows the measured temperature over fiber distance x for selected measurements. The highlighted peak temperatures are 55.9 °C at partial helix immersion, 66.7 °C at complete helix immersion, and 68.7 °C when helix, connector bodies, and a part of the probe body are immersed.

left side, the maximum temperature measured along the helix is plotted over the measurement time, while on the right side the temperature is plotted over fiber distance for selected times.

The most critical result of this test is that the DTS temperature measured with the fully immersed helix is only 66.7 °C, leaving a gap of $\approx$ 3 °C to the actual fiber temperature. Thus, when the helix is heated via Joule heating, every measured fiber temperature with the heated helix will underestimate the actual fiber temperature within the helix. Furthermore, the peak temperature measured with the DTS at the helix location provides the best estimate of the helix temperature.

The optimistic argument is that the temperature underestimation should be constant for all heating levels. When a comprehensive calibration experiment is used to determine calibration curves for various heating powers spanning the full measurement range, this systematic temperature-measurement error will not influence the velocity estimation. However, it is obvious that the temperature underestimation depends on the temperature inside the probe body. If this temperature were to vary significantly over the measurement duration and influence the temperature underestimation, the previous calibration hypothesis would fail.

In conclusion, this preexamination test reveals that the fiber length in the probe's helix is too short, and measurements of a heated helix underestimate its temperature. This issue of fiber length may be negligible if the optimistic argument outlined above is valid.

4.3.2 Examination in the horizontal water channel

A convenient side effect of the Probe V2 design is that its helix fits well into the water channel's measurement section, as depicted in Figure 4.7. Therefore, the first experiment is conducted in the water channel to examine the sensitivity of Probe V2 to flow that is directed perpendicular to its axis. In detail, the objective is to measure the sensitivity of the temperature difference $\Delta T_{1,\infty}$

to variations in flow velocity and to test the reproducibility of this relationship with a second measurement set.

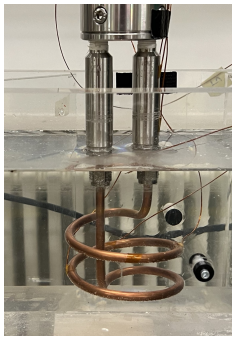

Figure 4.7: Photo of Probe V2 mounted above the water channel. The helix is immersed in the water channel's measurement section.

The measurement procedure is outlined as follows:

- Before inserting Probe V2 into the water, TCs (type T) are fixed to the probe with adhesive strips. Four are attached to the probe's helix and two additional ones to one of the cooling cylinders, which are located between the helix and the probe body.
- In contrast to the previous experiment in the water channel (see Section 4.1), the local velocity is not measured with PIV. Instead, the *Kobold MIM-1220H* volume flow sensor is mounted next to the pump that drives the channel. The velocity is computed as bulk flow velocity

$$u = \frac{\dot{V}}{A_{\mathrm{WC}}}. \tag{4.1}$$

  The water channel's cross section A_{WC} amounts to $12\,\mathrm{cm} * 12\,\mathrm{cm} = 144\,\mathrm{cm}^2$.
- The volume flow is adjusted by utilizing three different pumps of different sizes. The two smaller pumps, *Toolcraft TO-7159155* and *Toolcraft TO-7159158*, are controlled with a power supply, and the third pump, *Gardena 3500/4*, is controlled via throttling.
- The heating power is set with a constant current using the power supply *EPS/HC 40400-30-M*.
- The DTS is set to acquire in double-ended mode with a measurement time of 60 s, and the internal temperature processing of the device is used. No external calibration is applied.

Two **measurement sets**, covering a power per length ranging from 10.2 to 156 W/m and a velocity ranging from 0 to 60 mm/s, were acquired using this setup. Measurement sets were acquired in consecutive **subsets** that maintained a constant velocity while increasing the heating power every 10 min. Each **measurement point** is an average over the final 5 min of each 10 min interval. The processed results of these two measurement sets are plotted in Figure 4.8 and Figure 4.9.

Figure 4.8 shows the results in $\Delta T_{1,\infty} - u$ plots. T_1 is determined from the peak in the DTS measurement at the helix location, compare Figure 4.6. T_∞ is measured with a PT1000 sensor in the water channel, and u is calculated from the volume flow measurements according to equation (4.1). The figure displays each measurement set in a subplot and highlights the acquisition order of the subsets. Measurements that are acquired at the same day mostly display the expected behavior of declining $\Delta T_{1,\infty}$ with increasing velocity. Between consecutive subsets that are acquired on different days, a deviation is apparent throughout the data. Furthermore, the first measurement set contains two unexpected behaviors: the $\Delta T_{1,\infty}$ values acquired on day 2 with 10.2 W/m are

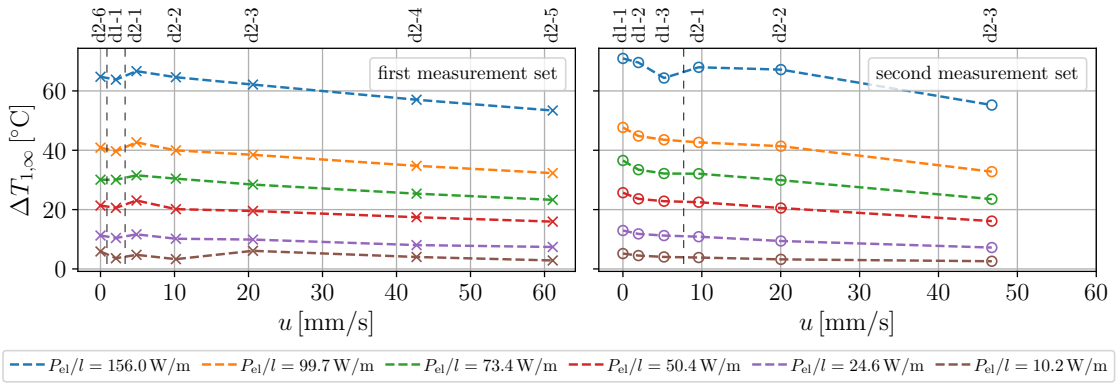

Figure 4.8: Measurements with Probe V2 in the water channel are plotted in subfigures that are sorted by measurement set. The data are plotted in $\Delta T_{1,\infty} - u$ graphs. T_1 is determined by the helix peak from the DTS measurements. The first measurement set is depicted on the left and the second on the right. Both measurement sets were acquired on two consecutive days. To highlight the unexpected influence of temporal sequence, annotations above the plots indicate when each measurement subset (containing multiple heating powers at the same flow rate) was acquired. 'd1-2' refers to day 1 subset 2.

not monotonically decreasing, and most of the d2-6 $\Delta T_{1,\infty}$ values are smaller than the d2-1 $\Delta T_{1,\infty}$ values at higher velocity.

Figure 4.9 (a) displays the same measurement data as Figure 4.8 in $\Delta T_{1,\infty} - u$ diagrams, with a subplot for each heating power level. Thus, all constant-heating-power lines are resolved over their respective $\Delta T_{1,\infty}$ range. Using one of the TCs fixed to the probe's surface, T_3 is estimated and plotted in $\Delta T_{3,\infty} - u$ subplots in Figure 4.9 (b). These TC data must be interpreted with caution, because attachment of the TCs with adhesive strips failed multiple times throughout the experiment. Only the one TC used to estimate T_3 remained attached to the helix surface throughout the experiment. However, it is not guaranteed that it did not slightly move and that its contact to the helix surface changed. Aside from these uncertainties, the TC data reveal interesting insights: On the one hand, they also reveal significant offsets within and between measurement sets that partially correlate with the $\Delta T_{1,\infty}$ data acquired by the DTS. On the other hand, the course of the 10.2 W/m curve of the first measurement set reveals the expected sensitivity behavior in the $\Delta T_{3,\infty}$ data, whereas the $\Delta T_{1,\infty}$ by the DTS demonstrate a random zigzag behavior.

In conclusion, the depicted results show that significant uncertainties are present in this system. First of all, the reproducibility is poor. Even though both measurement sets were acquired using the same procedure, the measured temperature differences vary strongly between measurement points at identical heating power and velocity. Furthermore, letting the setup rest over night clearly leads to offsets within each measurement set. It is unknown whether these uncertainties are rooted in the DTS measurement, in the heat transfer, or in both. The fact that the TC measurements (even though of limited accuracy either) also reveal significant offsets indicates that part of the reproducibility issue is attributable to the heat transfer. Because of the poor result quality, further conversion of the results into Nusselt numbers is omitted.

4.3.3 Examination in the borehole-mimicking test rig

Although the measurements in the water channel already demonstrated a lack of reproducibility, Probe V2 is tested in the borehole-mimicking test rig. In contrast to the prior experiment, which tested Probe V2 in horizontal flow oriented perpendicular to its axis, this experiment tests the probe in upward vertical flow. As the flow direction is identical to the flow direction of the buoyancy-driven flow caused by free convection, fewer inconsistencies are expected at low velocities. Again,

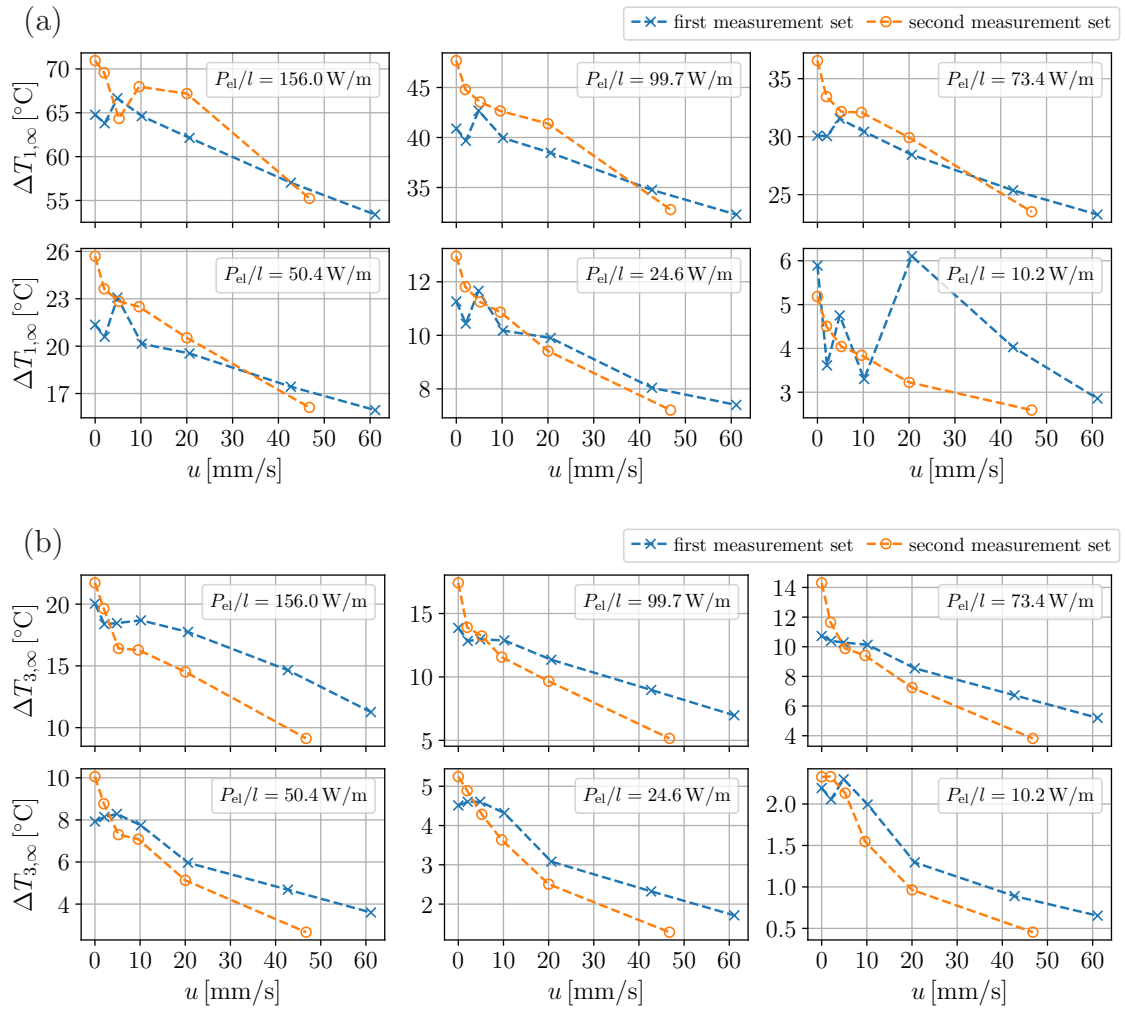

Figure 4.9: Measurements with Probe V2 in the water channel are plotted in subfigures that are sorted by heating power. (a) $\Delta T_{1,\infty} - u$ plots: T_1 is determined by the helix peak from the DTS measurements. (b) $\Delta T_{3,\infty} - u$ plots: T_3 is determined by a TC that is fixed to the helix's sheath using an adhesive strip.

the objective is to measure the sensitivity of the temperature difference $\Delta T_{1,\infty}$ to variations in flow velocity and to test the reproducibility of this relationship with a second set of measurements.

The experimental setup consists of Probe V2 (compare Figure 3.11), the *AP Sensing N4386B* DTS, the *EPS/HC 40400-30-M* power supply, and the borehole-mimicking test rig (compare Figure 3.6), which includes a pump, a valve, and a flow-rate sensor. Before inserting the probe into the test rig, a PT1000 RTD is fixed to the centralizer below the probe, and a TC is fixed to the helix surface using an adhesive strip. Before applying the adhesive strip, the surface is thoroughly cleaned, and after applying the strip, the probe rests for one day before being inserted into the water. Finally, Probe V2 is positioned at mid-height in the test rig, centrally inside its inner pipe.

Two measurement sets are acquired according to the following procedure. Each measurement set is acquired in subsets. For each subset, the volume flow rate $\dot{V}$ is held constant, and the constant current I is increased for every measurement point. Thus, every measurement point has a distinct combination of $\dot{V}$ and I. During the first measurement set, each measurement point is held constant for 20 min, and the measurement points are set sequentially. For the second measurement set, each measurement point is held constant for 12 min, and between all measurement points, the heating power is turned off for 12 min. The reduction from 20 to 12 min is implemented because it

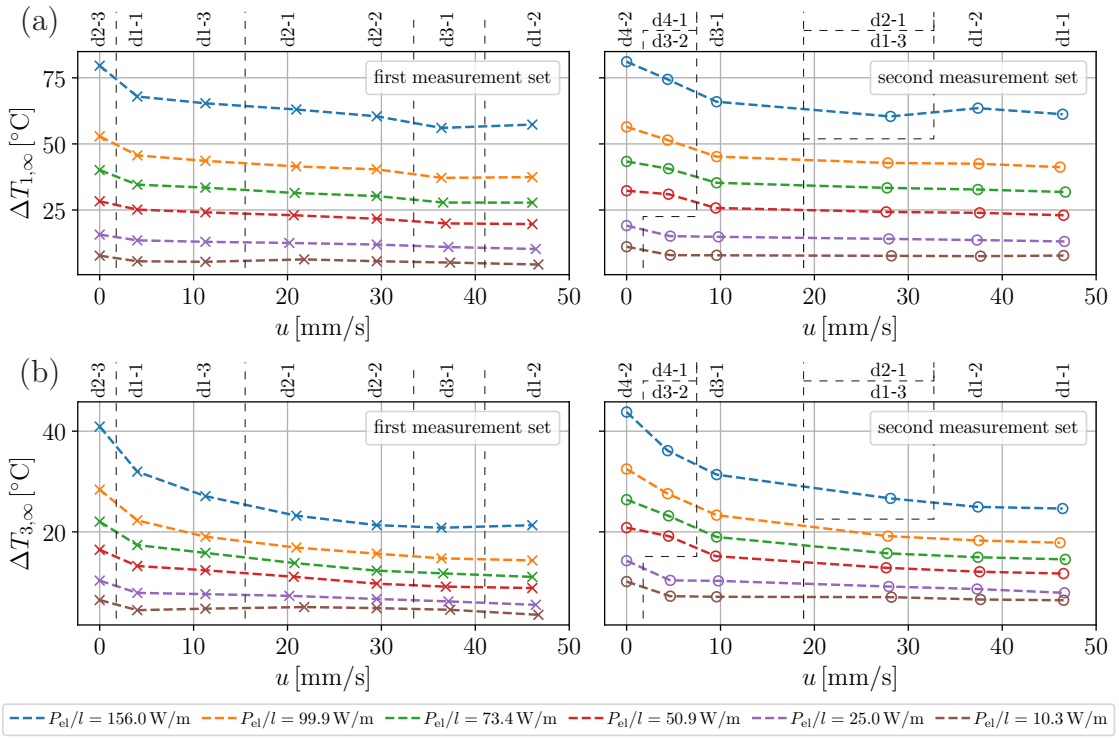

Figure 4.10: Measurements with Probe V2 in the borehole-mimicking test rig are plotted in subfigures that are sorted by measurement set. (a) depicts $\Delta T_{1,\infty} - u$ graphs. Recall that T_1 is determined by the helix peak measured with the DTS. (b) depicts $\Delta T_{3,\infty} - u$ graphs. Recall that T_3 is measured with a thermocouple that is fixed to the helix surface. In both subfigures, the first measurement set is depicted on the left and the second on the right. Both measurement sets were acquired on two consecutive days. To further highlight the unexpected influence of temporal sequence, annotations above the plots indicate when each measurement subset (containing multiple heating powers at the same flow rate) was acquired. 'd1-2' refers to day 1 subset 2.

was observed during the first measurement set that steady state is attained within less than 5 min. The 12 min unheated resting period allows estimation of T_∞ with the DTS data, which would be necessary if the probe were applied in a borehole without an additional RTD.[2] Both measurement sets were acquired over several days. During the second set, problems in the data acquisition led to loss of the TC and RTD data on days 2 and 3 of the measurement. Therefore, the subset at $u \approx 20$ mm/s is missing, and on the fourth day, half of the day 3 measurements were repeated. To extract a single measurement, the acquired data are averaged over a five-minute period at the end of each heating interval.

The results are displayed in Figure 4.10, sorted by measurement set, and in Figure 4.11, sorted by heating power. In both figures, $\Delta T_{1,\infty} - u$ plots are displayed in (a) and $\Delta T_{3,\infty} - u$ plots in (b). T_1 is determined by the DTS at the helix peak (see Figure 4.6); T_3 is measured with a TC that is fixed to the helix surface; T_∞ is measured with a PT1000 located below the helix and thus upstream of it in the test rig; and u is calculated from the volume flow rate measurement according to equation (3.9) with $A_b = 0$.

Figure 4.10 again reveals that offsets occur when the setup rests over night. This is especially evident in the plot of the second measurement set in Figure 4.10 (a) with the $u \approx 5$ mm/s and $u \approx 30$ mm/s subsets. In both cases, some of the subsets' measurements were acquired on the same day as measurements of the subset neighboring to the right. These same-day measurement points

[2] No T_∞ estimates by the DTS are shown here for brevity. However, this approach is repeated with Probe V3 as described in Section 5.1.

align with the expected continuous trend of decreasing $\Delta T_{1,\infty}$ for increasing u, whereas the others disrupt this trend:

- in the $u \approx 5\,\mathrm{mm/s}$ subset, the measured $\Delta T_{1,\infty}$ increased significantly in the day 4 data compared to the day 3 data and
- in the $u \approx 30\,\mathrm{mm/s}$ subset, the measured $\Delta T_{1,\infty}$ decreased significantly in the day 2 data compared to the day 1 data.

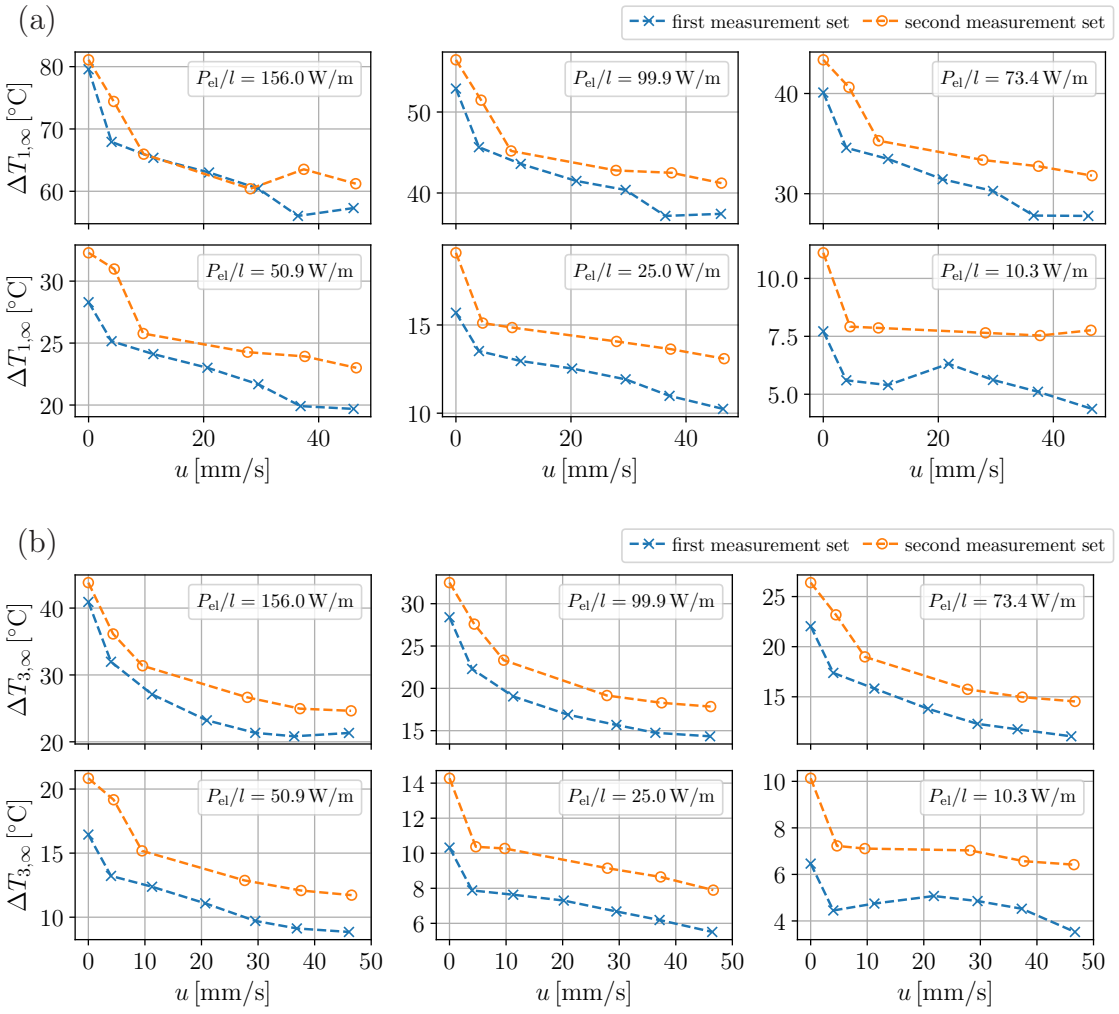

Figure 4.11: Measurements with Probe V2 in the borehole-mimicking test rig are plotted in subfigures that are sorted by heating power. (a) $\Delta T_{1,\infty} - u$ plots: T_1 is determined by the helix peak from the DTS measurements. (b) $\Delta T_{3,\infty} - u$ plots: T_3 is determined by a TC that is fixed to the helix's sheath using an adhesive strip.

Figure 4.11 compares both measurement sets, sorted by heating power. Therefore, every constant power-per-length subset is displayed in its respective ΔT range. In terms of reproducibility, these results seem very similar to those of the previous section in the water channel that are displayed in Figure 4.9. Large offsets between measurement sets occur, rendering any further processing unfeasible. Compare Figure 3.3 to recall that uncertainties in $\Delta T_{3,\infty}$ of 0.1 °C already lead to significant errors in the velocity determination, and the offsets observed here range from 2 to 5 °C. When analyzing the trends of the results, only the power-per-length subsets in the top row of Figure 4.11 (b) display the expected curve shape (as displayed in Figure 3.3).

In conclusion, the results of Probe V2 in the borehole-mimicking test rig are very similar to those in the prior water-channel experiment, which confirms the conclusion of the previous subsection.

4.4 Intermediate conclusion

Table 3.5 defines the starting point of the experiments described above by stating hypotheses, assumptions, strategies, and objectives. The objectives were to assess the validity of the heat-transfer modeling (SO1), to process the Probe V1 data with the findings of the heat transfer modeling (SO2), to investigate Probe V2 focusing on reproducibility (SO3), and to evaluate the uncertainties and the measurement range of Probe V2 (SO4) before testing it in a real borehole (SO5). With respect to the strategies and objectives, the findings of the sections above are discussed once more in the following paragraphs. Subsequently, the assumptions and hypotheses are reviewed. Finally, the need for a shift in objectives is deduced.

In Section 4.1, conventional temperature sensors are fixed in and to a self-built probe, and the heat-transfer modeling, comprising radial heat conduction within the probe and convective heat transfer outside the probe, is investigated. A set of experiments proves that it is critical to correct for the radial heat conduction inside the probe cylinder. Regarding the convective heat transfer, the measured Nusselt numbers align well with an empirical correlation. However, all experiments were acquired consecutively on a single day, and the subsequent experiments clearly demonstrate that offsets between measurements are linked to resting time between the measurements. Nonetheless, SO1, as specified in Table 3.5, is successfully carried out and validates the modeling approach.

With the experimental confirmation from Section 4.1 that radial heat conduction leads to a large temperature offset between the fiber (T_1) and the surface (T_3), this effect is considered by re-evaluating the Probe V1 data in Section 4.2. This processing strategy elevates the measured Nusselt numbers to the same order of magnitude as the empirical correlation used for comparison. However, the Nusselt numbers exhibit a large, unexpected spreading: subsets acquired with constant heating power are significantly offset from each other, sorted by heating power. Thus, although SO2 from Table 3.5 was successfully carried out, the results remain inconclusive.

In Section 4.3, Probe V2 is investigated in three stages. First, a preexamination of its temperature measurement capabilities reveals that the fiber length contained in the probe is too short. Because of the quite coarse spatial resolution of the DTS device, the measurement at the helix coordinates is always influenced by the fiber sections that lead from the helix into the probe body. Then, in two consecutive stages, two similar velocity-measurement investigations, according to SO3 in Table 3.5, are carried out: one in horizontal flow perpendicular to the probe's axis, and one in upward vertical flow parallel to the probe's axis. Both investigations cover similar ranges of velocities and heating powers twice, which results in two measurement sets each. The results from both experiments confirm the sensitivity of the measured temperature differences to changes in velocity. However, the results also reveal that offsets occur in the measured temperature differences when the test rig rests over night between consecutive measurements or for multiple days between measurement sets. These offsets occur in both $\Delta T_{1,\infty}$ (T_1 measured by the DTS) and $\Delta T_{3,\infty}$ (T_3 measured by a TC fixed to the helix surface). Furthermore, these offsets between repeated measurement sets are very large, ranging from ≈ 2 to $\approx 5\,°\mathrm{C}$. In comparison, Figure 3.3 identifies that $0.1\,°\mathrm{C}$ may be an acceptable uncertainty range, which already leads to significant error margins in the velocity measurement. Therefore, any further investigations to characterize and apply Probe V2 as a velocity sensor (SO4 and SO5 in Table 3.5) are omitted.

To find the cause of these unexpectedly large offsets, the assumptions and hypotheses from Table 3.5 are revisited below.

The assumptions A1, A3, and A5 are considered to remain valid, but A2 and A4 are questioned: In assumption A2, the convective heat transfer depends on 'flow velocity and constant conditions', yet the previous results demonstrate offsets, which seem to originate in the convective heat transfer. However, two non-constant phenomena were observed during the measurements. First, the water's ambient temperature rises from $\approx 20\,^{\circ}\mathrm{C}$ to $\approx 30\,^{\circ}\mathrm{C}$ during the experiments. Second, dissolved solids precipitate in the water tank and also on the probe's surface. In particular, the second phenomenon is not covered by the modeling. If dissolved solids precipitate on the probe's surface, an additional layer for heat conduction is introduced, and the surface roughness of the probe's surface changes, which in turn may influence the flow close to the surface that governs the convective heat transfer. With regard to assumption A4, the reliability of the DTS measurement is revisited. First, the fiber length inside Probe V2 is too short for a DTS measurement, which is influenced only by the temperature in the helix fiber. Furthermore, an additional literature research reveals that precise DTS measurements are only achievable with in situ calibration [23, 31, 70] (compare Subsections 2.3.2 and 2.3.3). Des Tombe et al. demonstrate that DTS measurements with uncertainties less than $0.1\,^{\circ}\mathrm{C}$ are achievable. Thus, calibration and a probe design that respects the DTS device's spatial-resolution limitation are necessary for high-accuracy DTS measurements.

The hypothesis H1 remains the primary working hypothesis despite lack of reproducibility in the Probe V2 results. Hypothesis H2 likewise remains supported; however, based on the current state of knowledge, the transferability from the test rig to the borehole is considered highly uncertain. If the day-to-day offsets observed in the experimental data persist, they are likewise expected to occur between the test rig and the borehole.

Considering all the findings of the present chapter, the overarching goal *calibrating the sensor and applying it in the field* cannot be realized until the reasons for the observed offsets are understood. Further research must focus on optimizing the DTS measurement performance and understanding the underlying phenomena that impede the reproducibility of the heat transfer.

5 Reproducibility analysis

In the prior experiments with Probe V1 and Probe V2, offsets occurred that could not be clearly traced back to either uncertainty margins of the DTS measurements or to effects impacting the heat transfer. Therefore, the investigations in the present chapter focus on first establishing a more reliable DTS temperature measurement with quantifiable uncertainty margins so that the measured temperature difference, $\Delta T_{1,\infty}$, is a reliable measure of the investigated heat transfer.

Consequently, two new probe iterations, Probe V3 and Probe V4, which are introduced in Subsection 3.2.5, were developed. With respect to the spatial resolution limitation of DTS devices, both probe designs comprise increased fiber length. Furthermore, all fiber-optic DTS measurements are calibrated according to the double-ended calibration algorithm presented in Subsection 2.3.3. In Appendix B, the reference temperature sensors used for the DTS calibration procedure are tested, and the observed uncertainties and drift phenomena are analyzed and discussed. Subsequently, Appendix C demonstrates the impact of the DTS calibration procedure using a series of test measurements.

The investigations focus on extracting a reliable temperature measure with known uncertainty margins from the respective probes, so that all uncertainties exceeding this margin must be linked to the heat transfer (SO1 in Table 3.6). The overarching objective of the research described in this chapter is to investigate whether the velocity dependence of the heat transfer can be consistently reproduced in the laboratory with the borehole-mimicking test rig (SO2 in Table 3.6), and – if successful – to evaluate the uncertainty margins and the measurement range of fiber-optic TA in water (SO3 in Table 3.6).

First, Section 5.1 investigates the helix-shaped probe, Probe V3. Then, Probe V4, the double-ring probe, is investigated in Section 5.2. Its temperature-measurement capability is validated before conducting an extensive parameter study, which is consecutively presented and analyzed. Finally, Section 5.3 investigates two phenomena that impact the heat transfer of any probe in the borehole-mimicking test rig: precipitation of solid particles and bubble formation on the probe's surface.

5.1 Experimental investigation of Probe V3

Probe V3, introduced in Figure 3.12, is a thin, helically shaped metal capillary with two optical fibers inside. Its manufacturing process is outlined in Appendix A.1. Similar to the prior probes, the Probe V3 design retains the helical shape. Furthermore, it combines 2.5 m of heated fiber length, which is five times the spatial resolution of the *AP Sensing N4386B* DTS device used, with a slim design that influences the flow less than the prior probe designs.

Appendix C introduces the fiber-optic setup for the experiments with Probe V3, and Appendix C.3 demonstrates the temperature measurement uncertainty in the validation bath with calibrated DTS data. The spatio-temporally averaged temperature measurement uncertainty of the DTS in the validation bath sections is a constant offset of either 0.1 or 0.2 °C. The fact that the error is constant appears positive because calibration will eliminate it for sufficiently long averaged data.

Subsection 5.1.1 reveals the problem of determining the helix temperature: Due to an overshoot phenomenon that occurs at steep temperature gradients in the DTS measurements of the *AP Sensing N4386B* DTS, no clear temperature plateau occurs in the DTS trace at the location of Probe V3. After discussing this behavior, an approach is introduced to extract a temperature measurement from the overshoot-influenced Probe V3 section in the DTS data. However, the reliability of this helix temperature remains questionable. Afterward, Subsection 5.1.2 describes the parameter space and experimental procedure of the investigation in the borehole-mimicking test rig. The results of this investigation are presented in Subsection 5.1.3.

5.1.1 Determination of helix temperature

The measured temperature signal of the 2.5 m-long fiber section inside Probe V3 is influenced by the above-outlined overshoot phenomenon. To analyze this phenomenon, Figure 5.1 displays the temperatures measured with the fiber section in the 50 °C calibration bath. The graphs display the single-ended and double-ended temperature signals that have been calibrated as outlined in Subsection 2.3.3. Overshoots on the order of 2 °C appear in the measured temperature trace of the fiber, which is immersed in a monitored water bath at constant temperature. Figures C.2 to C.7 show that these overshoots occur consistently along the entire fiber length.

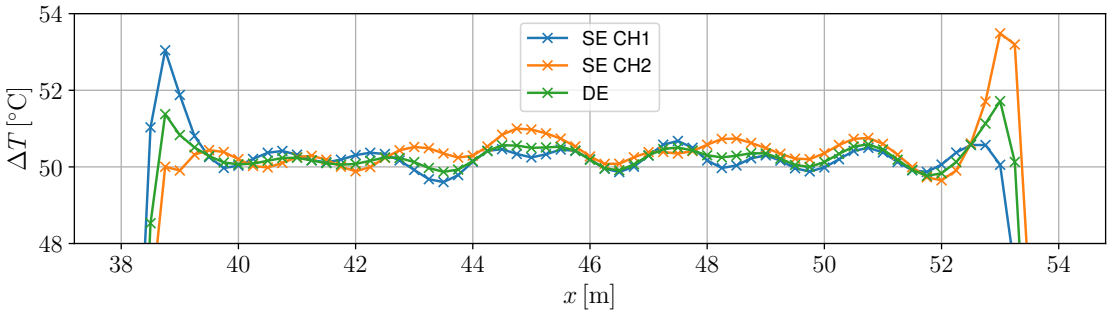

Figure 5.1: Visualization of an overshoot phenomenon that occurs at steep temperature gradients measured with the *AP Sensing* DTS. For the single-ended (SE) signals, the signal overshoots in measurement direction. Consequently, for channel 1, the overshoot occurs on the left side of the heated section because the laser pulse is emitted at $x = 0$ m into the fiber. In contrast, channel 2 emits a laser pulse from $x = x_{\max}$ into the fiber, and the overshoot occurs on the right side of the section. The double-ended (DE) signal, which is a combination of both single-ended signals, shows smaller overshoots at both ends of the hot-bath section.

To analyze the origin of this overshoot behavior, Figure 5.2 presents the measured Stokes and anti-Stokes intensities that were processed to obtain the temperatures shown in Figure 5.1. These unprocessed signals demonstrate that the overshoot phenomenon is not a result of the subsequent processing of the signals into temperature data. Personal contact with *AP Sensing* led to the hypothesis that this phenomenon is attributed to the pulse compression coding used for data acquisition in the *AP Sensing N4386B* DTS device (see, for example, Section "3.3.3.4 Pulse compression coding" in Hartog [30]). In the long calibration sections, the impact of the overshoot is not critical because the first and last two meters of the section are simply ignored. However, in the 2.5 m-long fiber section of Probe V3, this overshoot phenomenon leads to difficulties in determining the actual fiber temperature.

Figure 5.3 displays the temperature measured in the sections of the two fibers inside Probe V3 with the single-ended and double-ended signals. The displayed data were acquired in the borehole-mimicking test rig at two heating power levels and a constant flow rate. It seems that the temperatures measured in the helix sections are strongly influenced by the overshoot phenomenon. It is

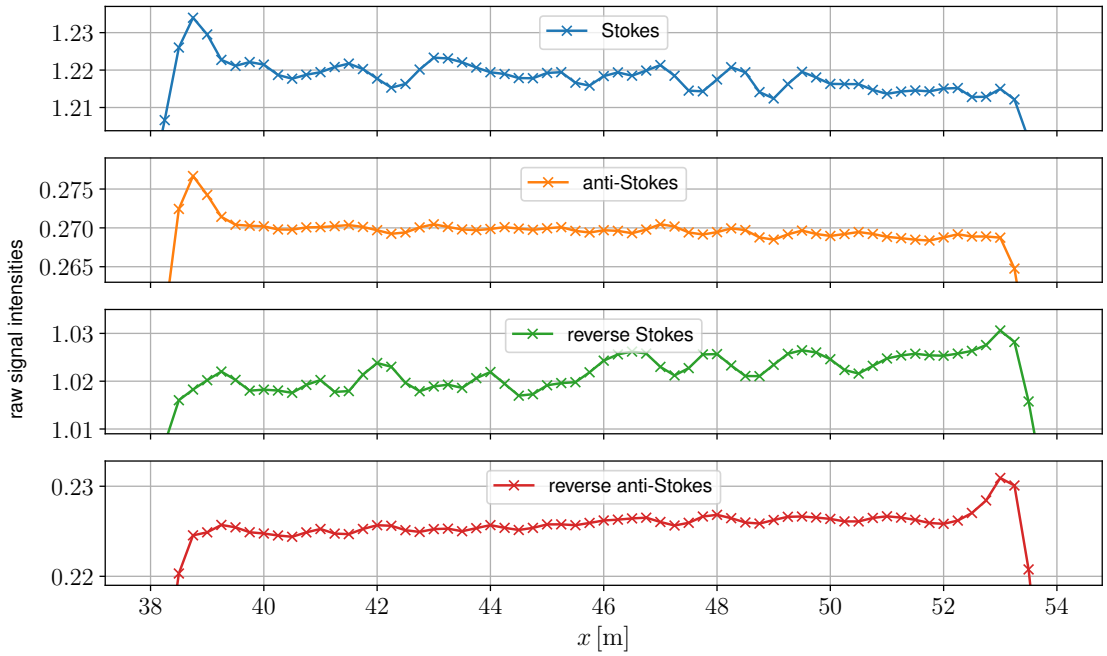

Figure 5.2: Visualization of the raw data from the temperature traces displayed in Figure 5.1. The Stokes and anti-Stokes signals are measured by channel 1, and the reverse signals are measured by channel 2. The overshoot is already present in the raw data.

hoped that the three coordinates in the center of each section provide a reasonable estimation of the fiber temperature inside the helix. Spatio-temporal averages of these points from the double-ended measurement are used to determine both the fiber temperature T_1 and the ambient temperature T_∞ for the measurements detailed below in Subsection 5.1.2.

The overshoot behavior of the single-ended data from the hot bath in Figure 5.1 is not consistent with the single-ended data from the helix section in Figure 5.3. Throughout all constant-temperature baths, the overshoot occurs only on the left side of the constant-temperature section in single-ended data acquired with channel 1. However, in the helix section, it occurs on both sides. This behavior remained inconclusive until the probe was tested with the *Silixa* DTS.

Figure 5.4 displays temperature measurements along the fiber inside Probe V3 with the *Silixa* DTS. The displayed data originate from a heating test in calm air (left plot) and from a measurement in the borehole-mimicking test rig at 5 l/min. The figure shows that the *Silixa* DTS is able to resolve the heated section without exhibiting overshoot phenomena. The temperature profile that evolves when Probe V3 is heated inside a vertical upward water flow is linked to the helix geometry. As elaborated in the caption of Figure 5.4, the Probe V3 section is coldest near its center and hottest at its ends because the heat transfer efficiency varies significantly throughout the sections of Probe V3. Another argument supporting the realization that the heat transfer efficiency varies along the helix length is that the profile shown in the right graph scales with flow velocity: at the depicted flow rate of 5 l/min, the temperature drop along helix section ② is $\approx 1\,^\circ$C, and at a flow rate of 50 l/min, where the heat transfer everywhere at the helix surface is more efficient, the temperature drop is $\approx 0.2\,^\circ$C.

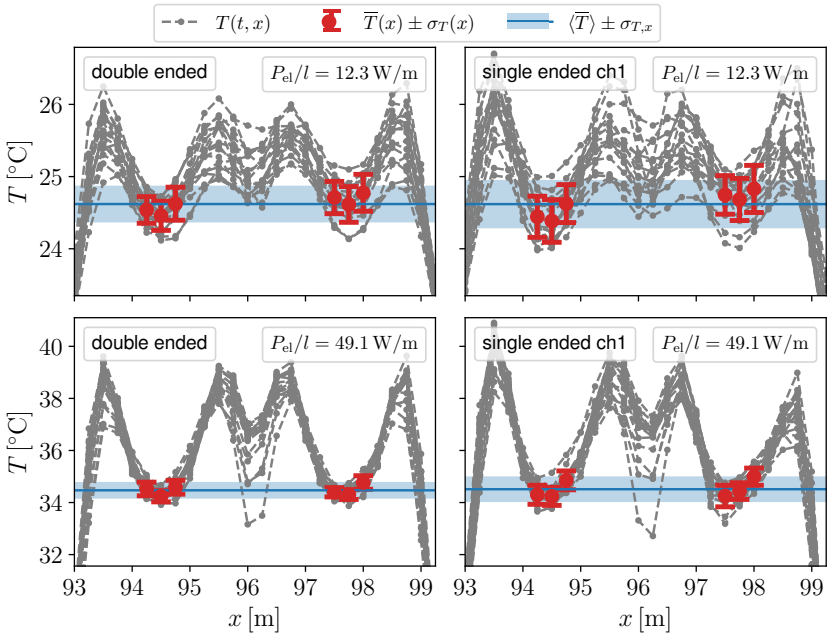

Figure 5.3: Determination of the Probe V3 temperature with the *AP Sensing* DTS. The displayed data originate from measurements in the borehole-mimicking test rig with a volumetric flow rate set to 5 l/min at two heating power levels that result from constant-current heating at 5 A and 10 A. The same data are processed with the double-ended and single-ended calibration algorithms. The gray dashed lines indicate the $T(t,x)$ measurements acquired over 18 min along the helix section. At approximately $x = 96$ m, a splice connects the two fibers from the helix. Thus, the helix section occurs twice in each graph, to the left and right from the splice. At the selected coordinates, which are located at the center of each helix section, red markers with error bars indicate temporal averages $\overline{T}(x)$ and their standard deviations $\sigma_T(x)$. The blue line and blue-shaded rectangle show the spatio-temporal average $\langle\overline{T}\rangle$ with its standard deviation $\sigma_{T,x}$ of all data points from the selected coordinates. The spatio-temporal average represents the measured value of T_1 in the fiber.

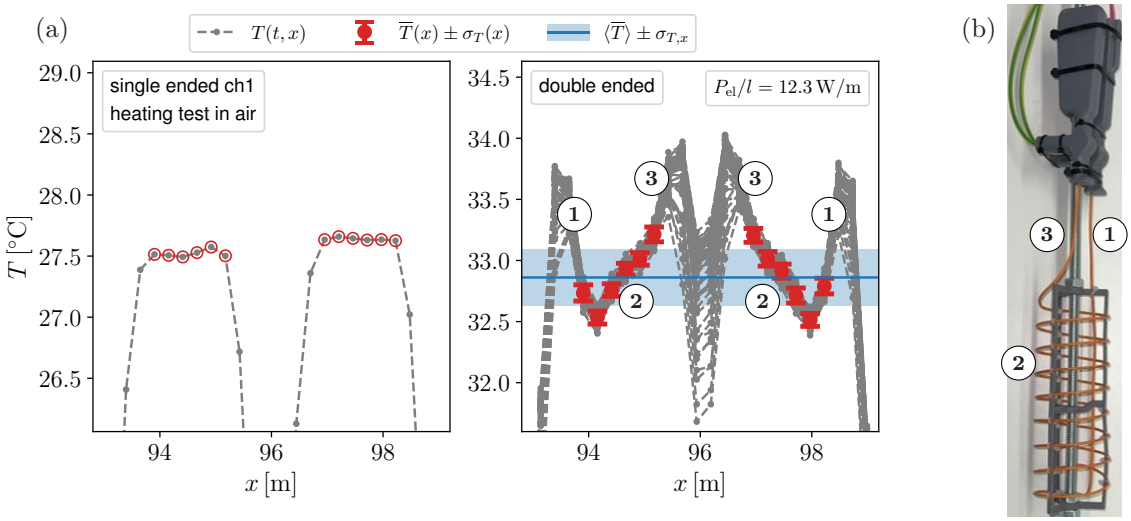

Figure 5.4: Determination of the Probe V3 temperature with the *Silixa* DTS. In the left graph of (a), a heating test in calm air demonstrates that no overshoot phenomenon occurs in the temperature trace along the Probe V3 fiber section and that six coordinates at nearly constant temperature are identified in each Probe V3 fiber section. The right graph of (a) shows a measurement in the borehole-mimicking test rig at 5 l/min and 5 A. The measured data demonstrate a profile of non-constant temperature, somewhat similar to Figure 5.3. However, both profiles here are very symmetric and can be linked to the helix geometry displayed in (b). ① and ③ are straight sections between the helix and the connector bodies. In these sections, the heat transfer depends on the boundary-layer buildup and becomes less efficient with increasing section length. Furthermore, both section ends contain 40 mm of heated capillary that is well insulated inside the connector bodies. Section ② represents the actual helix section. The measurement shows that the heat transfer is most efficient at the first helix revolution and becomes gradually less efficient along its length. Similar to what is described in Figure 5.3, the spatio-temporal average $\langle\overline{T}\rangle$ represents the fiber temperature T_1.

5.1.2 Parameter space and experimental procedure

The parameter study comprises 8 datasets, obtained using the borehole-mimicking test rig introduced in Subsection 3.2.1. Each dataset maintains a constant heating current and contains multiple measurement points at varying volume flow rates, each held constant for 20 min. Between each set of two successive heated measurement points, the heating is turned off for 20 min.

Steady state is obtained within one minute of heating because the capillary used in Probe V3 is very thin. Accordingly, 18 min of each period are considered steady state and are used to determine T_1 with the spatio-temporal average $\langle\overline{T}\rangle_{\text{heated}} \equiv T_1$. The ambient temperature is determined by the spatio-temporal average $\langle\overline{T}\rangle_{\text{not heated}} \equiv T_\infty$ over two unheated 9 min-long durations, one before and one after the heating period.

The considered parameter space of set volume flow rates $\dot{V}$ and heating currents I is given in Table 5.1. The heating power per unit length P/l is computed from the set constant-current values with an electrical resistance of 1.184 Ω (compare Appendix A.1) and a heated capillary length of 2.54 m. The bulk flow velocity is computed using equation (3.9) with the area A_b blocked by the threaded rod that amounts to $A_\text{b} = \pi/4 \cdot 12\,\text{mm}$.

Of the 8 acquired datasets, 5 were obtained with the *AP Sensing* DTS at constant-current values of 5 A and 10 A in tap water. One year later, 3 more datasets were acquired with the *Silixa* DTS at constant-current values of 2.5 A, 5 A, and 7.5 A. For these later measurements, the test rig was filled with deionized water, additional sieves and flow straighteners were mounted, and the most sophisticated bypass-valve configuration shown in Figure 3.2.1 was used.

5.1.3 Results

The measured datasets are presented in Figure 5.5 as $\Delta T_{1,\infty}$ diagrams, sorted into subplots by heating current. All datasets, except the very first one, exhibit the expected hyperbolic curve shape predicted by Figure 3.3. However, significant offsets between measurements occur, which are much larger than the acceptable uncertainty range, which is estimated to be $\approx 0.1\,°\text{C}$ in Subsection 3.1.2. Again, the question arises as to whether these offsets originate in the heat transfer, the DTS measurement, or in both. As the DTS measurement is now calibrated and consistently performs well in the long validation section (compare Appendix C), one may assume that such large offsets do not originate from it. However, in the *AP Sensing* data, the overshoot phenomenon remains a device-specific black box that influences the entire fiber length of Probe V3.

As a concluding remark it has to be stated that based on the experiments with the *AP Sensing* DTS, the probe design seemed to have failed in its intention to provide sufficient fiber length for a reliable DTS measurement. At this time, it could not be ruled out that the DTS measurement

Table 5.1: Parameter space of the experiments with Probe V3 in the borehole-mimicking test rig. The controlled variables – heating current and volume flow rate – are given together with their corresponding conversions to heating power per unit length and bulk flow velocity.

Set current and corresponding heating power per length												
I	[A]	2.5	5	7.5	10							
P_el/l	[W/m]	3.1	12.3	27.6	49.1							
Set volume flow rate and estimated bulk flow velocity												
$\dot{V}$	[l/min]	0	1.25	2.5	3.75	5	7.5	10	15	20	30	40	50
u	[mm/s]	0	1.2	2.4	3.6	4.7	7.1	9.5	14.2	19.0	28.5	38.0	47.5

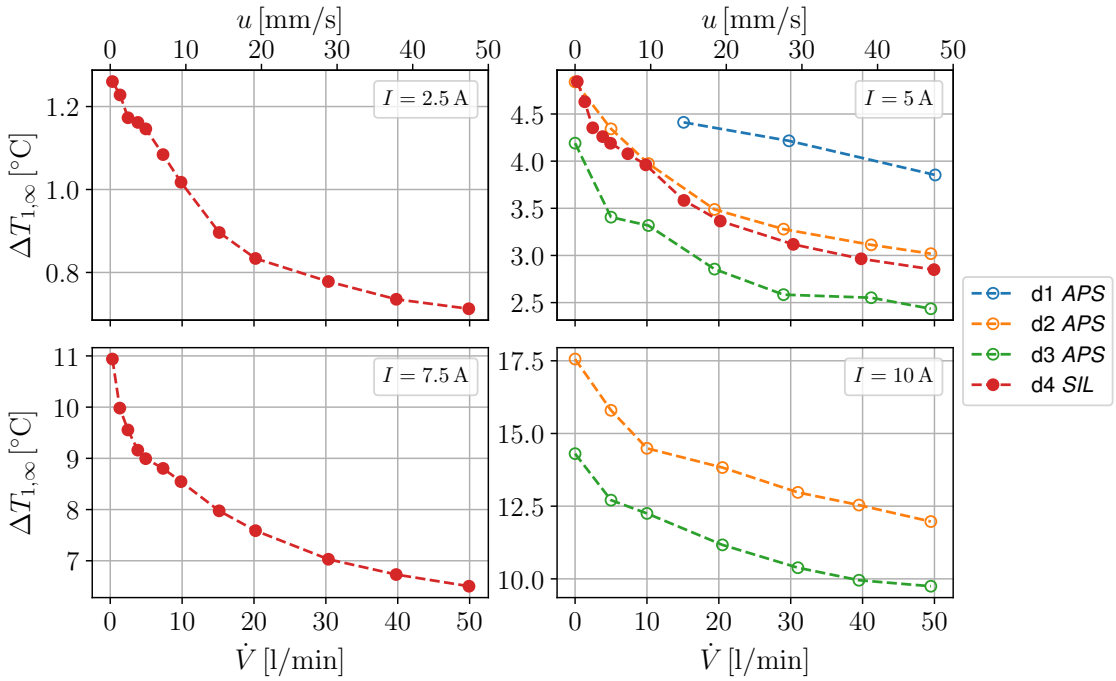

Figure 5.5: Results of the investigation of Probe V3 in the borehole-mimicking test rig displayed in $\Delta T_{1,\infty}$–$\dot{V}$ plots. Eight datasets are displayed in four subplots sorted by heating current. 'd1 *APS*' refers to measurements on day 1 with the *AP Sensing* DTS. '*SIL*' refers to the *Silixa* DTS.

was the cause for the offsets. Thus, the next design, Probe V4, was developed with the focus to contain even more fiber length. However, considering the findings with Probe V4 presented below, the offsets observed here are primarily linked to the heat transfer, as it is likely that unmodeled phenomena such as lime precipitation from the tap water and bubble formation of dissolved gases occurred during these measurements. Both phenomena are discussed with respect to the Probe V4 results in Section 5.3.

5.2 Experimental investigation of Probe V4

The double-ring probe, Probe V4, which is introduced in Figure 3.13, is made of two capillary rings that each contain 9 m of fiber. This fiber length significantly exceeds the influence length of the overshoot phenomenon observed in the *AP Sensing* DTS data to ensure an unambiguous and reliable DTS temperature measurement for each ring. In spite of the large fiber length contained in the rings, Probe V4 remains fairly slim, so that only a minor influence on the flow is expected.

The full fiber setup, which also comprises the calibration and validation baths, is presented in Figure 3.8. All DTS data presented in the following are calibrated using the double-ended algorithm (see Subsection 2.3.3) with the hot-bath and cold-bath sections. A comparison of uncalibrated and calibrated data is shown in Appendix C.1 with Figures C.2 and C.6 for the *AP Sensing* DTS device and with Figures C.8 and C.9 for the *Silixa* DTS device.

Below, the processing of the measured data is explained in Subsection 5.2.1, and a validation experiment that estimates the uncertainty of the Ring 1 temperature measurement is described in Subsection 5.2.2. Subsequently, the parameter space of the investigation in the borehole-mimicking

test rig is introduced in Subsection 5.2.3, and the results are presented in Subsection 5.2.4. Furthermore, a scaling analysis and a calibration test are performed with the results in Subsections 5.2.5 and 5.2.6.

5.2.1 Data processing

"The acquired data comprises temperature measurements by the DTS and PT1000 sensors as well as volume flow rate measurements. The latter two are logged at a rate of 2 Hz with their respective measurement devices, whereas the DTS settings are more complicated. To perform the double-ended (DE) calibration, Stokes and anti-Stokes backscatter intensities are required from both channels. The *AP Sensing* device is configured to log the measured data every 60 seconds for each channel. For each log file, the device alternately measures each channel three times for 10 seconds and averages the data internally. The *Silixa* device provides a higher signal-to-noise ratio and offers much shorter averaging intervals of ≥ 5 s. Its data is logged every 20 seconds, with each log containing consecutive 10-second measurement intervals for each channel. Both DTS devices sample the fiber temperature every 0.25 m, and they both have a spatial resolution of 0.5 m according to their datasheets.

To process and calibrate the data, all log files are imported into a single data structure and synchronized using their timestamps. The 2 Hz data are averaged to match the sampling rate of the respective DTS device. The calibration of the Stokes and anti-Stokes intensities measured by the DTS is performed using the DE algorithm and the code published by Des Tombe et al. [23]. As a temperature reference, the calibration algorithm uses the PT1000 temperature data and both fiber passages through the cold and hot bath sections.

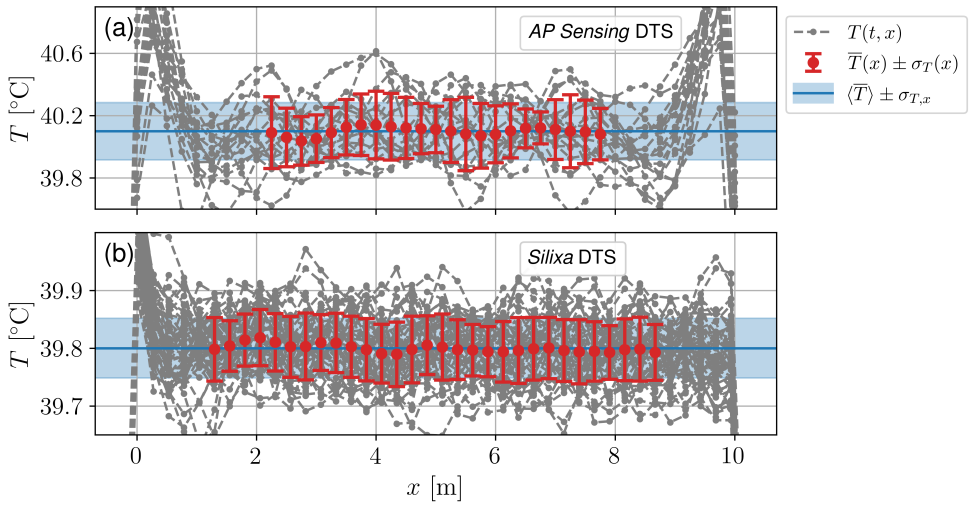

Figure 5.6: "Ring 1 temperature data points $T(t, x)$ acquired over a 20-minute interval are plotted together with the temporal average $\overline{T}(x)$, spatio-temporal average $\langle\overline{T}\rangle$, and respective standard deviations. Subplot (a) shows measurements from the *AP Sensing* DTS, and subplot (b) from the *Silixa* DTS. Note the different ordinate scales." [RTK25] (Figure reprinted from [RTK25])

To illustrate the averaging process of the calibrated DTS data and compare the two DTS devices, Figure 5.6 shows the temperature distribution along Ring 1 over a 20-minute period for both devices. The plots display the measured temperatures $T(t, x)$, the temporal averages $\overline{T}(x)$ per local coordinate with standard deviations $\sigma_T(x)$, and a section (spatio-temporal) average $\langle\overline{T}\rangle$ with its corresponding standard deviation $\sigma_{T,x}$. The data from the *AP Sensing* device, shown in

Figure 5.6 (a), reveal an overshoot phenomenon at both ends of the ring section, with an unaffected region between the overshoots. This overshoot behavior was observed in previous measurements [see Subsection 5.1.1] and is the main reason why fiber length inside the ring is highly prioritized in the probe design. The *Silixa* data are shown in Figure 5.6 (b) with a much finer ordinate resolution and do not exhibit this overshoot phenomenon. On the left side of the ring section, a small overshoot is visible, caused by a sharp bend of the fiber at the ring's entry. All other temperature transitions along the fiber are resolved without overshoot, as seen on the right side of the ring section [and in the water-bath sections in Figures C.8 and C.9].

The extracted temperature value for a constant temperature section, such as the ring and water bath regions, is an average over several meters of fiber in the respective section. Each constant temperature section is defined with a gap distance to it's rising or falling edges. For the *AP Sensing* device, a large gap of 2 m is chosen because the overshoot data exhibit a large positive bias in the first meter and a slight negative bias in the second meter. For the *Silixa* data, a 1 m gap is chosen conservatively to avoid any edge effects.

Eventually, the resulting spatio-temporal averages of the ring sections are used to determine the temperature differences. In the case of the heated Ring 1, the spatio-temporal average delivers the ring's core temperature $\langle \overline{T} \rangle_{\mathrm{Ring\,1}} \equiv T_1$, and in the case of the unheated Ring 2, the environment temperature is measured as $\langle \overline{T} \rangle_{\mathrm{Ring\,2}} \equiv T_\infty$. The temperature difference relevant for convective heat transfer $\Delta T_{3,\infty}$ is then calculated by subtracting $\Delta T_{1,3}$, cp. equations (3.2) and (3.3)." [RTK25][1]

5.2.2 Validation of temperature measurement

"To estimate the uncertainty of the temperature measurement with the double-ring probe, a validation experiment is performed with Ring 1, which measures T_1 when heated. For this test, the validation bath provides a controllable, constant-temperature environment. Its torus containing a duplex cable coil is removed, and Ring 1, equipped with a PT1000 temperature sensor at its center, is placed next to the heater.

Eight measurement points (MPs) are acquired by maintaining four temperature levels for 30 minutes each: MP 1 at unheated ambient temperature, MP 2 at 25 °C, MP 3 at 30 °C, and MP 4 at 40 °C. Afterwards, the process is repeated resulting in MP 5-8. Throughout the experiment, the hot and cold calibration baths remain in operation, and both DTS and PT1000 data are logged as previously described. A steady-state 20-minute-long interval is then identified and considered for each MP.

Residuals are calculated by subtracting the PT1000 reference temperature T_{ref} from the DTS-measured Ring 1 temperature. Figures 5.7 (a) and (c) display the time-averaged residuals measured along the fiber coordinate within Ring 1 for MP 2 and 6, respectively for each DTS device. An overview of spatio-temporal residuals for all MPs is shown in Figure 5.7 (b) and (d). With the *AP Sensing* DTS, the averaged residuals range from 0.2 to 0.3 °C. Compared to the expected residual based on the PT1000 measurement error, which is a mostly constant bias within a limiting deviation of $0.1\,^{\circ}\mathrm{C} + 0,0017\,|T|$, the Ring 1 residuals are two to three times higher. In contrast, the residuals measured with the *Silixa* DTS remain within the PT1000 deviation limits. Based on these results, the uncertainty of the temperature measurement with Ring 1 is deduced to be within ±0.1 °C for the Silixa DTS and within ±0.3 °C for the AP Sensing DTS.

[1] References in the cited text have been updated to refer to the corresponding content within this document.

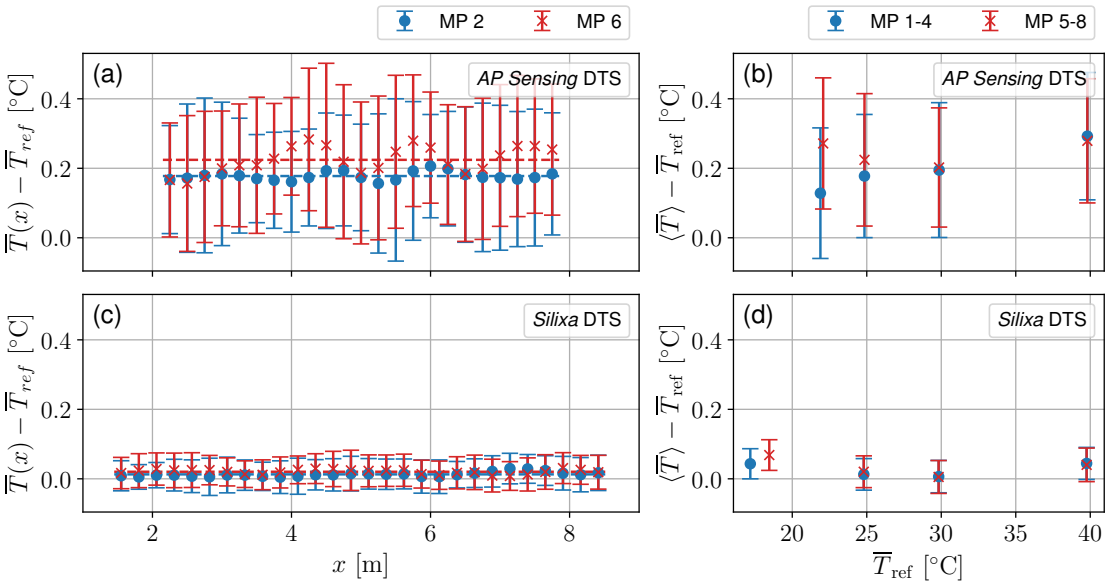

Figure 5.7: "The residuals of the Ring 1 validation experiment are shown for both DTS devices. In (a) and (c), the time-averaged residuals with their standard deviations are plotted along the fiber coordinate for MP 2 and MP 6 (both at 25 °C), cp. Figure 5.6. The spatio-temporally-averaged residuals for all MPs are shown in (b) and (d)." [RTK25] (Figure reprinted from [RTK25])

This experiment allows for estimating the uncertainty in the absolute temperature measurement with Ring 1. However, the quantity of interest for velocity estimation is the temperature difference relative to the ambient water temperature measured by Ring 2. To verify whether both rings measure the same temperature using the *Silixa* DTS, the probe is inserted into the test rig, and the volume flow rate is increased stepwise without heating either ring. In this configuration, both rings should measure identical temperatures, which indeed resulted in very similar temperatures between Ring 1 and Ring 2, i.e., a constant offset of only 0.04 °C." [RTK25][2]

5.2.3 Parameter space and experimental procedure

"The parameter study comprises 161 datasets, obtained using the test rig shown in Figure 3.6. Each dataset maintains a constant heating current and contains multiple MPs with increasing or decreasing volume flow rates, each held constant for 30 minutes. The final 20 minutes of each period are considered steady state and are averaged to determine $\Delta T_{1,\infty}$ at the respective volume flow rate. Subsequently, $\Delta T_{3,\infty}$ is obtained by subtracting $\Delta T_{1,3}$, cp. equations (3.2) and (3.3).

The considered parameter space of set volume flow rates $\dot{V}$ and heating currents I is provided in Table 5.2. The heating power $P_e l$ and flow velocity u presented in the table are estimated based on the assumptions of a constant electrical resistance of 48 mΩ and a constant bulk flow velocity, respectively. Table 5.3 displays further essential distinctions between acquired datasets, namely the applied DTS device and the water type inside the test rig alongside the resulting number of datasets per parameter combination. Initially, the test rig was filled with tap water, and temperature data from the glass fibers were acquired using the *AP Sensing* DTS. The temperature data acquisition was then switched to the *Silixa* DTS. Following this, the test rig was drained, thoroughly cleaned of lime residues deposited by the tap water, and refilled with deionized water. Subsequently, the remaining datasets were acquired, first with the *Silixa* DTS and then with the *AP Sensing* DTS.

[2] References in the cited text have been updated to refer to the corresponding content within this document.

Table 5.2: "Parameter space of the controlled variables – heating current and volume flow rate – and their corresponding conversions to heating power per unit length and bulk flow velocity." [RTK25] (Table reprinted from [RTK25])

Set current and corresponding heating power per length													
I	[A]	3.5	5	6	7.5	10	15.5						
P_{el}/l	[W/m]	2.6	5.2	7.5	11.7	20.8	50.0						
Set volume flow rate and estimated bulk flow velocity													
$\dot{V}$	[l/min]	0	1.25	2.5	3.75	5	7.5	10	15	20	30	40	50
u	[mm/s]	0	1.2	2.4	3.6	4.7	7.1	9.5	14.2	19.0	28.5	38.0	47.5

Table 5.3: "Number of acquired datasets, categorized by DTS device and water type in the test rig." [RTK25] (Table reprinted from [RTK25])

	AP Sensing	*Silixa*
tap water	47	67
deionized water	13	34

In retrospect, the combination of deionized water and the *Silixa* DTS delivers the most repeatable results, which are represented by the red curves in Figure 5.8. The datasets available for this combination focus on heating currents of 5, 7.5, and 15.5 A, resulting in 11, 8, and 8 datasets, respectively. For the other heating currents, only very few datasets exist. A detailed dataset register can be accessed together with the data" [RTK25][3] as outlined in the data availability statement in Appendix E.

5.2.4 Results

"All measured datasets are presented in Figure 5.8 as $\Delta T_{3,\infty}$–$\dot{V}$ diagrams, sorted into subplots by heating current. Additionally, Ri isolines highlight that free convection is expected to influence the measurements at low flow velocities. Scaled to their respective temperature ranges, all curves exhibit a similar shape, with $\Delta T_{3,\infty}$ being highly sensitive to $\dot{V}$ at lower velocities and less sensitive at higher velocities. Offsets occur between datasets repeated at the same heating current, leading to potentially significant measurement errors when estimating fluxes from the measured temperature difference. Yet, for the data acquired in deionized water, the offsets appear to be very small.

As the applied tap water is very hard (18.7 °dH, yearly average in 2024 [65]), the offsets appear to be linked to lime deposition in the test rig, particularly when deposits form on the probe's surface and lime particles accumulate at the sieves, causing blockages. Datasets with blocked sieves are strong outliers, showing elevated $\Delta T_{3,\infty}$ values (see Figure 5.8 (f)). During the datasets obtained in tap water, the tank was drained, cleaned, and refilled multiple times. The blockage of the sieves by crystallized lime may cause an inhomogeneous velocity profile in the test section and thus change the local velocity at the probe's surface, which disturbs the forced convection heat transfer. This sieve-blockage hypothesis, however, does not explain the offset at zero and near zero velocities. Another hypothesis is that, coinciding with sieve blockages, lime deposits and gas bubble formation on the probe surface influence the measurements and lead to the observed offsets between the curves. Both are known to affect heat transfer in hot-film measurements [34].

As clearly depicted in Figure 5.8, the datasets acquired in deionized water outperform the others in terms of reproducibility. Particularly, datasets acquired consecutively with the same heating

[3] References in the cited text have been updated to refer to the corresponding content within this document.

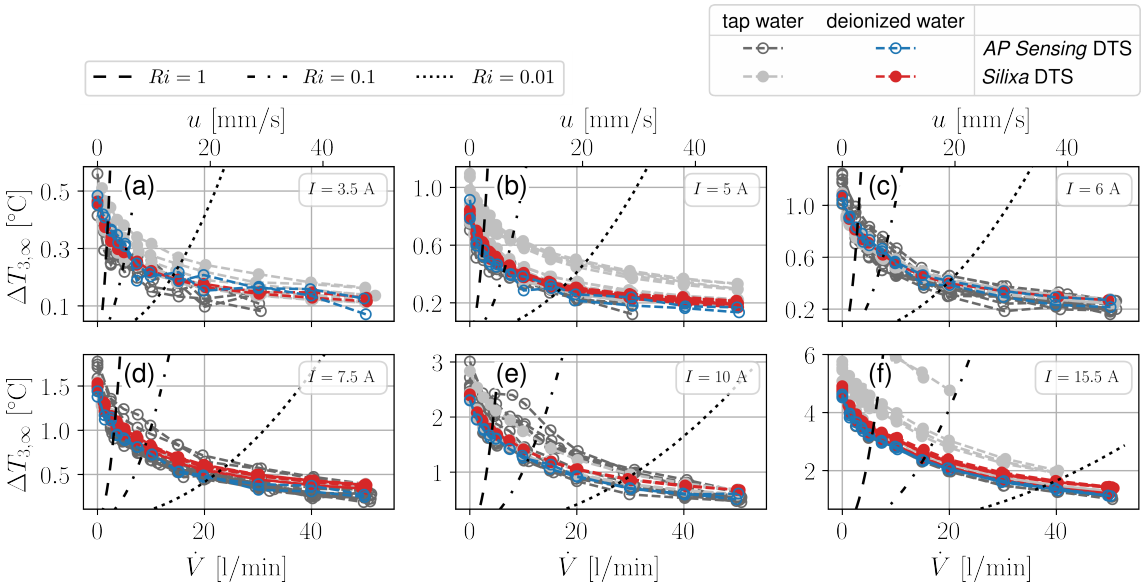

Figure 5.8: "All resulting datasets are plotted in $\Delta T_{3,\infty}$–$\dot{V}$ diagrams, sorted into subplots by heating current. Accordingly, the measured temperature differences vary significantly in magnitude between subplots, yet their overall shapes remain similar. The gray data points represent measurements in tap water, whereas the red and blue datasets were acquired in deionized water, which significantly improves repeatability. The Ri lines are drawn to indicate that free convection is expected to influence the measurements, especially in the lower velocity range." [RTK25] (Figure reprinted from [RTK25])

power align precisely. However, when repeated after several days, noticeable offsets occur, implying a bias error that depends on changing environmental conditions. It is furthermore important to note that the utilized deionized water was not deaerated, such that dissolved air in the water may have formed bubbles on the probe's surface. As such, the heat transfer might have been affected accordingly, thus leading to the observed errors (see Subsection 5.3.2 for a more detailed explanation).

When analyzing the datasets acquired with the *Silixa* DTS in deionized water at heating currents 5, 7.5 and 15.5 A, an order depending on the test rigs water temperature, and thus the Prandtl number is revealed. As the test rig is not actively cooled, heat dissipation at the heated probe and the pump causes the water temperature in the test rig to vary between 22 and 32 °C, which results in a variation in Pr of up to 22 %. In empirical correlations, the environment temperature effect on forced convection is comprised in the Pr dependence of Nu. $\Delta T_{3,\infty}$ is inversely proportional to Nu, which in turn scales with Pr to the power of n

$$\frac{1}{\Delta T_{3,\infty}} \propto Nu \propto Pr^n. \tag{5.1}$$

Depending on the applied empirical correlation, n is in the range of 1/3 (e.g. Gnielinski [28] for low $Re < 1000$) to 1/2 (e.g. King [35]). An attempt to diminish the observed offsets between the datasets by scaling the measured temperatures $\Delta T_{3,\infty}$ with Pr^n is outlined in Subsection 5.2.5, and Subsection 5.2.6 provides an analysis of this scaling approach.

The measured datasets are non-dimensionalized by calculating Nu_l and Re_l using Equations (2.53), and (2.56). Ideally, in forced convection problems, all datasets should collapse onto a single line in the Nu–Re diagram. If this were the case, calibration of the probe would only be required at a single heating power, yet remain valid across all heating powers. The Nu–Re plot in Figure 5.9 reveals deviations of our findings from this ideal behavior. The curves are mostly sorted by heating power in ascending order, with higher heating power resulting in higher Nusselt numbers, which

is investigated in the following Subsection 5.2.5. In terms of shape, the correlations slope deviates from the measurements at lower Reynolds numbers, because the correlation does not account for free convection phenomena. This behavior aligns with the criterion that forced convection dominates at low Richardson numbers. For all datasets, $Ri < 0.1$ holds for $Re \geq 125$, where the correlations shape is more similar to that of the measured datasets.

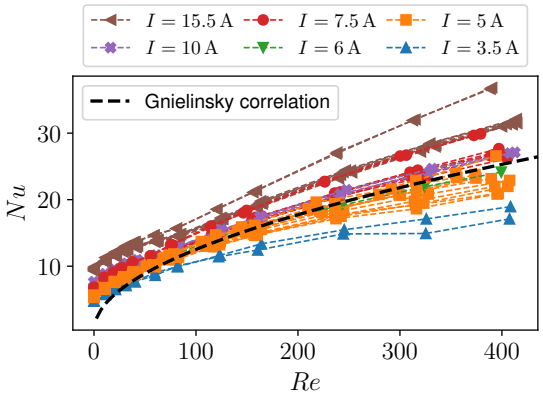

Figure 5.9: "Non-dimensionalized data, acquired in deionized water with the *Silixa* DTS, are displayed in a Nusselt–Reynolds number plot. The datasets do not collapse onto a single line; instead, they appear sorted by heating power." [RTK25] (Figure reprinted from [RTK25])

Recall from Subsection 3.1.1 that the insulation's thermal conductivity k_i is necessary for the calculation of $\Delta T_{2,3}$ with equation (3.3), and that k_i must be estimated in retrospect with the results. Therefore, a literature reference for forced convection heat transfer, i.e. the empirical correlation by Gnielinski, is displayed in Figure 5.9. To estimate k_i, the alignment of the data with the Gnielinski correlation is tested for multiple values of k_i, which results in vertical shifts of the scattered datasets relative to the correlation. By positioning the Gnielinski correlation approximately in the center of the datasets, as shown in Figure 5.9, k_i is estimated to 0.28 W/(m·K)." [RTK25][4]

5.2.5 Scaling analysis

"In the preceding paragraphs, two interrelationships were identified for the datasets acquired in deionized water with the *Silixa* DTS.

1. Within the $\Delta T_{3,\infty}$–$\dot{V}$ graphs, a scaling based on the fluid temperature T_∞ and thus Pr is observed.
2. When all datasets are plotted in the Nu–Re diagram, they appear to scale with the heating power.

To analyze the observed trends more quantitatively in terms of scaling laws,

$$\Delta T_{3,\infty} \; Pr^n \tag{5.2}$$

and

$$Nu \left(\frac{P_\mathrm{el}}{l} \right)^m \tag{5.3}$$

[4] References in the cited text have been updated to refer to the corresponding content within this document.

are evaluated for various exponents n and m, and a criterion is defined to determine the exponents that best collapse the datasets. Particularly, the standard deviation divided by the mean

$$\zeta_T(n) = \frac{\sigma(\Delta T_{3,\infty} Pr^n)}{\mu(\Delta T_{3,\infty} Pr^n)}; \quad \zeta_{Nu}(m) = \frac{\sigma\left(Nu\left(\frac{P_{\mathrm{el}}}{l}\right)^m\right)}{\mu\left(Nu\left(\frac{P_{\mathrm{el}}}{l}\right)^m\right)} \tag{5.4}$$

is used normalized with the base case ($n = 0$ and $m = 0$)

$$\xi_T(n) = \frac{\zeta_T(0) - \zeta_T(n)}{\zeta_T(0)}; \quad \xi_{Nu}(m) = \frac{\zeta_{Nu}(0) - \zeta_{Nu}(m)}{\zeta_{Nu}(0)} \tag{5.5}$$

as criterion to judge the best exponent. According to this definition, $\xi \leq 1$ and increases from zero to one if the scaling approach reduces spreading. The limiting case $\xi = 1$ corresponds to complete elimination of spreading, while $\xi < 0$ indicates increased spreading.

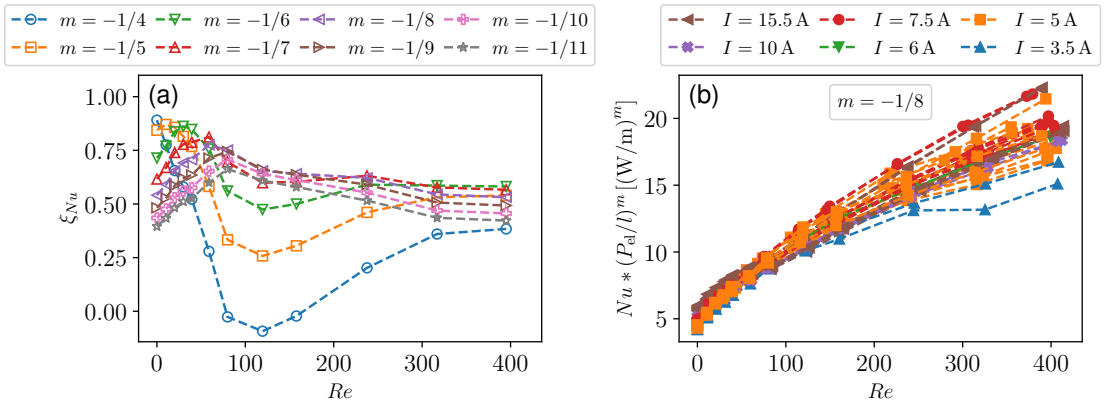

Figure 5.10: "Analysis of the Nu data to remaining influences of the heating power by multiplication with $(P_{\mathrm{el}}/l)^m$. In (a) the scaling criterion ξ_{Nu} – evaluated for various m – is plotted over Re to identify the best exponent. The scaling improvement depends significantly on Re, thus a single best scaling exponent cannot be identified. In (b) the scaled results are displayed for the exponent $m = -1/8$, which performs well over a wide Re range." [RTK25] (Figure reprinted from [RTK25])

$\xi_{Nu}(m)$ is shown in Figure 5.10 (a) for a wide range of m. The convergence of the data improves by up to 85 % at $Re \leq 40$ and around 60 % in the higher Re range. Interestingly, different scaling exponents are optimal depending on the Reynolds number range. At low Re, exponents with greater absolute values perform best, whereas at high Re, exponents with smaller absolute values are more effective, indicating a link to the convection regimes. However, the exponent $m = -1/5$ performs best around $Re = 50$ and $Re = 400$ but poorly around $Re = 100$, contradicting the idea that the optimal scaling exponent depends solely on the convection regime. The scaled data are shown in Figure 5.10 (b) with $m = -1/8$, which performs well over a wide Re range. Compared to Figure 5.9, the variance of the curves is reduced; however, a complete collapse of the data cannot be achieved with any constant value of m, and the datasets remain sorted by heating power.

To evaluate the temperature dependent Pr scaling, $\xi_T(n)$ is displayed in Figure 5.11 for the 5, 7.5, and 15.5 A datasets. For the 5 A data, the scaling achieves only marginal improvements, whereas for the 7.5 and 15.5 A data, it improves convergence by more than 30 % over a wide range of flow rates. To assess the improvement, the following calibration test is additionally performed with the Pr-scaled data." [RTK25][5]

[5] References in the cited text have been updated to refer to the corresponding content within this document.

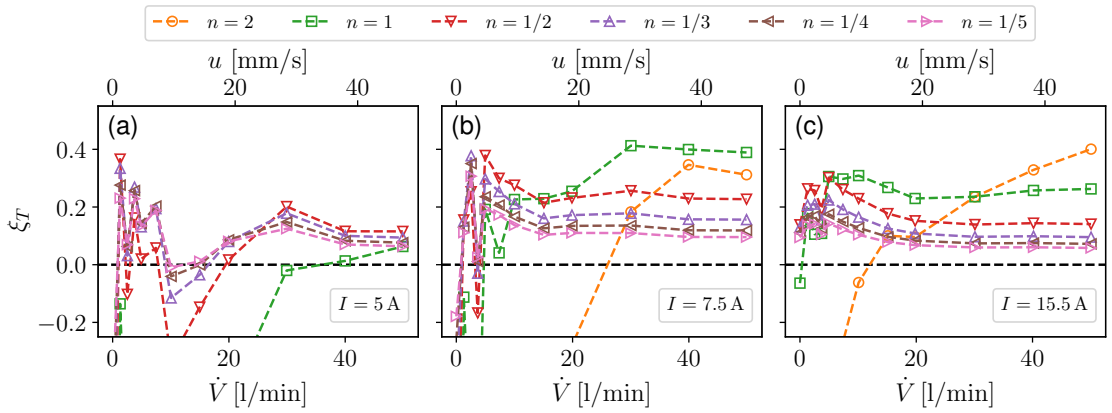

Figure 5.11: "Analysis of the influence of the T_∞-dependent Pr on the $\Delta T_{3,\infty}$ data. Therefore, $\Delta T_{3,\infty}$ is multiplied by Pr^n. Subplots (a), (b), and (c) show the ξ_T criterion for various scaling exponents n and heating currents of 5 A, 7.5 A, and 15.5 A, respectively." [RTK25] (Figure reprinted from [RTK25])

5.2.6 Calibration test

"Recall that one major goal of this research is to develop a flow sensor that – once calibrated – can quantitatively measure unidirectional volume flow rates or corresponding bulk-flow velocities. This concept is tested using the datasets acquired in deionized water at 5, 7.5, and 15.5 A. For each heating-current level, a calibration curve is generated by fitting the first dataset acquired in deionized water to the function

$$\dot{V}_{\mathrm{est}}(\Delta T_{3,\infty}) = \frac{a}{\Delta T_{3,\infty}^{b}} + c\ \Delta T_{3,\infty} + d, \tag{5.6}$$

which reproduces the hyperbolic relationship between flow rate and temperature difference. The constant coefficients a, b, c and d in Equation (5.6) are determined in the fitting process by the *optimize.curve_fit* function from *SciPy*. The resulting calibration functions are then used to estimate the volume flow rates $\dot{V}_{\mathrm{est}}$ for the remaining measurements conducted in deionized water. In Figure 5.12, the estimated volume flow rate $\dot{V}_{\mathrm{est}}$ is plotted alongside its relative estimation error

$$\mathrm{err}(\dot{V}_{\mathrm{est}}) = \frac{\left|\dot{V} - \dot{V}_{\mathrm{est}}\right|}{\dot{V}} \tag{5.7}$$

over the measured volume flow rate $\dot{V}$. The $\dot{V}_{\mathrm{est}}$–$\dot{V}$ diagrams (upper row in Figure 5.12) indicate small deviations from the ideal estimation (black dashed line), which correspond to the little observed offsets in Figure 5.8. However, once converted into relative deviations, these deviations translate into significant errors in flow rate measurements as emphasized by the $\mathrm{err}(\dot{V}_{\mathrm{est}})$–$\dot{V}$ diagrams (lower row in Figure 5.12). In datasets acquired with the *Silixa* DTS and volume flow rates of 7.5 l/min (7.1 mm/s) and higher, the relative error remains below 35 %. For measurement sets acquired immediately after the calibration set, the relative error remains below 15 % within the same range of flow rates.

As described in the previous section, offsets between the datasets may depend on Pr, which varies with the ambient temperature inside the water tank. The effect of scaling the measured temperature differences with Pr (cf. Equation 5.2) is analyzed by conducting the calibration test using the scaled data. The estimation errors for $n = 1/2$ and $n = 1$ are shown in Figure 5.13 together with the unscaled case (i.e. $n = 0$) for heating currents of 5, 7.5, and 15.5 A, respectively. The 5 A error data in Figures 5.13 (a–c) exhibit a rather unordered scatter of the error curves, and the estimation error increases noticeably in the $n = 1$ case. In contrast, the 7.5 and 15.5 A

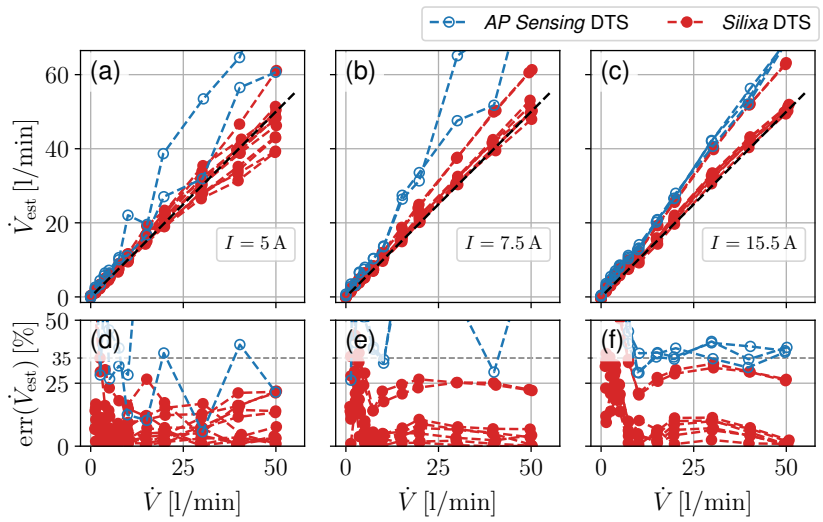

Figure 5.12: "Flow-rate estimations based on equation (5.6) and corresponding error estimations from equation (5.7) for datasets obtained in deionized water. The estimated volume flow rates are shown in subplots (a), (b), and (c) for data acquired at heating currents of 5, 7.5, and 15.5 A, respectively; the corresponding estimation errors are shown in subplots (d), (e), and (f)." [RTK25] (Figure reprinted from [RTK25])

data in (d–f) and (g–i) reveal a different behavior. In the unscaled case, most errors are small, with the exception of two outlier datasets each. These outlier datasets improve significantly when scaled, but the errors for the other datasets also increase substantially when scaled. The latter effect is not captured by the ξ_T criterion (Figure 5.11), because outliers dominantly contribute to the standard deviation in this sparse dataset. Thus, their improvement seemingly leads to higher convergence, while the other datasets diverge.

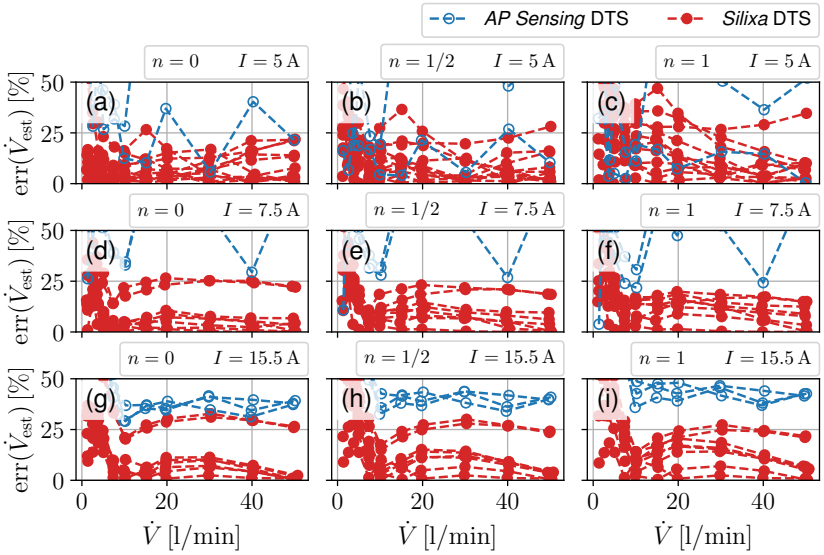

Figure 5.13: "Combining the analysis of the Pr influence (see Figure 5.11) with the calibration test (see Figure 5.12), estimation errors for various heating powers and scaling exponents were calculated. The unscaled case ($n = 0$) is shown in the first column, while the second and third columns display increasingly scaled data with $n = 1/2$ and $n = 1$, respectively. The data in the second and third rows (5 and 7.5 A) contain two outlier datasets in the *Silixa* DTS measurements. The error of these outlier datasets decreases with increased scaling, but the error of the other datasets increases slightly." [RTK25] (Figure reprinted from [RTK25])

These results refute the hypothesis that changes in ambient temperature are the primary cause of the observed deviation in heat transfer between datasets. However, as the correction slightly improves the data, it may become a useful tool when a predominant unknown error source, such as the presumed bubble formation explained in Subsection 5.3.2, are identified and corrected." [RTK25][6]

5.3 Phenomena impacting the heat transfer

Recall from the HFA fundamentals in Section 2.5 that contamination of the probe's surface by deposition of solid particles and bubble formation impacts the heat transfer that is exploited in TA. Therefore, the occurrence of these phenomena must be prevented by using deionized, filtered, and deaerated water.

First, Subsection 5.3.1 shows that solid particles precipitated on the surface of Probe V4 during the experiments in tap water. Subsequently, Subsection 5.3.2 demonstrates with a separate dummy-probe experiment that bubble formation may have occurred throughout all experiments within the borehole-mimicking test rig.

5.3.1 Precipitation of solids

The $\Delta T_{1,\infty}$–$\dot{V}$ plots of the experiments with Probe V4 display a significant difference in reproducibility when the test rig is filled with tap water compared to deionized water (compare Figure 5.8). In tap water, the measured temperature differences are not at all reproducible between different measurement days. This behavior is expected to be linked to the precipitation of solid particles, which occurs everywhere in the test rig when it is operated with tap water. Figure 5.14 displays three photos of Ring 2 in clean state after manufacturing, after experiments in tap water, and after experiments in deionized water. Figure 5.14 (b) shows that small white particles, presumably lime, deposited on the probe's surface throughout the experiments in tap water. Note that both the probe and the test rig were meticulously cleaned between the tap water and deionized water experiments.

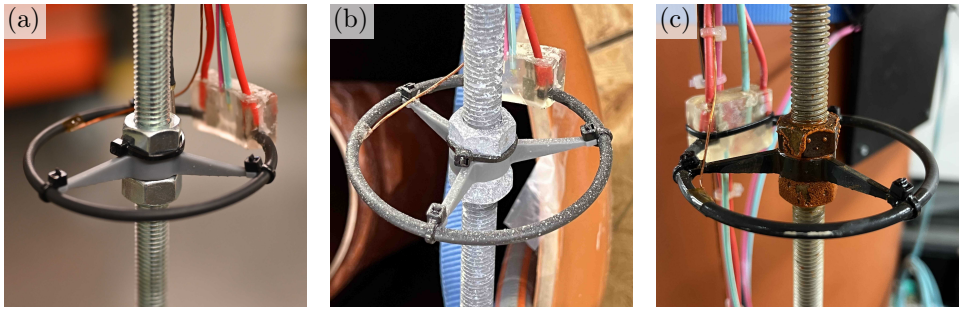

Figure 5.14: Demonstration that solids precipitate on the surface of Probe V4 during experiments in tap water but not during experiments in deionized water. (a) shows Ring 2 of Probe V4 after manufacturing, (b) shows it after experiments in tap water, and (c) shows it after experiments in deionized water.

[6] References in the cited text have been updated to refer to the corresponding content within this document.

5.3.2 Bubble formation investigation

"Generally, in drinking water processing the water is aerated as a first step to substitute unwanted dissolved gases and to oxidize dissolved metals, which are then removed by a subsequent filtration step [48]. Since this aeration process is performed at low temperature and may be conducted at elevated pressure, the water – once released from a tap – is likely to be oversaturated with oxygen. Consequently, oxygen bubbles might quickly form when the water is released from a pressurized pipe. This effect happens in the case for the tap water used in the present study, which also serves as the source for producing the used deionized water in a local demineralisation system.

Moreover, both tap water and deionized water remain slightly oversaturated when transferred into a container from their source. A slow diffusion process appears to lead to equilibrium within a few hours for a small container. During this timespan, gas bubbles may form on hydrophobic surfaces, such as the probe's surface. This effect should be prevented by deaerating the water [12] or by using only hydrophilic surfaces. However, the existing data contain the uncertainty that bubble formation may have occurred and influenced the heat transfer.

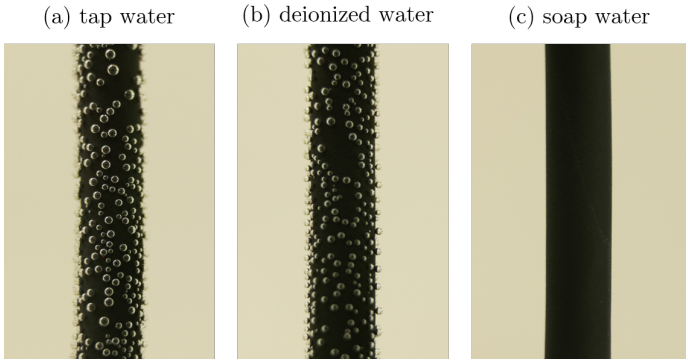

Figure 5.15: "Bubble formation was tested using three dummy probes placed in tap water (a), deionized water (b), and deionized water with soap (c). The dummy probes consist of the same steel capillary and outer insulation layer as those used in the double-ring probe. Pictures were taken 24 h after the containers were filled and the probes inserted." [RTK25] (Figure reprinted from [RTK25])

To test whether the bubble-formation-hypothesis holds true for the chosen material of the presented proof-of-concept study, a test series for bubble formation on the probes surface has been conducted. The result are shown in Figure 5.15, which saliently demonstrate the expected bubble formation. In particular, dummy probes, consisting of a piece of the same capillary used to build the ring probes and covered with the identical batch of heat-shrink tubing, are placed into different water baths to investigate and demonstrate this effect. In both tap water and deionized water, the dummy probe's surface becomes fully populated with small gas bubbles after resting for 24 h in the freshly filled containers, see Figure 5.15 (a) and (b). The bubbles grow significantly over the first day. If the probes are moved or the water stirred, larger bubbles detach, while smaller ones remain. When the dummy probe was removed from the water after the two days, the bubbles burst, and upon reinsertion, no new bubbles formed in the following days. After four days, the tap water and deionized water containers were heated to 40 °C. As the solubility of gases decreases with increasing water temperature, bubbles formed again at the dummy probes. In contrast to the first two containers, soap was added to the third container to modify the underlying wetting properties. No bubbles form on the dummy probes surface in this case, as shown in Figure 5.15 (c).

Considering the intended borehole application, the question arises whether bubble formation will also occur there on heated surfaces. The concentration of gases in the water is generally unknown, however, discussing the sensitivities to temperature and pressure may be insightful. The solubility

of gases decreases with increasing temperature, rendering heated surfaces the preferred locations for bubble formation in a saturated fluid. However, solubility depends primarily on pressure, increasing as pressure rises. When water is pumped out of a borehole, it experiences a pressure drop, and thus, depending on its initial concentration of dissolved gases, bubbles may form. In contrast, when water is pumped into a borehole pressure rises, solubility increases, and bubble formation is not expected." [RTK25][7]

[7] References in the cited text have been updated to refer to the corresponding content within this document.

6 Conclusions and outlook

The present thesis comprises an iterative experimental investigation of fiber-optic TA in water with an active DTS approach. Motivated by the intention to develop a fiber-optic distributed flowmeter sensor for the application in boreholes of the Earth's crust, the overarching goal was to bridge the gap from qualitative to quantitative flowmeter measurements by first determining the measurement range and uncertainty, and subsequently assessing the applicability in the Earth's crust.

In this TA approach, the temperature measured with the glass fiber is a function of the heat transfer from the heated hybrid cable to the ambient fluid. As the heat transfer becomes more effective at higher flow velocities, the measured glass fiber temperature is solely a function of the flow velocity as long as the heat transfer is not influenced by other circumstances. The heat transfer comprises the effects of conduction inside the hybrid cable and convection at the surface of the hybrid cable. The heat conduction is modeled by the one-dimensional heat diffusion equation in radial direction, while the heat convection is modeled using empirical correlations. This heat-transfer modeling provides a sensible reference and enables an a priori estimation of the measurement range and of an acceptable uncertainty range for the temperature measurement. However, each probe must be calibrated, since empirical correlations are not precise solutions and because the similarity between the investigated probe geometries and the empirical reference case of a cylinder in cross flow is imperfect.

An iterative research procedure was implemented in which a validation test for the heat-transfer modeling was conducted and four fiber-optic probe generations were examined in a borehole-mimicking test rig. The procedure was structured into assumptions, stated hypotheses, and pursued strategies and objectives as outlined in Section 3.3. The first research stage focused on validating the heat-transfer modeling, calibrating the fiber-optic probe in the laboratory, and demonstrating its applicability in a real borehole. As concluded in Section 4.4, the modeling approach was validated and sensitivity to flow-velocity changes was demonstrated. Reproducibility issues and difficulties in determining the probe temperature from the measured DTS data prevented successful calibration and rendered an in situ demonstration unfeasible. Because confidence in the measured DTS temperatures was insufficient, the observed offsets could not be interpreted unambiguously. The entire procedure – including the probe design and the DTS measurement approach – was therefore reassessed. The underlying assumptions were revised and the specific objectives adjusted, as summarized in Table 3.6. In the second research stage, emphasis shifted to the DTS measurement technique by introducing calibration of raw data to temperatures and by designing new probes in accordance with the DTS spatial-resolution limitations. The first improved probe design, Probe V3, provided five times the spatial resolution of the DTS device used. However, the overshoot phenomenon in data from the *AP Sensing N4386B* DTS device impeded unambiguous temperature identification for the heated probe, again undermining confidence in the DTS data and obscuring interpretation. Consequently, the subsequent probe generation, Probe V4, incorporated sufficient glass-fiber length not only to meet the spatial resolution of the DTS device but also to exceed the influence length of the overshoot phenomenon. A validation experiment confirmed that the temperature measurements of Probe V4 are reliable within a limited uncertainty range.

An extensive measurement campaign was conducted with Probe V4 in the borehole-mimicking test rig, resulting in 161 datasets. "Each dataset has a constant heating power in the range of 2.6–50 W/m and consists of twelve velocity measurement points ranging from 0–50 l/min. As additional parameter, the test rig was operated with both tap water and deionized water. Also, two different DTS devices [*AP Sensing N4386B* and *Silixa XT M*] were contrasted as a more hardware-related parameter variation.

Overall, the results demonstrate measurable sensitivity of the temperature differences to changes in flow velocity, which generally qualifies the DTS-approach for the measurement of water flow rates. However, reproducibility of the results remains a substantial challenge, which put a question mark on the transfer of the proposed approach to realistic flow scenarios. Particularly in tap water, the observed reproducibility issues are primarily attributed to lime deposition on the probes surface and in the test rig. The offsets were of such magnitude that subsequent data processing was considered infeasible. Test-rig operation with deionized water significantly reduced the reproducibility issues and the data acquired with the preferred DTS device in deionized water allowed an estimation of the velocity with an error of less than 35 % within the range of 7.1–47 mm/s, which is largest, when datasets were acquired several days apart. For datasets acquired consecutively, the error remains below 15 % in the same range.

The reproducibility turned out to be influenced by a parameter on a slow timescale, because datasets acquired subsequently correspond well, while datasets acquired multiple days apart revealed varying offsets from each other. Furthermore, when all datasets are plotted non-dimensionally in a Nu–Re diagram, the datasets remain sorted by heating power. This unexpected behavior prevents that calibration curves from a single heating power may be used for all heating powers. The consequent attempts to improve reproducibility by correcting for variations in the temperature-dependent Pr number and accounting for the observed influence of heating power on the Nu–Re relationship did not lead to major improvements. Additional investigation into water properties uncovered that both used water types were not sufficiently deaerated. From this insight in combination with the observed drifting behavior it is hypothesized that air bubbles form and grow on the probe's surface (as demonstrated in a proof-of-concept experiment in Subsection 5.3.2), which ultimately influences the heat transfer.

The identified strong sensitivity to water purity renders this approach impractical for the motivated application – i.e. to measure flow velocities along a borehole's axis. In such flow scenarios the water composition is not only unknown, but is also expected to vary along the borehole's length. Consequently, only the application in pumping tests, that inject water into the borehole, appears to be candidating for the approach with the additional cost to maintain and quantify the properties of the injected water. From a fundamental metrological point of view, the results are nonetheless insightful and interesting: First, every single dataset acquired with the preferred DTS device shows – even at the lowest heating power – that the measured $\Delta T_{1,\infty}$ is always monotonically decreasing with increasing volume flow rate. Secondly, the high reproducibility of subsequently acquired datasets infers that reproducible measurements are achievable if the unknown influence in the heat transfer is either known or prevented to occur." [RTK25][1] These insights outline the general potential of the proposed approach to measure flow velocities in applications where either the robustness or the length of glass-fiber sensors is advantageous or required and where the requirements on water purity are met.

How-to perform TA in water with fiber optic sensors and consequential implications for the applications in boreholes is summarized in the following:

[1] References in the cited text have been updated to refer to the corresponding content within this document.

1. The impacts of variation in water properties and of flow velocity changes on the heat transfer in water are on the same order of magnitude. Thus, TA can be realized for flow-velocity measurements only if the impact of water properties is suppressed by using deionized, filtered, and deaerated water; see also Section 2.5.

2. In the implementation of TA with fiber-optic thermometry using DTS, special care is required to measure the temperature with sufficient accuracy:

   - Calibration of the DTS data with fiber sections at known reference temperatures is required to achieve a quantifiable high accuracy of the DTS temperature measurement.
   - The spatial resolution is limited by the DTS device and is mostly on the order of $\sim 0.5\,\mathrm{m}$. If more confined sections or point measurements are of interest, coiling the fiber in a capillary loop is a valid option.
   - Heat transfer modeling enables the calculation of the temperature offset between the fiber location and the surface relevant for the heat transfer. This procedure enables a better insight into the heat transfer and comparison of the measured data with literature data. It is optional because the calculated offset is constant in steady-state heat transfer and the required calibration will account for it.

3. Regarding the applicability of TA in boreholes, it is evident that the water quality standards – see 1. – are not met. The successful application of TA in boreholes would require either creative solutions to achieve such conditions – e.g. pumping deionized, filtered, and deaerated water into a borehole – or advanced knowledge of the downhole water properties and their impact on the heat transfer. Both options seem unrealistic.

A realistic future application for the probe-development concept can be anticipated only in a domain beyond the scope of this work. The coiled-fiber-in-capillary concept from Probe V4 may be useful in fiber-optic TA in air to develop point sensors that are sensitive to both flow velocity and flow direction. As demonstrated with a proof-of-concept experiment in Appendix D, it is possible to build U-shaped probes that are sensitive to flow direction and flow velocity. A combination of such U-shaped probes should be capable of measuring both flow direction and flow velocity. Therefore, such sensors may serve as a useful extension of large fiber-optic distributed TA setups that are applied to measure time-resolved atmospheric boundary-layer flow profiles. Further research efforts in the design, manufacturing, and calibration of this new sensor concept are required.

7 References

Bibliography

[1] M. Abdoli, K. Lapo, J. Schneider, J. Olesch, and C. K. Thomas. Toward quantifying turbulent vertical airflow and sensible heat flux in tall forest canopies using fiber-optic distributed temperature sensing. *Atmospheric Measurement Techniques*, 16(3):809–824, 2023. ISSN 1867-1381. DOI 10.5194/amt-16-809-2023.

[2] T. Agemar, J. Weber, and I. S. Moeck. Assessment and Public Reporting of Geothermal Resources in Germany: Review and Outlook. *Energies*, 11(2):332, 2018. ISSN 1996-1073. DOI 10.3390/en11020332.

[3] A. Albers, H. Steger, R. Zorn, and P. Blum. Evaluating an enhanced thermal response test (ETRT) with high groundwater flow. *Geothermal Energy*, 12(1):1, 2024. ISSN 2195-9706. DOI 10.1186/s40517-023-00278-y.

[4] M. P. Anderson. Heat as a Ground Water Tracer. *Groundwater*, 43(6):951–968, 2005. ISSN 1745-6584. DOI 10.1111/j.1745-6584.2005.00052.x.

[5] M. Balderacchi, P. Benoit, P. Cambier, O. M. Eklo, A. Gargini, A. Gemitzi, M. Gurel, B. Kløve, Z. Nakic, E. Predaa, S. Ruzicic, P. Wachniew, and M. Trevisan. Groundwater Pollution and Quality Monitoring Approaches at the European Level. *Critical Reviews in Environmental Science and Technology*, 43(4):323–408, 2013. ISSN 1064-3389. DOI 10.1080/10643389.2011.604259.

[6] A. Banerjee, L. Creedon, N. Jones, L. Gill, and S. Gharbia. Dynamic Groundwater Contamination Vulnerability Assessment Techniques: A Systematic Review. *Hydrology*, 10(9):182, 2023. ISSN 2306-5338. DOI 10.3390/hydrology10090182.

[7] J. Bear. *Hydraulics of Groundwater*. McGraw-Hill, 1979. ISBN 0-07-004170-9.

[8] V. F. Bense, T. Read, O. Bour, T. Le Borgne, T. Coleman, S. Krause, A. Chalari, M. Mondanos, F. Ciocca, and J. S. Selker. Distributed Temperature Sensing as a downhole tool in hydrogeology. *Water Resources Research*, 52(12):9259–9273, 2016. ISSN 1944-7973. DOI 10.1002/2016WR018869.

[9] R. B. Bird, W. E. Steward, and E. N. Lightfoot. *Transport Phenomena, Revised 2nd Edition*. Wiley, 2007. ISBN 978-0-470-11539-8.

[10] R. Bracke and E. Huenges. Roadmap Tiefengeothermie für Deutschland. 2021. DOI 10.24406/IEG-N-645792.

[11] J. Bredehoeft. Monitoring Regional Groundwater Extraction: The Problem. *Groundwater*, 49(6):808–814, 2011. ISSN 1745-6584. DOI 10.1111/j.1745-6584.2011.00799.x.

[12] H. H. Bruun. Hot-film anemometry in liquid flows. *Measurement Science and Technology*, 7 (10):1301–1312, 1996. ISSN 0957-0233, 1361-6501. DOI 10.1088/0957-0233/7/10/003.

[13] H. S. Carslaw and J. C. Jaeger. *Conduction of Heat in Solids*. Oxford University Press, Oxford, New York, second edition, second edition edition, 1986. ISBN 978-0-19-853368-9.

[14] N. Chapman and A. Hooper. The disposal of radioactive wastes underground. *Proceedings of the Geologists' Association*, 123(1):46–63, 2012. ISSN 0016-7878. DOI 10.1016/j.pgeola.2011.10.001.

[15] J. J. Charonko. Laser velocimetry. In *Experimental Aerodynamics*. CRC Press, 2017. DOI 10.1201/9781315371733.

[16] R. Chen, A. Yan, Q. Wang, and K. P. Chen. Fiber-optic flow sensors for high-temperature environment operation up to 800°C. *Optics letters*, 39(13):3966–9, 2014. DOI 10.1364/OL.39.003966.

[17] T. Chen, Q. Wang, B. Zhang, R. Chen, and K. P. Chen. Distributed flow sensing using optical hotwire grid. *Optics express*, 20(8):8240–9, 2012. DOI 10.1364/OE.20.008240.

[18] T. S. Chen, B. F. Armaly, and N. Ramachandran. Correlations for Laminar Mixed Convection Flows on Vertical, Inclined, and Horizontal Flat Plates. *Journal of Heat Transfer*, 108(4):835–840, 1986. ISSN 0022-1481. DOI 10.1115/1.3247020.

[19] S. W. Churchill and M. Bernstein. A Correlating Equation for Forced Convection From Gases and Liquids to a Circular Cylinder in Crossflow. *Journal of Heat Transfer*, 99(2):300–306, 1977. ISSN 0022-1481. DOI 10.1115/1.3450685.

[20] S. W. Churchill and H. H. Chu. Correlating equations for laminar and turbulent free convection from a horizontal cylinder. *International Journal of Heat and Mass Transfer*, 18(9):1049–1053, 1975. ISSN 00179310. DOI 10.1016/0017-9310(75)90222-7.

[21] D. C. Collis and M. J. Williams. Two-dimensional convection from heated wires at low Reynolds numbers. *Journal of Fluid Mechanics*, 6(3):357–384, 1959. ISSN 0022-1120, 1469-7645. DOI 10.1017/S0022112059000696.

[22] S. Denzel, T. Ertel, and I. Blankenhorn. Grundzüge der Grundwassererkennung in Baden-Württemberg. *Altlasten Spektrum*, (1997):218–224, Jan. 1997.

[23] B. Des Tombe, B. Schilperoort, and M. Bakker. Estimation of Temperature and Associated Uncertainty from Fiber-Optic Raman-Spectrum Distributed Temperature Sensing. *Sensors*, 20(8):2235, 2020. ISSN 1424-8220. DOI 10.3390/s20082235.

[24] B. F. des Tombe, M. Bakker, F. Smits, F. Schaars, and K.-J. van der Made. Estimation of the Variation in Specific Discharge Over Large Depth Using Distributed Temperature Sensing (DTS) Measurements of the Heat Pulse Response. *Water Resources Research*, 55(1):811–826, 2019. ISSN 1944-7973. DOI 10.1029/2018WR024171.

[25] B. Edalat, P. Krach, and K. Volk. Bestimmung der Gebirgsdurchlässigkeit. Technical Report Heft 8, Landesanstalt für Umweltschutz Baden-Württemberg, Karlsruhe, 1991.

[26] J. Fischer and B. Fellmuth. Temperature metrology. *Reports on Progress in Physics*, 68(5):1043, 2005. ISSN 0034-4885. DOI 10.1088/0034-4885/68/5/R02.

[27] S. Gao, A. P. Zhang, H.-Y. Tam, L. H. Cho, and C. Lu. All-optical fiber anemometer based on laser heated fiber Bragg gratings. *Optics express*, 19(11):10124–30, 2011. DOI 10.1364/OE.19.010124.

[28] V. Gnielinski. Berechnung mittlerer Wärme- und Stoffübergangskoeffizienten an laminar und turbulent überströmten Einzelkörpern mit Hilfe einer einheitlichen Gleichung. *Forschung im Ingenieurwesen A*, 41(5):145–153, 1975. ISSN 1434-0860. DOI 10.1007/BF02560793.

[29] J. Happel and H. Brenner. *Low Reynolds number hydrodynamics: with special applications to particulate media*, volume 1 of *Mechanics of fluids and transport processes*. Springer Netherlands, Dordrecht, 1983. ISBN 978-90-247-2877-0. DOI 10.1007/978-94-009-8352-6.

[30] A. H. Hartog. *An introduction to distributed optical fibre sensors*. Series in fiber optic sensors. CRC press, Taylor & Francis Group, Boca Raton, FL, 2017. ISBN 978-1-4822-5957-5.

[31] M. B. Hausner, F. Suárez, K. E. Glander, N. van de Giesen, J. S. Selker, and S. W. Tyler. Calibrating single-ended fiber-optic Raman spectra distributed temperature sensing data. *Sensors*, 11(11):10859–79, 2011. DOI 10.3390/s111110859.

[32] F. P. Incropera, D. P. DeWitt, T. L. Bergman, and A. S. Lavine, editors. *Fundamentals of heat and mass transfer*. Wiley, Hoboken, NJ, 6. ed edition, 2007. ISBN 978-0-471-45728-2.

[33] IPCC, editor. *Renewable energy sources and climate change mitigation: special report of the Intergovernmental Panel on Climate Change*. Cambridge Univ. Pr, Cambridge, 2012. ISBN 978-1-107-60710-1.

[34] J. Jimenez, R. Martinez-Val, and M. Rebollo. Hot-film sensors calibration drift in water. *Journal of Physics E: Scientific Instruments*, 14(5):569–572, 1981. ISSN 0022-3735. DOI 10.1088/0022-3735/14/5/010.

[35] L. V. King. On the Convection of Heat from Small Cylinders in a Stream of Fluid: Determination of the Convection Constants of Small Platinum Wires with Applications to Hot-Wire Anemometry. *Philosophical Transactions of the Royal Society of London Series A*, 214:373–432, 1914. DOI 10.1098/rsta.1914.0023.

[36] H. Kramers. Heat transfer from spheres to flowing media. *Physica*, 12(2-3):61–80, 1946. ISSN 00318914. DOI 10.1016/S0031-8914(46)80024-7.

[37] G. P. Kruseman and N. A. de Ridder. *Analysis and evaluation of pumping test data*. Number 47 in ILRI publication. International Institute for Land Reclamation and Improvement, Wageningen, 2. ed. (completely rev.), reprint edition, 2000. ISBN 978-90-70754-20-4.

[38] K. Lapo, A. Freundorfer, L. Pfister, J. Schneider, J. Selker, and C. Thomas. Distributed observations of wind direction using microstructures attached to actively heated fiber-optic cables. *Atmospheric Measurement Techniques*, 13(3):1563–1573, 2020. ISSN 1867-8548. DOI 10.5194/amt-13-1563-2020.

[39] K. Lapo, A. Freundorfer, A. Fritz, J. Schneider, J. Olesch, W. Babel, and C. K. Thomas. The Large eddy Observatory, Voitsumra Experiment 2019 (LOVE19) with high-resolution, spatially distributed observations of air temperature, wind speed, and wind direction from fiber-optic distributed sensing, towers, and ground-based remote sensing. *Earth System Science Data*, 14(2):885–906, 2022. ISSN 1866-3516. DOI 10.5194/essd-14-885-2022.

[40] Z. Li, J. Chen, M. Sugimoto, and H. Ge. Numerical simulation model of artificial ground freezing for tunneling under seepage flow conditions. *Tunnelling and Underground Space Technology*, 92:103035, 2019. ISSN 0886-7798. DOI 10.1016/j.tust.2019.103035.

[41] Z. Liang, C. Zhao, H. Zhou, Q. Liu, and Y. Zhou. Error correction of temperature measurement data obtained from an embedded bifilar optical fiber network in concrete dams. *Measurement*, 148:106903, 2019. ISSN 0263-2241. DOI 10.1016/j.measurement.2019.106903.

[42] P. Linstrom. NIST standard reference database number 69: NIST Chemistry WebBook. *National Institute of Standards and Technology*, 2003. DOI 10.18434/T4D303.

[43] G. Liu, W. Hou, W. Qiao, and M. Han. Fast-response fiber-optic anemometer with temperature self-compensation. *Optics Express*, 23(10):13562–13570, 2015. ISSN 1094-4087. DOI 10.1364/OE.23.013562.

[44] S. Lomperski and C. Gerardi. Assessment of Distributed Fiber Optic Sensors for Flow Field Temperature Mapping. American Society of Mechanical Engineers Digital Collection, 2014. DOI 10.1115/FEDSM2014-22156.

[45] L. Ma, C. Ma, Y. Wang, D. Y. Wang, and A. Wang. High-Speed Distributed Sensing Based on Ultra Weak FBGs and Chromatic Dispersion. *IEEE Photonics Technology Letters*, 28(12): 1344–1347, 2016. ISSN 1941-0174. DOI 10.1109/LPT.2016.2540662.

[46] L. Mack, M. Kähnert, Q. Rauschenbach, L. Frank, F. H. Hasenburg, J.-M. Huss, M. O. Jonassen, M. Malpas, Y. Batrak, T. Remes, N. Pirk, and C. K. Thomas. Stable Boundary Layers in an Arctic Fjord-Valley System: Evaluation of Temperature Profiles Observed From Fiber-Optic Distributed Sensing and Comparison to Numerical Weather Prediction Systems at Different Resolutions. *Journal of Geophysical Research: Atmospheres*, 130(2), 2025. ISSN 2169-8996. DOI 10.1029/2024JD042825.

[47] W. H. McAdams. *Heat transmission*. McGraw-Hill, Auckland, 3rd ed., international student ed edition, 1958. ISBN 978-0-07-085483-3.

[48] P. J. Moel, J. Q. J. C. Verbert, and J. C. v. Dijk. *Drinking water: principles and practices*. World Scientific Publ, Singapore, reprint edition, 2007. ISBN 978-981-256-836-6.

[49] F. J. Molz, R. H. Morin, A. E. Hess, J. G. Melville, and O. Güven. The Impeller Meter for measuring aquifer permeability variations: Evaluation and comparison with other tests. *Water Resources Research*, 25(7):1677–1683, 1989. ISSN 1944-7973. DOI 10.1029/WR025i007p01677.

[50] F. J. Molz, G. K. Boman, S. C. Young, and W. R. Waldrop. Borehole flowmeters: field application and data analysis. *Journal of Hydrology*, 163(3):347–371, 1994. ISSN 0022-1694. DOI 10.1016/0022-1694(94)90148-1.

[51] O. J. Ohanian, A. J. Boulanger, and K. T. Lowe. Distributed Anemometry via High-Definition Fiber Optic Sensing. In *AIAA Scitech 2019 Forum*, AIAA SciTech Forum. American Institute of Aeronautics and Astronautics, 2019. DOI 10.2514/6.2019-2108.

[52] F. Paillet, R. Crowder, and A. Hess. High-Resolution Flowmeter Logging Applications with the Heat-Pulse Flowmeter. *Journal of Environmental and Engineering Geophysics*, 1(1):1–11, 1996. ISSN 1083-1363. DOI 10.4133/JEEG1.1.1.

[53] B. S. Petukhov and V. N. Popov. Theoretical calculation of heat exchange and frictional resistance in turbulent flow in tubes of an incompressible fluid with thermophysical properties. *TVT*, 1(1):85–101, 1963.

[54] H. Prinz and R. Strauß. *Ingenieurgeologie*. Springer, Heidelberg, 5 edition, 2011. ISBN 978-3-8274-2472-3.

[55] M. Raffel, C. E. Willert, F. Scarano, C. J. Kähler, S. T. Wereley, and J. Kompenhans. *Particle Image Velocimetry: A Practical Guide*. Springer International Publishing, Cham, 2018. ISBN 978-3-319-68851-0 978-3-319-68852-7. DOI 10.1007/978-3-319-68852-7.

[56] T. Read, O. Bour, J. S. Selker, V. F. Bense, T. Le Borgne, R. Hochreutener, and N. Lavenant. Active-distributed temperature sensing to continuously quantify vertical flow in boreholes. *Water Resources Research*, 50(5):3706–3713, 2014. ISSN 0043-1397. DOI 10.1002/2014WR015273.

[57] T. Renner. Untersuchung der Eignung von faseroptischen Temperaturmessungen zur Quantifizierung von Volumenströmen. Master Thesis. Institute of Fluid Mechanics, Karlsruhe Institue of Technology. 2020.

[58] J. A. Roumasset and C. A. Wada. Optimal and Sustainable Groundwater Extraction. *Sustainability*, 2(8):2676–2685, 2010. ISSN 2071-1050. DOI 10.3390/su2082676.

[59] C. Sayde, C. K. Thomas, J. Wagner, and J. Selker. High-resolution wind speed measurements using actively heated fiber optics. *Geophysical Research Letters*, 42(22):10,064–10,073, 2015. ISSN 1944-8007. DOI 10.1002/2015GL066729.

[60] J. S. Selker, L. Thévenaz, H. Huwald, A. Mallet, W. Luxemburg, N. van de Giesen, M. Stejskal, J. Zeman, M. Westhoff, and M. B. Parlange. Distributed fiber-optic temperature sensing for hydrologic systems. *Water Resources Research*, 42(12), 2006. ISSN 00431397. DOI 10.1029/2006WR005326.

[61] Silixa. Introduction to Distributed Temperature Sensing, 2022. URL https://silixa.com/resources/downloads/.

[62] N. Simon, O. Bour, N. Lavenant, G. Porel, B. Nauleau, B. Pouladi, L. Longuevergne, N. Simon, O. Bour, N. Lavenant, G. Porel, B. Nauleau, B. Pouladi, and L. Longuevergne. A Comparison of Different Methods to Estimate the Effective Spatial Resolution of FO-DTS Measurements Achieved during Sandbox Experiments. *Sensors*, 20(2), Jan. 2020. ISSN 1424-8220. DOI 10.3390/s20020570.

[63] N. Simon, O. Bour, N. Lavenant, G. Porel, B. Nauleau, B. Pouladi, L. Longuevergne, and A. Crave. Numerical and Experimental Validation of the Applicability of Active-DTS Experiments to Estimate Thermal Conductivity and Groundwater Flux in Porous Media. *Water Resources Research*, 57(1):e2020WR028078, 2021. ISSN 1944-7973. DOI 10.1029/2020WR028078.

[64] A. Sivasuriyan, D. S. Vijayan, R. Munusami, and P. Devarajan. Health assessment of dams under various environmental conditions using structural health monitoring techniques: a state-of-art review. *Environmental Science and Pollution Research*, 29(57):86180–86191, 2022. ISSN 1614-7499. DOI 10.1007/s11356-021-16749-3.

[65] Stadtwerke Karlsruhe. Wasserqualität des Trinkwassers aus den Karlsruher Wasserwerken, 2025. URL https://www.stadtwerke-karlsruhe.de/wMedia/docs/service/infomaterial/produkte/Trinkwasser-Jahresmittelwerte-KA.pdf.

[66] C. V. Theis. The relation between the lowering of the Piezometric surface and the rate and duration of discharge of a well using ground-water storage. *Transactions, American Geophysical Union*, 16(2):519, 1935. ISSN 0002-8606. DOI 10.1029/TR016i002p00519.

[67] C. K. Thomas, J.-M. Huss, M. Abdoli, T. Huttarsch, and J. Schneider. Solid-Phase Reference Baths for Fiber-Optic Distributed Sensing. *Sensors*, 22(11):4244, 2022. ISSN 1424-8220. DOI 10.3390/s22114244.

[68] A. Tselentis. Application of hot-wire (-film) flowmeters to water velocity measurements in wells. *Journal of Hydrology*, 58(3-4):375–381, 1982. ISSN 00221694. DOI 10.1016/0022-1694(82)90046-4.

[69] T. Tsubouchi and H. Masuda. On the experimental formulae of heat transfer from single cylinders by forced convection. *Reports of the Institute of High Speed Mechanics*, pages 1967–1968, 1967.

[70] N. van de Giesen, S. C. Steele-Dunne, J. Jansen, O. Hoes, M. B. Hausner, S. Tyler, and J. Selker. Double-ended calibration of fiber-optic Raman spectra distributed temperature sensing data. *Sensors*, 12(5):5471–85, 2012. DOI 10.3390/s120505471.

[71] J. G. V. van Ramshorst, M. Coenders-Gerrits, B. Schilperoort, B. J. H. van de Wiel, J. G. Izett, J. S. Selker, C. W. Higgins, H. H. G. Savenije, and N. C. van de Giesen. Revisiting wind speed measurements using actively heated fiber optics: a wind tunnel study. *Atmospheric Measurement Techniques*, 13(10):5423–5439, 2020. ISSN 1867-1381. DOI 10.5194/amt-13-5423-2020.

[72] S. Wilke, K. Menberg, H. Steger, and P. Blum. Advanced thermal response tests: A review. *Renewable and Sustainable Energy Reviews*, 119:109575, 2020. ISSN 13640321. DOI 10.1016/j.rser.2019.109575.

[73] J. H. Williams and F. L. Paillet. *Geophysical Logging For Hydrogeology.* The Groundwater Project, 2023. DOI 10.21083/UQGA6966.

[74] W. W. Woessner, A. C. Stringer, and E. P. Poeter. *An introduction to hydraulic testing in hydrogeology: basic pumping, slug, and packer methods.* The Groundwater Project, Guelph, Ontario, 2023. ISBN 978-1-77470-090-7. DOI 10.21083/978-1-77470-090-7.

[75] M. T. V. Wylie, A. W. Brown, and B. G. Colpitts. Distributed hot-wire anemometry based on Brillouin optical time-domain analysis. *Optics Express*, 20(14):15669–15678, 2012. ISSN 1094-4087. DOI 10.1364/OE.20.015669.

[76] R. Örlü and R. Vinuesa. Thermal anemometry. In *Experimental aerodynamics*, pages 257–304. CRC Press, 2017. DOI 10.1201/9781315371733.

List of conference contributions

[RK24] David Rautenberg and Jochen Kriegseis. Active Distributed Temperature Sensing to determine flow velocities in boreholes based on a cylinder in cross-flow approach. In *European Geosciences Union General Assembly EGU24, Vienna, Austria*, April 2024. DOI 10.5194/egusphere-egu24-9310.

[RLTK22] Tom Renner, David Lah, Thomas Trick, and Jochen Kriegseis. Determination of flow velocities using fiber-optic temperature measurements. In *20th International Symposium on the Application of Laser and Imaging Techniques to Fluid Mechanics, Lisbon, Portugal*, July 2022. ISBN 978-989-53637-0-4. DOI 10.55037/lxlaser.20th.160.

List of journal publications

[RRTK24] David Rautenberg, Tom Renner, Thomas Trick, and Jochen Kriegseis. Determination of flow velocities using fiber-optic temperature measurements. *Experiments in Fluids*, 65(2):22, 2024. DOI 10.1007/s00348-023-03741-5.

The manuscript below, is – at the submission date of the present thesis – submitted and under review. It is published as pre-print.

[RTK25] David Rautenberg, Christoph K. Thomas, and Jochen Kriegseis. Laboratory investigation and evaluation of a ring-shaped actively heated fiber-optic distributed temperature sensing sensor for flow-speed quantification in boreholes. *ESS open archive,* 2025. DOI 10.22541/essoar.176521523.33565411/v1.

Author contributions for journal papers

Author contributions for the journal publication

Determination of flow velocities using fiber-optic temperature measurements

Published in:

Exp Fluids 65, 22 (2024). DOI: 10.1007/s00348-023-03741-5

Authors:

David Rautenberg, Tom Renner, Thomas Trick, and Jochen Kriegseis

Author Contributions:

DR Conceptualization, Data Acquisition, Data Evaluation, Visualization, Writing – original draft

TR Conceptualization, Data Acquisition, Data Evaluation, Writing – Review

TT Project Administration, Writing – Review

JK Project Administration, Writing – Review and Editing

Author contributions for the preprint publication

Laboratory investigation and evaluation of a ring-shaped actively heated fiber-optic distributed sensing sensor for flow-speed quantification in boreholes

Published as preprint in:

ESS Open Archive December 08, 2025. DOI: 10.22541/essoar.176521523.33565411/v1

Authors:

David C. Rautenberg, Christoph K. Thomas, and Jochen Kriegseis

Author Contributions:

DR Conceptualization, Methodology, Software, Validation, Formal Analysis, Investigation, Data Curation, Writing – Original Draft, Visualization

CT Validation, Formal Analysis, Resources, Writing – Review and Editing

JK Conceptualization, Formal Analysis, Resources , Writing – Review and Editing, Supervision, Project Administration, Funding Acquisition

Author Confirmation:

David C. Rautenberg	DR	Date: 23.02.2026	Signature:	
Christoph K. Thomas	CT	Date: 13.02.2026	Signature:	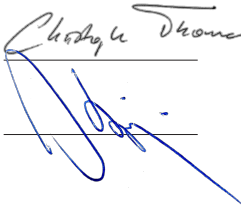
Jochen Kriegseis	JK	Date: 21.02.2026	Signature:	

Acronyms and symbols

Acronyms

CCA	constant current anemometry
CTA	constant temperature anemometry
DTS	distributed temperature sensing
FBG	fiber-Bragg grating
HFA	hot-film anemometry
HWA	hot-wire anemometry
MILS	moving instantaneous line source
OTDR	optical time-domain reflectometry
PIV	particle image velocimetry
RTD	resistance temperature detector
TA	thermal anemometry
TC	thermocouple

Dimensionless numbers

Bi	Biot number
Gr	Grashof number
Nu	Nusselt number
Nu_l	Nusselt number using the cylinder's overflow length as L_{char}
Pe	Peclet number
Pr	Prandtl number
Ra	Rayleigh number
Re	Reynolds number
Re_l	Reynolds number using the cylinder's overflow length as L_{char}
Ri	Richardson number

Latin letter – Upper case

A	area

A	attenuation integral in double-ended DTS calibration algorithm
C	coefficient containing time-variant influences in DTS calibration
D	coefficient containing time-variant influences in DTS calibration
D	diameter
E	energy
E	voltage
E	emissive radiation power per unit area
E_0	initial laser pulse energy
ΔE_{BS}	backscattered energy fraction from a section Δx
$\dot{E}$	energy rate per unit time
E_b	emissive radiation power per unit area of a black body
E_{AB}	Seebeck voltage between conductors A and B
G	irradiation power per unit area
H	height
I	electrical current
I	logarithmic ratio of measured Stokes and anti-Stokes intensities
K	coefficient of permeability
K_+	molecule fraction that contributes to Stokes Raman scattering
K_-	molecule fraction that contributes to anti-Stokes Raman scattering
L	length
L_{char}	characteristic length
P	scattering intensity
P_+	scattering intensity of Stokes signal
P_-	scattering intensity of anti-Stokes signal
P_{el}	electrical power
$\dot{Q}$	heat flow rate
$\dot{Q}_i$	heat flow rate by $i \in [\mathrm{conv} : \mathrm{convection}, \mathrm{cond} : \mathrm{conduction}, \mathrm{rad} : \mathrm{radiation}]$
R	capture fraction
R	electrical resistance
R_0	electrical resistance at a defined reference
R_{w}	electrical resistance of a hot wire
R_i	heat transfer resistance to $i \in [\mathrm{conv} : \mathrm{convective}, \mathrm{cond} : \mathrm{conductive}]$ heat transfer
S	scattering coefficient

S_+	scattering coefficient of Stokes signal
S_-	scattering coefficient of anti-Stokes signal
S_i	Seebeck coefficient for conductor $i \in [\mathrm{A}, \mathrm{B}]$
T	temperature
T_i	temperature at location $i \in [0, 1, 2, 3, \mathrm{S}, \infty]$ (S: surface, ∞: ambient)
T_m	mean of temperatures T_S and T_∞
T_B	forward channel temperature with double-ended calibration
T_F	backward channel temperature with double-ended calibration
T_W	weighted temperature with double-ended calibration
T_w	temperature of a hot wire
T	transmissivity
$\Delta T_{i,j}$	temperature differences between locations i and j; $i, j \in [0, 1, 2, 3, \infty]$
$\dot{V}$	volumetric flow rate
$\dot{V}_\mathrm{est}$	estimated volumetric flow rate
$\{A, B, C\}$	coefficients in RTD temperature equation
$\{A, B, n\}$	coefficients in HWA calibration
$\{C_1, C_2\}$	integration constants
$\{M, N\}$	maximal index values of $\{m, n\}$ in DTS calibration

Latin letter – Lower case

a	thermal diffusivity
c	speed of light
c_p	specific heat capacity at constant pressure
d	diameter
d_i	diameter, $i \in [1, 2, 3]$
f	frequency
g	gravitational acceleration
h	height
h	heat transfer coefficient
h_P	Planck constant
i	inclination
k	thermal conductivity
k_j	thermal conductivity for material $j \in [\mathrm{f} : \mathrm{fluid}, \mathrm{s} : \mathrm{solid}, \mathrm{i} : \mathrm{insulation}, \mathrm{st} : \mathrm{steel}]$

l	length
p	pressure
q	heat flux
q_i	conductive heat flux in direction of coordinate $i \in [x, y, z, r, \phi]$
q_{rad}	radiative heat flux
$\dot{q}_{\mathrm{g}}$	volume specific heat generation rate
r	radius
r_i	radius, $i \in [1, 2, 3]$
t	time
u	velocity
u_{D}	Darcy velocity
u_{eff}	effective velocity
x	coordinate of fiber length
$\{m, n\}$	indices in DTS calibration
$\{m, n\}$	exponents in scaling analysis
$\{x, y, z\}$	Cartesian coordinate system
$\{r, \phi, z\}$	cylindrical coordinate system

Greek letters

α	absorptivity of irradiation
α	temperature coefficient in HWA
α_1	attenuation of light with wavelength λ
α_+	attenuation of light with wavelength λ_+
α_-	attenuation of light with wavelength λ_-
$\Delta\alpha$	differential attenuation
β	expansion coefficient
γ	sensitivity of Stokes and anti-Stokes scattering to temperature
ϵ	porosity
ϵ_{eff}	effective porosity
ϵ	emissivity of thermal radiation
ζ_{Nu}	standard deviation normalized by mean
ζ_T	standard deviation normalized by mean
η	detector efficiency

η_+	detector efficiency of Stokes signal
η_-	detector efficiency of anti-Stokes signal
κ	permeability
κ_i	length ratios specifying the geometry
λ	wavelength
λ_+	wavelength resulting from Stokes Raman scattering
λ_-	wavelength resulting from anti-Stokes Raman scattering
μ	arithmetic mean
μ	dynamic viscosity
ν	kinematic viscosity
ξ_{Nu}	relative deviation of ζ_{Nu} to reference case
ξ_T	relative deviation of ζ_T to reference case
ρ	density
σ	Boltzmann constant
σ	standard deviation

Mathematical operators

$\partial\,(...)$	partial derivative
$\mathrm{d}\,(...)$	total derivative
Δ	difference
Δ	Laplace operator
∇	nabla operator
$\mathbf{a}$	vector/tensor (bold print)
$\ln\varphi$	natural logarithm of variable φ
$\mathrm{err}(\varphi)$	absolute percentage error of variable φ
$\exp\varphi$	exponantial function of variable φ
$\overline{\varphi}$	temporal average of variable φ
$\langle\varphi\rangle$	spatial average of variable φ
$\langle\overline{\varphi}\rangle$	spatio-temporal average of variable φ

List of Figures

List of Tables

A Probe manufacturing

The manufacturing processes for Probe V3 and Probe V4 are outlined below, with photographs of key manufacturing steps and concise descriptions, mostly in bullet points. Section A.1 focuses on Probe V3, and Section A.2 focuses on Probe V4.

A.1 Manufacturing Probe V3

The Probe V3 design consists of a helical structure built from an insulated steel capillary that is filled with two glass fibers. The housings connected to the capillaries ends contain the fiber wiring and the soldered electrical connections to the power supply cables. Furthermore, a slim holding structure maintains the capillary's helical shape. All components are mounted on a threaded rod with 3D-printed centralizers, as depicted in Figure A.1. An approximately 92 m-long duplex cable is connected to the probe (see top left in the figure).

The procedure for manufacturing Probe V3 is outlined with the following list:

1. preparation of the stainless steel capillary (cross-sectional dimensions of the capillary: outer diameter 1/16", inner diameter 0.75 mm; supplied by *Altmann Analytics GmbH*)

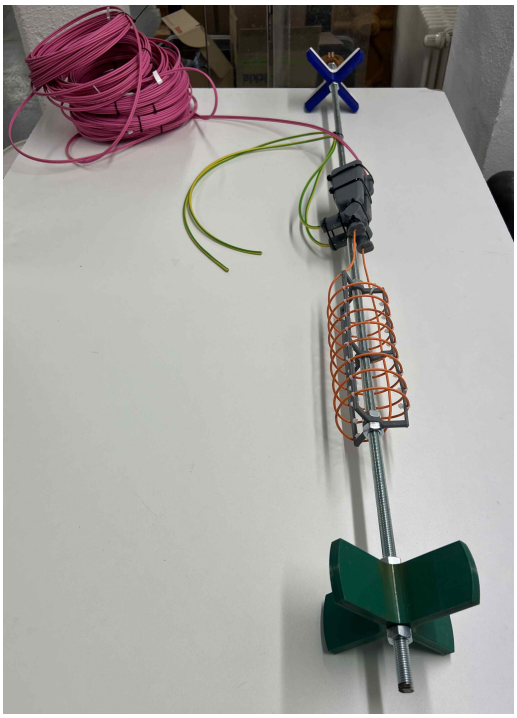

Figure A.1: Probe V3 overview photograph showing all parts of the assembled probe: Connected to a long duplex cable are the housings with the helically bent capillary, which is held in shape by a slim 3D-printed structure. The probe and two centralizers are connected to a threaded rod to enable central positioning in the pipe of the test rig.

a) cut the capillary to the desired length of 2605 mm

b) fix the capillary into the groove of an aluminum profile to prevent bending

2. cover the capillary with the insulative sheath (using a sheath from a fiber-optic patch cable: *84150564 2503913/21 HUBER+SUHNER FIBEROPTIC 1 x 50/OM3 BendOptimized LSFH jacket material*)
3. strip the sheaths of ≈ 4 m duplex-cable (duplex Patchkabel multimode I-V(ZN)H2x1G50/125µm OM4; article no. FCA-IVH2X1G54-2.0 by gt-netstore.de) fibers, and insert fibers into the capillary
4. solder electrical wires onto capillary
5. connect both fiber ends with a fusion splice and fix the fiber wiring to the housings (compare Figure A.2)
6. permanently fix and seal the housing parts using epoxy glue
7. bend the capillary into a helical shape (compare Figure A.3)

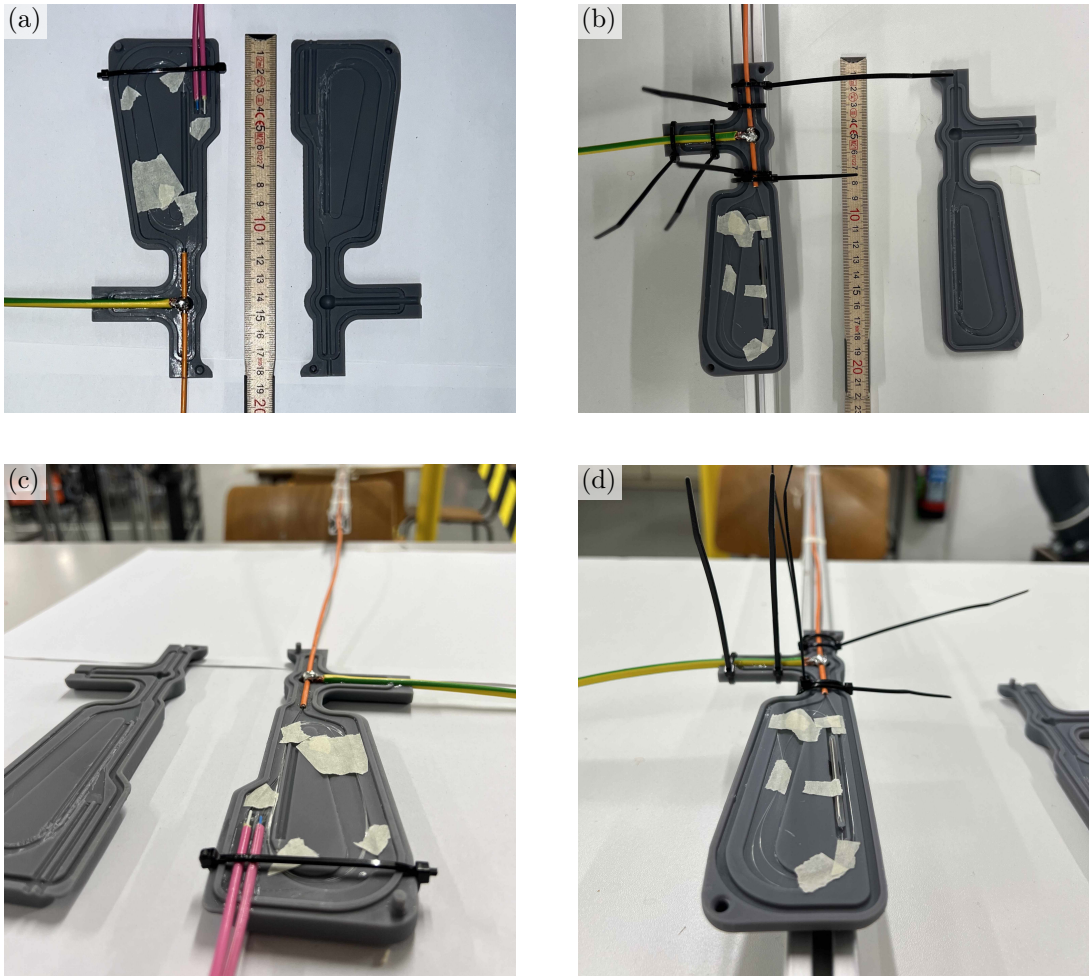

Figure A.2: Photographs of the connector housings of Probe V3 during manufacturing. Both the fiber wiring layout and the soldered electrical connections are presented. (a) and (c) depict the housing, which connects the supply glass-fiber cables and houses two loops of uncovered fiber. (b) and (d) depict the housing containing the fiber splice, which connects both fibers.

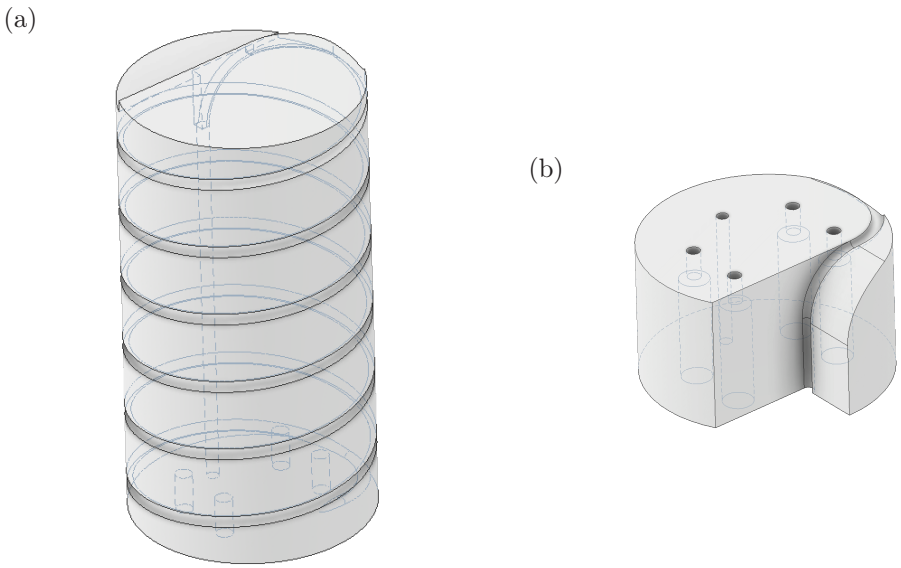

Figure A.3: Matrices used to bend the Probe V3 capillary into shape. The models shown in (a) and (b) were 3D-printed and used to bend the helix of Probe V3.

8. fix the helically shaped, but still very flexible, capillary to the holding structure
9. fix the helix-holding structure and housings onto the threaded rod

Further notes regarding the Probe V3 manufacturing process are:

- The bending matrices are 3D-printed using a fused deposition modeling printer. As depicted in Figure A.3 the bending matrices worked fine for a test capillary. During the manufacturing process of Probe V3, however, the fiber needs to be inserted into the capillary before bending the capillary. Thus, to ensure mountability, slits were cut into the matrices to position the capillary into the inner hole of the matrix before bending.
- Because of elastic deformation during bending, the diameter of the bending matrix is 20 % smaller than the final helix diameter.
- The housings (compare Figure A.2) and the helix-holding structure were manufactured by stereolithography 3D-printing.
- The soldering wire used is not compatible with stainless steel. As the copper leads are tightly wrapped around the capillary before soldering, the electrical connection remains stable, yet its electrical resistance varies. Thus, to measure the electrical resistance of the helical probe, a bit of the sheath is scraped off and another wire is connected using a clamped connection, as depicted in Figure A.4. The electrical resistance of the partial length is successfully measured to $1.184 \pm 0.0258\,\Omega$ with a *KEITHLEY 2000* multimeter at eight heating currents ranging from 1 to 15 A and scaled to $1.247 \pm 0.027\,\Omega$ for the full heated capillary length (2547 mm full heated capillary length, 2417 mm partial capillary length used for resistance measurement). After the measurement of the probe's electrical resistance, the sheath is repaired using epoxy glue.

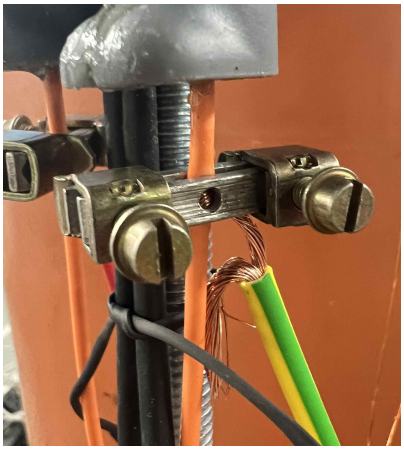

Figure A.4: The electrical resistance of the Probe V3 capillary is measured using cables that are firmly clamped onto the capillary at a distance of 25 mm + 40 mm from the soldering points.

A.2 Manufacturing Probe V4

The Probe V4 design comprises two open capillary rings, which are each filled with fiber coils that contain 9 m of fiber length. The rings are insulated with heat-shrink tubing and clamped to copper wires for electrical connection. The wiring at the open end of the ring is cast in epoxy, and the rings are fixed to a threaded rod with a stereolithography 3D-printed structure. Furthermore, centralizers are fixed to the threaded rod to centralize the probe in the test rig's pipe. Connected to the rings are electrical wires and an approximately 80 m-long fiber-optic duplex cable.

The procedure for manufacturing Probe V4 is outlined with the following list:

1. preparation of the ring capillary
    a) cut the capillary to the desired length and deburr sharp edges
    b) bend the capillary into a ring shape using a 3D-printed matrix
    c) install the heat-shrink tube (*HellermannTyton HIS-3-6/2 BK*)
    d) mount the clamps for electrical wiring
    e) measure the electrical resistance ($R = 0.048 \pm 0.003\,\Omega$, using a *DISA TYPE 55M01* bridge circuit)
2. fiber installation
    a) from the fiber-optic duplex cable (DIAMOND 302-302-271T200 Duplex Patchcord ctc133 OM3 Biegeoptimierte Faser TB3), select one cable and strip its sheaths over a length of 25.5 m to reveal its glass fiber
    b) thread the prepared fiber 40 times through Ring 1, cover 0.5 m of fiber with protective sheaths, thread the fiber 40 times through Ring 2, and add 3 m of protective sheath to the remaining fiber (compare Figure A.5 (a) and (b))
    c) connect both fibers of the duplex cable with a fusion splice
3. epoxy casting
    a) design and 3D-print casting molds
    b) mount and seal casting molds

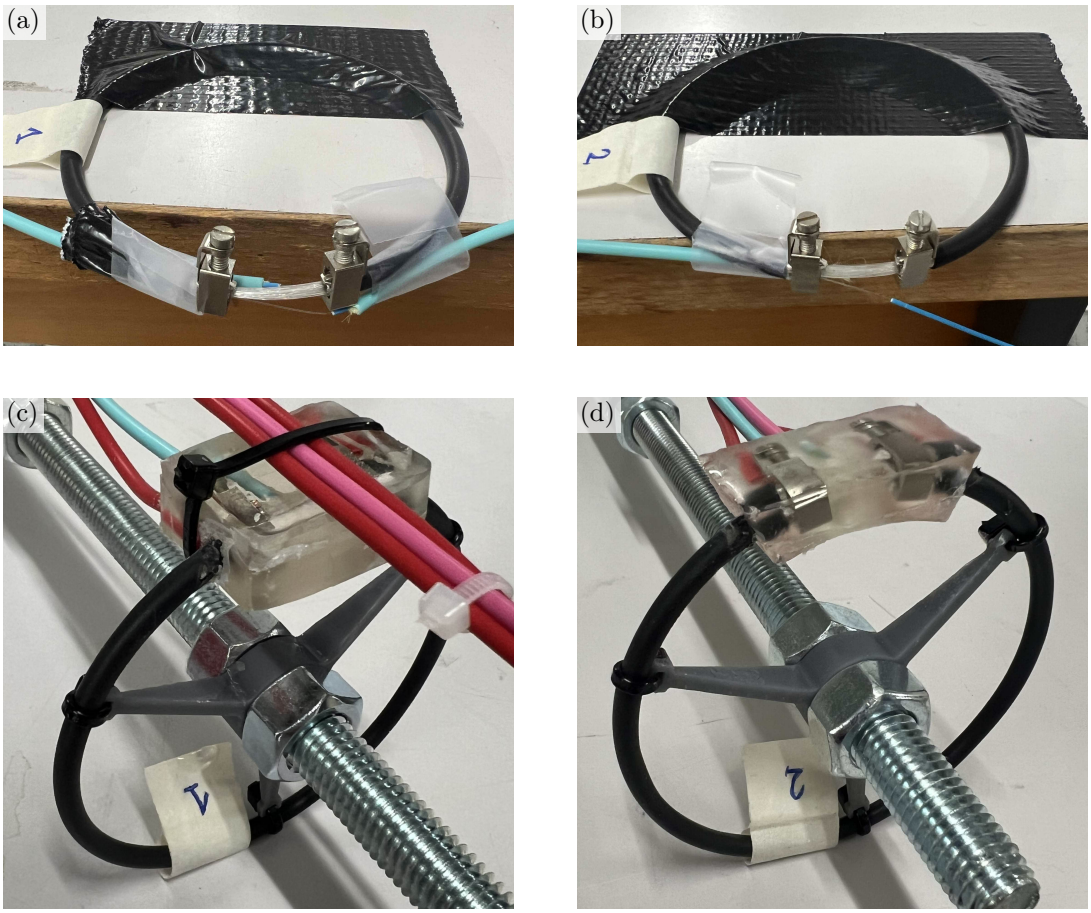

Figure A.5: Photographs of the Probe V4 manufacturing process. Both rings are shown in (a) and (b) after the fiber has been threaded through them, and in (c) and (d) after completion.

c) cast with epoxy

d) remove molds

4. mount the Probe onto the threaded rod together with centralizers (see Figure A.5 (c) and (d), Figure A.6 (b), and Figure A.7)

In particular, the installation of the fiber into the rings is a tricky endeavor because it carries a high risk of damaging and breaking the fiber. A positioning mistake in the ring-fiber arrangement occurred before casting, as depicted in Figure A.6. This positioning error led to a sharp bend in the fiber entering Ring 1 (upper fiber in Figure A.6 (a)). Rearranging the fibers at this stage was not carried out because of the high risk of breaking the fiber. In the first building iteration (depicted in Figure A.6 (b) on the right) the fiber broke at the second ring.

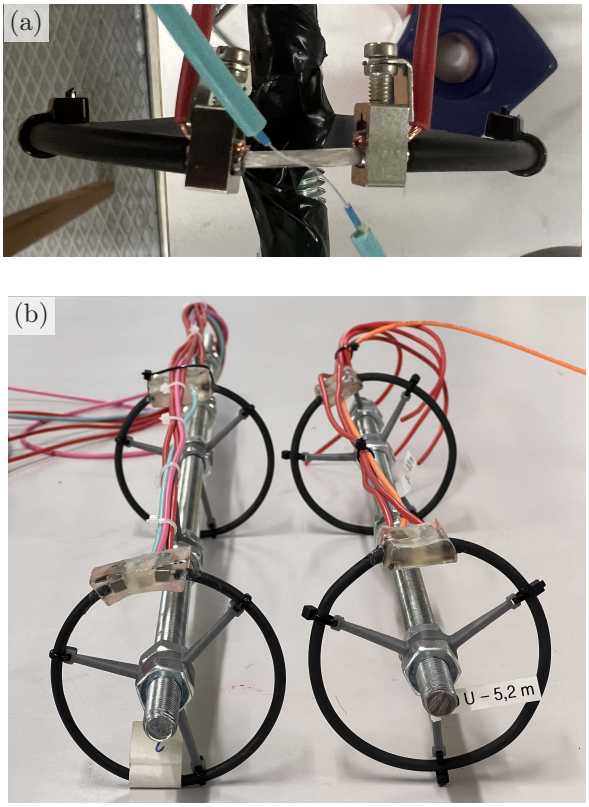

Figure A.6: (a) Photograph detailing an unintended fiber-crossing problem, which results in a sharp bend radius of the optical fiber entering Ring 1 of Probe V4. (b) Photograph showing both iterations of Probe V4. The first iteration (right side) is connected to only one fiber, as the return fiber broke during the casting process. Accordingly, only single-ended DTS measurements were possible with the first iteration. To enable double-ended DTS measurements, a second iteration (left side) was manufactured.

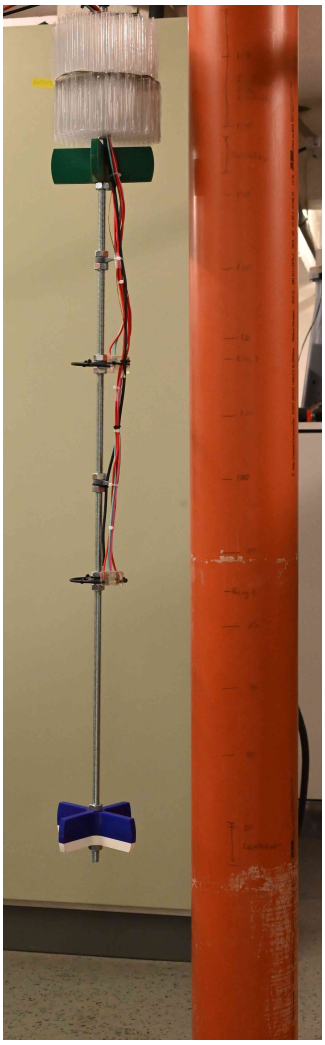

Figure A.7: Photograph of the finalized Probe V4 hanging next to the inner pipe of the test rig.

B Reference temperature sensors

A drift was observed in the reference temperature sensors used in Chapter 4. After the experiments in Chapter 4 were carried out, a test compared the two PT1000 sensors used in Chapter 4 with two new sensors. This test revealed that the utilized sensors measure temperatures with a constant offset of about $\pm 0.2\,°C$ relative to the new sensors. A consultation with the manufacturer revealed that the sensors are protected with glass-silk sleeves that are not guaranteed to be waterproof and that their application in water led to the drift. This drift is not discussed as an error source in Chapter 4 because the observed measurement offsets are in th

e range of $2 \ldots 5\,°C$ and this drift contributed at most $0.2\,°C$.

In consequence, a brand-new set of four PT1000 sensors was used for the experiments in Chapter 5. For waterproofing, the cables were covered with heat-shrink tubes, and epoxy glue was applied at the transitions between the heat-shrink tubes and the sensors' metal housings. The sensors were tested prior to the experiments in Chapter 5, as described in Section B.1.

Both DTS devices have the option to acquire PT100 data. In Section B.2, the PT100 data from the *AP Sensing* DTS are compared with the PT1000 data, and in Section B.3, the PT100 data from the *Silixa* DTS are compared with the PT1000 data.

The comparison of the *Silixa* DTS PT100 data with the PT1000 data reveals that a drift also occurred in one of the new waterproofed PT1000 sensors. Thus, Section B.4 investigates the performance of all PT1000 sensors during the Probe V4 experiments presented in Section 5.2 and analyzes the impact of the observed sensor drift on the DTS calibration.

B.1 PT1000 test before the Probe V3 experiments

Figure B.1 (a) shows the PT1000 sensors used to monitor the temperatures in both calibration baths, the validation bath, and the borehole-mimicking test rig. They were tested in ice water, see Figure B.1 (b), and in boiling water, see Figure B.1 (c).

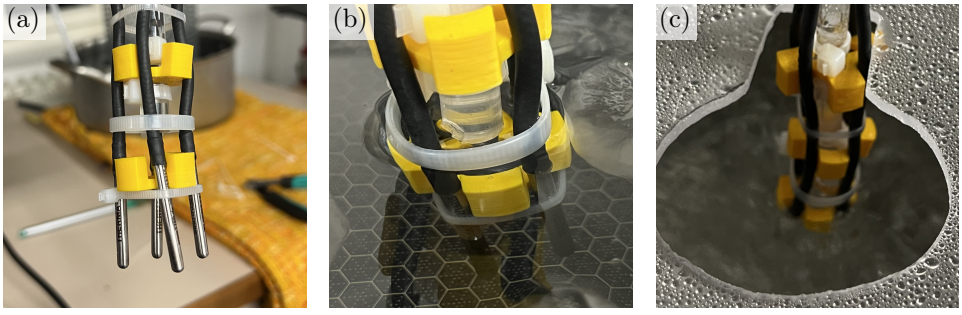

Figure B.1: Photographs of the PT1000 sensor arrangement during the performance test: (a) in air, (b) in ice water, and (c) in boiling water.

Two segments of this test are plotted in Figure B.2, one from the ice bath and one from the hot bath. In each plotted segment, a 90 s-long averaging interval is marked with a light-blue background. The averaged temperatures and electrical resistances from these sections are displayed in Table B.1. One could calibrate the R_0 value of the sensors using the ice-water measurement by defining $R_0 \equiv R_{\text{ice water}}$. Recall that the measured electrical resistance is converted to temperature by equation (2.11). The R_0 calibration procedure seems to improve the measurement in the boiling water, as displayed in the third section of Table B.1.

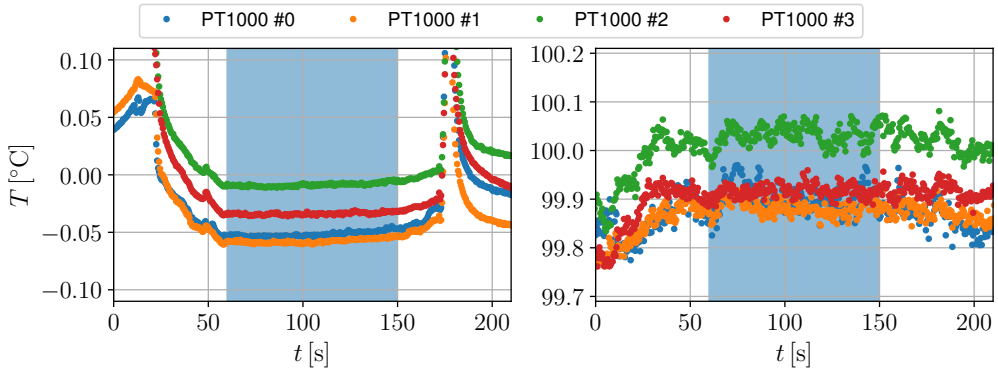

Figure B.2: Result plots from the PT1000 test. On the left, a segment of the ice-bath immersion is shown, and on the right, a segment of the boiling-water immersion is shown. The light-blue areas mark 90 s-long averaging intervals.

Table B.1: Tabular overview of the averaged temperatures and electrical resistances measured in the PT1000 performance test, as well as boiling-water temperatures calculated with R_0 correction.

sensor	T [°C]	R [Ω]
	ice water	
#0	-0.051579	999.798414
#1	-0.057606	999.774858
#2	-0.008669	999.966117
#3	-0.033785	999.867956
	boiling water	
#0	99.901101	1384.679889
#1	99.882237	1384.608340
#2	100.031278	1385.173631
#3	99.916830	1384.739550
	boiling water with R_0 correction	
#0	99,974	
#1	99.964	
#2	100.0435	
#3	99.965	

In conclusion, all sensors measure the temperature within the expected $\pm(0.1\,°\text{C} + 0.0017\,|T|)$ range (according to DIN EN IEC 60751; class AA). The R_0 correction further improves the measurement. However, the R_0 correction is not applied to the measurements in Chapter 5 because the improvement is very small. Furthermore, doubts remain as to whether the measured ice water temperature is actually 0 °C and whether the boiling water temperature is 100 °C. In the ice bath,

the temperature drifts slowly and depends on the mixing and the amount of ice inside the bath[1]. In the hot bath, the temperature is not necessarily 100 °C because the water's boiling temperature depends on the ambient pressure. During the experiment, the ambient pressure was measured to be 999 mbar with an old, analog absolute pressure gauge (with an unknown uncertainty range). At 999 mbar, water should boil at 99.6 °C. The proper ways to perform the R_0 calibration are either to use a fixed-point temperature, for example, the triple point of water, which requires expensive equipment, or to use a fixed-point-calibrated sensor as a reference in a water bath. Neither of these two options was available at the time of the experiment.

B.2 Analysis of the PT100 sensors by the AP Sensing DTS

The PT100 data measured with the *AP Sensing N43856B* DTS are analyzed with the time series from day 3 of measurements with Probe V3 in Figures B.3 and B.4.

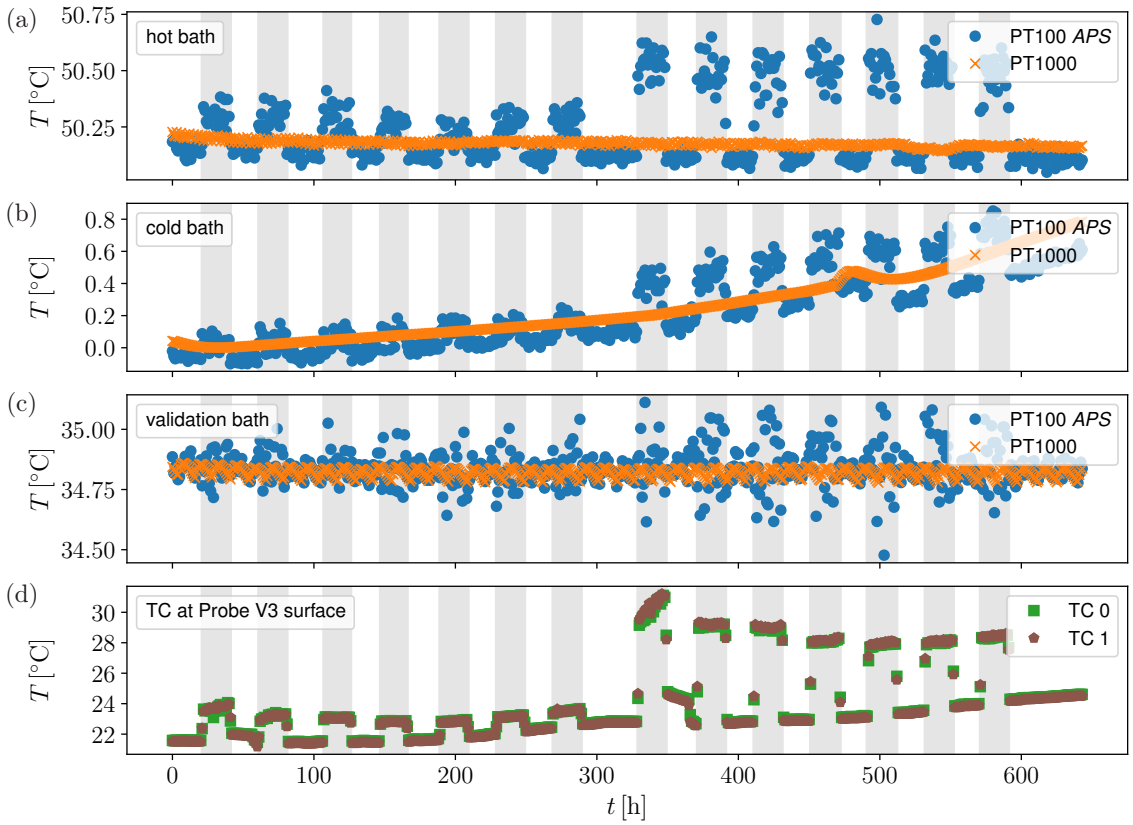

Figure B.3: Comparison of the PT100 sensors from the *AP Sensing* DTS with the PT1000 sensors read by the *NI 9219* data acquisition module. (a), (b), and (c) display the temperatures measured by both a PT100 and a PT1000 sensor in each of the water baths. (d) displays the TC that are glued to the surface of Probe V3 to indicate when the heating is turned on and when it is turned off. Heating Probe V3, which is located in the borehole-mimicking test rig, unexpectedly influences the PT100 measurements.

Figure B.3 (a)-(c) display the temperatures measured by both a PT100 and a PT1000 sensor in each of the three water baths. Furthermore, in Figure B.3 (d), data from TC sensors that are

[1] Because of this finding, the amount of ice was significantly increased in the cold bath during the experiments in Chapter 5. The volume was first filled with ice cubes, and then the voids were filled with water.

fixed to the surface of Probe V3 are shown to indicate when the probe was heated. The PT100 data from the *AP Sensing* DTS react to Probe V3 being heated, although the PT100 sensors are located in a water bath next to the borehole-mimicking test rig that contains the heated Probe V3. Figure B.4 highlights the magnitude of the deviations between the PT100 and PT1000 sensors.

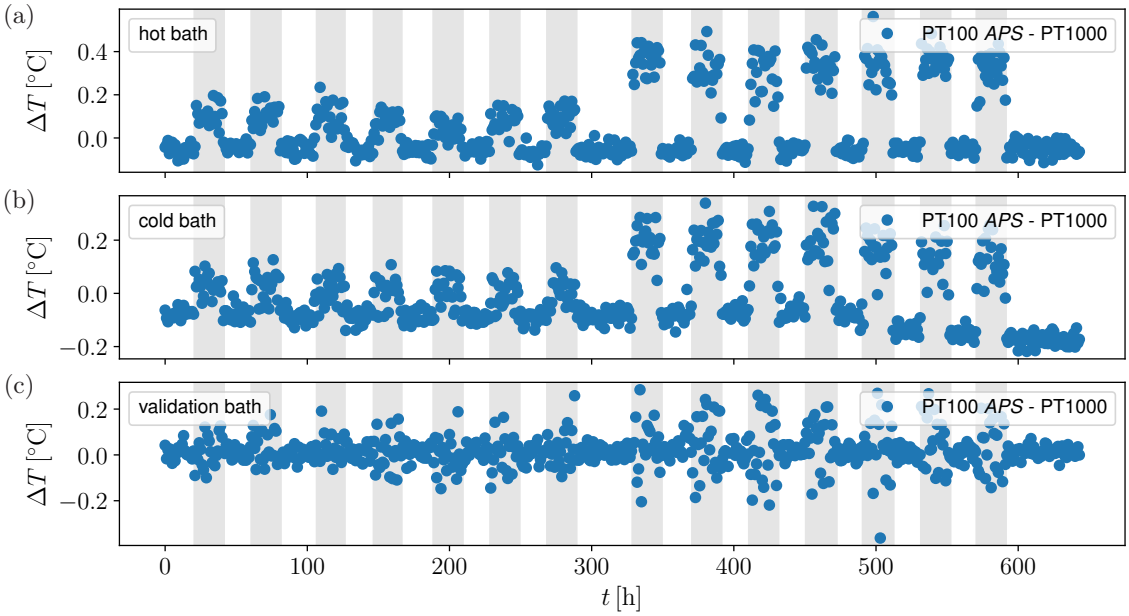

Figure B.4: Highlight plot of the temperature differences measured by the PT100 and PT1000 sensors that are located in identical water baths but read by different data-acquisition devices. See Figure B.3 for the measured temperatures by the PT100 and PT1000 sensors.

Probe V3 is connected to the DTS device via a $\sim 90\,\text{m}$-long fiber-optic duplex cable that should not conduct electrical current. Thus, the DTS device should only detect the heating through a change in the measured backscattering signal. It remains an open question how heating influences the PT100 measurement. As a result of this, the PT100 sensors of the *AP Sensing* DTS were not used for the calibration of the DTS data.

Note that a constant offset in a PT100 measurement is usually attributed to the physical sensor and not to the electrical device, which is used to measure the sensor's electrical resistance. This jumpy behavior, however, cannot be explained by the physical sensor and is expected to be an error introduced by the measurement device. Note also that this phenomenon did not occur when the PT100 sensors from the other DTS device were used in the calibration baths during the Probe V4 experiments.

B.3 Analysis of the PT100 sensors by the Silixa DTS

Throughout the experiments with Probe V4 and the *Silixa XT M* DTS, two PT100 probes connected to the DTS were inserted into the hot and cold calibration baths, in addition to the PT1000 sensors. After the experiments, a comparison test with these PT100 sensors and four PT1000 sensors was carried out. As displayed in Figure B.5, the sensors were fixed together with cable ties, and the sensor tips were covered with a 3D-printed housing to prevent direct contact with ice in the $0\,^{\circ}\text{C}$ water bath.

Figure B.5: Photograph of the PT1000 sensors and the PT100 (*Silixa XT* DTS) sensors used in a water bath test. All sensors are fixed together with cable ties, and a 3D-printed structure covers the sensor tips to prevent direct contact between the sensor tips and the ice in the ice bath. The black cables of the PT1000 sensors and the long metal tubes of the PT100 sensors are recognizable.

The procedure of the experiment is illustrated by the temperature traces in Figure B.6 (a). The sensor package was sequentially inserted into three water baths for $8 - 10\,\text{min}$. Figure B.6 (b) and (c) focus on the temperature ranges of the $0\,°\text{C}$ and $50\,°\text{C}$ water baths, respectively. This test highlights two behaviors: first, the PT100 sensors seem to react more slowly and are offset from the PT1000 measurements. Second, one of the PT1000 sensors (the one used in the hot calibration bath) shows an offset relative to the other three PT1000 sensors.

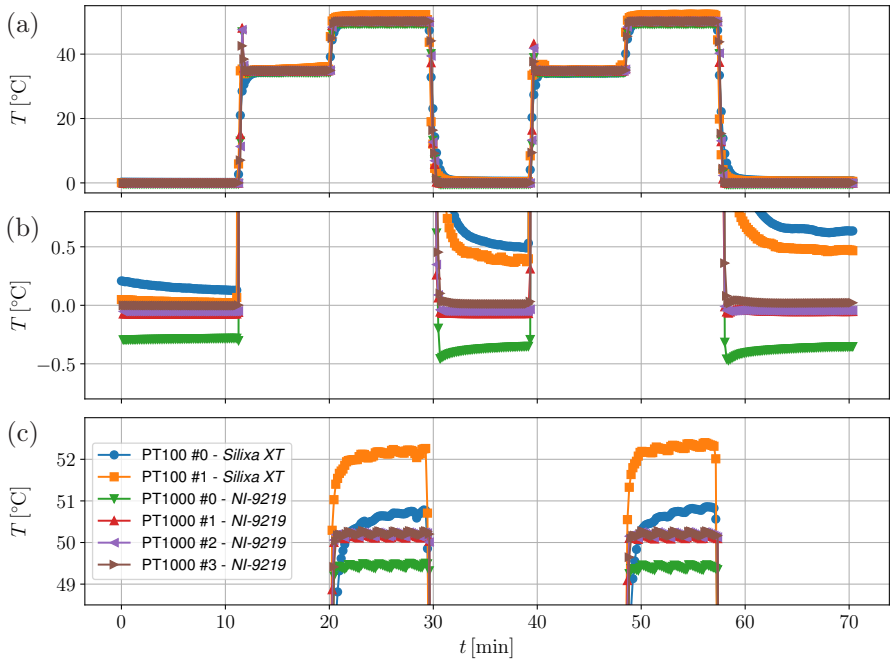

Figure B.6: Plots from the water-bath test with PT1000 sensors read by the *NI 9219* data-acquisition module and PT100 sensors read by the *Silixa XT* DTS device. In the upper plot (a), the full temperature trace of the test is shown. The plots below focus on the ranges near $0\,°\text{C}$ (b) and near $50\,°\text{C}$ (c). It becomes obvious that the PT100 sensors and the PT1000 sensor #0 deviate from the other three PT1000 sensors.

As the PT100 sensors are embedded in long metal cylinders (see Figure B.5), it is expected that they react more slowly than the PT1000 sensors. The sensor offset is suspected to result from an R_0 offset of each PT100. The classification of the PT100 sensors according to DIN EN IEC 60751 is unknown.

The PT1000 #0 offset (green line), however, is unexpected and indicates that this sensor has drifted since the test prior to the experiments with Probe V3 (see Section B.1). Further analysis of this drift behavior during the Probe V4 experiments and its impact on the $\Delta T_{1,\infty}$ values measured by Probe V4 is provided below.

B.4 Analysis of the PT1000 data during the Probe V4 experiments

The PT1000 probes, which are read by the *NI 9219* data acquisition device, are used throughout Chapter 5 to monitor the temperatures in water baths. The temperatures are then used for the calibration of the DTS data from Probe V3 and Probe V4. For waterproofing, the PT1000 probes were coated with heat-shrink tubing. However, after prolonged exposure to water, some of the sensors drifted. In the following, this drifting behavior and its impact on the measurements are discussed.

Figure B.7 shows averaged PT1000 data for each water bath over the complete duration of the experiments with Probe V3. The hot water bath data in Figure B.7 (a) contain multiple outliers and reveal drift behaviors that is discussed below in conjunction with Figure B.8. Figure B.7 (b) shows the PT1000 data from the cold water bath. Its temperature remains fairly constant over the measurements. During the first twenty data files, a small amount of variation and two outliers to higher temperatures are noted. All of these can be explained by the amount of ice supplied to the water. During this time, it was found that – to maintain a constant temperature at 0 °C – the ice needs to be refilled after at most eight hours of measurement. Thus, the PT1000 measurements in the ice bath are considered correct, and no adverse impact on the calibration is expected, as the PT1000 always provided a correct reference for the actual fiber temperature. Figure B.7 (c) shows the data from the PT1000 in the validation bath. It clearly shows that the measured temperature decreased until data file #61. Between data files #61 and #62, the sensor was replaced, which confirms that the prior sensor drifted. As this validation bath was always intended as an extra bath for backup and calibration validation only, its data were actually not used, and the drift of this sensor did not influence any measurement in Chapter 5.

The behavior of the PT1000 sensor in the hot calibration bath is detailed in Figure B.8. In addition to the PT1000 data, the data from the PT100 sensor by the *Silixa* DTS device and the 'corrected' PT1000 data are also displayed. Furthermore, five occurrences of large offsets are highlighted. Offset point ② is the only offset where the PT1000 measured correctly because the heater of the water bath was, by mistake, set 0.5 °C higher than usual. All the other misaligned sections are drift offsets. The reason why the sensor recovered from its deviation after drift sections ①, ③, and ④ is that a longer measurement break of multiple days followed each of these sections, during which the fiber torus that contains the PT1000 sensor was removed from the water bath.

The question arises as to how large the impact of this drift in the reference temperature (which is used for the calibration of the DTS data) is on the measurement of $\Delta T_{1,\infty}$. T_1 is measured with the Probe V4 Ring 1 section of the calibrated DTS data, and T_∞ is measured with the Probe V4 Ring 2 section. Since the water-bath heater operated consistently up to data file #69, it is assumed that the correct hot-bath temperature for data files #70-75 is 50 °C ('PT1000 correction' in Figure B.8). For data file #73, the temperature is underestimated by 1.23 °C, and for data file #75, the temperature is underestimated by 1.74 °C. These particular datafiles are selected as they contain datasets at the highest and lowest heating power and thus the highest and lowest measured $\Delta T_{1,\infty}$ ranges.

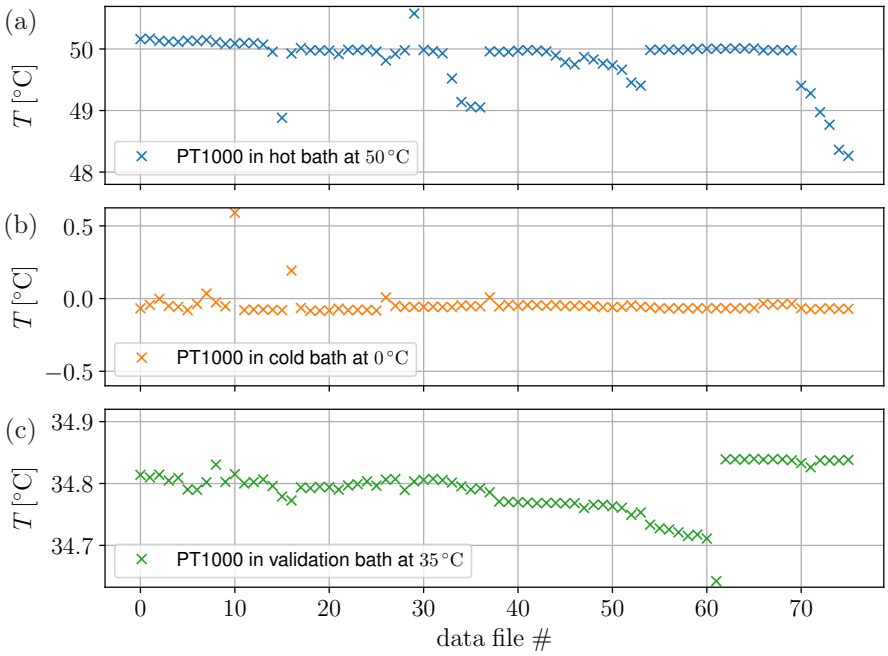

Figure B.7: Averaged PT1000 temperatures over the data files acquired during the measurements with Probe V4. Note that a data file contains one to four datasets. The PT1000 data of the hot calibration bath are displayed in (a), in (b) those of the cold calibration bath, and in (c) those of the validation bath. Although each bath was expected to have identical temperature throughout the experiments, drifts in the measured temperatures occurred.

Figure B.9 shows how these offsets impact the calibration of datasets from the respective data files. It demonstrates that, at the highest heating power, the PT1000 measurement error propagates into a significant error on the order of 0.3 °C. Therefore, the data files #70-75 are processed with the corrected PT1000 value. However, the data files in tap water were not reprocessed with corrected PT1000 data, as the offsets observed in these measurements are an order of magnitude higher than 0.3 °C. Reprocessing of these data, accordingly, would not lead to any overall improvement.

In conclusion, the most important data acquired in deionized water are either not influenced by the PT1000 drift or have been corrected for it. The tap water data are not corrected for PT1000 errors, as these lead only to minor errors compared to the observed errors that presumably originate from precipitation of dissolved solids and bubble formation.

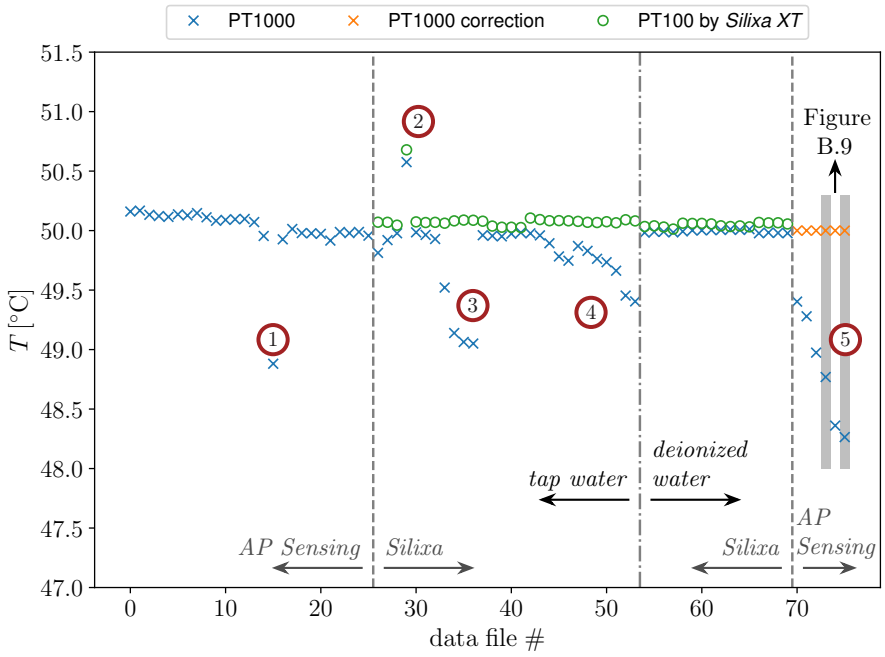

Figure B.8: Analysis plot of the drift behavior of the PT1000 sensor used in the hot-water bath during the experiments with Probe V4. Averaged data are plotted along the data file index, similar to Figure B.7 (a). In addition, the data from the PT100 sensor of the *Silixa XT* DTS, which was also located in the hot-water bath, and a correction for the data files #70–75 are plotted. Furthermore, circled numbers mark drift regions, and arrows highlight which DTS device and which water type was used for the respective measurement.

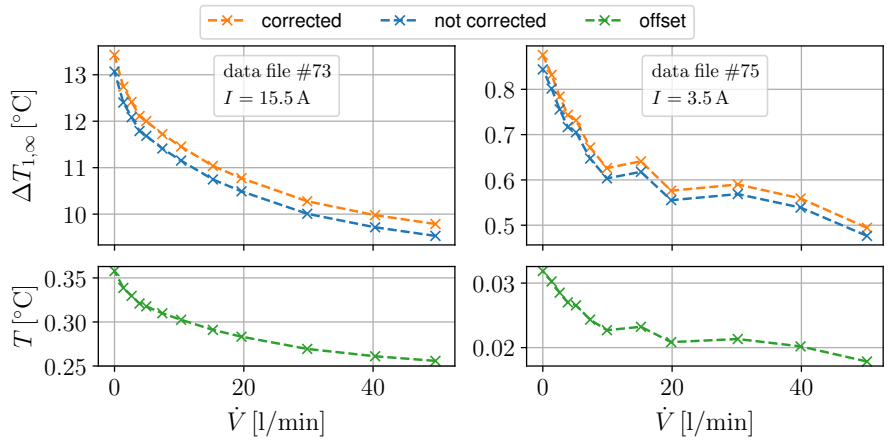

Figure B.9: Plots showing the impact of the PT1000 sensor drift in the hot bath used for calibration of the DTS data for the data files #73 and #75, which are highlighted in Figure B.8. The index #73 data underestimate the hot calibration bath temperature by 1.23 °C, and the index #75 data underestimate the hot calibration-bath temperature by 1.74 °C. The heating current is 15.5 A for index #73 and 3.5 A for index #75. The upper plots display the measured $\Delta T_{1,\infty}$ values for both the uncorrected and corrected cases, while the lower plots display the offset between the two cases.

C DTS configurations

A key finding from Chapter 4 is that the DTS measurement can introduce large uncertainties. Therefore, it is crucial to consider the spatial resolution of the DTS in the design of the experiment and to calibrated the DTS data using monitored constant-temperature sections as a reference (see Subsections 2.3.2 and 2.3.3). In the following, uncalibrated data are compared with two different calibration strategies in Section C.1, the effect of data averaging is shown in Section C.2, and the uncertainty in the validation bath section is discussed in Section C.3.

Most of these investigations are conducted with the *AP Sensing N4386B* DTS and the fiber setup of Probe V3, which is shown in Figure C.1. It comprises Probe V3, 92 m of duplex cable, and three monitored constant-temperature sections, which are introduced in Subsection 3.2.4. Each section contains several meters of duplex cable, a PT1000 reference sensor, and, for the experiments displayed here, also contains PT100 reference sensors that are directly connected to the DTS device. These are utilized for internal calibration of the DTS device.

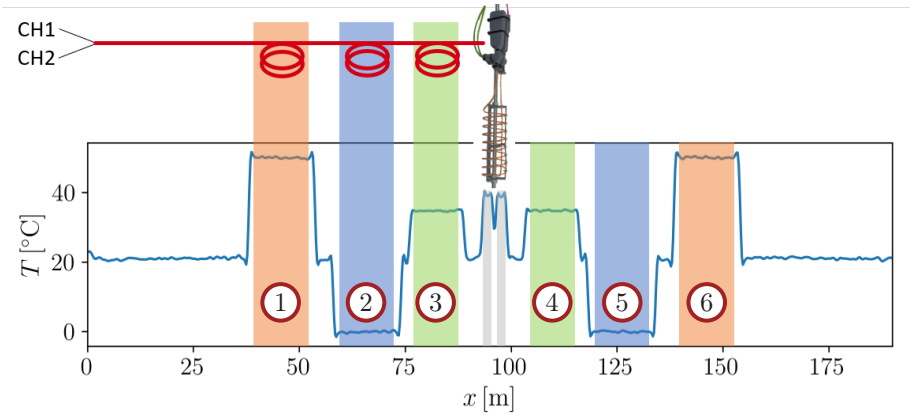

Figure C.1: Visualization of the DTS setup and numbering of the fiber sections in the monitored reference baths.

Furthermore, to show the impact of calibration on the data from the other DTS device (*Silixa XT M*), two investigations are presented using the Probe V4 setup, which is introduced in Figure 3.8. The data are from the validation experiment described in Subsection 5.2.2, in which Ring 1 of Probe V4 is inserted into the validation bath.

C.1 Comparison of calibration configurations

Table C.1 shows several different classifications for the DTS data acquisition and calibration, and Table C.2 provides an overview of the following six figures that demonstrate the effect of these settings. The data from setup 1 were acquired with a DTS measurement time of 30 s per channel. With setup 2, the DTS measurement time is set to 10 s per channel because of the higher signal to noise ratio with the *Silixa* DTS.

Figures C.2 to C.9 are all calibration analysis figures for a configuration outlined in Table C.2. Each calibration analysis figure shows the full temperature trace in the upper plot and temperature deviations in the lower plot. The temperature deviations can only be computed for sections with known reference temperature. Based on the deviations to the reference temperatures the performance of specific DTS settings and calibration algorithms can be judged. Thereby, it is concluded that **TSB – rbs 1,2,5,6 – DE** T_W delivers the best performance (nomenclature according to Table C.1). Thus, this calibration procedure is favored and applied throughout Chapter 5.

Table C.1: Classification of investigated DTS calibration configurations.

by signal	
SE CH1	single-ended channel 1
SE CH2	single-ended channel 2
DE	double-ended

by calibration algorithm	
NC	no calibration
I	internal calibration by DTS
TSB	by des Tombe, Schilperoort, Bakker [23]

by used reference bath section (rbs)
1,2
1,5
1,2,5,6

by signal in DE-TSB	
T_F	channel 1 signal
T_B	channel 2 signal
T_W	weighted signal of both channels

by setup: probe and DTS	
1	Probe V3, *AP Sensing N4386B*
2	Probe V4, *Silixa XT M*

Table C.2: Overview of the figures displaying the results of the DTS-calibration-configuration investigation. (T_F, T_B, and T_W are introduced at the end of Section 2.3.3).

Figure	calibration algorithm	reference bath section	signals	setup
Figure C.2	NC	/	SE CH1, SE CH2	1
Figure C.3	I	rbs 1,2	SE CH1, SE CH2, DE	1
Figure C.4	I	rbs 1,5	SE CH1, SE CH2, DE	1
Figure C.5	TSB	rbs 1,2	SE CH1, SE CH2, DE	1
Figure C.6	TSB	rbs 1,2,5,6	SE CH1, SE CH2, DE	1
Figure C.7	TSB	rbs 1,2,5,6	DE: T_F, T_B, T_W	1
Figure C.8	NC	/	SE CH1, SE CH2	2
Figure C.9	TSB	rbs 1,2,5,6	SE CH1, SE CH2, DE	2

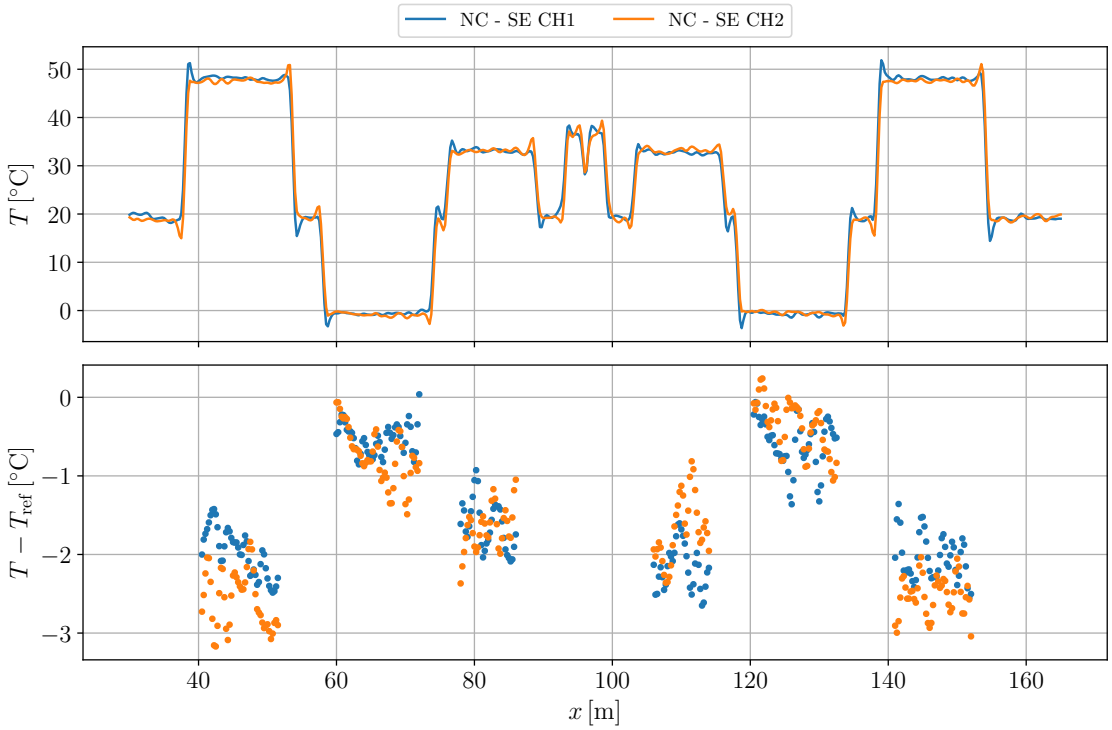

Figure C.2: Calibration comparison plot series: **NC – SE CH1, SE CH2 – setup 1** according to Tables C.1 and C.2. The upper plot displays the measured DTS temperature as a function of fiber distance, and the lower plot shows the temperature difference between the DTS and the PT1000 measurement from each water bath. Note that CH2 measures from right to left.

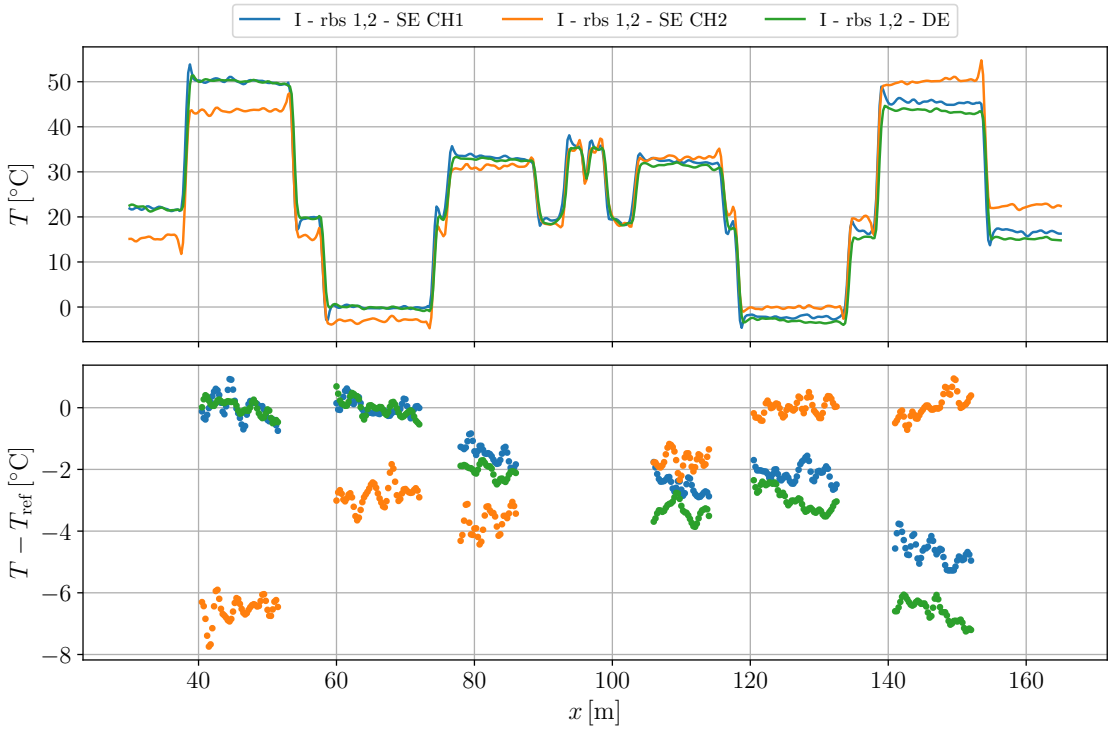

Figure C.3: Calibration comparison plot series: **I – rbs 1,2 – SE CH1, SE CH2, DE – setup 1** according to Tables C.1 and C.2. The upper plot displays the measured DTS temperature as a function of fiber distance, and the lower plot shows the temperature difference between the DTS and the PT1000 measurement from each water bath. Note that CH2 measures from right to left.

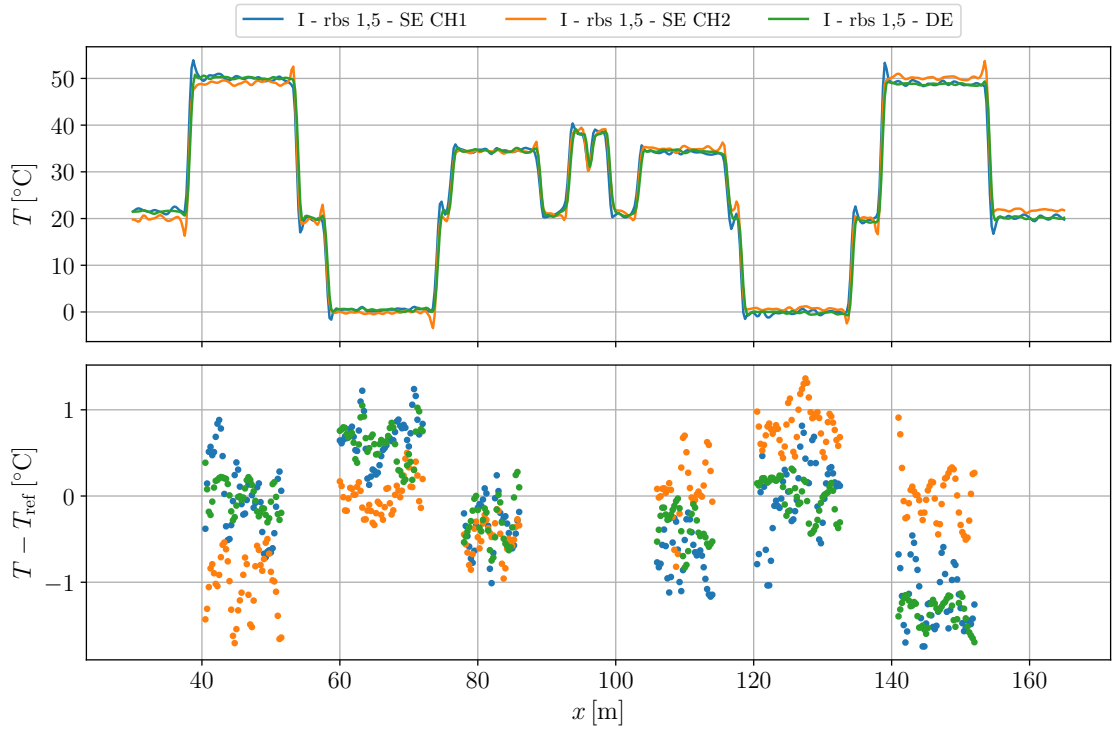

Figure C.4: Calibration comparison plot series: **I – rbs 1,5 – SE CH1, SE CH2, DE – setup 1** according to Tables C.1 and C.2. The upper plot displays the measured DTS temperature as a function of fiber distance, and the lower plot shows the temperature difference between the DTS and the PT1000 measurement from each water bath. Note that CH2 measures from right to left.

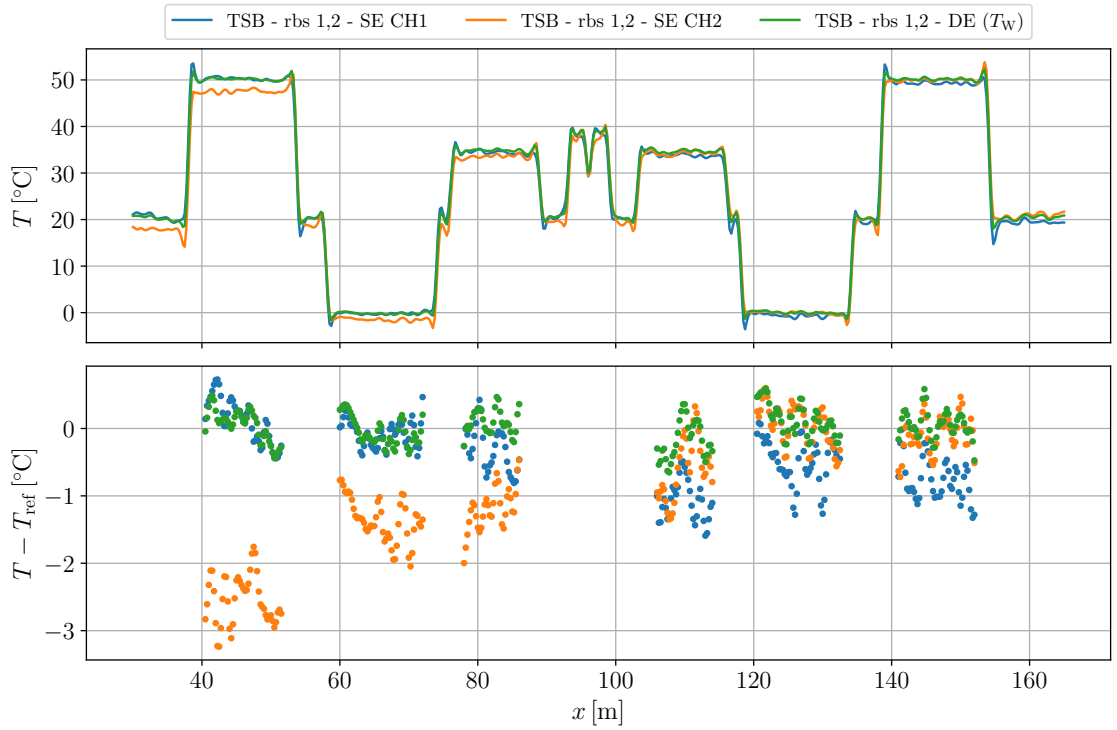

Figure C.5: Calibration comparison plot series: **TSB – rbs 1,2 – SE CH1, SE CH2, DE – setup 1** according to Tables C.1 and C.2. The upper plot displays the measured DTS temperature as a function of fiber distance, and the lower plot shows the temperature difference between the DTS and the PT1000 measurement from each water bath. Note that CH2 measures from right to left.

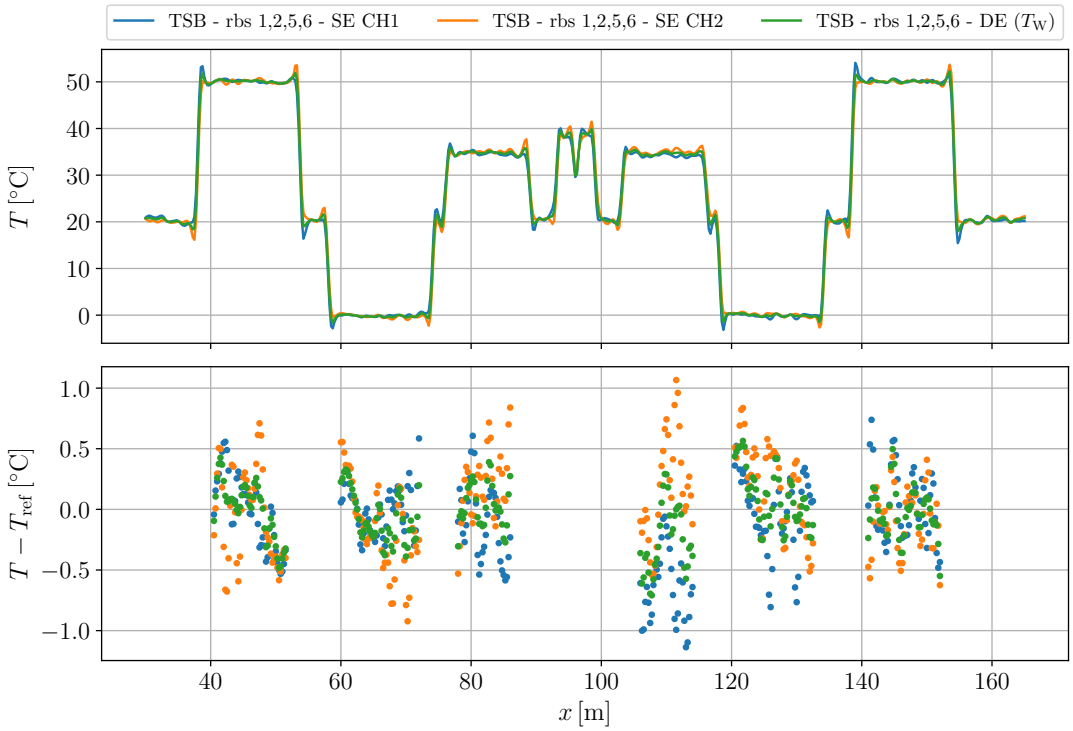

Figure C.6: Calibration comparison plot series: **TSB – rbs 1,2,5,6 – SE CH1, SE CH2, DE – setup 1** according to Tables C.1 and C.2. The upper plot displays the measured DTS temperature as a function of fiber distance, and the lower plot shows the temperature difference between the DTS and the PT1000 measurement from each water bath. Note that CH2 measures from right to left.

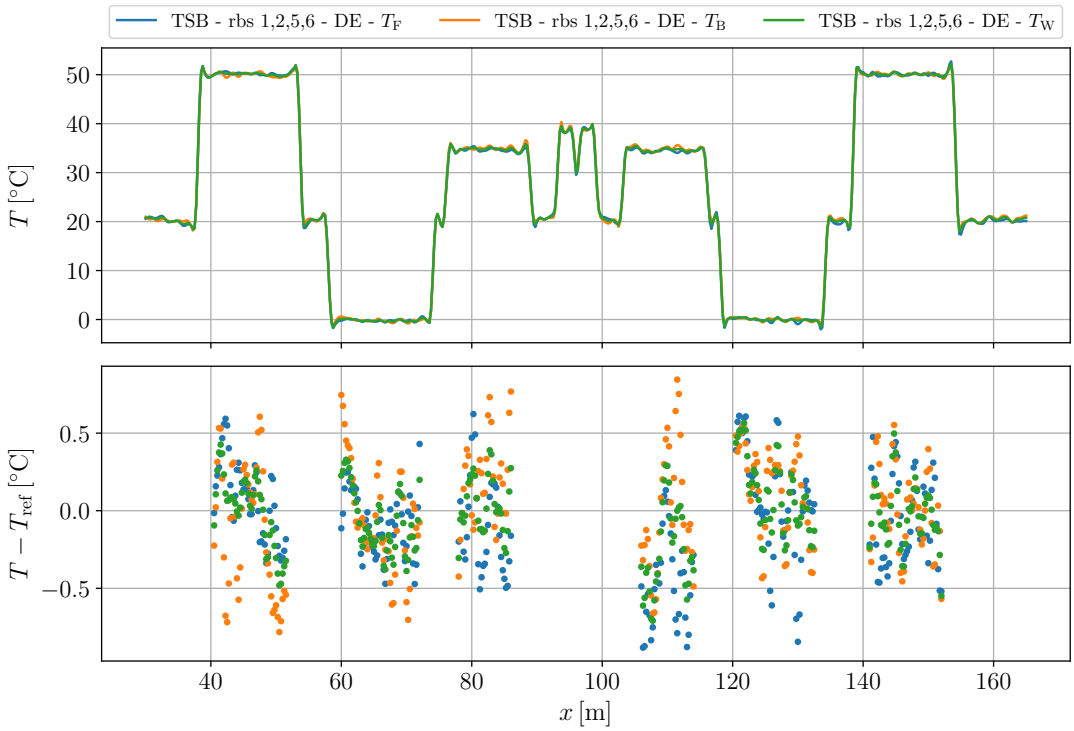

Figure C.7: Calibration comparison plot series: **TSB – rbs 1,2,5,6 – DE:** T_F, T_B, T_W **– setup 1** according to Tables C.1 and C.2. The upper plot displays the measured DTS temperature as a function of fiber distance, and the lower plot shows the temperature difference between the DTS and the PT1000 measurement from each water bath. Note that T_B is calculated from CH2 data, which is measured from right to left.

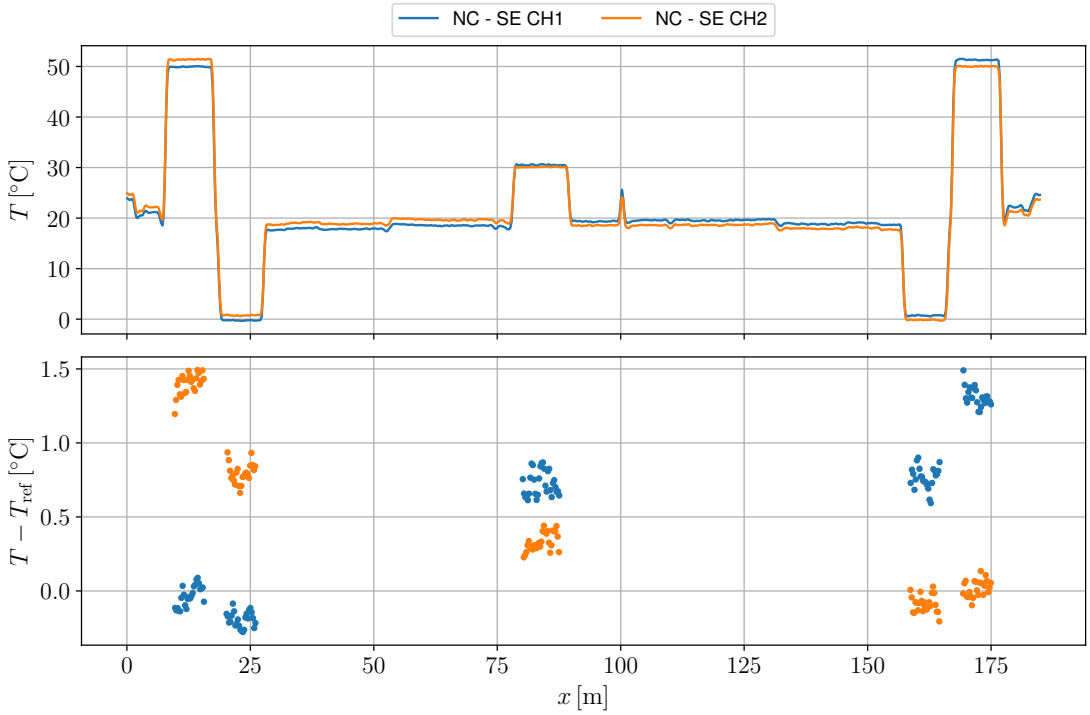

Figure C.8: Calibration comparison plot series: **NC – SE CH1, SE CH2 – setup 2** according to Tables C.1 and C.2. The upper plot displays the measured DTS temperature as a function of fiber distance, and the lower plot shows the temperature difference between the DTS and the PT1000 measurement from each water bath. Note that CH2 measures from right to left. The peak at $x = 100\,\mathrm{m}$ results from the return fiber coming from Ring 2 that is connected to the epoxy cast of Ring 1 (see Figure A.5 (c)).

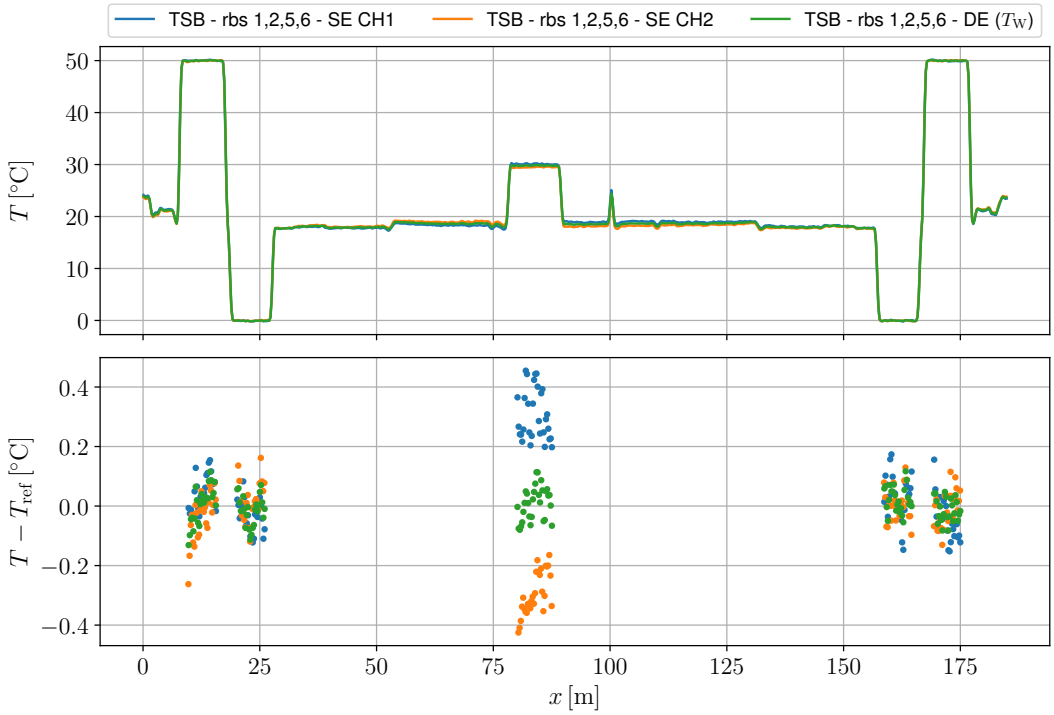

Figure C.9: Calibration comparison plot series: **TSB – rbs 1,2,5,6 – SE CH1, SE CH2, DE – setup 2** according to Tables C.1 and C.2. The upper plot displays the measured DTS temperature as a function of fiber distance, and the lower plot shows the temperature difference between the DTS and the PT1000 measurement from each water bath. Note that CH2 measures from right to left. The peak at $x = 100\,\mathrm{m}$ results from the return fiber coming from Ring 2 that is connected to the epoxy cast of Ring 1 (see Figure A.5 (c)).

C.2 Impact of time averaging on DTS measurements

The impact of time averaging is investigated in the two figures below. Figure C.10 compares the effect of DTS-internal averaging with averaging in the post-processing. As only minor differences occur, the shorter measurement time of 30 s per channel is used with the *AP Sensing* DTS throughout Chapter 5. Figure C.11 demonstrates the general improvement due to time averaging for the data series acquired with a measurement time of 30 s per channel.

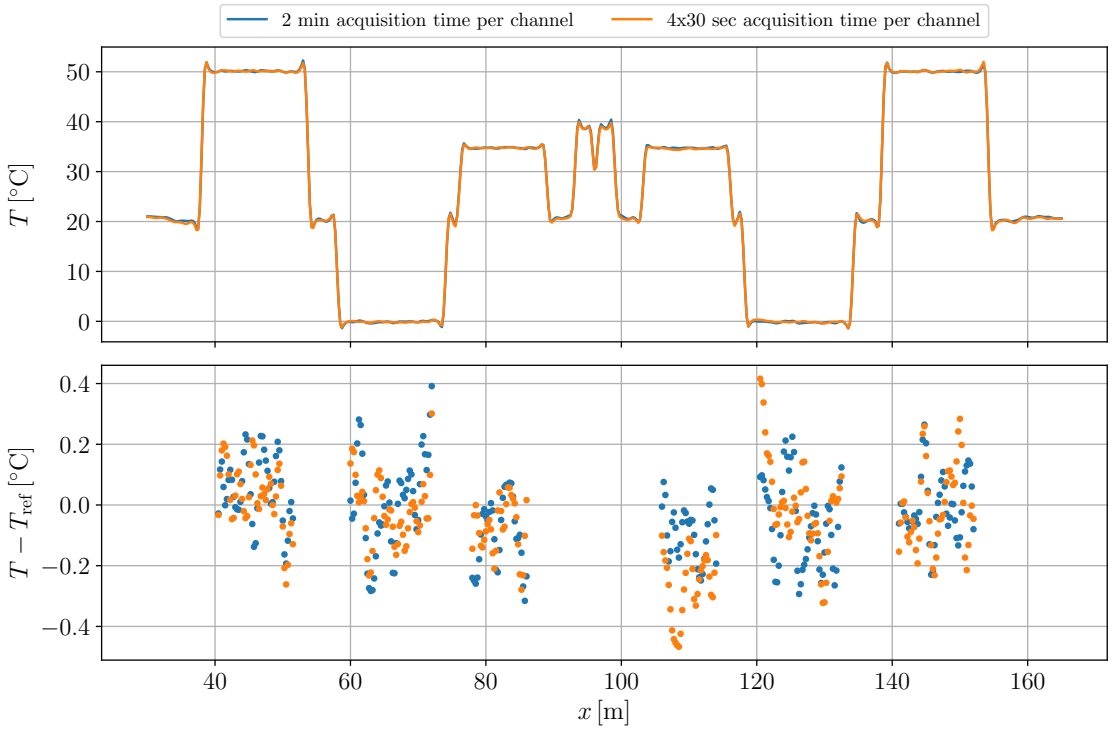

Figure C.10: Comparison of two measurements with different acquisition times of the DTS device to investigate whether DTS internal averaging is superior to averaging in the post processing. For a fair comparison, the data with shorter acquisition time are averaged in the post-processing. The DTS calibration settings of the investigated data are TSB – rbs 1,2,5,6 – DE (T_{W}) – setup 1 according to Table C.1.

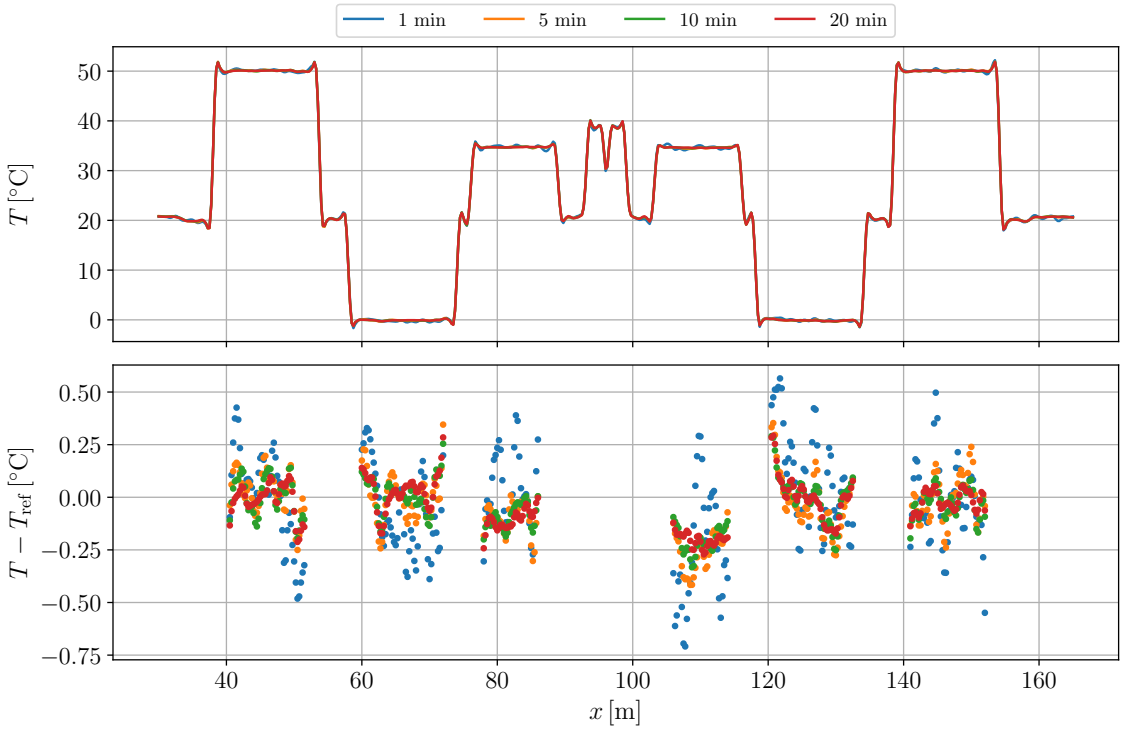

Figure C.11: The plots depict four DTS data traces, each averaged over a different duration in the post-processing. The DTS data were acquired with a measurement time of 30 s per channel. The DTS calibration settings of the investigated data are TSB – rbs 1,2,5,6 – DE (T_W) – setup 1 according to Table C.1.

C.3 Uncertainty estimation in validation bath

In Figure C.12, the DTS measurement uncertainty is estimated for the calibration bath measurements using the Probe V3 setup with the *AP Sensing* DTS device. The calibration bath appears twice in the measured DTS trace as constant-temperature sections 3 and 4 in Figure C.1. The cumulative average CA with the cumulative standard deviation CSD and the moving average MA with the moving standard deviation MSD are used for this estimation as introduced below.

A measured variable φ

$$\varphi = [\varphi_1, \varphi_2, \varphi_3, \ldots, \varphi_n] \tag{C.1}$$

is stored in a list or vector format that contains its values over a time series with N elements. The cumulative average of φ is defined as

$$\mathrm{CA}_n = \frac{1}{n}\sum_{i=1}^{n}\varphi_i \qquad n \in \{1, 2, ..., N\}, \tag{C.2}$$

the cumulative standard deviation is defined as

$$\mathrm{CSD}_n = \sqrt{\frac{1}{n-1}\sum_{i=1}^{n}(\varphi_i - \mathrm{CA}_n)^2} \qquad n \in \{1, 2, ..., N\}, \tag{C.3}$$

the moving average across m samples is defined as

$$MA_n = \frac{1}{m}\sum_{i=n-m+1}^{n}\varphi_i \qquad n \in \{m, m+1, ..., N\}, \tag{C.4}$$

and the moving standard deviation is defined as

$$MSD_n = \sqrt{\frac{1}{m-1}\sum_{i=n-m+1}^{n}(\varphi_i - \mathrm{MA}_n)^2} \qquad n \in \{m, m+1, ..., N\}. \tag{C.5}$$

In the following analysis $m = 10$ is used for the computation of MA and MSD.

In Figure C.12, the measured temperatures – reference temperature T_{ref} and the spatial averages $\langle T \rangle$ – are plotted together with the evaluation of $CA \pm CSD$ and $MA \pm MSD$ for the temperature difference in the validation bath sections $\langle T \rangle - T_{\mathrm{ref}}$. Recall, that $\langle T \rangle$ is a spatial average of the DTS temperature for $x = 78...86\,\mathrm{m}$ (section 3 in Figure C.1) and $x = 106...114\,\mathrm{m}$ (section 4 in Figure C.1), and that T_{ref} is the temperature measured by the PT1000 sensor located next to the fiber in the validation bath.

Figure C.12 (a) demonstrates that the scatter margin of the reference temperature remains negligibly small and can accordingly be considered as quasi-constant at $T_{\mathrm{ref}} = 34.810\,^{\circ}\mathrm{C}$ with a standard deviation of $0.027\,^{\circ}\mathrm{C}$. The spatial averages of the DTS data from the validation bath sections 3 and 4 are plotted next to the T_{ref} data. Their offset and fluctuations to the reference measurement is analyzed in Figure C.12 (b) and (c). Figure C.12 (b) shows – using the cumulative average

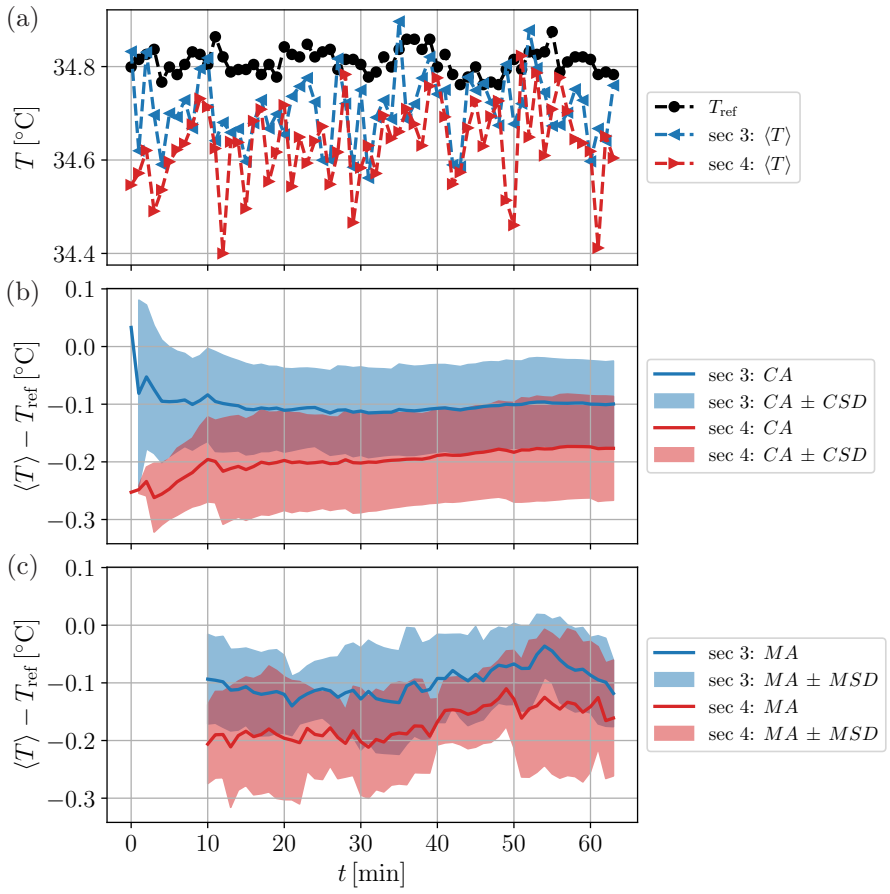

Figure C.12: Analysis of the temperature measurements in the validation bath sections (sections 3 and 4 in Figure C.1). (a) shows the measured reference temperature T_{ref} with the spatial averages $\langle T \rangle$ from both fiber sections. A cumulative average plot of $\langle T \rangle - T_{\mathrm{ref}}$ is shown in (b) and a moving average plot is shown in (c). Recall that CA, CSD, MA, and MSD are computed according to equations (C.2) to (C.5). The DTS calibration settings of the investigated data are TSB – rbs 1,2,5,6 – DE (T_{W}) – setup 1 according to Table C.1, and the acquisition time is set to 30 s per channel.

and cumulative standard deviation – that after approximately ten minutes (corresponding to ten data points), the fluctuations are reduced by an order of magnitude. However as both cumulative averages slowly increase until minute 60, such long averaging interval may be required for full convergence. Figure C.12 (c) highlights with the moving average plot – using 10 data points – that the fluctuations are reduced by an order of magnitude when the measured temperatures are averaged over 10 min. Since the remaining scatter margin is small compared to the overall observed offset to the reference temperature, a ten-minute average is considered sufficient.

From the plots in Figure C.12, it is concluded that only a small temperature measurement error is introduced by the DTS measurements when

- the DTS data are calibrated using the algorithm TSB – rbs 1,2,5,6 – DE T_{W} (according to Tables C.1 and C.2),
- the DTS data are averaged over an 8 m-long section of constant temperature, and
- the DTS data are averaged over ≈ 10 min.

Note that no clear temperature measurement uncertainty value is determined here because the PT1000 sensors used for reference have an uncertainty in the same order of magnitude. That is a limiting deviation of $\pm(0.1\,^{\circ}\mathrm{C} + 0.0017\,|T|)$ according to DIN EN IEC 60751, class AA. The uncertainty of the mean values averaged from the DTS data seems to be slightly larger, on the order of $\pm 0.2\,^{\circ}\mathrm{C}$. A single point measured by the DTS has a higher uncertainty, which is expected to remain within a range of $\pm 0.5\,^{\circ}\mathrm{C}$ (see Figure C.7).

Furthermore, Figure C.13 demonstrates that the validation bath residuals remain within the previously indicated range of $\pm 0.2\,^{\circ}\mathrm{C}$ throughout all Probe V3 measurements with the *AP Sensing* DTS device.

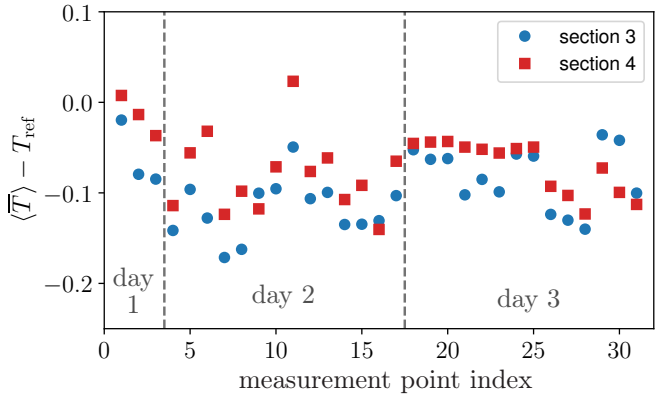

Figure C.13: Validation-bath residuals acquired during the Probe V3 measurements with the *AP Sensing* DTS device. The residuals are computed from the spatio-temporal averages of the DTS temperatures measured in both validation-bath fiber sections (sections 3 and 4 in Figure C.1). Temporally, the data are averaged over the measurement-point duration of 18 min, as introduced in Subsection 5.1.2.

D Direction-sensitive DTS TA in air

The word anemometry, which originates from the Greek words ‘ánemos’–wind and ‘métron’–measure, already indicates that TA was invented and is more widespread in measurement of gaseous flows, mostly air. Furthermore, fiber-optic DTS TA is already an established scientific measurement technique, as outlined in Subsection 2.6.1 with method (iv). Very long glass-fiber-containing steel capillaries are used to measure spatially distributed velocity profiles in the atmospheric boundary layer. However, directional ambiguities arise in this measurement concept. Thus, Lapo et al. [38] addressed this issue by mounting small cones as microstructures on the capillary that influence the heat transfer differently, depending on flow direction. With the fiber-coiled-in-capillary concept invented for Probe V4 in mind, the problem of directional ambiguity further leads to the idea of building a point sensor, called U-probe, capable of measuring flow direction. This probe may not solve the prevailing direction-ambiguity problem on the existing long fiber sections, but it provides a point sensor design that can be added multiple times to the prevailing long fiber setup. When these point sensor probes are connected to the existing fiber and heating device, no additional hardware is necessary to evaluate them. Thus, such a point-sensor concept is a cost-effective solution to obtain wind-velocity and wind-direction information at multiple locations throughout the long fiber setup. Below, first the U-probe design is introduced, then its capability to measure flow velocity and flow direction is demonstrated in a wind-tunnel experiment, and finally an integrated concept for multiple U-probes is proposed.

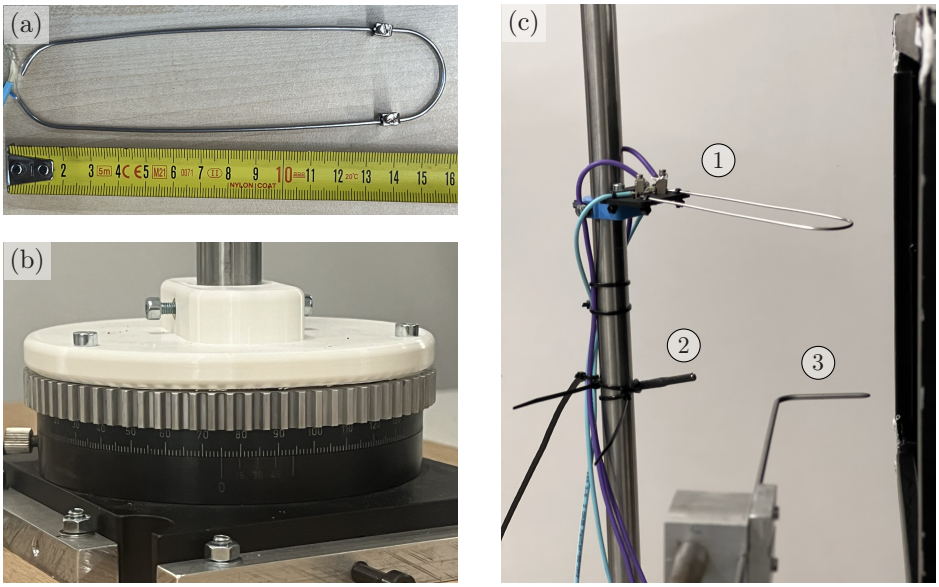

Figure D.1: Photographs of the U-probe and the experimental setup in the wind tunnel. (a) depicts the U-probe during the manufacturing process, (b) shows the goniometer used to precisely set the rotation angle, and (c) shows the nozzle of the wind tunnel on the right and all sensors used in the experiment: the U-probe ①, the PT1000 ②, and the pitot tube ③.

A photograph of the U-probe is shown in Figure D.1 (a). The U-probe consists of a steel capillary bent into a U-shape and filled with four threads of a glass fiber. The manufacturing process of the U-probe is outlined as follows:

1. bending the capillary (cross-sectional dimensions of the capillary: outer diameter 1/16 ", inner diameter 0.75 mm; supplied by *Altmann Analytics GmbH*) into a U-shape and attaching the clamps for electrical connection
2. measuring the electrical resistance of the capillary with a *DISA TYPE 55M01* bridge circuit: $R = 0.136\,\Omega$
3. separating the last few meters of a duplex cable (DIAMOND 302-302-271T200 Duplex Patch-cord ctc133 OM3 bend-optimized fiber TB3) into two strands
4. stripping a few meters of sheath from one of the strands
5. threading the fiber through the capillary four times so that the fiber exiting the capillary has a length of at least 2 m
6. connecting both fiber ends with a fusion splice

Subsequently, the U-probe is mounted on a steel rod that is placed inside the goniometer shown in Figure D.1 (b). The goniometer enables rotation of the U-probe with a precision of 0.1 °.

Figure D.1 (c) shows the setup in the wind tunnel. Three sensors – the U-probe ①, a PT1000 sensor ②, and a pitot tube ③ – are placed just behind the nozzle into a Goettinger-type wind tunnel with open measurement section. The hot-fiber temperature T_1 is measured with the U-probe using the *Silixa XT M* DTS device, the air temperature T_∞ is measured with the PT1000 sensor, and the flow velocity u is measured with the pitot tube. The pitot tube is operated with a *Setra C239* differential pressure sensor that was calibrated using a Betz manometer before the measurements.

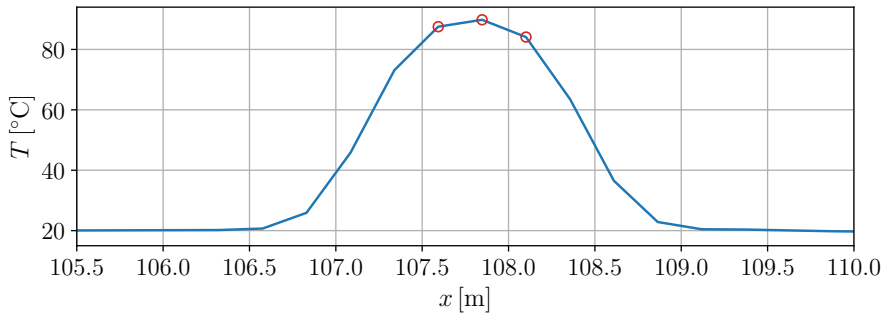

Figure D.2: Temperature profile of the heated U-probe measured with DTS. The red circular markers indicate three coordinates that are averaged to obtain the U-probe temperature.

A DTS temperature measurement trace for the heated U-probe is shown in Figure D.2. No clear temperature plateau emerges, as the fiber length inside the probe is only just above twice the DTS device's spatial resolution. The three marked points are averaged as measurement of T_1.

The U-probe is tested for its sensitivity to flow velocity and flow direction with two experiments that were acquired on two consecutive days. Figure D.3 presents plots of the measured temperature difference $\Delta T_{1,\infty}$ and measured velocity u over time for a dataset of these experiments. The plots show that each parameter setting was held for 8 min and that steady state is attained quickly. For each parameter setting, the latter six minutes of the acquired data are averaged. The results of both experiments are shown in Figure D.4. The $\Delta T_{1,\infty}$–u plot in Figure D.4 (a) demonstrates the sensitivity of the U-probe to varied flow velocities for two constant heating currents at a constant angle of 0 °. The long parallel sections of the U-probe are aligned in streamwise direction at this 0 ° angle. Furthermore, four measurement points from the data acquired on the next day demonstrate

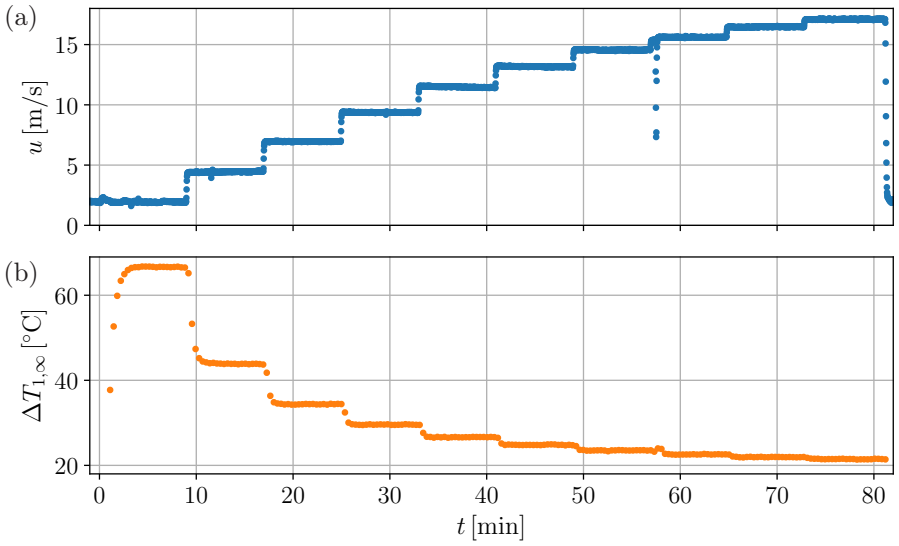

Figure D.3: Temporal sequences of measured velocity u and temperature difference $\Delta T_{1,\infty}$ in the U-probe wind-tunnel experiment: the velocity u is measured with the pitot tube (a), and the temperature difference $\Delta T_{1,\infty}$ is measured with the U-probe and the PT1000 sensor (b). The displayed time sequences are from the 6 A dataset shown in Figure D.4 (a).

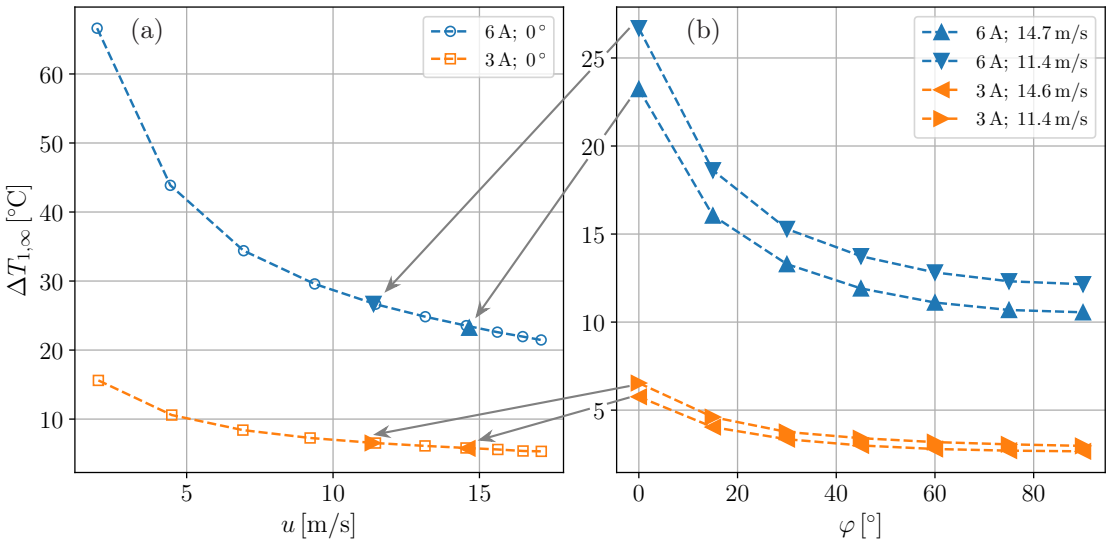

Figure D.4: Results from the U-probe wind-tunnel experiment displayed in $\Delta T_{1,\infty}$–u and $\Delta T_{1,\infty}$–φ diagrams. The graph in (a) depicts the velocity dependence of the heat transfer at an angle of 0 °, which means that the straight sections of the U-probe align with the airflow direction. The graph in (b) depicts the angular sensitivity of the heat transfer. The 0 ° values of (b) are also plotted in (a) to demonstrate reproducibility.

that these measurements are highly reproducible. Figure D.4 (b) presents measurements that test and show the angular sensitivity of the U-probe for two heating currents and two flow velocities.

A single U-probe is not able to measure both flow velocity and flow direction, as both parameters affect the measured temperature of the constantly heated probe. In hot-wire anemometry, this problem was solved with the invention of multiwire probes: probes that contain two or three wires, usually positioned at ±45 ° to the expected main flow direction, enable the measurement of both flow direction and velocity. Two wires enable the measurement of one flow-direction component and three wires of both flow-direction components (see, e.g., Section "9.4 Calibration and its relations - Multiwire probes" in Örlü and Vinuesa [76]). Multiwire probes are used in wind-tunnel experiments

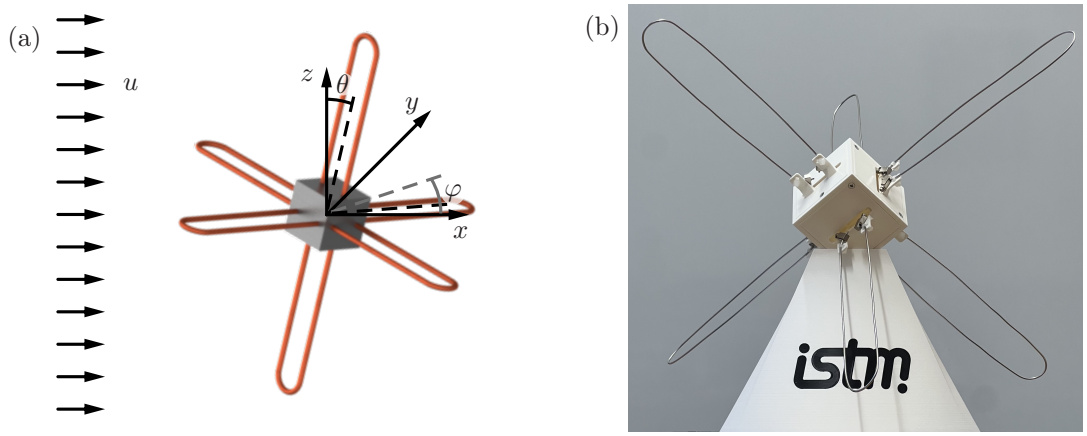

Figure D.5: The extended multi-probe concept for fiber-optic thermal anemometry in air. Six U-probes are connected to a cube to enable measurement of flow velocity and flow direction. (a) shows a sketch of this probe concept, which highlights a 3-dimensional rotation of the probe relative to the airflow. (b) presents a photograph of a demonstration prototype that does not contain any glass fibers.

with a clear main flow direction, and directional ambiguity in main flow direction does rarely occur. However, for measurements in atmospheric flows, the main flow direction is the unknown value of interest. Therefore, Figure D.5 visualizes the proposed concept that contains six U-probes mounted on a cube. The intention is that at least three wires always face the main flow direction and that at least one wire is influenced by the wake of the cylinder. In the wake of the cylinder a different behavior is expected, although it is not yet clear how the wake influences the heat transfer. The wake may lead to slower velocities and thereby more inefficient heat transfer, but the wake may also lead to increased mixing and thus more efficient heat transfer. The wake is expected to lead to fluctuations in the heat transfer that may be recognizable, but there may also be angles at which the wake influences all three downstream U-probes only very slightly. Systematic research on the U-probe multiwire concept is required to assess its potential for measuring atmospheric flows.

E Data availability

Data from the first research stage (Chapter 4) are available upon request. Data from the second research stage (Chapter 5; Appendices B, C, and D) are openly available: https://doi.org/10.35097/g5qy8es9ef8f4ftp.

F Artificial intelligence prompts

Microsoft Copilot was used via an commercial data protection access to facilitate the writing process of the present work with the following prompts:

Prompt 1: "I will ask you for spelling checks of short text sections of an academic text I am writing with latex.
Please keep latex syntax intact in your corrected sentences.
Please outline your corrections.
Provide two corrections:
In the first correction, focus only on grammar and spelling.
In the second correction, provide a version of the text optimized for formal academic tone."

Prompt 2: "I will provide you with a larger text of an academic text I am writing with latex.
Perform a spelling and grammar check only.
Please keep latex syntax intact in your corrected sentences.
Provide the corrected sentences in a diff-style format:
original sentence - corrected sentence - Comment outlining your corrections."